TREE RING RECONSTRUCTION OF MODERN ATMOSPHERIC RADIOCARBON DIOXIDE VARIABILITY OVER THE SOUTHERN OCEAN

by

Rachel Mary Corran

A thesis submitted to the Victoria University of Wellington in fulfilment of the requirements for the degree of Doctor of Philosophy

May 2021

ABSTRACT

The Southern Ocean is the largest ocean carbon sink region. However, its trend of increasing carbon uptake has shown variability over recent decades. It is important to understand the underlying mechanisms of anthropogenic carbon uptake such that the future response of the Southern Ocean carbon sink under climate forcing can be predicted.

The carbon uptake of the Southern Ocean is characterised by the balance of outgassing of CO_2 from carbon-rich deep water and sequestration of anthropogenic carbon into surface waters. Atmospheric radiocarbon dioxide ($\Delta^{14}CO_2$) in the Southern Hemisphere is sensitive to the release of CO_2 from the upwelling of 'old' ^{14}C-depleted carbon-rich deep water at high southern latitudes, but is insensitive to CO_2 uptake into the ocean. Thus $\Delta^{14}CO_2$ has the potential to be used as a tracer of the upwelling observed, thereby isolating the outgassing carbon component.

The Southern Ocean Region has limited atmospheric $\Delta^{14}CO_2$ measurements, with sparse long-term sampling sites and few shipboard flask measurements. Therefore in this PhD project I exploit annual growth tree rings, which record the $\Delta^{14}C$ content of atmospheric CO_2, to reconstruct $\Delta^{14}CO_2$ back in time. Within tree ring sample pretreatment for ^{14}C measurement I automate the organic solvent wash method at the Rafter Radiocarbon Laboratory. I present new annual-resolution reconstructions of atmospheric $\Delta^{14}CO_2$ from tree rings, from coastal sites in New Zealand and Chile, spanning a latitudinal range of 44 °S to 55 °S, for the period of interest, 1985 – 2015. Data quality analysis using a range of replicate ^{14}C measurements conducted within this project leads to assignment of ~1.9 ‰ uncertainties for all results, in line with atmospheric measurements.

In this project I also develop a harmonised dataset of atmospheric $\Delta^{14}CO_2$ measurements in the Southern Hemisphere for this period from different research groups, including the new tree ring $\Delta^{14}CO_2$ records alongside existing data. The harmonised atmospheric $\Delta^{14}CO_2$ dataset has a wide range of applications, but specifically here allows investigation of temporal and spatial variability of atmospheric $\Delta^{14}CO_2$ over the Southern Ocean over recent

decades, thereby also considering the role of upwelling in recent Southern Ocean carbon sink variability. Backward trajectories are produced for the tree ring sites from an atmospheric transport model, to help inform interpretation of results.

Over recent decades a latitudinal gradient of 3.7 ‰ is observed between 41 °S and 53 °S in the New Zealand sector, with a smaller gradient of 1.6 ‰ between 48 °S and 55°S in the Chile sector. This is consistent with other studies, with the spatial variability of atmospheric $\Delta^{14}CO_2$ attributed to air-sea ^{14}C disequilibrium associated with carbon outgassing from ^{14}C-depleted carbon-rich deep water upwelling at ~60 °S, driving a latitudinal gradient of atmospheric $\Delta^{14}CO_2$ in the Southern Hemisphere, with longitudinal variability also observed. A stronger atmospheric $\Delta^{14}CO_2$ latitudinal gradient is observed in the 1980s/1990s relative to later 1990s/2000s. Stronger atmospheric $\Delta^{14}CO_2$ latitudinal gradients observed in 1980s/1990s suggest stronger deep water upwelling thereby greater associated outgassing of ^{14}C-depleted CO_2. These $\Delta^{14}CO_2$-based observations are consistent with modelling studies that predict changes in deep-water upwelling have controlled decadal variability in CO_2 uptake, and are consistent with observation-based studies of decadal changes in rate of CO_2 uptake of the Southern Ocean. The results presented in this thesis present the first observation-based confirmation that decadal changes in the strength of deep-water upwelling can explain decadal changes in the rate of CO_2 uptake.

ACKNOWLEDGEMENTS

Undoubtedly my biggest thanks are to my supervisors: Jocelyn Turnbull, Sara Mikaloff-Fletcher and Nancy Bertler - their unwavering support and patience alongside their expertise have been invaluable. I could not have asked for a better group of inspiring and lovely supervisors – I truly struck gold! Office doors were always open for any problem or stupid question. Closely working with Jocelyn throughout my project, I have learnt an amazing amount with her guidance, whilst developing both scientific and life skills, which I could not have achieved without her ongoing encouragement.

Besides my supervisors, I have had the opportunity to work with many other scientists, of particular note: learning essential tree core sample preparation from Andrew Lorrey, and overcoming countless problems of method development with Andy Phillips. Thanks also to my reviewers; Quan Hua, Martin Manning and Kyle Clem, who provided really useful and detailed feedback.

Being trained to operate an accelerator mass spectrometer (AMS) by Albert Zondervan has been an amazing opportunity and I loved every minute - despite us all being somewhat frustrated during an extensive trouble-shooting period – I learnt so much and had chance to peek inside everything! Whilst Albert was on leave, I was 'in the driving seat' of the AMS, and could not have survived without the invaluable expertise of Chris Purcell on the ins and outs of accelerators.

I have also had the privilege of working alongside a great team at the Rafter Radiocarbon Laboratory, who have shown me the ropes and helped me process many of the samples for this project. Everyone (Margaret Norris, Cathy Ginnane, Helen Zhang, Jen Dahl, Julia Collins, Jeremy Parry- Thompson, Nikita Turton and Taylor Ferrick) provided help and support in different ways, including ensuring that the EA combustion line was working well and that all my samples were scheduled accordingly.

Outside of the laboratory I have had continual support and motivation from everyone at the National Isotope Centre (NIC, GNS Science) and other students at Victoria University of Wellington (VUW), for which I am always grateful.

I would also like to thank all the different people that contributed to the fun and success of the fieldwork for the project: researchers, field guides, private landowners and anyone that kindly helped us take tree core samples – a definite muscle-building exercise! This includes Carolyn McCarthy, Vince Beasley, Ricardo de Pol-Holz, Juan Carlos Aravena, Guillermo Duarte, Ian Turnbull, Jane Forsyth and Heritage Expeditions (with further detailed acknowledgements in Chapter 3).

I would not have come to pursue this PhD project if it hadn't been for my undergraduate degree at the University of East Anglia, England, where I had my first glimpse of research during a summer project with Andrew Manning, alongside the opportunity to study abroad in Melbourne, Australia.

Throughout my PhD I've had inspiring chats with friends around the world who never fail to crack me up and motivate me. Along the way I've met so many amazing people who will be lifelong friends and with whom I've had great experiences and made hilarious memories. I truly wouldn't have made it to this point with (some vague form of) sanity and a beaming smile across my face without you all!

Finally, a special mention goes to my mum and sister, who have stood by me (metaphorically - on the other side of the world), proof read far too many drafts over the years and always encouraged me to pursue what I love. Although separated by somewhat more than is required for covid social-distancing, I have also learnt that length of time and distance apart are definitely inversely proportional to our togetherness.

This PhD project would not have been possible without a grant from the Marsden Research Fund, GNS Science, NIWA and VUW (Marsden Fund contract GNS 1502, Is the Southern Ocean carbon sink sinking? Unravelling the Southern Ocean climate change response using atmospheric radiocarbon records., PI Jocelyn Turnbull).

CONTENTS

List of Figures

Figure 2.8: Turnbull et al., 2017, using data from Turnbull et al., 2007; Levin at al., 2010; Lehman et al., 2013: Example atmospheric $\Delta^{14}CO_2$ records from background sites in the Northern Hemisphere (Jungfraujoch (red), Vermunt (orange) and Niwot Ridge (pink)), and Southern Hemisphere (Wellington (black) and Cape Grim (blue)).

Figure 2.9: Turnbull et al., 2009: Modelled mean surface $\Delta^{14}CO_2$ for 2002 – 2007; LMDZ including all known processes impacting $\Delta^{14}CO_2$.

Figure 2.10: Graven et al., 2012b (a, left) and Levin et al., 2010 (b, right): a) Latitudinal transect of sites with $\Delta^{14}CO_2$ measurements by Scripps Institute of Oceanography, and Heidelberg Network (italics), demonstrating the difference of $\Delta^{14}CO_2$ between sites and the South Pole site for years with good data coverage (open dots 1988 – 1989, closed dots 2005 – 2007); b) Differences of smoothed curve fits of $\Delta^{14}CO_2$ from Heidelberg Network sites (red/oranges Northern Hemisphere, green/blues) and their Neumayer site at 70 °S.

Figure 2.11: Turnbull et al., 2017: Wellington $\Delta^{14}CO_2$ record of all collection and measurement methods, including sodium hydroxide (blues), flasks (red) and tree rings (greens) for the full (a) and recent (b) periods, with the smooth curve fit of the final dataset (black line).

Figure 3.1: Examples of dead trees (left, a), sparse vegetation (centre, b) and inaccessible trees (right, c) at coastal sites in Chile demonstrate the challenge of finding suitable trees in suitable locations for the project.

Figure 3.2: An example of seeking permission from a private landowner: talking to a farmer of a site in Chile about the project, before taking tree cores from his coastal farm.

Figure 3.3: Examples of single (left, a), cluster (centre, b) and forest (right, c) sampling sites, highlighting the different site types with suitable trees for the project.

Figure 3.4: Coastal trees do not grow uniformly, like those within a forest that are typically used for dendrochronology, instead with tree growth affected by the wind (left, a), and often with very uneven ground with protruding roots (right, b).

Figure 3.5: Ahipara (AHP), Northland: Scattered trees on a flat golf course next to the sea (top left, a, and right, b), with aerial view of ocean proximity (bottom, c).

Figure 3.6: Baring Head (BHD), Wellington: Aerial view of trees on a high coastal cliff, located east across the entrance of the Wellington Harbour.

Figure 3.7: Gillespies Beach (GBS), West Coast: Exposed trees behind a long beach (top left, a, centre, b, and right, c), with scattered baches (bottom, d).

Figure 3.8: Haast Beach (HAB), West Coast: Scattered trees around a paddock next to the beach (top left, a, centre, b, and right, c), with aerial view of ocean proximity (bottom, d).

Figure 3.9: Haast Beach Development (HBD), West Coast: Trees planted as a windbreak, with visible wind influence (top left, a, and right, b), running perpendicular from the edge of a lagoon next to the open ocean (bottom, c).

Figure 3.10: Okuru (OKU), West Coast: Scattered trees in a grassy paddock with small shrubs (top left and right, a, and, b respectively, adjacent to the ocean (bottom, c).

Figure 3.11: Haast Motor Camp (HMC), West Coast: trees of a wind break at the back of a paddock adjacent to the exposed lagoon beach (top left, a, and right, b), with surrounding paddocks and a house to the east (bottom, c).

Figure 3.12: Hump Ridge (High) (HRH), Southland: trees along an elevated stretch of a coastal forest walking track.

Figure 3.13: Sandhill Point (SHP), Southland: trees of an exposed coastal forest (top left, a) adjacent to the beach (top right, b) on a coastal peninsula (bottom, c).

Figure 3.14: Orepuki (ORP), Southland: scattered trees along an exposed cliff at the beach (top left, a, centre, b, and right, c), at the southeast end of a large bay (bottom, d).

Figure 3.15: Taramea (TRM), Southland: single scattered trees along the beachfront (top left, a, and right, b), on the east of a peninsula.

Figure 3.16: NZ-46S: Oreti Beach (ORT), Southland: plantation forest near the beach (top left, a, and right, b) at the southeast end of a large bay (bottom, c).

Figure 3.17: Mason Bay (Sandhill) (MBS), Stewart Island: middle of Mason Bay on the west of the island, downhill from a large sandhill and many dunes.

Figure 3.18: NZ-47S: Mason Bay Homestead (MBH), Stewart Island: slightly inland from Mason Bay on the west coast (left, a, and right, b), with windbreaks planted by a homestead (also see Figure 3.17d).

Figure 3.19: Kilbride Homestead (KLB), Stewart Island: windbreak by a homestead at the South of Mason Bay, a few hundred metres from the ocean.

Figure 3.20: Enderby Island (END): rata from a belt around the west of the island, extending 50 – 100m inland.

Figure 3.21: Hardwicke Settlement (HAR), Auckland Island: sheltered north facing bay on the island.

Figure 3.22: NZ-53S: World's Lonesliest Tree (WLT), Campbell Island: east of the main high range down the centre of the island.

Figure 3.23: Estaquilla (ESQ), Puerto Montt: scattered trees along exposed coastal cliffs.

Figure 3.24: Punihuil (PHL), Chiloe: paddocks on cliff tops (top left, a, and top centre, b) with trees along the boundary (top right, c), at the southern end of a large bay (bottom, d).

Figure 3.25: Cucao (CUC), Chiloe: scattered trees behind the beach and along the cliff-top.

Figure 3.26: Raul Marin Balmaceda (RMB), Aysen: small island close to the mainland (top left, a, and top centre, b) with wind breaks (top right, c) and other scattered trees, looking out to the open ocean (bottom centre, d).

Figure 3.27: Puerto Aguirre (PAG), Aysen: by a large channel (top left, a), with trees reaching down to the shores (top centre, b, and top right, c), and large islands towards the ocean (bottom centre, d).

Figure 3.28: Laguna San Rafael (LSR), Aysen: scattered trees along the shores of a glacier-fed lake.

Figure 3.29: Tortel (TOR), Aysen: small islands on a channel that leads to the open ocean.

Figure 3.30: Seno Skyring (SKY), Punta Arenas: scattered, weathered trees along the edge of an inlet leading to the open ocean.

Figure 3.31: Monte Tarn (TAR), Punta Arenas: steep hills on the edge of a large channel with marsh and scrub amongst scattered trees and forest areas.

Figure 3.32: Puerto Navarino (PNV), Isla Navarino: scattered trees grow in the windy conditions along the Beagle Channel.

Figure 3.33: East Navarino (ENV), Isla Navarino: scattered (and often dead) trees on a flat paddock by the Beagle Channel.

Figure 3.34: Omora Park (OMO), Isla Navarino: botanic forest park with a range of forest areas by a quiet track along the coast by the Beagle Channel.

Figure 4.1: Schematic of the three solvent wash methods, ANSTO and RRL Soxhlet solvent washes and RRL ASE solvent wash, detailing the different solvents, timings and conditions.

Figure 4.2: Summary diagram of the ANSTO and RRL cellulose extraction methods, detailing chemicals, timings and conditions.

Figure 4.3: $F^{14}C$ of modern tree ring subsamples spanning 1950 – 2000 (Table 4.2) with annual mean $F^{14}C$ of the atmospheric record from Wellington, New Zealand for context (Turnbull et al., 2017), with different colours representing method variations. Note that error bars are too small to identify on this scale.

Figure 4.4: $F^{14}C$ and $\delta^{13}C$ of bomb period and post-bomb period tree ring subsamples (Tables 4.1 & 4.2) of the solvent wash and cellulose extraction method comparison, with lines to guide the eye. Note that where multiple measurements were made using the same sample and method, the mean and standard error is used.

Figure 4.5: $F^{14}C$ of RRL cellulose-extracted sub-fossil kauri blank (blue), aligning with all solvent sequence and cellulose extraction method comparison results (red), and Soxhlet/ASE (yellow/green respectively) solvent wash method comparison results.

Figure 4.6: $F^{14}C$ of the RRL Soxhlet solvent wash method subsample minus $F^{14}C$ of the corresponding RRL ASE solvent wash method subsample for modern tree ring samples (left, a) and other samples (right, b), with error bars calculated from measurement uncertainty. The difference of $F^{14}C$ between methods demonstrates agreement of 6 pairs within 1 sigma, 3 pairs within 2 sigma, and 1 pair within 3 sigma. Other samples (b) include FIRI-D (non-modern wood), modern bone, FIRI-Q (leather), FIRI optional parchment and FIRI optional textile. Where multiple subsamples were analysed (Table 4.2), the mean and standard error were calculated and used for the comparison of methods. Error bars are larger in some cases due to lower ^{14}C counting statistics, but the differences of $F^{14}C$ for the comparisons of these different materials are all within 1 sigma.

Figure 5.1: BHD atmospheric $\Delta^{14}CO_2$ record (black) (smoothed timeseries subsampled for growth months November – February, data from Turnbull et al., 2017), with tree ring measurements from this thesis (green). Inset shows the bomb period and following years in more detail.

Figure 5.2: Results from bomb-pulse validation of tree core samples compared to the BHD atmospheric $\Delta^{14}CO_2$ record (smoothed timeseries subsampled for growth months November – February, data from Turnbull et al., 2017), grouped by sampling site: (top left, a) NZ-53S; (top right, b) CH-44S; (mid left, c) CH-48S; (mid right, d) CH-54S; (bottom centre, e) CH-55S.

Figure 5.3: Ring count validation for sites without bomb-pulse validation, where measured $F^{14}C$ of replicate tree cores are compared for Core 1 (green) and Core 2 (orange), with the timeseries (top row; a, b, c) and offset of each from the pair mean (bottom row; d, e, f): NZ-44S (a, d); NZ-46S (b, e); CH-53S (c, f).

Figure 5.4: $F^{14}C$ for measured years of CH-55S and CH-55S(w), with measured values for assigned years (left, a), and deviations from the pair mean (right, b).

Figure 5.5: $F^{14}C$ deviation for measured replicate tree rings from pair means, where tree rings are treated as a single sample for preparation and divided prior to EA combustion, with pairs grouped by tree core (left, a) and within/between AMS wheel (right, b).

Figure 5.6: $F^{14}C$ values of Kauri control replicates, separated by different sampling (left, a) and valid measurements shown relative to the control mean (right, b).

Figure 5.7: $F^{14}C$ of replicate tree cores, including timeseries and deviation from mean for cores with bomb-pulse validated ring counts, NZ-53S (a, c) and CH-48S (b, d), and a summary of all replicate tree cores (including those used successfully for ring count validation (bottom, e).

Figure 7.6: Average deviation $\Delta\Delta^{14}CO_2$ (‰) of each site from BHDCGO $\Delta^{14}CO_2$ record. Tree ring records are the average deviation 1985 – 2015, other records are the average deviation for the available years of each record (*).

Figure 7.7: Average deviation $\Delta\Delta^{14}CO_2$ (‰) of each site from BHDCGO $\Delta^{14}CO_2$ record for (growth months Nov – Feb) of the years 1986 – 1995, 1996 – 2005, 2006 – 2015. Tree ring records are the average deviation over the entire decade, other records are the average deviation for the available years of each record.

List of Tables

Table 5.4: Determined $F^{14}C$ uncertainty components associated with the tree ring ^{14}C measurements in this project, based on χ_ν^2 of different groups of replicate analyses.

Table 5.5: NZ tree ring records: NZ-44S, NZ-46S and NZ-53S: $\Delta^{14}C$ and $F^{14}C$ (and errors).

Table 5.6: : Chile tree ring records: CH-48S, CH-53S and CH-55S: $\Delta^{14}C$ and $F^{14}C$ (and associated errors).

Table 6.1: Details, including latitude (Lat, °N), longitude (Lon, °E) and altitude (Alt, masl), of atmospheric $\Delta^{14}CO_2$ records for the Southern Hemisphere for 1985 – 2015: Heidelberg (Levin et al., 2010); INSTAAR/UCI (Lindsay, 2016); RRL (Turnbull et al., 2017); SIO/LLNL (Graven et al., 2012b); SIO/CIO (Meijer et al., 2006); further references in text. All measurements were made by AMS except for early RRL measurements and Heidelberg. DRP data is not publicly available. Two records from the Northern Hemisphere are included (VER/JFJ and NWR (Lehman et al., 2013)) as these are also used in this analysis.

Table 6.2: Determined $\Delta^{14}CO_2$ offsets (and associated one sigma error) from RRL for each group (see text Section 6.2), determined from each intercomparison (see text Section 6.4), with the overall offset determined. See text for further details.

Chapter 1

Thesis Outline and Aims

The overarching purpose of this PhD project is to investigate variability of atmospheric $\Delta^{14}CO_2$ over the Southern Ocean in recent decades, as a tool to investigate decadal changes in the strength of deep water upwelling in the Southern Ocean. This is achieved through new atmospheric $\Delta^{14}CO_2$ measurements through tree ring reconstruction, and harmonization of existing atmospheric $\Delta^{14}CO_2$ measurements in the Southern Hemisphere from different groups.

This thesis is largely structured as a narrative of the project from motivation through to outcomes. I first present the background (Chapter 2), before a number of methods chapters associated with the new coastal $\Delta^{14}CO_2$ tree ring records presented as part of this PhD project; detailing fieldwork rationale and tree sampling (Chapter 3), method automation, ^{14}C methodology and data quality (Chapters 4 & 5). Chapters 6 and 7 present a harmonized atmospheric $\Delta^{14}CO_2$ dataset and use these results to investigate Southern Ocean upwelling.

In Chapter 2 (Background) I present the context for this thesis; first highlighting the motivation for this PhD project, stemming from the carbon cycle and climate change, before outlining the application of ^{14}C and tree rings.

In this PhD project I exploited annual growth tree rings, which record the $\Delta^{14}C$ content of atmospheric CO_2 in their annual growth rings, to reconstruct $\Delta^{14}CO_2$ back in time (1985 – 2015). Tree core samples were collected from a latitudinal distribution of the west coasts of Chile and New Zealand and Sub-Antarctic Islands, such that trees observe oceanic air masses with the prevailing westerly winds. A total of ~400 tree cores were collected from sites deemed appropriate for the project. Samples were assessed to select good quality cores with clear rings of sufficient material to analyse. Selected samples were subject to ring counting and slicing into annual growth rings with care and precision.

Chapter 3 (Sampling) provides background for all the tree ring samples within this PhD project, including site details, sampling protocol and sample preparation.

Selected tree ring samples were prepared for ^{14}C measurement, seeking to isolate the cellulosic carbon, believed to be the most representative of atmospheric carbon at the time the annual growth ring was formed, i.e., spring/summer growth months. In this PhD project I automate the organic solvent wash method, thereby improving sample processing efficiency, otherwise following existing protocol for the pretreatment of modern wood samples for ^{14}C measurement at the Rafter Radiocarbon Laboratory (RRL).

Chapter 4 (Method automation) is largely presented in the structure of a journal manuscript, including this solvent wash method automation for organic samples, including tree rings, at the RRL. However, I first briefly outline the established protocols for ^{14}C measurement of tree rings at the RRL, supplementary to the publication and relevant for the thesis narrative. Detailed background information of cellulose extraction and methodology is provided here, further to Section 2.3. This chapter has been submitted to *Radiocarbon* journal. For the purposes of this thesis, within the chapter I present the automation conducted within this PhD project, alongside prior development in the laboratory conducted by others (further detail in Chapter 4).

Independent validation of tree ring counts was conducted through ^{14}C measurement of annual growth tree rings corresponding to the ^{14}C bomb-pulse, elsewhere samples do not date back to the 1960s, multiple tree core samples from a site were compared. Having confirmed ring counts, ~400 tree ring samples were pretreated and measured for ^{14}C within this project. Data quality analysis using a range of replicate ^{14}C measurements conducted within this project led to the assignment of ~1.8 ‰ uncertainties for all results, in line with atmospheric measurements.

Chapter 5 (Data quality) details the independent ring count validation and thorough data quality analysis that I conducted of the tree ring ^{14}C measurements to ensure confidence in the accuracy and precision of my data before proceeding with analysis.

Having demonstrated that the tree ring $\Delta^{14}C$ records are comparable to atmospheric $\Delta^{14}CO_2$ measurements, I then consider existing regional atmospheric $\Delta^{14}CO_2$ measurements from different groups. I therefore develop a harmonised dataset of atmospheric $\Delta^{14}CO_2$ measurements in the Southern Hemisphere for this period from different groups, including the new tree ring $\Delta^{14}CO_2$ records alongside existing data. This is achieved through quantification of interlaboratory offsets through analysis of atmospheric $\Delta^{14}CO_2$ intercomparison activities.

Chapter 6 (Data harmonisation) presents this investigation into interlaboratory comparability and resulting harmonised dataset developed. The chapter is structured in preparation to be submitted for publication that will follow collaboration and further refinement. Background details of existing atmospheric $\Delta^{14}CO_2$ measurements are thus provided here, with additional methodology detail than is necessary for the overall project narrative. Existing atmospheric $\Delta^{14}CO_2$ measurements are presented in key figures and implied in the knowledge base presented in Chapter 2, with corresponding interpretation and analysis of atmospheric $\Delta^{14}CO_2$ in the Southern Hemisphere provided as part of the project narrative (Section 2.2).

Together the new tree ring $\Delta^{14}CO_2$ records and harmonised existing atmospheric $\Delta^{14}CO_2$ dataset allow investigation of temporal and spatial variability of atmospheric $\Delta^{14}CO_2$ over the Southern Ocean over recent decades, thereby also considering the role of upwelling in recent Southern Ocean carbon sink variability. Backward trajectories are produced for the tree ring sites from an atmospheric transport model, to help inform interpretation of results.

Chapter 7 (Analysis) comprises of this initial analysis, which naturally leads into Chapter 8 (Conclusion), which summarises the outcomes of this PhD project and discusses future work.

Chapter 2

Background

2.1 The Global Carbon Cycle

Carbon exists in the atmosphere in a range of compounds, including carbon dioxide (CO_2), methane (CH_4), and carbon monoxide (CO). Other carbon-containing compounds are present with much smaller atmospheric concentrations, thereby with minimal contribution to the carbon cycle. The atmosphere is one of the main reservoirs of the carbon cycle, alongside the terrestrial biosphere, ocean and geosphere, between which carbon exchange occurs through different processes.

Atmospheric CO_2 is the most abundant carbon-containing compound present in the atmosphere and is the main anthropogenic contributor to the perturbed greenhouse effect (e.g., Hansen et al., 1981; Lashof, 1989; Hansen et al., 2007). The greenhouse effect works through atmospheric greenhouse gases such as CO_2 trapping heat within the atmosphere via absorption and emission of long-wave radiation, i.e., heat. As the Earth has observed this increase in greenhouse gases such as CO_2, global temperatures have also risen; demonstrating the significant anthropogenic influence of the climate-carbon system (e.g., Hansen et al., 2006; Solomon et al., 2009; Hansen et al., 2013; Le Quéré et al., 2016).

2.1.1 Atmospheric CO_2

Atmospheric CO_2 concentration is dependent on the storage and distribution of carbon throughout the carbon cycle (Figure 2.1). Carbon exchange occurs through a complex range of physical, chemical and biological processes and interactions, including photosynthesis, respiration and surface ocean exchange (Sections 2.1.2 & 2.1.3). Exchange with the geosphere occurs, but over very long time scales, such that these exchanges can be ignored when studying short periods such as the last century.

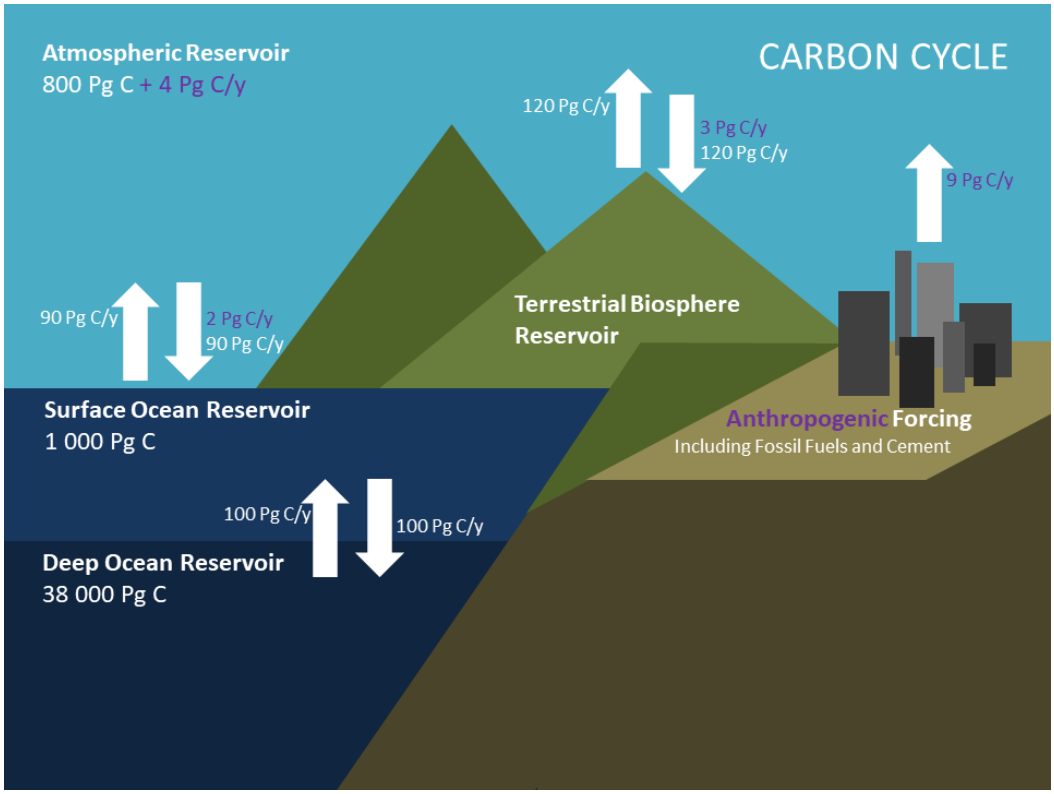

Figure 2.1: Simplified schematic of atmospheric carbon exchange and storage based on the global carbon cycle schematic of Ciais et al., (2013), with associated carbon storage in PgC (10^{15} gC), and carbon exchange fluxes in PgC per year. Anthropogenic influence is highlighted separately (purple).

Prior to industrialization (~1750), atmospheric CO_2 (determined from ice core records) was relatively stable, fluctuating ~180 – 290 ppm, whilst fossil carbon (i.e., coal, oil and gas) remained deep within the Earth, and thus largely isolated from the atmosphere (e.g., Siegenthaler and Oeschger, 1987; Petit et al., 1999; Siegenthaler et al., 2005; Luthi et al., 2008). During this period there was natural carbon exchange between the atmosphere, terrestrial biosphere and ocean that was balanced to some extent, leading to approximate equilibrium across the carbon reservoirs.

Since the industrial revolution, the burning of fossil fuels to 'fuel' the developing world has released previously isolated fossil carbon (375 +/-30 PgC 1750 – 2011, including LUC, see below) into the atmosphere as CO_2 (Ciais et al., 2013). These anthropogenic CO_2 emissions from fossil fuel burning have increased as a result of increased energy demand from

increasing population and the modern world (e.g., Raupach et al., 2007; Hoffman et al., 2009; Andres et al., 2012). Anthropogenic CO_2 emissions are therefore centered around densely populated areas, largely in the Northern Hemisphere. Cement production and land use change (LUC) including deforestation, also contribute to anthropogenic CO_2 emissions, with LUC responsible for 180 +/-80 PgC 1750 – 2011 (Ciais et al., 2013). LUC accounts for global net reduction in lnd carbon storage, a combination of many different factors (Houghton, 2003). Increasing anthropogenic CO_2 emissions from fossil fuel burning, cement production and LUC, have driven increasing atmospheric CO_2 thereby also perturbing the global carbon cycle (e.g., Canadell et al., 2007; Houghton, 2007).

The establishment of high-precision continuous atmospheric CO_2 measurements in 1958, initially in Antarctica, Hawaii and California, observed this trend of increasing atmospheric CO_2 (e.g., Keeling, 1960). Ongoing measurements with increased global coverage enable investigation into trends and variability of atmospheric CO_2 under anthropogenic forcing, including exchange within the carbon cycle (e.g., Tans et al., 1989; Gurney et al., 2002; Keeling et al., 2009; Dlugockencey et al., 2015).

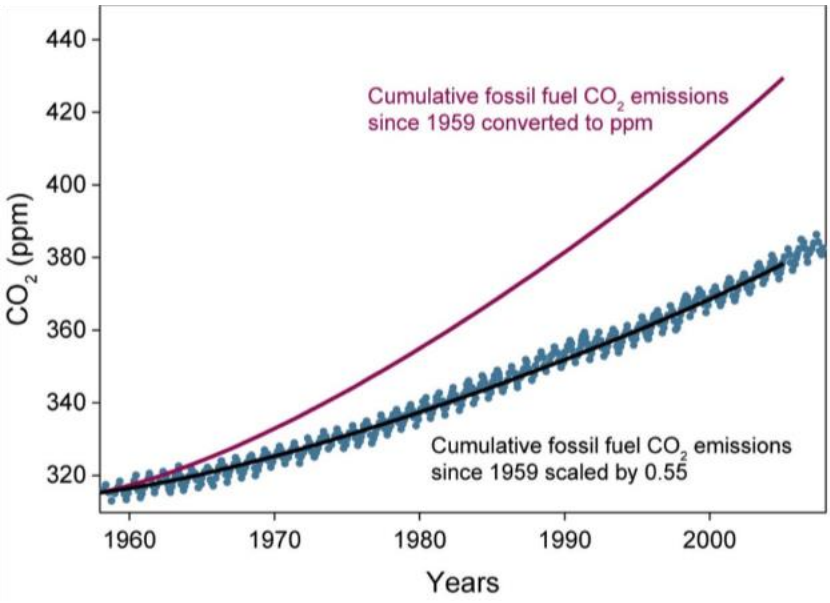

Figure 2.2: Schurr et al., 2016, data adapted from Keeling et al., 2014: Atmospheric CO_2 observations (blue), with CO_2 increase from fossil fuel emissions if all remained in the atmosphere (red), scaled by 0.55 (black), demonstrating anthropogenic CO_2 uptake by the terrestrial biosphere and ocean reservoirs.

Whilst atmospheric CO_2 is increasing with anthropogenic CO_2 emissions, the terrestrial biosphere and ocean reservoirs strive for equilibrium with the atmosphere. Since ~1750, only ~45 % of anthropogenic CO_2 emissions have remained in the atmosphere, whislt the remainder has been sequestered by the terrestrial biosphere and ocean carbon reservoirs (Figure 2.2) (e.g., Schimel et al., 2001; Sabine et al., 2004; Mikaloff-Fletcher et al., 2006; Sarmiento et al., 2010; Khatiwala et al., 2013). Their uptake of anthropogenic CO_2 has approximately followed the rate of increase of anthropogenic CO_2 emissions, such that the resultant airborne fraction (AF) of atmospheric CO_2 has remained roughly constant through time, with interannual variability also observed (e.g., Battle et al., 2000; Canadell et al., 2007; Raupach et al., 2008; Gloor et al., 2010). The carbon uptake of the terrestrial biosphere and ocean reservoirs therefore significantly affects the rate of increase of atmospheric CO_2.

The absorption rate of atmospheric CO_2 by the terrestrial biosphere and ocean reservoirs results from complex systems of physical processes and biogeochemical interactions that are also influenced by climate-carbon coupling (e.g., Lashof, 1989; Friedlingstein et al., 2001). Therefore it is important to understand the underlying mechanisms of the terrestrial biosphere and ocean carbon reservoirs, whilst also considering their response under anthropogenic forcing and climate change, such that we can predict future climate conditions (e.g., Prentice and Fung, 1990; Bousquet et al., 2000; Cox et al., 2000; Lenton, 2000; Friedlingstein et al., 2006; Ballantyne et al., 2012; Schimel et al., 2015; Sitch et al., 2015).

2.1.2 The Terrestrial Biosphere Carbon Sink

The terrestrial biosphere readily exchanges carbon with the atmosphere through photosynthesis and respiration. Most carbon enters the terrestrial biosphere through photosynthetic uptake, after which carbon is circulated through plants and allocated to different processes including respiration, through which carbon is eventually returned to the atmosphere with varying residence time (e.g., Schulze, 2006). Together photosynthesis and respiration carbon exchange fluxes drive a seasonal cycle of atmospheric CO_2, which is

larger in the Northern Hemisphere due to more land than in the Southern Hemisphere (e.g., Randerson et al., 1997).

Carbon that remains in the terrestrial biosphere is slowly cycled through with varied residence times associated with organic matter turnover within ecosystems (e.g., Houghton, 1995). For example, old carbon is present in wetland and permafrost soils as organic compounds in living biomass and dead organic matter. Some terrestrial carbon is transported from soils to rivers (or similar), such that some carbon is entrained within rivers/oceans, whilst other carbon is released to the atmosphere.

2.1.3 The Ocean Carbon Sink

Together, the global oceans cover 70% of the Earth's surface and are responsible for the storage of a large proportion of carbon on Earth.

The oceans naturally exchange carbon with the atmosphere. This carbon uptake and release is predominantly through exchange of CO_2 between the atmosphere and surface ocean, driven by differences in partial pressure of CO_2 (pCO_2) (e.g., Wanninkhof, 1992; Siegenthaler and Sarmiento, 1993; Takahashi et al., 2009). Ocean carbon is largely present as dissolved inorganic carbon (DIC; ~38 000 PgC; Ciais et al., 2013), comprising of carbonic acid (dissolved CO_2: H_2CO_3), bicarbonate (HCO_3^-) and carbonate (CO_3^{2-}) ion, which are all closely related through ocean chemistry (Equation 2.1). Increasing carbon uptake also affects this carbonate system, whereby more H^+ ions are produced, the very definition of acidity, such that ocean pH reduces, thus a larger fraction of DIC is stored as $CO_{2\,(aq)}$, and ultimately ocean carbon storage potential reduces (e.g., Orr et al., 2005). Most DIC originates from air-sea exchange of CO_2, before mixing with deeper waters.

$$CO_{2\,(g)} \Leftrightarrow CO_{2\,(aq)} + H_2O \Leftrightarrow H_2CO_3 \Leftrightarrow H^+ + HCO_3^- \Leftrightarrow 2H^+ + CO_3^{2-} \quad (2.1)$$

Other oceanic carbon exists as particulate and dissolved organic carbon (POC and DOC), which account for a much smaller fraction of oceanic carbon (~700 PgC), typically with a

long turnover time of 1000 years or more (Hansell et al., 2009). Organic carbon includes materials with primarily carbon structures, ranging from individual molecules to living organisms. POC and DOC mostly originate from biological processes within the ocean, including photosynthesis, respiration and microbial activity. A further small pool of carbon is marine biota, largely phytoplankton and other microorganisms (~3 PgC), with a rapid turnover time of days/weeks.

Surface ocean waters, e.g., mid-ocean basins and equatorial regions, are largely subject to horizontal mixing, such that they are at approximate equilibrium with the atmosphere. Conversely, deep water has characteristically different carbon content to the atmosphere. This is a result of slow ocean mixing compared to the atmosphere, as well as the predominantly horizontal nature of this mixing. Where vertical mixing occurs, upwelled water may be either rich or poor in DIC relatively to the atmosphere, such that it acts as a source or sink, respectively, of atmospheric CO_2.

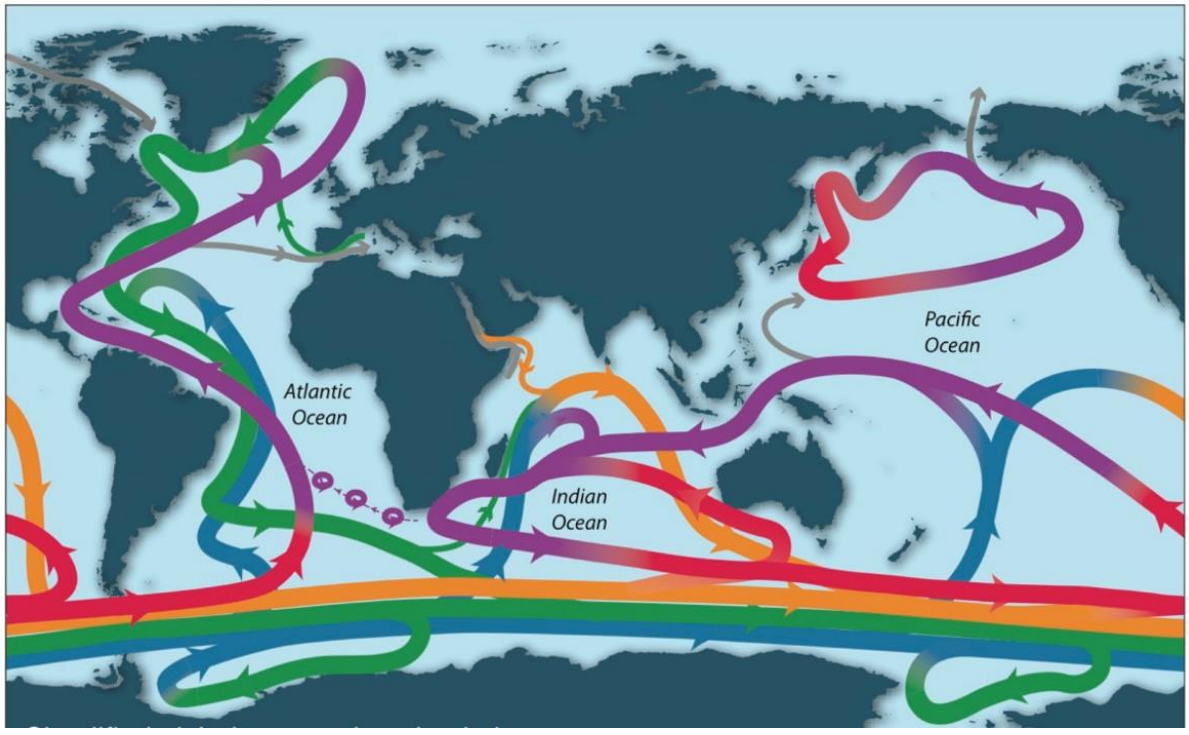

Figure 2.3: Talley et al., 2013; updated from Talley et al., 2011, based on Schmitz, 1995, Rahmstorf, 2002 and lumpkin and Speer, 2007: Schematic of thermohaline circulation, with upper ocean and thermocline (purple), denser thermocline and intermediate water (red), Indian and Pacific deep water (orange), NADW (green) and Antarctic Bottom Water (blue).

Consequently, ocean carbon uptake is largely controlled by global ocean circulation, known as thermohaline circulation, driven by temperature and salinity gradients (Figure 2.3). The combination of thermohaline circulation with the greater solubility of CO_2 in colder waters results in the solubility pump.

The solubility pump is the key process that controls ocean carbon uptake through ocean mixing and associated carbon export to deep water, where most carbon is stored. Most deep water originates from surface water at high latitudes of the North Atlantic. Here cold water from the north combines with saline water from the south, forming the North Atlantic Deep Water (NADW). The dense waters sink and progress south via the west Atlantic. Eventually the NADW reaches the Antarctic Ocean, joining the deep-water Antarctic Circumpolar Current (ACC), with the Upper Circumpolar Deep Water (UCDW) and Lower Circumpolar Deep Water (LCDW). Strong wind-driven currents in the Southern Ocean led to subduction of surface water at mid-southern latitudes associated with sequestration of carbon into the ocean as Antarctic Intermediate Water (AIW), with upwelling of carbon-rich deep-water masses at higher southern latitudes with associated natural CO_2 outgassing (further details below). Southern Ocean upwelling plays a crucial role in the solubility pump, thereby also global heat, fresh water and carbon distribution (e.g., Arrigo et al., 2008; Bonning et al., 2008; Marshall and Speer, 2012).

In addition to the solubility pump, the biological pump, comprising of the soft-tissue and carbonate pumps, acts to transport carbon within the ocean. The soft-tissue pump is driven by primary productivity in the surface ocean, leading to photosynthetic carbon uptake, i.e., $CO_{2(aq)}$, thereby reducing $CO_{2(aq)}$ in the surface ocean, with some carbon returned through respiration or sinking as dead organic matter. The carbonate pump acts opposite to the soft-tissue pump: increasing surface ocean $CO_{2(aq)}$ through formation of calceous shells (Equation 2.2). The shells subsequently sink and redissolve into $CO_{2(aq)}$. The soft-tissue pump is dominant within the biological pump, thereby reducing surface ocean $CO_{2(aq)}$.

$$Ca^{2+}_{(aq)} + 2HCO^{-}_{3\,(aq)} \Leftrightarrow CaCO_{3\,(s)} + H_2O + CO_{2\,(aq)} \qquad (2.2)$$

The rate of anthropogenic carbon uptake of the ocean is controlled by the solubility pump and rate of ocean mixing to sequester carbon. It is important to understand these mechanisms driving carbon uptake. Whilst air-sea exchange and surface ocean carbon chemistry are largely understood, other biogeochemical mechanisms and the solubility pump, i.e., ocean circulation variability are poorly constrained (e.g., Tamsitt et al., 2017). Model results indicate minimal variability of the biological pump over recent decades, whilst significant uptake of anthropogenic CO_2 is observed with ocean convection at high latitudes, although the response of associated ocean circulation to anthropogenic forcing is not determined.

2.1.4 The Southern Ocean Carbon Sink

The Southern Ocean is the largest ocean carbon sink region, accounting for ~40% of the global ocean carbon sink (Figure 2.4) (e.g., Mikaloff-Fletcher, 2006; Le Quéré et al., 2007). The temporal and spatial variability of the Southern Ocean carbon sink is determined by a complex system of physical and biogeochemical interactions, including air-sea gas exchange, wind-driven upwelling of deep water, sea surface temperature, salinity, surface ice cover and biological productivity (e.g., Bakker et al., 1997; Hauck et al., 2015).

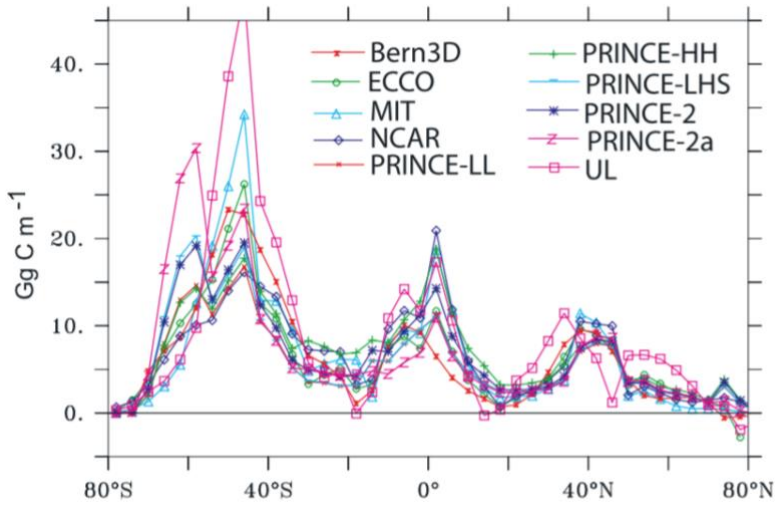

Figure 2.4: Mikaloff-Fletcher et al., 2006: Zonally and temporarily (1765 – 1995) integrated anthropogenic CO_2 uptake by the global ocean from a range of ocean inverse products, demonstrating that the Southern Ocean is an important region of carbon uptake.

Much of the Southern Ocean is characterized by turbulent mixing throughout the water column. Prevailing westerly winds (~30 °S – 60 °S) drive northwards Ekman transport (horizontal transport due to surface wind stress), creating a divergence that leads to upwelling of intermediate and deep-water masses that have been long isolated from the atmosphere, i.e., NADW, UCDW and LCDW (Figure 2.5). These 'old' deep water masses are naturally carbon rich as a result of the solubility pump and soft tissue pumps, whereby cold deep waters have increased $CO_{2\,(aq)}$ solubility and contain decomposed organic matter. Their upwelling therefore leads to outgassing of CO_2 at the ocean surface driven by the pCO2 gradient.

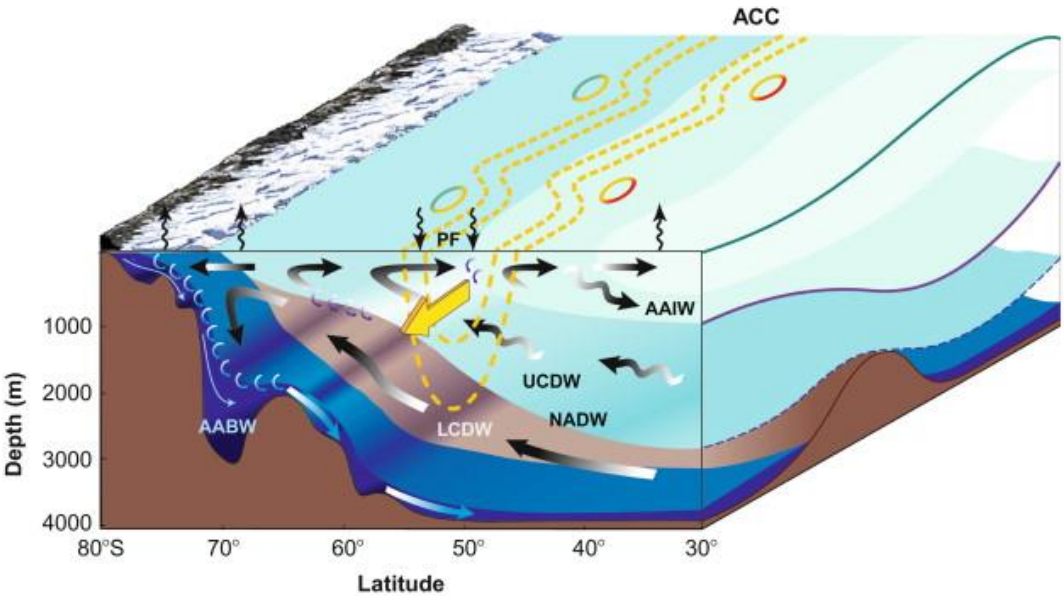

Figure 2.5: Olbers and Visbeck, 2005 redrawn from Speer et al., 2000: Transect of movement of water masses in the Southern Ocean, with Antarctica to the left. Further details in text.

Whilst Ekman-driven upwelling occurs at high southern latitudes, at mid-high southern latitudes the wind-driven northwards Ekman transport produces a convergence. The convergence of water masses drives the subduction of surface waters north of the ACC (Caldeira and Duffy, 2000). With increasing atmospheric CO_2 and low surface ocean carbon due to the solubility and biological pumps, surface waters are depleted in carbon relative to the atmosphere, thus uptake anthropogenic CO_2. These surface waters then sink and sequester entrained carbon into the ocean as AIW (Figure 2.5). The region is also characterized by low iron levels (and other limited nutrient availability), which control

phytoplankton biomass, thus limiting primary productivity and associated $CO_{2\,(aq)}$ uptake (e.g., Boyd et al., 2000; Buesseler et al., 2004; Coale et al., 2006). The biological pump is therefore limited in its role of anthropogenic carbon uptake.

The net Southern Ocean carbon uptake is therefore a combination of the outgassing of natural CO_2 and uptake of anthropogenic CO_2 (e.g., Ito et al., 2010). Consequently, in preindustrial times the Southern Ocean was a net carbon source to the atmosphere as a result of upwelling carbon-rich water masses. Now under anthropogenic forcing and increasing atmospheric CO_2, the Southern Ocean is an important region for anthropogenic carbon uptake. Upwelling of carbon-rich water leads to outgassing of natural CO_2, although with a smaller difference in pCO_2 as atmospheric CO_2 increases. Meanwhile sinking surface waters absorb and sequester atmospheric CO_2 proportionate to the atmospheric CO_2 content. Recent trends and variability in the Southern Ocean carbon sink are poorly constrained due to limited understanding of these driving mechanisms, in part owing to historic limited sampling of this vast, remote region.

2.1.5 Recent Variability of the Southern Ocean Carbon Sink

Le Quéré et al., (2007) reported a weakening of the Southern Ocean carbon sink ~1980s – 2000s relative to increasing uptake trends (in line with increasing atmospheric CO_2), based on atmospheric inverse methods. Here this deviation from the increasing trend is referred to as the Southern Ocean carbon sink anomaly.

Lovenduski et al., (2008) produced further evidence of this relative weakening, with particular focus on biogeochemical processes and modulations of the Southern Annular Mode (SAM) index. The SAM index describes the dominant mode of atmospheric variability of mid-high latitudes of the Southern Hemisphere. It is characterised by a band of westerly winds around Antarctica, with a positive mode indicating reduced pressure at the pole and strengthening winds at higher southern latitudes (e.g., Hall and Visbeck, 2002).

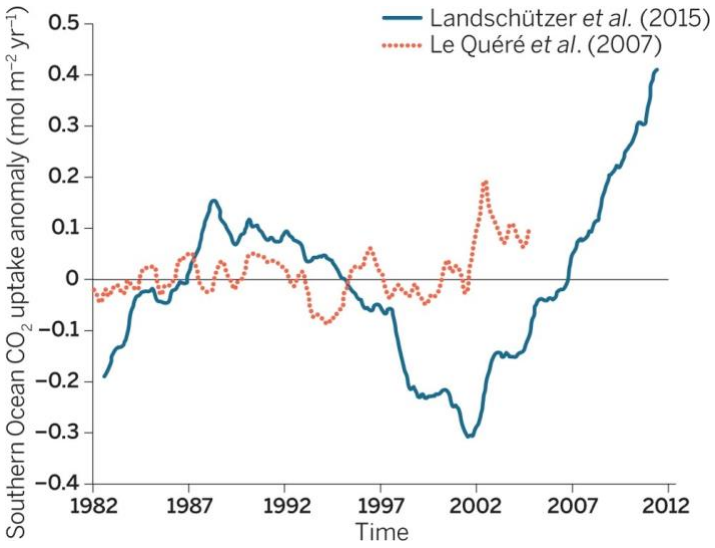

Figure 2.6: (Mikaloff-Fletcher, 2015): Southern Ocean carbon sink anomalies from Le Quéré et al., (2007) (red) and Landschutzer et al., (2015) (blue), averaged between 30 °S and 90 °S, with anomalies calculated relative to the 1980s average.

These two studies attributed a negative Southern Ocean carbon sink anomaly to strengthening and polewards-shift of the westerly winds, associated with a positive trend in the SAM index. The changes in the SAM index and westerly winds have been attributed to increasing atmospheric CO_2 and the ozone hole (Lenton et al., 2009). The strong westerly winds drive increased northwards Ekman transport: producing a stronger divergence and driving more upwelling of carbon-rich deep water to the surface, thus increasing outgassing of natural CO_2 and reducing the net Southern Ocean carbon uptake. Le Quéré et al., (2007) also suggested that poleward intensifying winds, associated with a warming climate, could continue to weaken the Southern Ocean carbon sink in the future.

However, Law et al., (2008) found insufficient evidence to form the same conclusion of a negative Southern Ocean carbon sink anomaly, suggesting that such model-estimated trends are influenced by choice of atmospheric observations, heat, fresh-water and wind fluxes.

More recently a positive Southern Ocean carbon sink anomaly was reported, with reinvigoration observed 2002 – 2012 (Figure 2.6) (Landschutzer et al., 2014 & 2015; Mikaloff-Fletcher et al., 2015; Munro et al., 2015). Observational databases and analysis

techniques improved, and it became clear that the Southern Ocean carbon sink was not saturating. This would not have been observed in the period previously studied, i.e., until 2004 (e.g., Le Quéré et al., 2007). Findings of Landschutzer et al., (2014, 2015) are consistent with the predicted negative anomaly of Southern Ocean carbon uptake during the 1990s but demonstrate considerable strengthening after 2002. It was suggested that this change could be related to change in the positive trend of the SAM index, however no corresponding reversal in associated strengthening westerly winds is observed (Landschutzer et al., 2014; Mikaloff-Fletcher, 2015). The reinvigoration has since been linked to a number of factors, including sea surface temperature (SST) and variability of atmospheric circulation, suggested to lead to reduced Ekman transport and consequently reduced upwelling and associated outgassing of natural carbon (Landschutzer et al., 2015; Mikaloff-Fletcher, 2015). Analysis of SST suggests that this observed trend is driven by small imbalances between temperature driven solubility changes, biology, and upwelling of deep waters (Landschutzer et al., 2015).

Findings of a model-based study of DeVries et al., (2017) are consistent with this, indicating that ocean circulation variability, i.e., weaker upwelling after ~2000, could explain the observed changes in the Southern Ocean carbon uptake.

Following this reinvigoration, the Southern Ocean carbon sink appears to have remained strong after 2010 (e.g., Gruber et al., 2019). The consensus is of a long-term trend towards a stronger sink, similar to that expected from increasing atmospheric CO_2, with a relatively constant strength on timescales of a few decades, i.e., absorbing comparable proportions of anthropogenic CO_2.

Observations demonstrate clear presence of decadal variability over the past few decades, with strong decadal trends a robust feature of surface ocean data (e.g., Landschutzer et al., 2016; McKinley et al., 2017; Ritter et al., 2017; Gruber et al., 2019). There is strengthening evidence that the ocean carbon sink is characterised by decadal variability, with particularly strong variability in the Southern Ocean carbon sink in recent decades.

Current generation ocean models generally don't reproduce the strong decadal variations observed, also observing different substantial interannual variations. Whilst observation-

based estimates largely agree on decadal trends, there is much less agreement in interannual variability and substantial uncertainty given the limited number of observations.

Therefore whilst the aforementioned studies are largely consistent in the overall trends of the Southern Ocean carbon uptake anomaly, they are largely model-based, thus there still remains uncertainty surrounding the drivers and mechanisms controlling the variability, with the sparsity of regional observations for validation remaining a challenge. Until understanding of the processes controlling this sink develops, it will not be clear if or how long this response is likely to continue into the future. However, it is difficult to diagnose the different underlying mechanisms through CO_2 data alone. New observations of tracers that separate these processes are therefore key to allow this separation.

2.2 Atmospheric $\Delta^{14}CO_2$ and ^{14}C in the Global Carbon Cycle

The three most abundant carbon isotopes within the Earth system are ^{12}C (98.89%), ^{13}C (1.11%) and radiocarbon (^{14}C; 0.0000000001%). ^{12}C and ^{13}C are stable isotopes, thereby with constant abundance in the overall Earth system following creation through nucleosynthesis in stars (Trumbore et al., 2016). ^{14}C is a naturally occurring carbon isotope predominantly produced through cosmogenic interaction with nitrogen in the stratosphere (Equation 2.3) (Lal and Peters, 1962). Subsequently, ^{14}C readily combines with oxygen to ^{14}CO, which is further oxidised to $^{14}CO_2$ on a time scale of months (e.g., MacKay et al., 1963). Atmospheric ^{14}C in $^{14}CO_2$ is then exchanged and distributed throughout the carbon cycle. Eventually the instability of the nucleus of ^{14}C produces nitrogen through radioactive decay (Equation 1.4), with a half-life of 5730 (Godwin, 1962).

$$^{14}_{7}N + {}^{1}_{0}n \rightarrow {}^{14}_{6}C + {}^{1}_{1}p \quad (2.3)$$

$$^{14}_{6}C \rightarrow {}^{14}_{7}N + \beta^{-} + \gamma(energy) \quad (2.4)$$

The carbon isotopes exist in a range of forms within the carbon cycle and are distributed differently to one another as a result of fractionation, and cosmogenic production/radioactive decay of ^{14}C.

^{14}C is typically expressed relative to ^{12}C as a ratio, i.e., $^{14}C/^{12}C$, such that age can be determined from decay of ^{14}C relative to ^{12}C for isolated bodies, or allowing investigation into sources and sinks of (radio)carbon with different characteristic $^{14}C/^{12}C$.

Conventionally the $^{14}C/^{12}C$ of a sample is placed in context of the $^{14}C/^{12}C$ ratio of an internationally agreed standard: NBS oxalic acid (OxI) primary standard material (NIST standard reference material SRM4990B), which is prepared alongside sample material. Measurement alongside a standard helps to remove systematic error associated with ^{14}C measurement. All ^{14}C laboratories report results directly related to OxI or indirectly through a standard directly related to OxI (Stuiver and Polach, 1977). The absolute radiocarbon standard is determined as 95 % of the activity, A, of OxI in 1950, normalised to $\delta^{13}C$ = -19.0 ‰ (Olsson, 1970) (details below).

^{14}C is measured through decay counting and accelerator mass spectrometry (AMS), thus there are two different routes through which reported results can be measured and calculated. Decay counting measures the activity of a sample, A_s, as decays per unit time for a given number of carbon atoms. AMS measures ^{14}C atoms detected alongside currents of ^{12}C and (often) ^{13}C. ^{14}C reporting conventions were established prior to the application of AMS, thereby historically referring to A, and more recently referring to the ^{14}C-count/^{12}C-current ratio, R, used here (Stuiver and Polach, 1977; Donahue et al., 1990; Reimer et al., 2004; Zondervan et al., 2015).

Due to the wide range of ^{14}C applications, there is a range of formats in which ^{14}C results can be reported, typically containing a correction for mass-dependent fractionation (normalisation) and sometimes a decay correction.

Mass-dependent fractionation occurs where processes are biased towards lighter or heavier molecules, i.e., those containing ^{12}C, ^{13}C or ^{14}C, with relative variability related to isotopic mass. This thereby affects the relative abundance of the different isotopes, i.e., $^{13}C/^{12}C$ and $^{14}C/^{12}C$ ratios. Therefore to account for different mass-dependent fractionation (or 'normalise' results), a mass-dependent fractionation correction is typically applied.

$$\left[\frac{^{14}C}{^{12}C}\right]_{sample[-25‰]} = \left[\frac{^{14}C}{^{12}C}\right]_{sample[\delta‰]} \left[\frac{1+\frac{-25}{1000}}{1+\frac{\delta}{1000}}\right]^2 \quad (2.5)$$

$$R_{SN} = R_S\left[\frac{0.975}{1+\frac{\delta}{1000}}\right]^2 \quad (2.6)$$

$$F = \frac{R_{SN}}{R_{ON}} = \frac{R_S\left[\frac{0.975}{1+\frac{\delta}{1000}}\right]^2}{0.95\, R_{O[-19‰]}} \quad (2.7)$$

Mass-dependent fractionation of ^{14}C relative to ^{12}C, can be estimated through measurement of mass-dependent fractionation of ^{13}C relative to ^{12}C, because the mass difference of ^{14}C – ^{12}C is approximately twice that of ^{13}C – ^{12}C. Therefore to remove the mass-dependent fractionation component, it is convention that results are reported with a corresponding $\delta^{13}C$ (derived from $^{13}C/^{14}C$; Equations 2.5 & 2.6) value of -25 ‰ whilst the OxI value corresponds to a $\delta^{13}C$ value of -19 ‰ (Stuiver and Polach, 1977). This correction is required for ^{14}C results to be useful for dating or to isolate the tracer signal, and is thus widely applied. Combining the $^{14}C/^{12}C$ ratio of a sample (normalised to $\delta^{13}C$ = -25 ‰ with the corresponding OxI $^{14}C/^{12}C$ ratio (normalised to $\delta^{13}C$ = -19 ‰ produces Fraction Modern, $F^{14}C$ (Equation 2.7), from which other ^{14}C reporting formats can be determined (Reimer et al., 2004).

$$\Delta^{14}C = \left[\frac{\left[\frac{^{14}C}{^{12}C}\right]_{sample[-25‰]}}{0.95\left[\frac{^{14}C}{^{12}C}\right]_{O[-19‰]} \exp\left[\frac{[y-1950]}{8267}\right]} - 1\right] \times 1000 \quad (2.8)$$

In addition to mass-dependent fractionation, radioactive decay of OxI is considered when seeking the absolute amount of ^{14}C. This is because the ^{14}C content of the standard OxI material and the sample reduces over time with radioactive decay. Therefore some

reporting formats account for this with a decay correction, whereby OxI/sample are corrected to 1950 (the year used by convention).

An example of this is $\Delta^{14}C$ ($\Delta^{14}C$ or $Del^{14}C$), derived from $F^{14}C$, with corrections for mass-dependent fractionation (normalisation) and decay included (Equation 2.8). Note that Delta (Del, Δ) notation (parts per thousand, permil, ‰) is used because typically observed differences between samples and standard are small. Within the atmospheric radiocarbon community, atmospheric $\Delta^{14}CO_2$ is used, generally considered to be representative of $\Delta^{14}C$ in $^{14}CO_2$, given the fast oxidation of ^{14}C to ^{14}CO and $^{14}CO_2$.

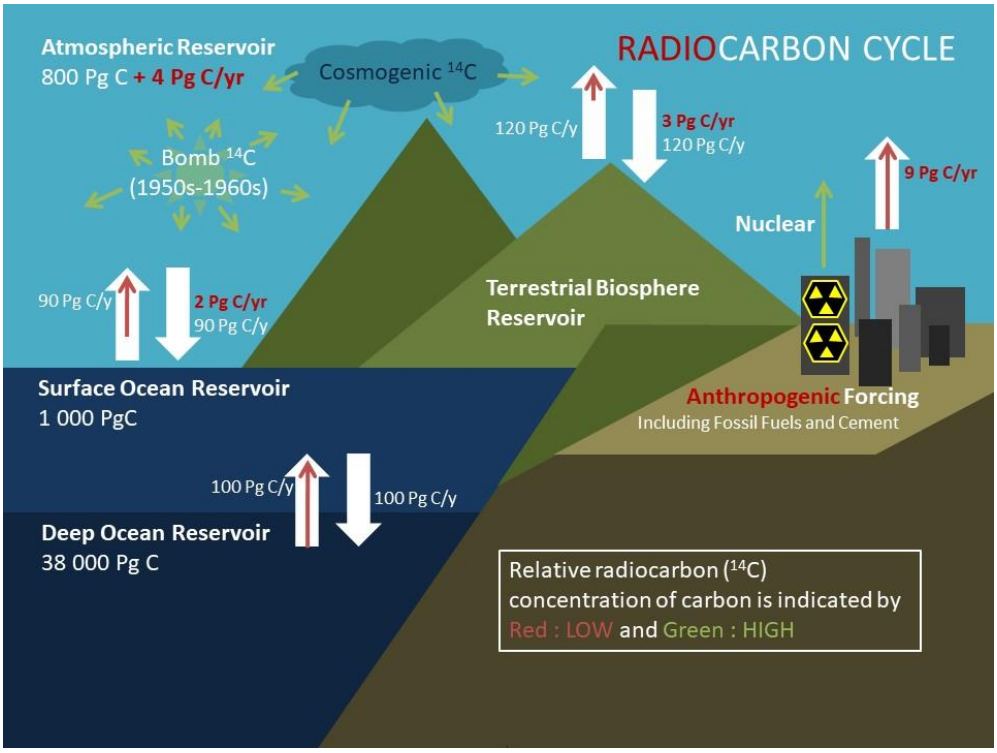

Figure 2.7: Simplified schematic of atmospheric carbon exchange (see Figure 2.1; from Ciais et al., 2013), with carbon fluxes relatively ^{14}C-depleted/enhanced highlighted in red/green respectively, demonstrating the fluxes that influence atmospheric $\Delta^{14}CO_2$.

^{14}C is distributed differently in the carbon cycle to ^{12}C and ^{13}C, partly due to fractionation. However it is the combination of atmospheric cosmogenic production and radioactive decay that naturally creates the unique distribution of ^{14}C through the carbon cycle and

determines atmospheric $\Delta^{14}CO_2$ (Figure 2.7). Following cosmogenic production, predominantly in the stratosphere, ^{14}C mixes through the troposphere before exchanging with other carbon reservoirs, i.e., terrestrial biosphere and ocean. ^{14}C exchange flux (isoflux) are a combination of carbon exchange and ^{14}C isotopic disequilibrium, thereby providing insight into carbon residence times and exchange processes within the global carbon cycle (e.g., Levin and Hesshaimer, 2000; see below).

2.2.1 Pre-industrial Atmospheric $\Delta^{14}CO_2$

Prior to the industrial revolution (~1750), ^{14}C was at an approximate steady state within the carbon cycle, with cosmogenic production rates balancing radioactive decay. Within the atmosphere, cosmogenic production was somewhat balanced by ocean carbon exchange, with atmospheric $\Delta^{14}CO_2$ ~100 ‰ over the last 10 000 years (e.g., Stuiver and Braziunas, 1993).

Despite atmospheric ^{14}C production, about two thirds of total ^{14}C was in the deep ocean as a result of large carbon storage, with only approximately 2 % in the atmosphere. Although the deep ocean was responsible for significant (radio)carbon storage, due to its isolation from other carbon reservoirs and slow mixing rate, radioactive decay characterised relatively reduced $\Delta^{14}CO_2$, carbon-rich deep waters. Upwelling of these carbon-rich/^{14}C-depleted deep waters at high latitudes of the Southern Ocean led to natural CO_2 outgassing, thereby also reducing atmospheric $\Delta^{14}CO_2$ (e.g., Rodgers et al., 2011 & Section 2.1.4).

In contrast to this, the surface ocean and terrestrial biosphere had more similar $\Delta^{14}C$ content to the atmosphere because of the shorter carbon residence times of these reservoirs.

Long term atmospheric $\Delta^{14}CO_2$ was subject to gradual natural variability, as a result of perturbations of cosmogenic production and the global carbon cycle, including variability of winds over the Southern Ocean affecting upwelling. Cosmogenic production is affected by

changes in solar activity and the Earth's magnetic field on long time scales (e.g., Suess, 1965; Stuiver and Quay, 1980; Stuiver and Braziunas, 1989).

2.2.2 The Suess Period

As the carbon cycle and climate evolve, so does the distribution of the carbon isotopes and the 'radiocarbon cycle'. Following the industrial revolution, emissions of ^{14}C-free CO_2 from fossil fuel burning led to increased atmospheric CO_2 but atmospheric dilution of ^{14}C, thus reduced $\Delta^{14}CO_2$, commonly known as the Suess Effect (Suess, 1955). The Suess Effect, i.e., perturbation of atmospheric $\Delta^{14}CO_2$ from fossil fuel emissions, was first determined from tree ring measurements, observing a decrease in atmospheric $\Delta^{14}CO_2$ of ~20 ‰ 1890 – 1945 (~0 – -20 ‰) (Tans et al., 1979; Stuiver and Quay, 1981; Turnbull et al., 2016). The perturbation was subsequently observed in exchange of ^{14}C between carbon reservoirs, characterising the 'Suess Period' (~1890 – 1945), until ^{14}C from atmospheric nuclear bomb testing dominated ^{14}C exchange.

2.2.3 The Bomb Period

Following the Suess Period, atmospheric nuclear bomb testing during the 1950s – 1960s ('bomb period') released ^{14}C ('bomb ^{14}C') into the stratosphere (e.g., Rafter and Fergusson, 1957; Nydal and Lovseth, 1965).

The first direct atmospheric $\Delta^{14}CO_2$ measurement was made in 1954 in Wellington, New Zealand, with further global $\Delta^{14}CO_2$ surface observation networks established to observe bomb ^{14}C (e.g., Rafter, 1955; Nydal and Lovseth, 1983; Levin et al., 1985; Manning et al., 1990).

A significant increase in atmospheric $\Delta^{14}CO_2$ was observed, reaching more than 800 ‰, which since decreased following the nuclear test ban treaty of 1963 and subsequent distribution of bomb ^{14}C throughout the carbon cycle (Figure 2.8) (e.g., Nydal and Lovseth, 1983; Levin et al 1985; Manning et al 1990; Hua et al., 2013).

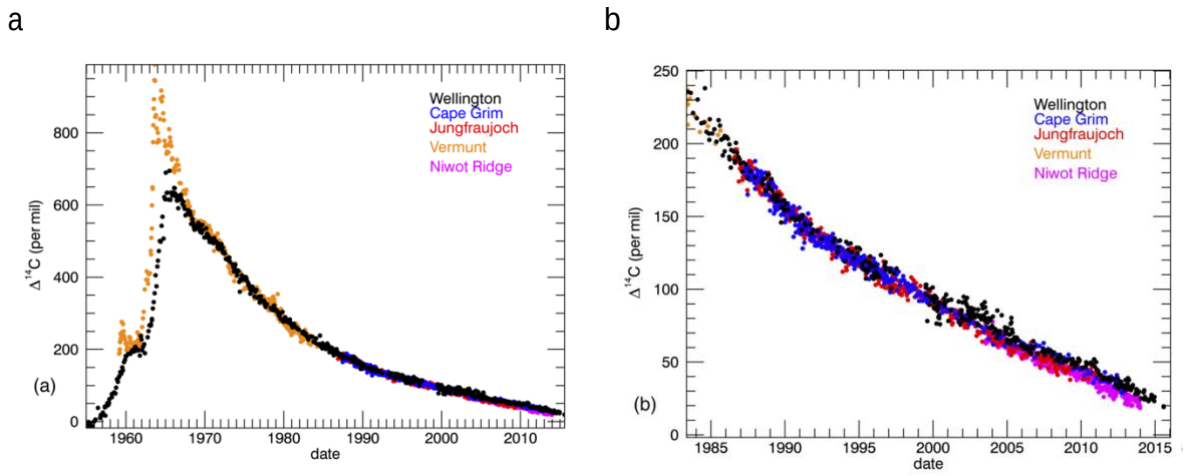

Figure 2.8: Turnbull et al., 2017, using data from Turnbull et al., 2007; Levin at al., 2010; Lehman et al., 2013: Example atmospheric $\Delta^{14}CO_2$ records from background sites in the Northern Hemisphere (Jungfraujoch (red), Vermunt (orange) and Niwot Ridge (pink)), and Southern Hemisphere (Wellington (black) and Cape Grim (blue)).

The bomb testing was predominantly in the Northern Hemisphere with most ^{14}C released into the Northern Hemisphere stratosphere between 1961 and 1963. Bomb ^{14}C entered the troposphere through stratosphere – troposphere exchange (STE) predominantly in the mid-high northern latitudes, creating a large interhemispheric gradient. This led to a tropospheric $\Delta^{14}CO_2$ peak of ~600 ‰ in 1965 in the Southern Hemisphere; later and lower than the Northern Hemisphere due to the interhemispheric atmospheric transport time and dilution (e.g., Nydal and Lovseth 1983; Manning et al., 1990). Bomb ^{14}C thereby enabled investigation of interhemispheric atmospheric transport (e.g., Nydal and Lovseth, 1965; Tans, 1981; Hua et al 2013).

During the height of the bomb period, large seasonal variations in tropospheric $\Delta^{14}CO_2$ were observed due to seasonality of STE, with maximum STE in late spring. Therefore bomb ^{14}C also enabled investigation of STE (e.g., Nydal and Lovseth, 1968; Telegadas, 1971; Manning et al., 1990; Hesshaimer and Levin, 2000).

STE led to maximum atmospheric $\Delta^{14}CO_2$ at the surface in summer (northern hemisphere), slightly offset by heterotrophic respiration of pre-bomb level $\Delta^{14}CO_2$ (e.g., Randerson et al., 2002). Heterotrophic respiration is associated with longer carbon residence time (~10 years)

of soil, bacteria, fungi and animals, compared to autotrophic respiration of plants where carbon is cycled faster and thus has minimal influence on atmospheric $\Delta^{14}CO_2$. During this period of rapid atmospheric $\Delta^{14}CO_2$ increase, carbon release from heterotrophic respiration therefore had greatly depleted (pre-bomb level) $\Delta^{14}CO_2$ relative to the atmosphere, acting to somewhat reduce the signal of increased $\Delta^{14}CO_2$ from STE. Similarly to STE, bomb ^{14}C provided a mechanism through which to investigate carbon turnover within the terrestrial biosphere (e.g., Trumbore, 2000; Naegler and Levin, 2009).

Following the height of the bomb period atmospheric $\Delta^{14}CO_2$ rapidly decreased with uptake by the terrestrial biosphere and ocean carbon reservoirs, which increasingly contributed to atmospheric $\Delta^{14}CO_2$ spatial variability following the dominance of bomb ^{14}C from STE (e.g., Randerson et al., 2002; Levin et al., 2010). Ocean isofluxes were greatest over the Southern Ocean, driven by a strong air-sea $\Delta^{14}CO_2$ gradient and high winds, further supporting the atmospheric $\Delta^{14}CO_2$ latitudinal gradient from STE of bomb ^{14}C.

Atmospheric $\Delta^{14}CO_2$ monitoring during following decades has served as a unique opportunity to use ^{14}C as a diagnostic tracer of the carbon cycle on annual and decadal timescales including exchange processes and reservoir turnover, in addition to atmospheric transport, e.g., interhemispheric and STE (see above), and ocean circulation (e.g., Broecker and Peng, 1974 & 1982; Broecker et al., 1985; Caldeira et al., 1998; Levin and Hesshaimer, 2000; Guilderson et al., 2000; Randerson et al., 2002; Naegler and Levin, 2006 \& 2006(b); Sweeney et al., 2007).

2.2.4 The Post-Bomb Period

With rapidly reducing atmospheric $\Delta^{14}CO_2$ following uptake of bomb ^{14}C by the terrestrial biosphere and ocean carbon reservoirs, by ~1980s, controls of atmospheric $\Delta^{14}CO_2$ significantly evolved, including increasing fossil fuel ^{14}C-free CO_2 emissions playing a more prominent role in the decreasing trend of atmospheric $\Delta^{14}CO_2$ (e.g., Levin and Hesshaimer, 2000; Randerson et al., 2002; Levin et al., 2010; Currie et al., 2011).

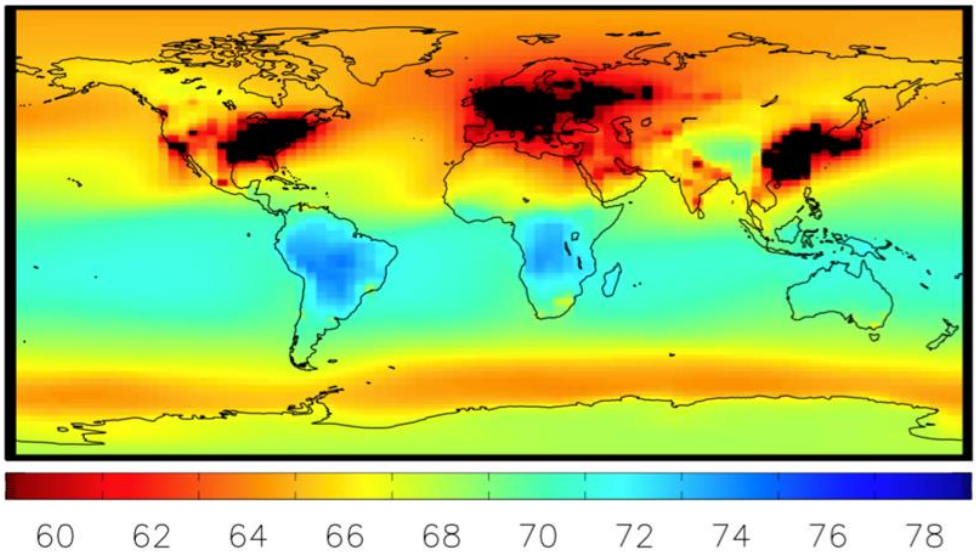

Figure 2.9: Turnbull et al., 2009: Modelled mean surface $\Delta^{14}CO_2$ for 2002 – 2007; LMDZ including all known processes impacting $\Delta^{14}CO_2$.

Now containing significant bomb ^{14}C, the rapidly overturning terrestrial biosphere and surface ocean carbon reservoirs approached ^{14}C equilibrium with the atmosphere. Consequently isofluxes reduced from reducing ^{14}C isotopic disequilibria, contributing to a slowing trend of atmospheric $\Delta^{14}CO_2$ decrease and a reducing seasonal cycle (terrestrial biosphere).

Approximately 20 years after the bomb period (i.e., ~1985), the global terrestrial biosphere reached approximate equilibrium with the atmosphere, whereby subsequently the net effect of heterotrophic respiration returned bomb ^{14}C to the atmosphere (e.g., Levin and Hesshaimer, 2000; Naegler and Levin, 2009b). Typically the 'start' of the post-bomb period is characterised as the change in direction of this isoflux. Although the terrestrial biosphere reached approximate global ^{14}C equilibrium with the atmosphere, equilibrium was reached sooner in faster carbon turnover regions, i.e., the tropics, but delayed in boreal regions with slower turnover rates. Significant interannual variability was also driven by variability of average $\Delta^{14}C$ of carbon released through heterotrophic respiration.

Meanwhile, with anthropogenic fossil fuel ^{14}C-free CO_2 emissions increasing almost exponentially, the Suess Effect began influencing global $\Delta^{14}CO_2$ trends and variability, and is

now the strongest influence on the long term trend of globally decreasing atmospheric $\Delta^{14}C$ (e.g., Levin and Hesshaimer, 2000; Levin et al., 2010; Graven, 2015). Despite fossil fuel emissions increasing, they have had a steady influence on atmospheric $\Delta^{14}CO_2$, because decreasing atmospheric $\Delta^{14}CO_2$ drives a reducing ^{14}C isotopic disequilibrium, thus reduced sensitivity to fossil fuel ^{14}C-free CO_2 emissions.

Fossil fuel emissions are the main influence on the atmospheric $\Delta^{14}CO_2$ seasonal cycle in the Northern Hemisphere, with contribution from the terrestrial biosphere (e.g., Levin and Hesshaimer, 2000). Fossil fuel emissions are also predominantly in the populous Northern Hemisphere, therefore also driving reduced atmospheric $\Delta^{14}CO_2$ in the mid-latitudes of the Northern Hemisphere relative to the tropics and contributing to a latitudinal gradient in combination with the terrestrial biosphere (Figures 2.8 & 2.9).

Urban and industrial regions have characteristically lower $\Delta^{14}CO_2$ than background clean air, thus allowing fossil fuel CO_2 emissions to be quantified; one of the main current applications of atmospheric $\Delta^{14}CO_2$ measurements (e.g., Meijer et al., 1996; Levin et al., 2003; Turnbull et al., 2006; Turnbull et al., 2009; Miller et al., 2012).

Nuclear power has also steadily grown over the post-bomb period, predominantly in the Northern Hemisphere, thereby contributing a small but steadily increasing amount of ^{14}C to global atmospheric $\Delta^{14}CO_2$.

2.2.5 Atmospheric $\Delta^{14}CO_2$ in the Southern Hemisphere

Whilst globally atmospheric $\Delta^{14}CO_2$ is decreasing, modern (post-bomb) atmospheric $\Delta^{14}CO_2$ in the Southern Hemisphere is characterised somewhat differently to the Northern Hemisphere (Figure 2.9).

The Southern Hemisphere largely comprises of ocean, thus observes minimal atmospheric $\Delta^{14}CO_2$ seasonal cycle from fossil fuel emissions and the terrestrial biosphere (e.g., Levin et al., 2010). Surface waters, e.g., mid-ocean basins and equatorial regions, are subject to

wind-driven horizontal mixing, thereby with rapid carbon turnover times similar to the terrestrial biosphere. However, much stronger regional variability is observed in the ocean carbon reservoir than the terrestrial biosphere, with much slower mixing between surface and deep ocean waters; characterised by global thermohaline circulation, including the upwelling of carbon-rich deep waters at high latitudes of the Southern Ocean (Section 2.1.3).

Today the disequilibrium of ^{14}C at the air-sea interface is much smaller than it was close to the bomb period. The rapid increase of atmospheric $\Delta^{14}CO_2$ during the bomb period led to a large air-sea ^{14}C isotopic disequilibrium, thus air-sea exchange controlled the associated isoflux (e.g., Naegler et al., 2006b). Now with atmospheric $\Delta^{14}CO_2$ gradually decreasing and significant bomb ^{14}C in the surface ocean, the air-sea ^{14}C isotopic disequilibrium is much smaller. The subduction of surface waters at mid southern latitudes that sequesters anthropogenic carbon thus has minimal influence on atmospheric $\Delta^{14}CO_2$, because of the small air-sea ^{14}C isotopic disequilibrium. Therefore where atmospheric $\Delta^{14}CO_2$ was controlled by air-sea exchange, it is now (from ~1980s) sensitive to the upwelling of long-isolated (thus carbon-rich but ^{14}C-depleted) deep waters to the surface at mid-high southern latitudes (Graven et al., 2012a; Section 2.1.4).

Whilst the net Southern Ocean carbon sink is a combination of the sequestration of anthropogenic carbon into surface waters and outgassing of natural carbon from upwelled waters, modern atmospheric $\Delta^{14}CO_2$ is only sensitive to the outgassing from 'old' ^{14}C-depleted carbon-rich upwelled deep-water masses. The wind-driven upwelling drives natural ^{14}C-depleted CO_2 outgassing in the Southern Ocean Region, leading to reduced $\Delta^{14}CO_2$ in the overlying atmosphere ~50 – 70 °S, the dominant influence on spatial variability of atmospheric $\Delta^{14}C$ in the Southern Hemisphere (Figure 2.9) (e.g., Levin and Hesshaimer, 2000; Randerson et al., 2002; Levin et al., 2010; Graven et al., 2012b). A relative atmospheric $\Delta^{14}CO_2$ minimum is thus observed ~50 – 70 °S (Figure 2.10a), contributing to a latitudinal gradient with higher atmospheric $\Delta^{14}C$ around the tropics, including the return of bomb ^{14}C to the atmosphere from the terrestrial biosphere and surface ocean with faster carbon turnover.

a b

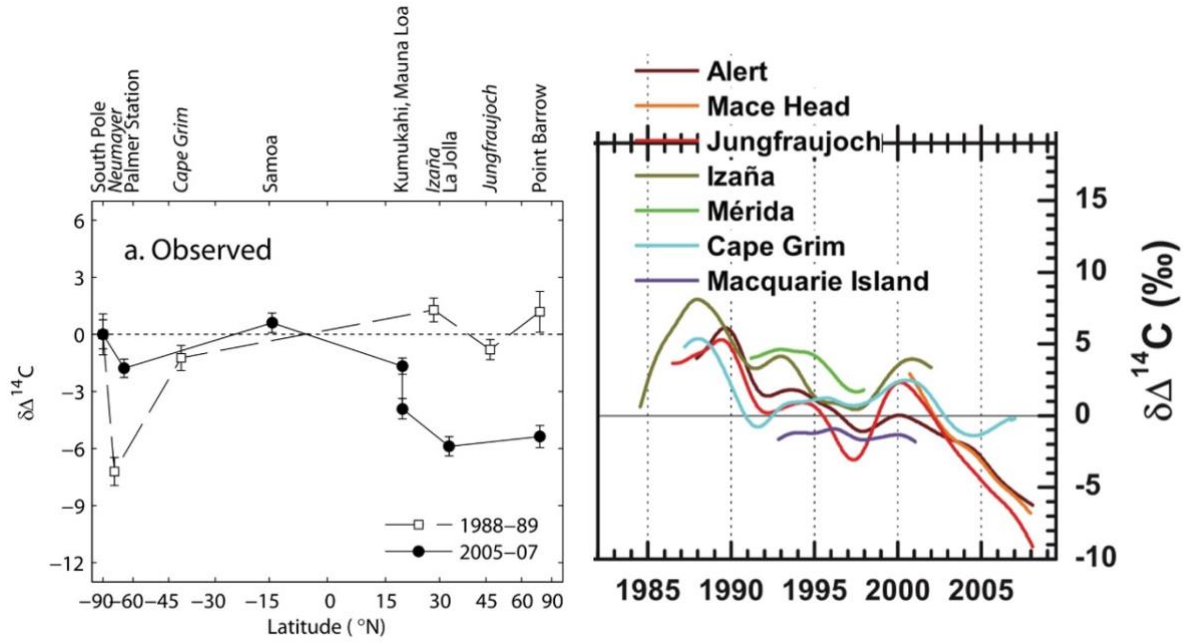

Figure 2.10: Graven et al., 2012b (a, left) and Levin et al., 2010 (b, right): a) Latitudinal transect of sites with $\Delta^{14}CO_2$ measurements by Scripps Institute of Oceanography, and Heidelberg Network (italics), demonstrating the difference of $\Delta^{14}CO_2$ between sites and the South Pole site for years with good data coverage (open dots 1988 – 1989, closed dots 2005 – 2007); b) Differences of smoothed curve fits of $\Delta^{14}CO_2$ from Heidelberg Network sites (red/oranges Northern Hemisphere, green/blues) and their Neumayer site at 70 °S.

2.2.6 Atmospheric $\Delta^{14}CO_2$ Interhemispheric Gradient

Globally, an interhemispheric gradient of atmospheric $\Delta^{14}CO_2$ is therefore observed, dominated by fossil fuel ^{14}C-free CO_2 emissions in the mid-latitude Northern Hemisphere and ^{14}C-depleted CO_2 outgassing in the Southern Ocean Region (Figure 2.10a) (e.g., Levin et al., 2010; Graven et al., 2012b). In the 1980s the overall interhemispheric gradient observed was minimal, and similarly small in the 1990s. However the atmospheric $\Delta^{14}CO_2$ interhemispheric gradient has now evolved into a more developed gradient around 2000s, whereby the Northern Hemisphere is depleted relative to the Southern Hemisphere (Figure 2.10b). This developing interhemispheric gradient cannot be totally attributed to fossil fuel emissions, thus suggesting potential variability of the Southern Ocean $\Delta^{14}CO_2$ signal.

Such variability of atmospheric $\Delta^{14}CO_2$ in the Southern Ocean Region is subtle, (i.e., a few permil, similar to measurement precision) (Chapter 5), whilst considerable interannual variability is observed. Therefore although measurable variability may exist, there is currently limited observations through which this can be investigated, thus the evolving interhemispheric gradient is not fully accounted for (Graven et al., 2012b).

Existing atmospheric $\Delta^{14}CO_2$ observations are by a number of different research groups (Section 6.2), which have previously been considered comparable, thus somewhat considering data together (e.g., Levin et al., 2010; Graven et al., 2012b). However interlaboratory offsets have not been quantified to allow accurate interpretation of observed atmospheric $\Delta^{14}CO_2$ signals (Chapter 6).

The Southern Ocean $\Delta^{14}CO_2$ signal is driven by the upwelling of carbon-rich, ^{14}C-depleted deep water ~50 – 70 °S. Atmospheric $\Delta^{14}CO_2$ in the Southern Hemisphere is thus controlled by the same mechanism proposed to influence Southern Ocean carbon sink variability in recent decades (Section 2.1.5). Therefore ^{14}C can be applied as a tracer of the carbon cycle to distinguish the natural upwelling component (and associated CO_2 outgassing) from net carbon exchange (Manning et al., 1990; Randerson et al., 2002; Turnbull et al., 2009; Graven et al., 2012a). High-precision atmospheric $\Delta^{14}CO_2$ measurements can therefore play an important role in investigating the drivers of observed variability of the Southern Ocean carbon sink in recent decades (Chapter 7).

2.3 Atmospheric $\Delta^{14}CO_2$ Reconstruction through ^{14}C Measurement of Tree Rings

Existing recent atmospheric $\Delta^{14}CO_2$ measurements in the Southern Hemisphere are detailed in Chapter 6. However, with limited recent regional atmospheric $\Delta^{14}CO_2$ measurements to conduct such investigation, ^{14}C measurements of annual growth tree rings can be exploited to reconstruct past atmospheric $\Delta^{14}CO_2$ (e.g., Hua et al., 2013).

Trees sequester atmospheric carbon through photosynthetic uptake of CO_2 during their growing season, of which a proportion is laid down in the corresponding annual growth ring.

The cellulosic carbon within an annual growth ring is believed to be the most representative fraction of atmospheric carbon at the time of formation (further details in Section 4.2). Cellulose does not exchange carbon after formation, such that the isotopic signature reflects the atmospheric signal at the time of recent carbon fixation, with a delay of about a month (Grootes et al., 1989a, b; Hua et al., 2000; Gaudinski et al., 2005). The contribution of previously stored carbohydrate to cellulosic carbon is considered as between 0 and 15 %, with earlywood sometimes containing carbon from the latter part of the previous year, butlatewood largely comprising of current growth year carbon (Grootes et al., 1989a, b; hua et al., 1999; Kagawa et al., 2006).

Prior to preparation of tree ring samples for ^{14}C measurement, the annual growth tree rings are counted and sliced from tree core samples (Chapter 3), thus it is important to understand some dendrochronology relevant to the formation and identification of annual growth tree rings.

2.3.1 General Principles of Tree Rings and Dendrochronology

The trunk is the primary `stem' of a tree, comprising of a range of cells in tissues, which can all divide and produce new cells (Fritts, 1976). Xylem is a tissue, predominantly comprising of tracheid cells, which form the woody cylinder of a tree and also conduct water. Tracheids are vertically oriented, have thick lignified cells, and die before becoming functional.

Annual growth rings are layers of concentric material produced during an annual growth period, which usually begins in spring and ends by autumn. Within an annual growth period, early growth (earlywood or springwood) is characterised by large and relatively thin-walled tracheids, producing a porous wood of low density and light colour. Later growth (latewood or summerwood) is characterised by small thick-walled tracheids, producing a less porous, more dense and darker wood. The earlywood-latewood transition is gradual in many species and less visible in others, producing varying cell-size and colour gradients. Contrasting this, ring boundaries occur as a result of the sudden change in cell size from small, thick-walled latewood cells at the end of an annual growth period, to the large, thin-walled earlywood cells of the subsequent annual growth period. This usually produces a sharp change in cell-

size and colour, which characterises a ring boundary, although some species demonstrate more diffuse boundaries.

The approximate age of a temperate forest tree can be determined through counting annual growth rings. Traditional dendrochronology seeks to produce a 'chronology' using cross-dating of different tree cores to validate the common tree ring patterns and compile records. Dendroclimatologists further investigate tree ring width patterns to assess interannual variation in context of climate and atmospheric studies. Seeking trees that are representative of the local environmental conditions and climate, sampled trees are commonly within a relatively uniform area, such as a forest. The sampled trees therefore usually have regular round trunks and desirable characteristics for sampling and dendrochronology.

Cross-dating is the most fundamental principle of dendrochronology, involving matching ring patterns between cores/trees within a given region to assign calendar years to rings (Fritts, 1976). Therefore, dendrochronologists typically take multiple cores from each tree sampled and from multiple trees at a site.

The process of cross-dating helps to highlight where rings may be locally absent or where false rings are present, thereby providing an experimental control on calendar years assigned to tree rings (Fritts, 1976). A locally absent (or partial) ring refers to a ring that does not appear in all cores taken from a single tree. This occurs due to different climatic conditions meaning that tree growth does not happen equally throughout the stem. False rings are rings that appear within a tree core, and often within that whole tree and other trees at the site, that are not annual growth rings (i.e., intra-annual). False rings form due to changing climatic conditions within a year, for example if there is a period of unfavourable growing conditions within the growing season, causing growth to slow, and thus forming a dense cell structure that resembles an annual growth ring. Sometimes environmental conditions limit growth such that no annual growth ring is produced, i.e., a missing ring. Cross-dating is therefore applied to determine calendar ages where there is the potential of no annual growth ring formed in some years and several intra-annual growth rings formed in other years.

Caution is taken when sampling to minimise the potential of these phenomena in samples. To minimise samples with locally absent rings, trees are chosen that have a consistent round trunk, such that no rings will be absent from a particular core due to a fluted or irregular trunk. Taking multiple cores from each tree sampled also helps to identify any cases of locally absent rings. All cores are taken at points away from branches growing off the main trunk to avoid any confusion in ring pattern where this occurs. False rings and missing rings are much harder to detect, because their presence is driven by climatic/environmental conditions and thus often exist not only throughout a tree, but in trees within a given region. Problems of false or missing rings are also commonly associated with particular species due to their climate sensitivity. Therefore, such trees are avoided where possible, otherwise a particularly conservative approach is taken for analysis.

The potential for such natural phenomena highlight the importance of conducting ring count validation, through cross-dating or otherwise, to ensure accurate ring counts. Due to rapidly changing atmospheric $\Delta^{14}C$ during the bomb period, 'bomb-pulse' dating is an alternative technique through which independent ring count validation can be achieved (see below, and Sections 4.2.2 & 5.1.1).

2.3.2 Bomb ^{14}C and Modern Tree Ring ^{14}C Analysis

Typically tree ring ^{14}C measurements have been used to reconstruct past atmospheric $\Delta^{14}CO_2$ for age calibration (e.g., Hogg et al., 2013; Hua et al., 2013; Reimer et al., 2013). The anthropogenic perturbation of atmospheric $\Delta^{14}CO_2$ through fossil fuel ^{14}C-depleted CO_2 emissions, i.e., the Suess Effect (Section 2.2.2), was also first observed through tree rings (Suess, 1955). The addition of bomb ^{14}C to the atmosphere has since provided a unique opportunity to use the rapid pulse of bomb ^{14}C to investigate the carbon cycle and associated mechanisms (Section 2.2.3).

Similarly to prior to the bomb period, tree ring ^{14}C measurements contribute to the modern ^{14}C calibration curve for determining calendar ages corresponding to ^{14}C measurements (e.g., Hua et al., 2013). The bomb period and beyond are novel in that we now have direct

atmospheric $\Delta^{14}CO_2$ measurements. Tree ring chronologies can be validated with atmospheric $\Delta^{14}C$ measurements, whilst determining regional atmospheric $\Delta^{14}CO_2$ calibration curves. Regional calibration curves are required due to the large rapid changes in atmospheric $\Delta^{14}CO_2$ and associated mixing times. Therefore any isolated organism can be dated using the appropriate ^{14}C calibration curve.

Further to this, ^{14}C bomb-pulse dating of tree rings provides independent validation of tree ring chronologies to compliment traditional dendrochronology (Sections 4.2.2 & 5.1.1). This allows tree ring analyses through challenging tropical regions and enables exploration into plant growth and climate variation (e.g., Bowman et al., 2011). These investigations aid environmental reconstructions and give unique insight into tropical system dynamics, contributing to carbon cycle and climate models (e.g., Biondi et al., 2007; Vieria et al., 2005). (An overview of modern tree ring ^{14}C applications is also provided within the publication of Chapter 4: Section 4.2.2.)

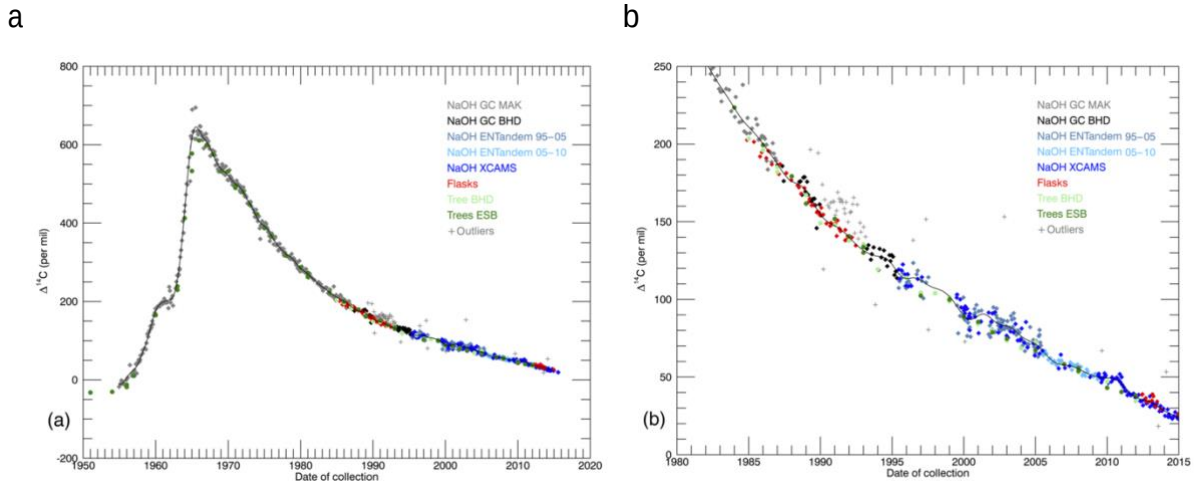

Figure 2.11: Turnbull et al., 2017: Wellington $\Delta^{14}CO_2$ record of all collection and measurement methods, including sodium hydroxide (blues), flasks (red) and tree rings (greens) for the full (a) and recent (b) periods, with the smooth curve fit of the final dataset (black line).

Due to the large rapid changes in atmospheric $\Delta^{14}CO_2$ during/following the bomb period, these tree ring samples often require additional pretreatment to isolate characteristic atmospheric $\Delta^{14}C$ from the year of annual growth tree ring formation (Section 4.2).

Following appropriate preparation, tree ring ^{14}C measurements have been demonstrated to reflect atmospheric $\Delta^{14}CO_2$ measurements (e.g., Hua et al., 2013; Norris, 2015). Tree ring ^{14}C measurements have annual resolution, specifically the summer growth months of November – February (Southern Hemisphere). At the Rafter Radiocarbon Laboratory, New Zealand, tree ring ^{14}C measurements following the bomb period observe good agreement with corresponding atmospheric $\Delta^{14}CO_2$ measurements (Figure 2.11; Turnbull et al., 2017). In this PhD project tree rings are therefore exploited as a tool through which recent atmospheric $\Delta^{14}CO_2$ over the Southern Ocean can be reconstructed and investigated, where direct atmospheric measurements are limited.

Chapter 3

Tree Ring Sampling

In this PhD project I use tree rings to investigate modern atmospheric $\Delta^{14}CO_2$ over the Southern Ocean (Sections 2.2.5 & 2.2.6). With limited sampling of the vast Southern Ocean Region (Chapter 6), I exploit annual growth rings of coastal trees to investigate atmospheric $\Delta^{14}CO_2$ variability over recent decades.

This chapter presents the fieldwork and sampling rationale, including sampling site details (Section 3.1) and preparation of tree core samples into annual growth tree rings ready for ^{14}C preparation (Section 3.2). Subsequent methodology for ^{14}C analysis of tree rings is presented in Chapter 4.

3.1 Sampling Sites

Sampling is conducted at ~10 – 20 coastal sites distributed throughout the mid-high southern latitudes of New Zealand and Chile, with a total of ~400 tree core samples collected. Samples from the New Zealand region are predominantly from a field campaign in the South Island of New Zealand (Jocelyn Turnbull and Margaret Norris, February 2017), with further samples from a scientific research cruise around New Zealand Sub-Antarctic Islands (Jocelyn Turnbull, February 2016). Similarly samples from southern Chile are from a separate field campaign (Jocelyn Turnbull and Rachel Corran, October 2017).

3.1.1 General Principles for Sampling Locations

Seeking to investigate atmospheric $\Delta^{14}CO_2$ variability over the Southern Ocean, sampling is conducted over mid-high latitudes of the Southern Hemisphere, where land borders the Southern Ocean. The sampling sites offer good latitudinal coverage which is important

because latitudinal variability is likely linked to the Southern Ocean (e.g., Levin et al., 2010; Graven et al., 2012; Section 2.2.6).

Prevailing westerly winds at these latitudes determine that samples are from the west coasts of land masses, such that observed air masses have predominantly oceanic pathways (referred to as 'ocean proximity' in Section 3.1.4). The sampling locations are very important, because where air masses are transported over land, other regional influences (i.e., terrestrial biosphere and anthropogenic sources) will affect results, thereby potentially masking the subtle atmospheric $\Delta^{14}CO_2$ variability of interest. For sites in Isla Navarino, southern Chile, tree ring ^{14}C measurements from two sampling locations are compared, i.e., one of which is a more coastal site, to evaluate any biospheric/anthropogenic local influences present (Section 5.2). Average backward air mass trajectories for the selected sampling locations are also retrospectively determined (Chapter 7).

Whilst limited land mass at these latitudes characterises the Southern Ocean, it drastically limits potential tree sampling sites: the continent of South America stretches down to ~55 °S and New Zealand extends down to ~47 °S (or ~53 °S including Sub-Antarctic Islands). These countries also span a good latitudinal range.

Together these principles determine that the west coasts of New Zealand and Chile are good sampling locations for this project.

a b c

Figure 3.1: Examples of dead trees (left, a), sparse vegetation (centre, b) and inaccessible trees (right, c) at coastal sites in Chile demonstrate the challenge of finding suitable trees in suitable locations for the project.

Suitable trees to sample rarely exist in the exposed coastal locations suitable for this project, because trees struggle to survive under the harsh environmental conditions (Figure 3.1). Many such coastal locations are thus characterised by sparse vegetation. Coastal regions with better conditions for growth are often inaccessible by road or foot, with dense impenetrable bush covering areas where trees grow. Much of the west coast of southern Chile (Patagonia) consists of many small islands and inlets, making accessible sites with suitable trees that observe oceanic air masses hard to find (referred to as 'location' in Section 3.1.4).

Google earth is a useful tool to explore locations for trees prior to sampling. This helps to assess coastal accessibility, ideally through road, track, or alternatives where latitudinal regions would otherwise be impractical or impossible, i.e., Sub-Antarctic Islands of New Zealand and northern Patagonia. For some areas, invaluable local guides advised and/or accompanied on fieldwork, with extensive knowledge of the sea and tree species (see acknowledgements and Section 3.3). Thorough research was conducted before heading out into the field, including the acquisition of permits where applicable, e.g., Department of Conservation permits for some New Zealand regions. In some cases permission was sought from private land owners when suitable locations were identified (Figure 3.2).

a b c

Figure 3.2: An example of seeking permission from a private landowner: talking to a farmer of a site in Chile about the project, before taking tree cores from his coastal farm.

3.1.2 Site Selection Criteria

Having investigated accessible locations with trees, the presence of suitable trees to sample is considered. This assessment is largely conducted on arrival at a site (with prior knowledge from google earth), when a more thorough understanding of location can be established. Trees are sought that largely observe oceanic air masses, i.e., onshore wind, trees situated directly on the coast, cliff-top or other suitably elevated positions with proximity to the coast.

a b c

Figure 3.3: Examples of single (left, a), cluster (centre, b) and forest (right, c) sampling sites, highlighting the different site types with suitable trees for the project.

The overriding common criterion for this project is that the sampled tree(s) must observe oceanic air masses, which is subsequently confirmed through backward air mass trajectories from an atmospheric transport model (Section 7.1.2). To achieve this, the collected tree core samples come from a variety of site types (referred to as 'site' in Section 3.1.4):

- SINGLE TREE ('single', Figure 3.3a): The simple case where a single tree is in an area of sparse or low-lying vegetation and within good proximity of the coast. This is a good indicator of strong onshore winds leading to harsh conditions for survival. Such trees therefore have minimal local (terrestrial) site interference and are thus ideal for this project.
- SMALL CLUSTER OF TREES ('cluster', Figure 3.3b): Several trees are close together in a similarly sparse environment to a single tree site. The most coastally located tree is sampled, or a large tree that will observe oceanic air masses passing over smaller coastal tree. Sometimes a cluster or row of trees is observed where farmers have

planted a 'wind break', which in turn indicates that this is also a good sampling site for this project, i.e., observes strong winds coming off the ocean.

- COASTAL FOREST ('forest', Figure 3.3c): Where there is an area of many trees, the most coastally located and exposed trees are sampled, similarly to a cluster. However, in forest areas the coast is often inaccessible, so tall trees are identified with growth predominantly above the canopy, such that they absorb air from the ocean and not recycled air within the canopy, thereby minimising terrestrial signals. Where trees are on ocean-facing hills, identified trees are sufficiently exposed relative to the majority of surrounding trees and topography.

In addition to trees and vegetation in the surrounding environment of sampled trees, other local site influences are also considered, including local houses or pollution sources. Detailed site notes are made when sampling, and areas where possible contamination may occur are largely avoided.

Having identified accessible coastal locations with suitably sited trees, the presence of trees suitable for dendrochronology and this particular project were investigated, which naturally determined sampling sites.

3.1.3 Tree Selection

The sampling locations for this project are exposed coastal sites, thus tree growth is not necessarily limited by climate. Variations in factors affecting a site, such as change in local environment, may cause marked differences in annual growth ring widths between different sides of a tree and different species (Section 2.3). The trunks of the exposed coastal trees that we seek for this project are usually influenced by the wind, with more growth downwind where there is less wind-stress (i.e., leeward; Figure 3.4a). Sampling different sides of such trees can thus result in different width annual growth rings. Therefore a greater amount of replication than is typical for dendrochronological studies would likely be necessary to cross-date and achieve a reliable chronology from our sites, which is simply not available at most of our locations with limited specimens. In contrast to traditional dendrochronology, here an accurate ring count is determined through ^{14}C bomb-

pulse validation (Section 5.1), and therefore cross-dating is not conducted, nor is a chronology established. Where tree core samples extend to the bomb period ring count validation is provided through analysis of rings spanning this period (Section 5.1.2). Where this is not possible, multiple cores are selected to analyse and provide a cross-check on ring counts (Section 5.1.3). Although a chronology is not required for this project, multiple cores from each tree and multiple trees at a site are collected to provide sufficient samples for analysis and replication.

a b

Figure 3.4: Coastal trees do not grow uniformly, like those within a forest that are typically used for dendrochronology, instead with tree growth affected by the wind (left, a), and often with very uneven ground with protruding roots (right, b).

The reality is that having found accessible locations with well-sited trees, many such exposed trees are often partially rotten, if not dead, due to the harsh conditions, and are thus unsuitable for dendrochronology. This is because rotten wood has begun to decompose, meaning that its previous structure with annual growth rings collapses, often with no ring boundaries visible. Rotten trees are often hard to identify from the exterior of the tree, but a rotten interior becomes apparent when sampling (Section 3.2.1).

Although most samples collected are suitable for dendrochronological analysis, throughout this project the number of tree species analysed across different sites is kept to a minimum for consistency (Section 2.3). When sampling at a site, previously sampled species are sought for consistency, whilst also sampling from a range of species that may be found at subsequent sites.

In addition to having suitable characteristics for dendrochronology, a selected tree must be positioned such that the core samples can be taken safely (Figure 3.4b). Practical factors such as clear access to the trunk without obstructing branches and stable ground from which to take the core are essential.

3.1.4 Sampling Site Details

Key details of sampling sites are summarised from field notes, which are then considered when selecting samples for ^{14}C analysis and subsequent data interpretation. The tree core sites selected for analysis are highlighted, whilst background information is relevant for the remaining archived samples (Table 3.1).

Table 3.1: Summary of Sampling Site locations in New Zealand and Chile: latitude (Lat), longitude (Lon), site code created for the project, location name, site type (as outlined in Section 3.1.2), and tree species.

Lat/°S	Lon/°S	Site Code	Location	Site Type	Tree Species
North Island New Zealand (sampled 2013 – 2017)					
35.16	173.16	AHP	Ahipara	Single	*Pinus radiata* (**pine**)
41.07	174.15	BHD	Baring Head	Cluster	*P.radiata* *Cupressus macrocarpa* (**macrocarpa**)
South Island New Zealand (February 2017)					
43.42	169.82	GBS	Gillespies Beach	Cluster	*C. macrocarpa*
43.86	169.00	(HAB) **NZ-44S**	Haast Beach	Single	*P. radiata*
43.89	168.93	HBD	Haast Beach Development	Cluster	*C. macrocarpa*

Continued...

Lat/°S	Lon/°S	Site Code	Location	Site Type	Tree Species
43.91	168.89	OKU	Okuru	Single	*Dacrydium cuppresinum* (**rimu**)
43.91	168.90	HMC	Haast Motor Camp	Cluster	*C. macrocarpa*
46.22	167.30	HRH	Hump Ridge	Forest	*D. cupressinum* *Notafagus fusca* (**red beech**) *Podocarpus totara* (**totara)**
46.25	167.32	SHP	Sandhill Point	Forest	*D. cuppresinum* *Prumnopitys ferruginea* (**miro**)
46.28	167.73	ORP	Orepuki	Cluster	*P. radiata*
46.38	168.03	TRM	Taramea (Riverton)	Single	*P. radiata*
46.44	168.23	(ORT) **NZ-46S**	Oreti Beach	Forest	*P. radiata*
New Zealand Sub-Antarctic Islands (February 2016 & February 2017)					
46.93	167.80	MBS	Mason Bay, Stewart Island	Forest	*D. cupressinum*
46.93	167.80	(MBH) **NZ-47S**	Mason Bay Homestead	Cluster	*C. macrocarpa* *P. radiata*
46.93	167.80	KLB	Kilbride Homestead	Cluster	*C. macrocarpa*
50.49	166.32	END	Enderby Island	Forest	*Metrosideros umbellata* (**southern rata**)
50.50	166.29	HAR	Auckland Island	Cluster	*M. umbellate*
52.55	169.15	(WLT) **NZ-53S**	Campbell Island	Single	*Picea sitchensis* (**sitka spruce**)

Continued...

Lat/°S	Lon/°S	Site Code	Location	Site Type	Tree Species
52.55	169.15	BEE	Beeman Cove, Campbell Island	Forest	*Dracophyllum longifolium* (**dracophyllum**)
Southern Chile (October 2017)					
41.39	-73.83	ESQ	Estaquilla	Cluster Forest	*Aextoxicon punctatum* (**olivillo**) *Drimys winteri* (**canelo**) *Embothrium coccineum* (**notro**) *Luma apiculata* (**myrtle**)
41.93	-74.03	PHL	Punihuil	Cluster	*A. punctatum* *C. macrocarpa* *Podocarpus nubigenus* (**manio macho**) *P. radiata* *Notafagus betuloides* (**coigue**)
42.59	-74.12	CUC	Cucao	Cluster	*A. punctatum* *N. betuloides*
43.78	-72.97	(RMB) **CH-44S**	Raul Marin Balmaceda	Cluster	*C. macrocarpa* *N. betuloides* *P. nubigenus* *P. radiata*
45.14	-73.51	PAG	Puerto Aguirre	Firest	*D. winteri* *N. betuloides* *P. nubigenus*
46.64	-73.87	LSR	Laguna San Rafael	Forest	*N. betuloides* *P. nubigenus*

Continued...

Lat/°S	Lon/°S	Site Code	Location	Site Type	Tree Species
47.79	-73.59	(TOR) **CH-48S**	Tortel	Forest	*N. betuloides* *P. nubigenus*
52.54	-71.92	(SKY) **CH-53S**	Seno Skyring	Single	*N. betuloides*
53.75	-70.97	(TAR) **CH-54S**	Monte Tarn	Forest	*N. betuloides* *Pilgerodendron uviferum* (**cypress)**
54.92	-69.32	(PNV) **CH-55S(w)**	Puerto Navarino	Cluster	*N. betuloides* *Notafagus pumilio* (**lenga**)
54.93	-67.32	(ENV) **CH-55S**	East Navarino	Cluster	*N. betuloides*
54.94	-67.65	OMO	Omora Park	Forest	*N. pumilio*

AHIPARA (AHP 35.16 °S Figure 3.5)

a

b

c

Figure 3.5: Ahipara (AHP), Northland: Scattered trees on a flat golf course next to the sea (top left, a, and right, b), with aerial view of ocean proximity (bottom, c).

- Ocean Proximity: towards the south end of a large bay on the west coast, with a peninsula to the south, extending out west.
- Location: adjacent to the beach with sand dunes, at the north end of a small coastal town, Ahipara, Northland, North Island New Zealand.
- Site: relatively flat golf course with scattered trees.

BARING HEAD (BHD 41.07 °S Figure 3.6)

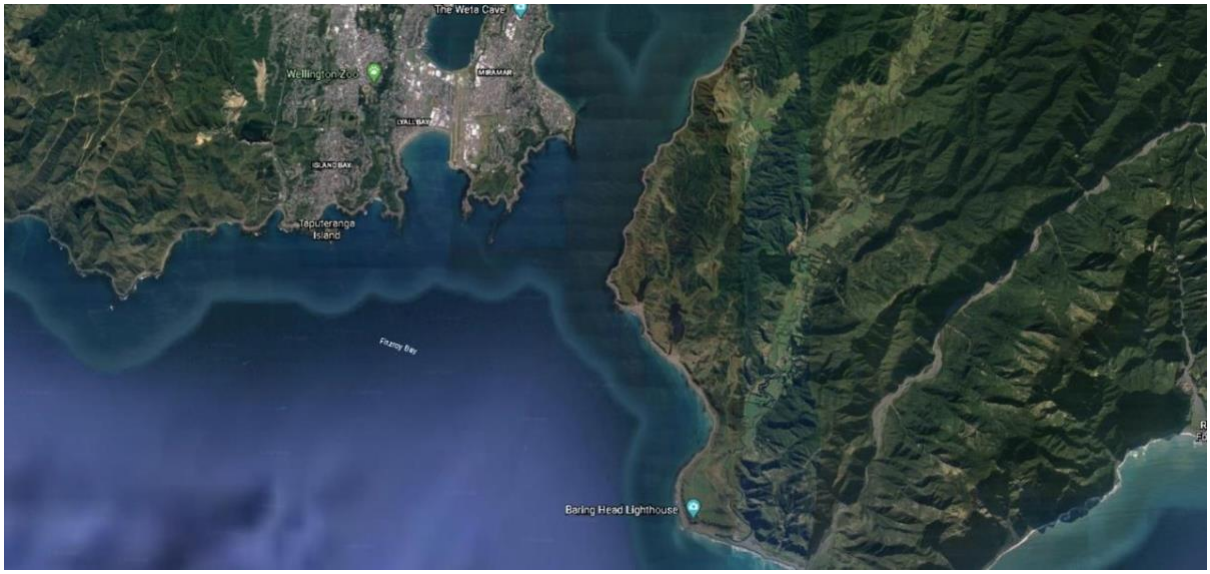

Figure 3.6: Baring Head (BHD), Wellington: Aerial view of trees on a high coastal cliff, located east across the entrance of the Wellington Harbour.

- Ocean Proximity: exposed peninsula, mid-south coast of North Island New Zealand.
- Location: cliff top, east across the bay from Wellington.
- Site: wind breaks and small clusters of trees around a house with grass surroundings.
- Site with long-term direct atmospheric $\Delta^{14}CO_2$ measurements; sampled trees are within ~100 m of the measurement site.

GILLESPIES BEACH (GBS 43.42 °S Figure 3.7)

a b c

d

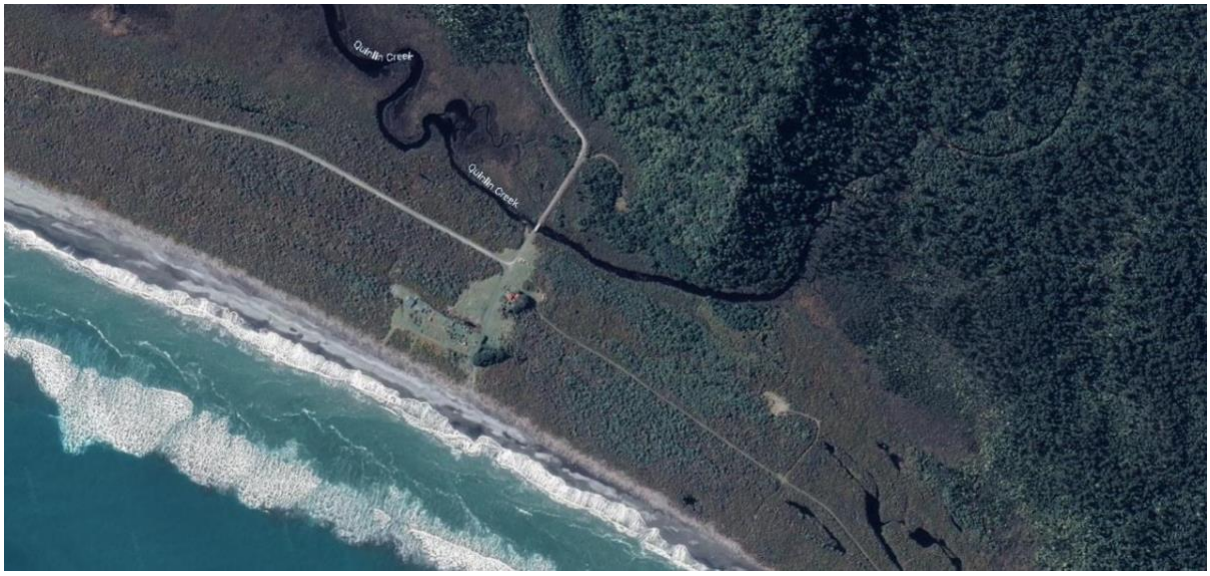

Figure 3.7: Gillespies Beach (GBS), West Coast: Exposed trees behind a long beach (top left, a, centre, b, and right, c), with scattered baches (bottom, d).

- Ocean Proximity: in the middle of a large exposed bay on the west coast.
- Location: on the beach, with baches close behind to the east. West Coast, South Island New Zealand.
- Site: row of trees behind the beach and signs of storm-damaged trees.

NZ-44S: HAAST BEACH (HAB 43.86 °S Figure 3.8)

a b c

d

Figure 3.8: Haast Beach (HAB), West Coast: Scattered trees around a paddock next to the beach (top left, a, centre, b, and right, c), with aerial view of ocean proximity (bottom, d).

- Ocean Proximity: on the west coast.
- Location: near the beach, with scrub before the trees. West Coast, South Island New Zealand.
- Site: a paddock adjacent to the beach, with damaged trees and branches.

HAAST BEACH DEVELOPMENT (HBD 43.89 °S Figure 3.9)

a

b

c

Figure 3.9: Haast Beach Development (HBD), West Coast: Trees planted as a windbreak, with visible wind influence (top left, a, and right, b), running perpendicular from the edge of a lagoon next to the open ocean (bottom, c).

- Ocean Proximity: on a lagoon just off the open ocean on the west coast.
- Location: New grassed development area to the south, trees exposed to westerly winds and the ocean. Unknown what occupied the development area previously, but likely farmland since the trees appear to be a shelter belt. West Coast, South Island New Zealand.
- Site: a line of trees running back from the beach, with round tree trunks chosen to core.

OKURU (OKU 43.91 °S Figure 3.10)

a

b

c

Figure 3.10: Okuru (OKU), West Coast: Scattered trees in a grassy paddock with small shrubs (top left and right, a, and, b respectively, adjacent to the ocean (bottom, c).

- Ocean Proximity: on the west coast.
- Location: a grassy close to the end of Hapuka River. West Coast, South Island New Zealand.
- a few scattered trees in open grass, with smaller shrubs and bushes towards the open sea.

HAAST MOTOR CAMP (HMC 43.91 °S Figure 3.11)

a

b

c

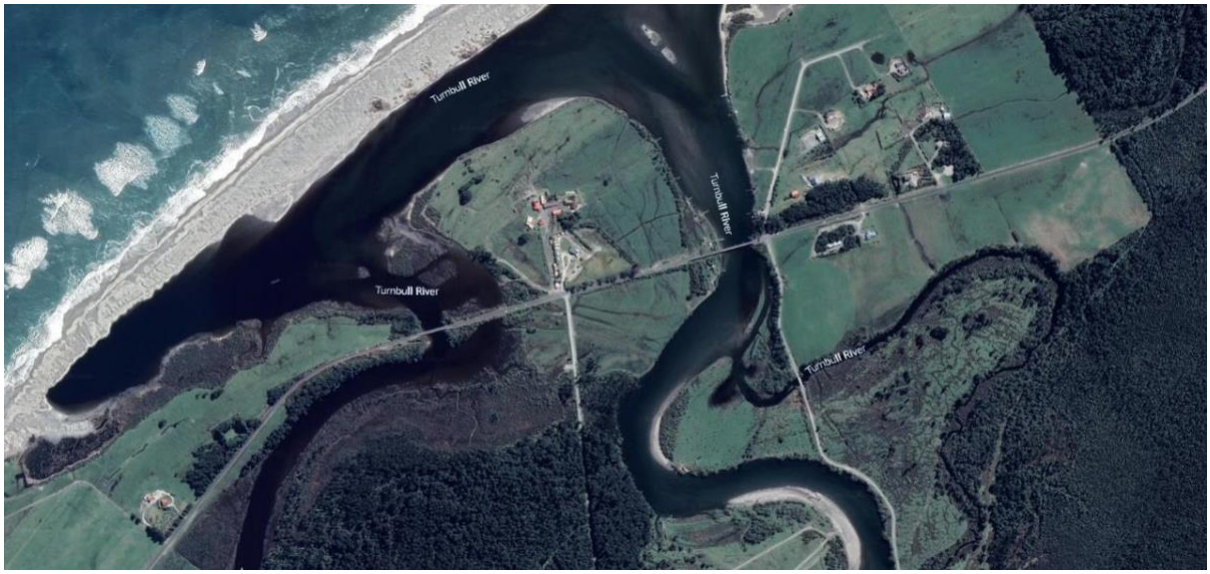

Figure 3.11: Haast Motor Camp (HMC), West Coast: trees of a wind break at the back of a paddock adjacent to the exposed lagoon beach (top left, a, and right, b), with surrounding paddocks and a house to the east (bottom, c).

- Ocean Proximity: on a lagoon divided off the open ocean of the west coast by a narrow sand spit.
- Location: exposed beach on the lagoon, between Hapuka River and Turnbull River, with paddocks around and a house to the east. West Coast, South Island New Zealand.
- Site: a paddock adjacent to the beach with trees in a line parallel to the beach at the back of the paddock.

HUMP RIDGE (HIGH) (HRH 46.22 °S Figure 3.12)

a b c

d

Figure 3.12: Hump Ridge (High) (HRH), Southland: trees along an elevated stretch of a coastal forest walking track.

- Ocean Proximity: slightly inland in the southeast of Fjordland National Park, Southland.
- Location: at an elevated position on a walking track in the coastal forest. South Island New Zealand.
- Site: trees just off the track, towards the coast, just down from the plateau, all located within old growth forest.

SANDHILL POINT (SHP 46.25 °S Figure 3.13)

a

b

c

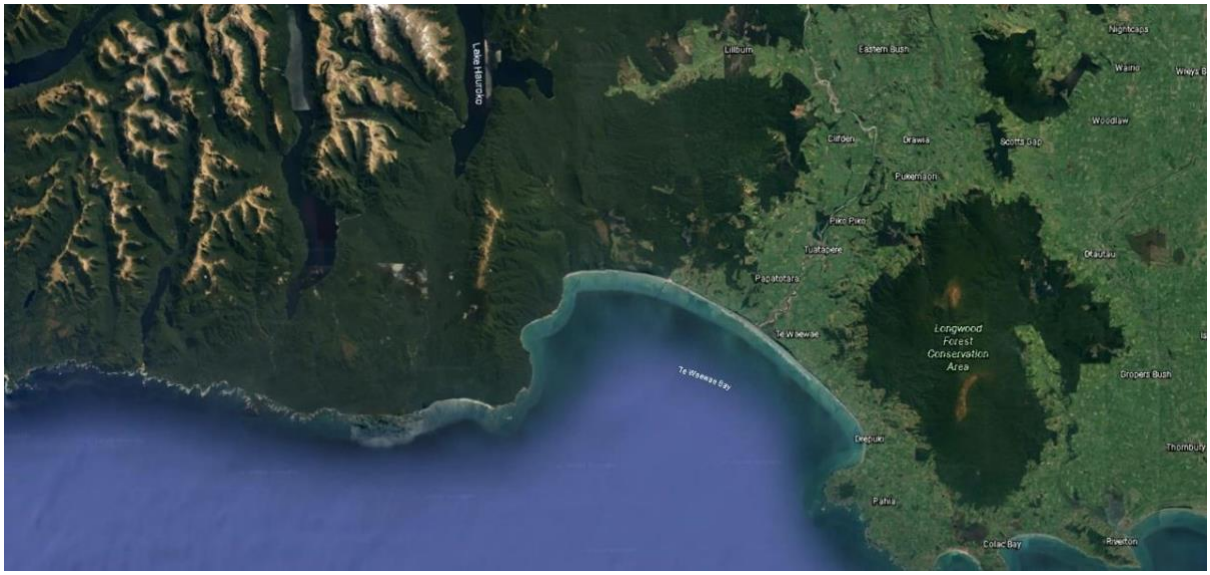

Figure 3.13: Sandhill Point (SHP), Southland: trees of an exposed coastal forest (top left, a) adjacent to the beach (top right, b) on a coastal peninsula (bottom, c).

- Ocean Proximity: an exposed coastal position in the south of Fjordland National Park, Southland.
- Location: a small coastal peninsula leading down from elevated coastal forest to the open sea. South Island New Zealand.
- Site: trees within the forest just above the track running parallel to the coastline by the sand and dunes.

OREPUKI (ORP 46.28 °S Figure 3.14)

a b c

d

Figure 3.14: Orepuki (ORP), Southland: scattered trees along an exposed cliff at the beach (top left, a, centre, b, and right, c), at the southeast end of a large bay (bottom, d).

- Ocean Proximity: just east of Fjordland National Park, at the southeast end of a large bay, Southland.
- Location: cliff at beach, a few houses around and a main road to the east. South Island New Zealand.
- Site: a few trees together very exposed to the west coast.

TARAMEA (RIVERTON) (TRM 46.38 °S Figure 3.15)

a

b

c

Figure 3.15: Taramea (TRM), Southland: single scattered trees along the beachfront (top left, a, and right, b), on the east of a peninsula.

- Ocean Proximity: the east side of a peninsula, forming the west end of a large bay.
- Location: beachfront by Riverton (small town), Southland, South Island New Zealand.
- Site: single trees along the beachfront, with sand dunes nearby.

NZ-46S: ORETI BEACH (ORT 46.44 °S Figure 3.16)

a

b

c

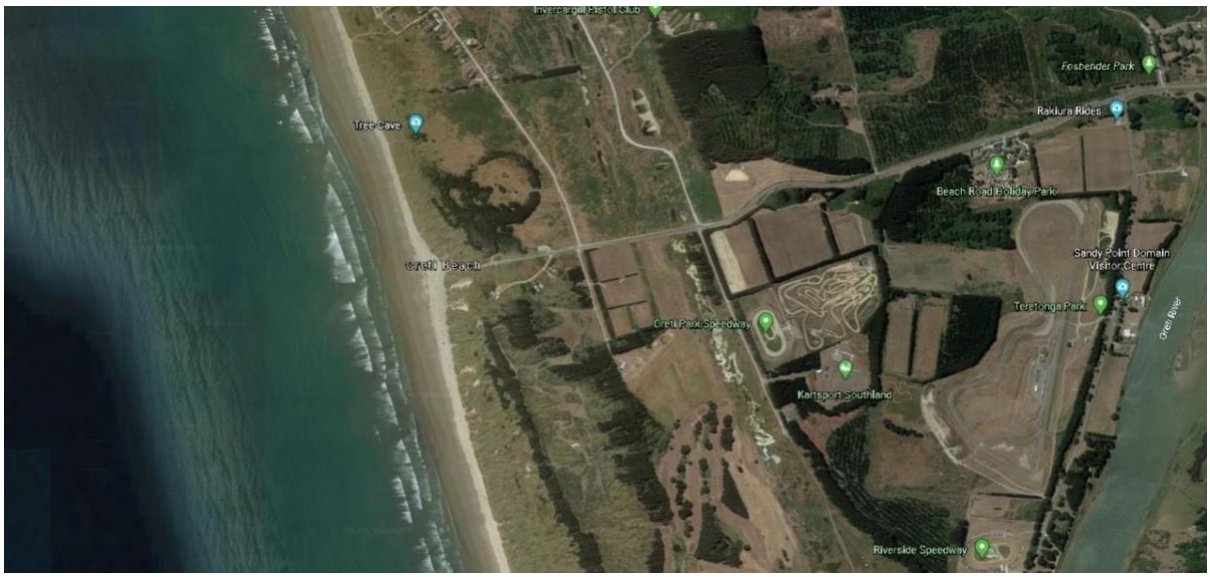

Figure 3.16: NZ-46S: Oreti Beach (ORT), Southland: plantation forest near the beach (top left, a, and right, b) at the southeast end of a large bay (bottom, c).

- Ocean Proximity: exposed position at the southeast end of a large bay, Southland.
- Location: by the side of a beach-access road. South Island New Zealand.
- Site: plantation forest close to the beach. Trees within forest sampled.

MASON BAY (SANDHILL), STEWART ISLAND (MBS 46.93 °S Figure 3.17)

a b c

d

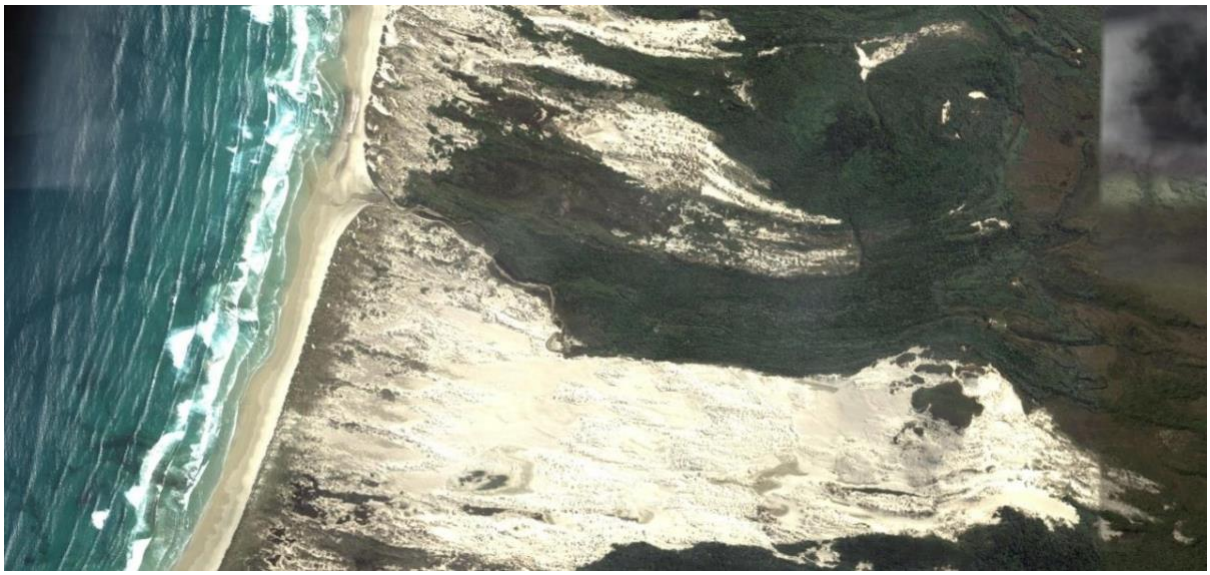

Figure 3.17: Mason Bay (Sandhill) (MBS), Stewart Island: middle of Mason Bay on the west of the island, downhill from a large sandhill and many dunes.

- Ocean Proximity: west coast of Stewart Island, just off the south coast of South Island New Zealand.
- Location: middle of Mason Bay, downhill from and east of a large sandhill and many dunes. Stewart Island.
- Large tree within ~500 m diameter forested area.

NZ-47S: MASON BAY HOMESTEAD, STEWART ISLAND (MBH 46.93 °S Figure 3.18)

a b

Figure 3.18: NZ-47S: Mason Bay Homestead (MBH), Stewart Island: slightly inland from Mason Bay on the west coast (left, a, and right, b), with windbreaks planted by a homestead (also see Figure 3.17d).

- Ocean Proximity: just under 1 km inland on the west coast of Stewart Island, just off the south coast of South Island New Zealand.
- Location: Somewhat inland from Mason Bay beach, extensive sandhills and some bush sections between coast and site. Stewart Island.
- Site: windbreaks along two sides of the homestead plot, with trees furthest away sampled. All trees are to the west of the homestead but could have occasional fire influence. Homestead was permanently occupied until ~1984, and may have used coal for heat. More recently the homestead is used by hut wardens, with wood used for heat and gas for cooking.

KILBRIDE HOMESTEAD, STEWART ISLAND (KLB 46.93 °S Figure 3.19)

a b c

d

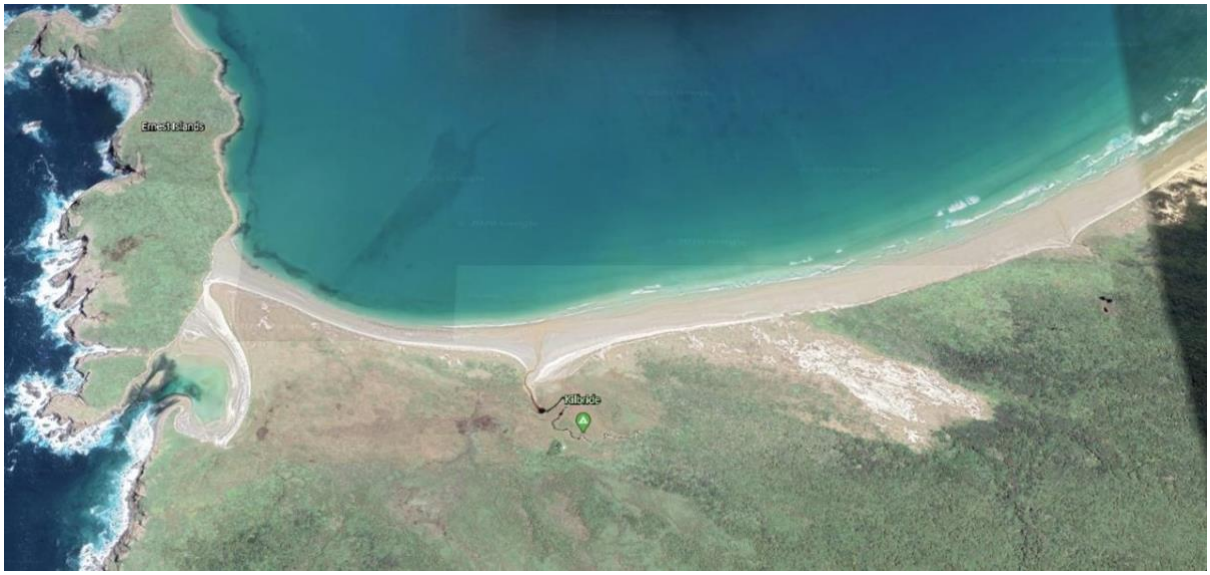

Figure 3.19: Kilbride Homestead (KLB), Stewart Island: windbreak by a homestead at the South of Mason Bay, a few hundred metres from the ocean.

- Ocean Proximity: a few hundred metres inland from the coast, west coast of Stewart Island, just off the south coast of South Island New Zealand.
- Location: bottom of Mason Bay, somewhat sheltered from direct westerly and southwesterly winds. Stewart Island.
- Site: windbreak in a line from the homestead, with trees furthest away sampled. Homestead was irregularly occupied by farmers until mid 1980s and may have used coal for heat. More recently used as a bach with likely more frequent use in 2000s, with wood used for heat and gas for cooking.

ENDERBY ISLAND (END 50.49 °S Figure 3.20)

Figure 3.20: Enderby Island (END): rata from a belt around the west of the island, extending 50 – 100m inland.

- Ocean Proximity: northwest coast and southwest coast (behind Sandy Bay, sea lion colony).
- Location: rata form a belt around the island, ~50 – 100 inland from the coast and extending for a few hundred metres inland. Enderby Island.
- Site: Sampled trees are on the outer edge of the forest belt.

HARDWICKE SETTLEMENT, AUCKLAND ISLAND (HAR 50.50 °S Figure 3.21)

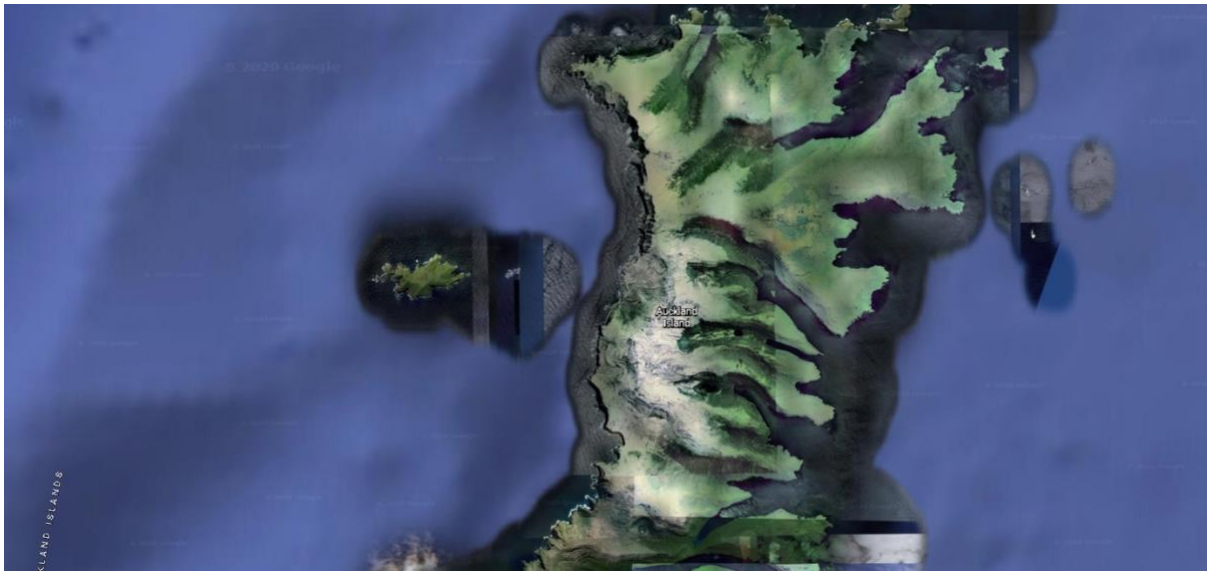

Figure 3.21: Hardwicke Settlement (HAR), Auckland Island: sheltered north facing bay on the island.

- Ocean Proximity: a north-facing bay.
- Location: many trees in the area were logged ~100 years ago. Was populated in the past but abandoned. Auckland Island.
- Site: a sheltered bay.

NZ-53S: WORLD'S LONELIEST TREE, CAMPBELL ISLAND (WLT 52.55 °S Figure 3.22)

Figure 3.22: NZ-53S: World's Lonesliest Tree (WLT), Campbell Island: east of the main high range down the centre of the island.

- Ocean Proximity: east of the main high range on Campbell Island.
- Location: was occupied in the early part of the 20th century, but the island has been uninhabited since the 1980s, with occasional visits by scientists and tourists. Campbell Island.
- Site: Camp cove; the tree is suspected to have been planted in 1904, although uncertain (Turney et al., 2016).

BEEMAN COVE, CAMPBELL ISLAND (BEE 52.55 °S)

- Ocean Proximity: east of the main high range of Campbell Island.
- Location: (see above); Campbell Island.
- Site: along the track above Beeman Cove; automated weather station at this site.

ESTAQUILLA (ESQ 41.39 °S Figure 3.23)

a b c

d

Figure 3.23: Estaquilla (ESQ), Puerto Montt: scattered trees along exposed coastal cliffs.

- Ocean Proximity: on the west coast.
- Location: cliffs and ocean-facing hills along a small track parallel to the coast, near Puerto Montt, Chile.
- Site: clusters of trees on farmland cliff-tops and tall trees on edge/uphill of coastal forests.
- ESQ(b) is a few hundred metres further south along the track.

PUNIHUIL (PHL 41.93 °S Figure 3.24)

a b c

d

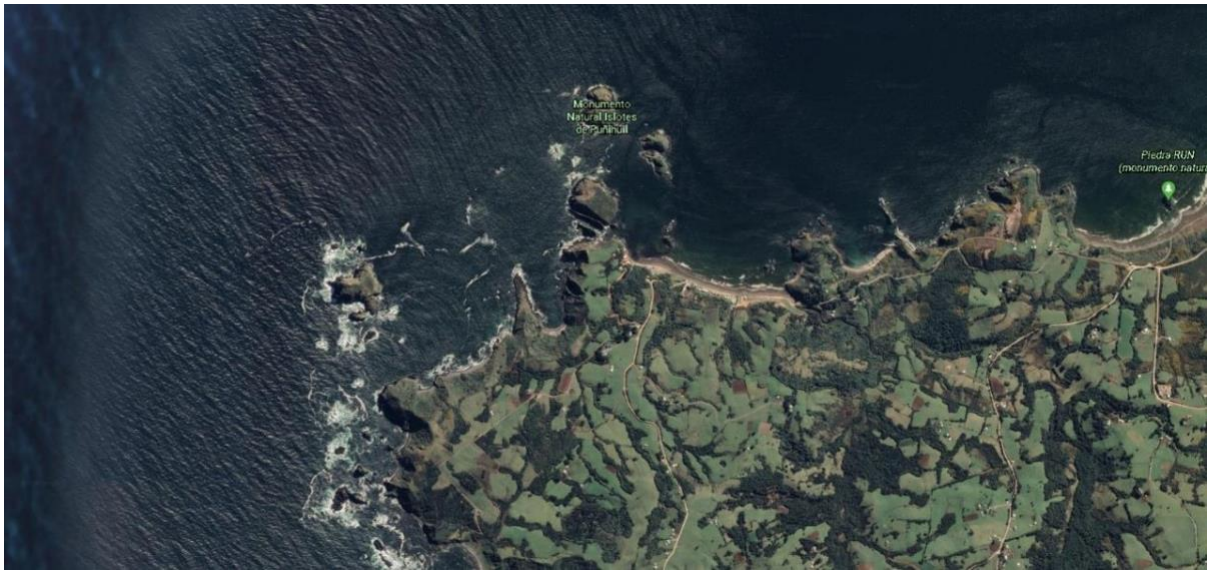

Figure 3.24: Punihuil (PHL), Chiloe: paddocks on cliff tops (top left, a, and top centre, b) with trees along the boundary (top right, c), at the southern end of a large bay (bottom, d).

- Ocean Proximity: northwest coast of Chiloe, west of mainland Chile.
- Location: at the southern end of a large bay, Chiloe, Chile.
- Site: trees on cliffs and hills behind the beach.

CUCAO (CUC 42.59 °S Figure 3.25)

a b c

d

Figure 3.25: Cucao (CUC), Chiloe: scattered trees behind the beach and along the cliff-top.

- Ocean Proximity: on the mid-west coast of Chiloe, west of mainland Chile.
- Location: exposed west coast with cliffs and steep hills, Chiloe, Chile.
- Site: cliff-top trees and others near cliff-bases near beaches.

CH-44S: RAUL MARIN BALMACEDA (RMB 43.78 °S Figure 3.26)

a b c

d

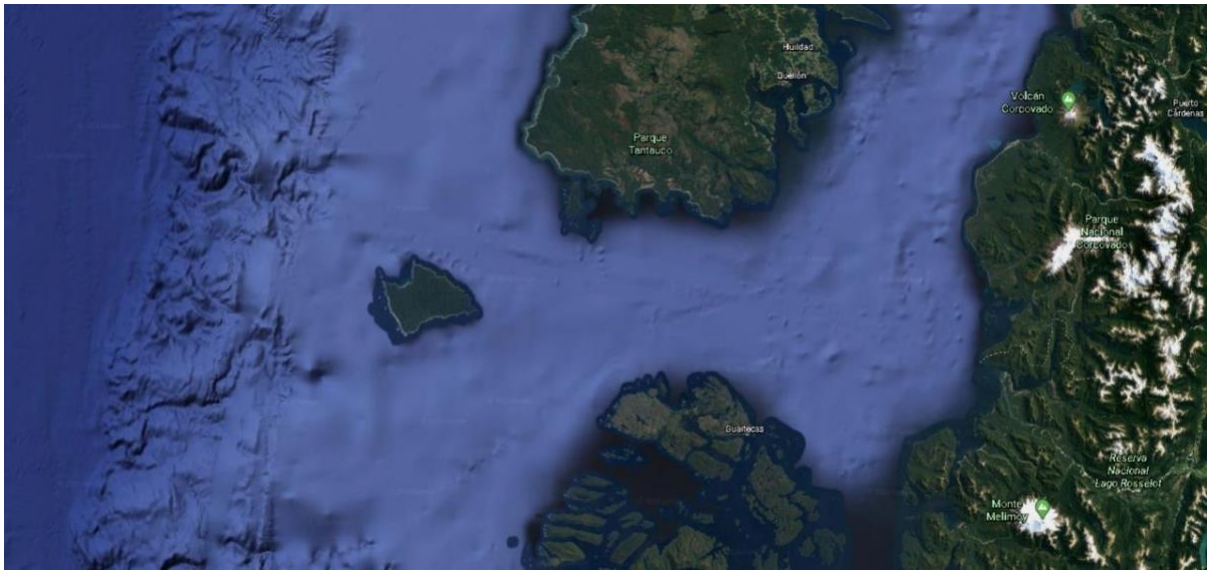

Figure 3.26: Raul Marin Balmaceda (RMB), Aysen: small island close to the mainland (top left, a, and top centre, b) with wind breaks (top right, c) and other scattered trees, looking out to the open ocean (bottom centre, d).

- Ocean Proximity: small island very close to the open ocean.
- Location: east coast of small, relatively flat RMB Island, with minimal human influence in the area (inhabited in the northeast), Aysen Region, Chile.
- Site: wind break of about 20 large trees by Fundo Los Leones Lodge and other scattered trees.

PUERTO AGUIRRE (PAG 45.14 °S Figure 3.27)

a b c

d

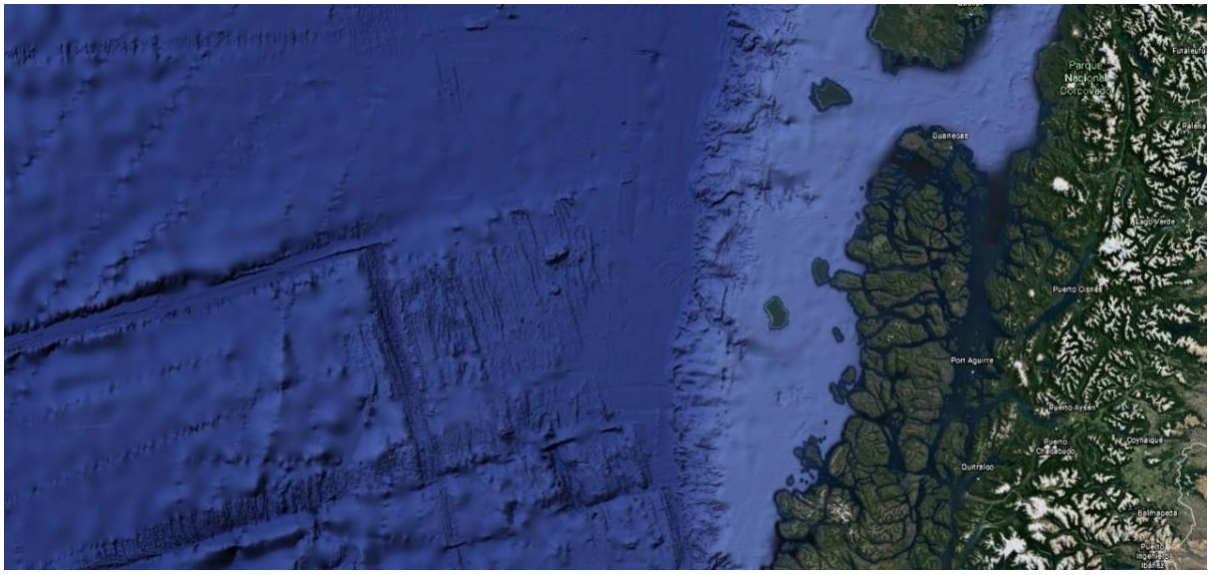

Figure 3.27: Puerto Aguirre (PAG), Aysen: by a large channel (top left, a), with trees reaching down to the shores (top centre, b, and top right, c), and large islands towards the ocean (bottom centre, d).

- Ocean Proximity: lying within a large channel extending from the open ocean in the north (just south of Chiloe), with many large islands to the west.
- Location: in the centre of a large bay on the north of relatively flat PAG Island, inhabited on the south coast, Aysen Region, Chile.
- Site: trees on the edge of a forest area leading down to a rocky breach, near the end of the air-strip.

LAGUNA SAN RAFAEL (LSR 46.64 °S Figure 3.28)

a b c

d

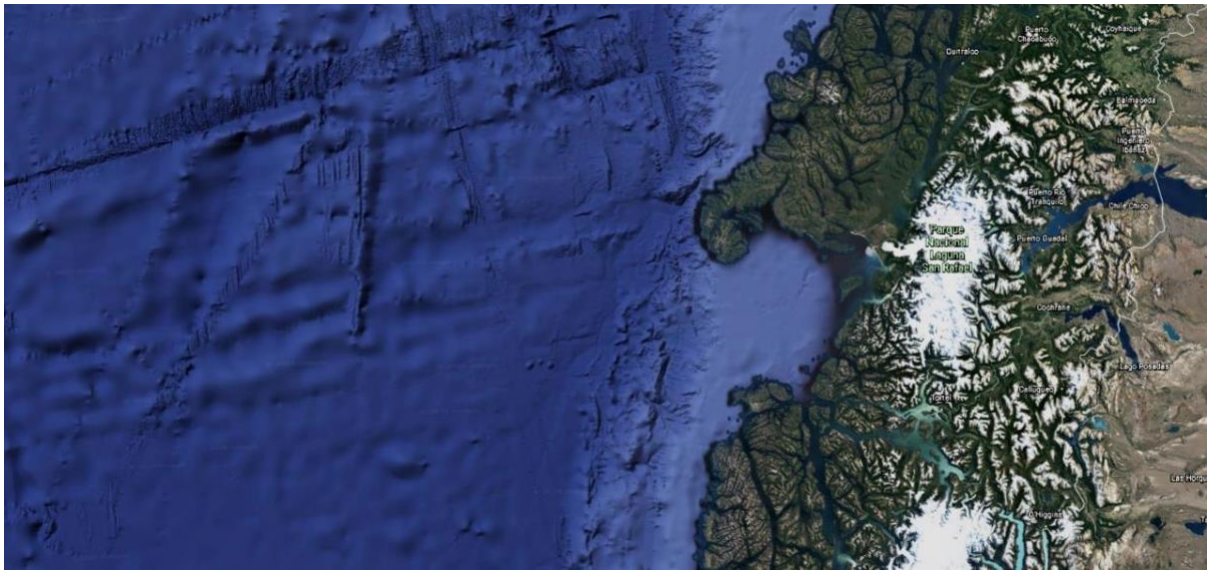

Figure 3.28: Laguna San Rafael (LSR), Aysen: scattered trees along the shores of a glacier-fed lake.

- Ocean Proximity: a peninsula with many inlets and smaller islands to the west before open ocean.
- Location: the northeast of glacier-fed LSR (lake) and west of snowy mountains, Aysen Region, Chile.
- Site: relatively flat grassy area with scattered trees and some forest area leading to the lake.

CH-48S: TORTEL (TOR 47.79 °S Figure 3.29)

a b c

d

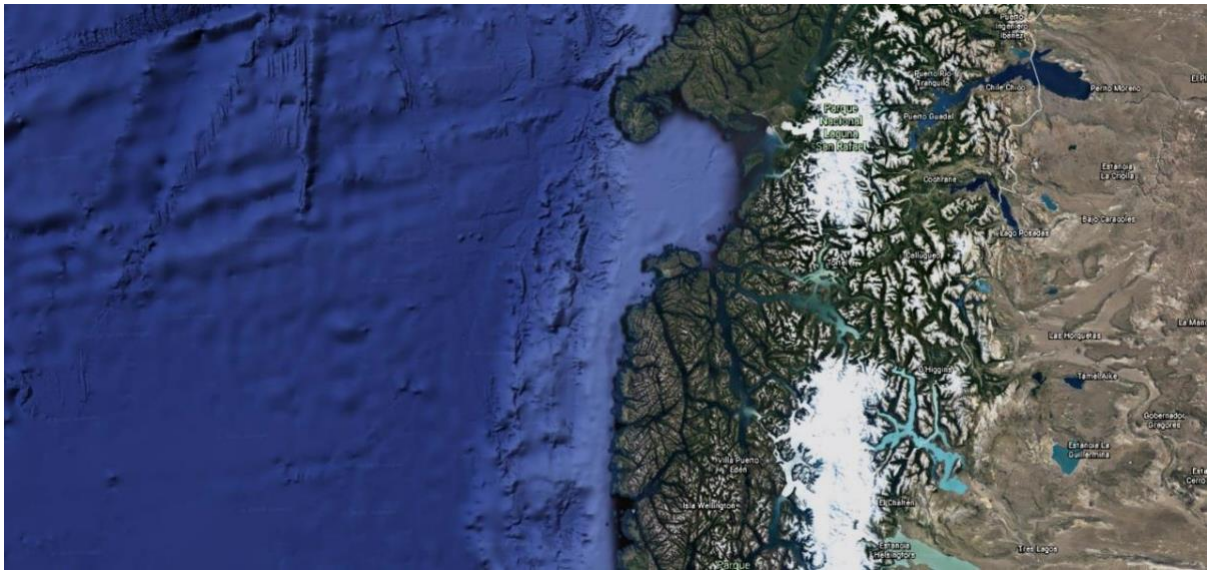

Figure 3.29: Tortel (TOR), Aysen: small islands on a channel that leads to the open ocean.

- Ocean Proximity: east of a large channel that divides off into smaller channels towards the open ocean, including past a snowy peninsula with many inlets and other islands.
- Location: small islands around a large channel and river estuary northwest of Tortel (inhabited), Aysen Region, Chile.
- Site: trees on steep rocky edges of a small island and at the edge of flat sandy estuarine-islands.

CH-53S: SENO SKYRING (SKY 52.54 °S Figure 3.30)

a b c

d

Figure 3.30: Seno Skyring (SKY), Punta Arenas: scattered, weathered trees along the edge of an inlet leading to the open ocean.

- Ocean Proximity: a complex network of inlets surrounding a large snowy mainland peninsula west of SKY.
- Location: very sparsely populated north coast of a large inlet (SKY), near Punta Arenas, Chile.
- Site: single and clustered trees on the inlet edge, just by a quiet road.
- \end{itemize}

CH-54S: MONTE TARN (TAR 53.75 °S Figure 3.31)

a b c

d

Figure 3.31: Monte Tarn (TAR), Punta Arenas: steep hills on the edge of a large channel with marsh and scrub amongst scattered trees and forest areas.

- Ocean Proximity: north of a large channel from the west coast, with small islands and inlets towards open ocean.
- Location: steep, exposed hills beyond the end of a track on the southeast coast of a mainland peninsula, near Punta Arenas, Chile.
- Site: some elevated marshy area with scattered trees and some forest area.
- Common site with collaborators.

CH-55S(w): PUERTO NAVARINO (PNV 54.92 °S Figure 3.32)

a b c

d

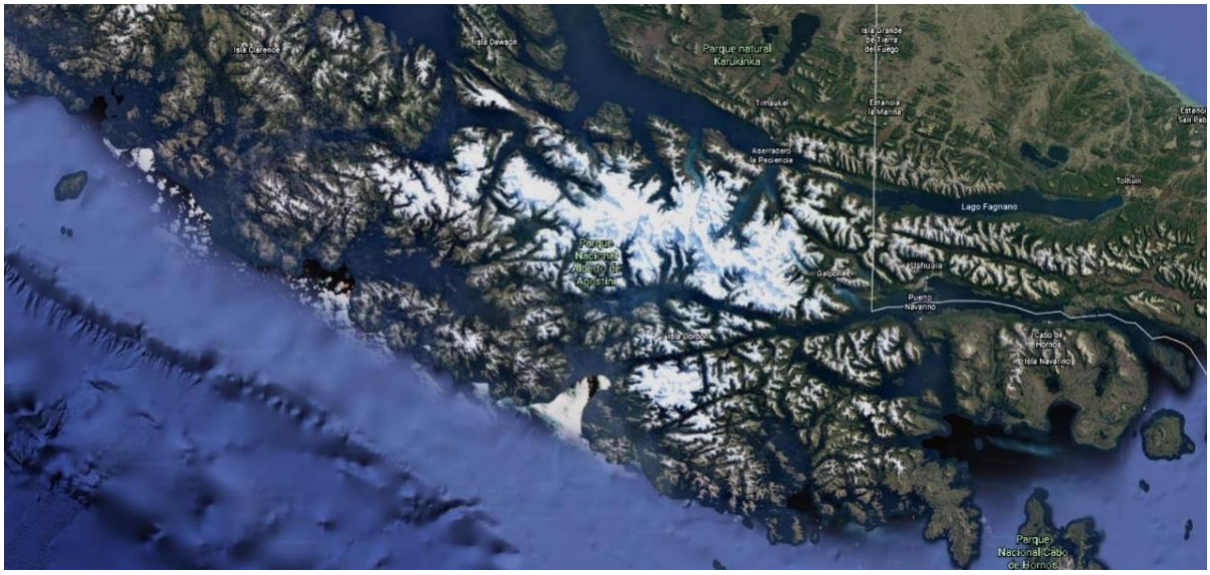

Figure 3.32: Puerto Navarino (PNV), Isla Navarino: scattered trees grow in the windy conditions along the Beagle Channel.

- Ocean Proximity: along the Beagle Channel, which extends from the west coast, between snowy islands.
- Location: the far northwestern point of Isla Navarino, Chile, therefore west(w) of Ushuaia (see below).
- Site: trees scattered around a relatively steep small hill.
- CH-55S(w)b is approximately a hundred metres east.

CH-55S: EAST NAVARINO (ENV 54.93 °S Figure 3.33)

a b c

d

Figure 3.33: East Navarino (ENV), Isla Navarino: scattered (and often dead) trees on a flat paddock by the Beagle Channel.

- Ocean Proximity: along the Beagle Channel, which extends from the west coast, between snowy islands.
- Location: the far northeastern point of Isla Navarino, Chile (south of the Beagle Channel). Note that Ushuaia, Argentina (city of ~50 000) lies on the north coast of the Beagle Channel, west of ENV.
- Site: large trees on fairly flat land leading from the water.

OMORA PARK (OMO 54.95 °S Figure 3.34)

a b c

d

Figure 3.34: Omora Park (OMO), Isla Navarino: botanic forest park with a range of forest areas by a quiet track along the coast by the Beagle Channel.

- Ocean Proximity: along the Beagle Channel, which extends from the west coast, between snowy islands.
- Location: aside a quiet track on the central north coast of Isla Navarino, Chile, therefore east of Ushuaia.
- Site: botanic forest park with some well-established forest and large areas subject to beaver damage.

3.2 Sampling

Having collected tree cores from the different field campaigns, a procedure is then followed that I established for this project to facilitate working with a large number of tree core samples.

Prior to the field campaign in southern Chile, the preparation of import permits had been organised with the Ministry of Primary Industries (MPI). Whilst in Chile we detailed the tree core samples collected, such that the samples were brought into New Zealand accompanied from the field with the appropriate paperwork. The samples were subsequently all logged into the laboratory database.

With no prior tree core knowledge or dendrochronology background, I follow (and adapt as required) protocols for tree core sample preparation, ring counting and ring slicing established by Andrew Lorrey (NIWA), working together on the first suite of samples. I gained experience working with tree core samples and learning from a specialist with extensive tree core knowledge.

3.2.1 Tree Core Collection

Field Equipment:

- Increment borers
- Labelled drinking straws (and craft knife)
- Multi-purpose tape
- Field notebook and pencil
- GPS
- Tube for collected samples

Tree core collection follows standard protocols developed by our research team, which are summarised here.

Preparation, prior to going on site, is always beneficial, and particularly important for adverse weather conditions and challenging environments. To improve efficiency, I implemented preparation of drinking straws for core collection.

Drinking straws are sliced down the side with a craft knife. This allows cores to partially dry after collection, before they are removed from the straws in the laboratory, thereby reducing mould growth and twisting of cores with uneven drying. Tree cores also slide easily into pre-prepared straws without resistance or damage, which previously occurred. Some multi-purpose tape is then attached to one end of the straw to create a label.

Tree cores are taken using an increment borer. The borers are of 4.3 mm diameter and 450 mm and 600 mm length (Haglof, Sweden), thereby extracting cylindrical cores of such dimensions. Although a larger diameter borer would provide additional sample material, a 4.3 mm diameter borer provides sufficient material for analysis and its use is much easier and less physically demanding. Shorter borers also offer more stability and ease for corers, although a longer borer is used where trees have a large diameter. Using multiple increment borers in the field allows tree core samples to be taken simultaneously, such that a group can be divided into pairs to improve sampling efficiency and maximise the number of tree cores collected.

Having identified the tree(s) of interest to core, details are recorded in the field notebook; important information such as latitude and longitude are recorded, alongside detailed notes of the site and tree. Photographs are also taken as a record.

When selecting a tree for coring, potential angles from which to access the tree and sufficiently work with the borer are identified. One of these is chosen to start, taking subsequent cores from the same tree.

The two parts of the increment borer are attached together ready for use, and the spatula is safely placed aside. The borer is then aligned with the centre of the tree at chest height and a slight upward angle. The upward angle aids the removal of the core when sliding it out of the tree, whilst working at chest height allows for maximum strength to be applied.

Applying weight to the borer whilst twisting (clockwise) into the tree allows the thread to gain hold of the tree after going through the bark. The borer is twisted into the tree until the length of the borer in the tree is deemed greater than the distance to the centre of the tree. Other justifiable reasons for stopping to core include reaching the end of the borer or reaching a rotten section of wood, which is often identified when the borer becomes quiet and very easy to twist.

When the decision is made to remove the core from the tree, the spatula is inserted upside-down, into the top of the borer. Turning the borer half a turn anti-clockwise breaks the core from the tree, allowing the spatula to be pulled out of the borer with the core. A prepared straw is slid onto the core, ensuring that the label end is at the bark-end, and taping both ends to ensure that no material is lost. The tree core is finally labelled with a site code and tree/core number, before placing in a tube.

The increment borer is removed from the tree by twisting anti-clockwise and pulling strongly so that the borer doesn't lose grip of the wood. Once the borer is out of the tree, it is checked for any residue, which can be removed with a small stick or similar. Used correctly, the borer does not harm the tree, with resin naturally soon sealing the small hole, which can also be plugged with local natural material. Multiple cores can subsequently be taken from different angles of the tree where accessible, or from nearby trees identified. When taking tree cores, the presence of locally absent, false and missing rings should be considered, such that a range of samples are collected to avoid such artefacts. A minimum of two tree cores are typically collected from a tree, and multiple trees at a given site. This is particularly important given the remote nature of many sampling sites, such that many tree cores are taken, to maximise potential of good quality cores and useful samples (Section 3.2.4).

3.2.2 Tree Core Mounting

On returning from the field, tree cores are removed from their straws as soon as possible. This allows them to dry faster and thus remain in better condition for analysis.

Common dendrochronology practice involves mounting tree cores onto wooden mounts using glue. However, I developed an alternative mounting technique (detailed below) for this project, seeking to reduce potential contamination for ^{14}C analysis, thus avoiding introducing both foreign wood material and glue.

Strips of corrugated cardboard are wrapped in aluminium foil, adding a label at one end. Aluminium foil is used such that the untreated (matte) side is in contact with the samples. The tree cores are carefully removed from the straws and mounted onto the cardboard with a few elastic bands and labelled accordingly. For consistency, the bark-end of cores is placed at the label end. The elastic bands are attached to secure the tree cores, yet loosely such that they don't damage the samples. Where tree cores have broken, additional elastic bands are used as necessary, with care taken to ensure the correct orientation. For particularly small fragments of broken tree core or loose bark, plastic film wrap is used to wrap them before mounting in place with an elastic band. Mounted cores can then thoroughly dry before progressing further or moving to storage.

3.2.3 Tree Core Organisation

Details of tree core samples are recorded in a tree core database that I established for this project. On returning from the field, information recorded in the field notebook is entered into the tree core database to formally document samples in the laboratory.

Included in the database are tree cores for this project, in addition to a few from other sites in New Zealand (e.g., Norris, 2015). The tree core database is also linked to the ^{14}C sample-processing database in the laboratory, such that samples can be easily located, and processes applied to a sample can be identified, i.e., whether remaining a core, sliced into tree rings or prepared for ^{14}C measurement.

Tree cores are stored with others from the same tree/site. The individual tree cores are lined up on their mounts, on sheets of foil-covered cardboard. The sheets are carefully stacked in boxes, which are labelled and stacked in the tree core storage cupboard. For international samples (Chile tree cores), the procedure is to retain these in the international

sample cupboard, in which they are similarly stored. This follows guidelines and requirements of MPI.

3.2.4 Tree Core Selection

An initial inspection of the tree core samples is conducted to discount any samples that are particularly broken or twisted, making them hard to work with. Broken tree cores are avoided where possible, because working with the cores can be difficult and ring counting across breaks can also be challenging. In addition to this, there may be some uncertainty of the orientation of small pieces of a tree core, which may have become switched in the straw or mount. This could occur due to a handling error at any point after collection, thus introducing further complications that can be avoided by using complete tree cores. Similarly, twisted cores, commonly caused by uneven drying, are largely disregarded from further investigation.

Further investigation seeks to identify the best tree core(s) from a site. Initially a large subset of tree cores is selected for preparation, using the naked eye and ever-growing experience to assess the visibility of annual growth rings from the rough exterior of tree cores. Different factors are considered when making the selection, but ultimately the suitability of a tree core is judged on the clarity of annual growth rings after preparation. This is a time-consuming process but becomes more efficient with experience. As preparation progresses, the sample selection evolves to reflect findings with different trees and species (summarised in Table 3.2).

Key desirable characteristics of tree core samples:

- BARK ATTACHED TO CORE (otherwise 'broken near bark-end' or 'bark separate' or 'bark not present'): No outer pieces of a core can have been lost when the bark is still attached to the core. However, when collecting a core the bark often breaks off. Keeping the bark is important to determine if any rings are attached to the bark, thus allowing the core to be used for further analysis. The outer rings of a core (near the bark-end) are particularly important because they affect the whole ring count.

- WHOLE TREE CORE SAMPLE (otherwise 'broken'): Using whole tree core samples (as detailed above) avoids any confusion of sample orientation or ring counting associated with separate broken pieces. Whole samples are also easier to prepare because they are longer and can be secured well.
- STRAIGHT TREE CORE SAMPLE (otherwise 'twisted' or 'bent'): tree cores can twist and bend whilst drying after collection, which is particularly common with very wet samples. Bent tree cores are particularly challenging to work with and break easily during preparation. Twisted tree cores mean that the tracheids change alignment along the sample, thus making preparation and ring counting particularly difficult.
- SUITABLE NUMBER OF ANNUAL GROWTH RINGS (otherwise 'not enough rings' or 'no bomb pulse'): ~60 years of growth are sought such that ring counts can be confirmed through bomb-pulse validation (Section 5.1). Where this is not possible then samples must span the period of interest in this project, i.e., ~30 years. Therefore where bomb-pulse validation cannot be performed, two cores from the same site can be used, whereby replicate measurements are conducted to validate ring counts (Section 5.1.3).
- RINGS THAT ARE EASY TO IDENTIFY (otherwise 'unclear rings' or often 'rotten'): Annual growth ring boundaries are easily identifiable where there is a strong colour gradient between latewood and earlywood of adjacent annual growth rings. Each ring can therefore be identified and counted. Different species have different tendencies to form either well-defined boundaries or not, although individual samples can also vary.
- WELL-DEFINED ANNUAL GROWTH RING BOUNDARIES (otherwise 'unclear rings' or often 'rotten'): When slicing annual growth rings, a sharp, precise boundary is desirable rather than a diffuse one, because it minimises uncertainty as to where the boundary lies. This makes the exact position to slice with the scalpel much clearer.
- SUITABLE WIDTH OF ANNUAL GROWTH RINGS (otherwise 'narrow rings'): Very narrow annual growth rings are not only hard to identify and count, but also particularly challenging to slice. Narrow rings mean that when rings are sliced with a scalpel, there is likely a greater uncertainty associated with human error. Longer annual growth rings minimise effects associated with slicing, because any material

from an adjacent ring will contribute relatively less material, thus have less influence on results.

- STRAIGHT ANNUAL GROWTH RING BOUNDARIES (otherwise 'curved ring boundaries'): When slicing rings with a scalpel, it is challenging and almost impossible, to slice at different angles on a ring boundary, meaning that some proportion of adjacent years' growth will be incorporated. Such slicing thus introduces uncertainties that can be minimised through using tree cores with straighter boundaries.

Table 3.2: Summary of tree core samples collected from New Zealand and Chile and further sampling potential: site code, tree number, core number, species and selection details for laboratory preparation.

Site	Tree	Core	Species	Selection Details
North Island New Zealand				
AHP	T1	C1	*P. radiata*	Ok, no bomb pulse
AHP	T2	C1	*P. radiata*	Broken
AHP	T2	C2	*P. radiata*	Broken near bark end
AHP	T3	C1	*P. radiata*	Ok, no bomb pulse
AHP	T4	C1	*P. radiata*	Ok, no bomb pulse
AHP	T4	C2	*P. radiata*	Broken near bark end
BHD	T3	C1	C. *macrocarpa*	Broken near bark end
BHD	T3	C2	C. *macrocarpa*	SELECTED
South Island New Zealand				
GBS	T1	C1	C. *macrocarpa*	Best of GBS, species
GBS	T1	C2	C. *macrocarpa*	Broken near bark end
GBS	T1	C3	C. *macrocarpa*	Broken near bark end
GBS	T2	C1	C. *macrocarpa*	Broken near bark end
GBS	T2	C2	C. *macrocarpa*	Broken near bark end

Continued...

Site	Tree	Core	Species	Selection Details
GBS	T2	C3	C. *macrocarpa*	Broken near bark end
NZ-44S	T1	C1	*P. radiata*	SELECTED
NZ-44S	T1	C2	*P. radiata*	SELECTED
NZ-44S	T2	C1	*P. radiata*	Best of HAB, bark separate
NZ-44S	T2	C2	*P. radiata*	Ok, bark separate
HBD	T1	C1	C. *macrocarpa*	Ok, bark separate
HBD	T1	C2	C. *macrocarpa*	Best of HBD, bark separate
HBD	T2	C1	C. *macrocarpa*	Broken near bark end
HBD	T2	C2	C. *macrocarpa*	Bark not present
HBD	T2	C3	C. *macrocarpa*	Broken near bark end
OKU	T1	C1	D. *cupressinum*	Species
OKU	T1	C2	D. *cupressinum*	Species
OKU	T2	C1	D. *cupressinum*	Species
OKU	T2	C2	D. *cupressinum*	Species
HMC	T1	C1	C. *macrocarpa*	Ok, bark separate
HMC	T1	C2	C. *macrocarpa*	Best of HMC, species
HMC	T2	C1	C. *macrocarpa*	Broken near bark end
HMC	T2	C2	C. *macrocarpa*	Broken near bark end
SHP	T1	C1	D. *cupressinum*	Species
SHP	T1	C2	D. *cupressinum*	Species
SHP	T2	C1	P. *ferruginea*	Ok, bark separate
SHP	T2	C2	P. *ferruginea*	Ok, bark separate
SHP	T3	C1	D. *cupressinum*	Species
SHP	T3	C2	D. *cupressinum*	Species

Continued...

Site	Tree	Core	Species	Selection Details
HRH	T1	C1	N. *fusca*	Bark not present, broken
HRH	T1	C2	N. *fusca*	Bark not present, broken
HRH	T2	C1	D. *cupressinum*	Species
HRH	T2	C2	D. *cupressinum*	Species
HRH	T3	C1	P. *totara*	Broken near bark end
HRH	T3	C2	P. *totara*	Broken near bark end
ORP	T1	C1	*P. radiata*	Bark not present
ORP	T1	C2	*P. radiata*	Broken near bark end
ORP	T1	C3	*P. radiata*	Ok core
ORP	T2	C1	*P. radiata*	Ok core
ORP	T2	C2	*P. radiata*	Ok core
ORP	T3	C1	C. *macrocarpa*	Bark not present, broken
ORP	T3	C2	C. *macrocarpa*	Broken near bark end
TRM	T1	C1	*P. radiata*	Ok, bark not present
TRM	T1	C2	*P. radiata*	Ok, bark not present
TRM	T2	C1	*P. radiata*	Ok, bark not present
TRM	T2	C2	*P. radiata*	Best of TRM
NZ-46S	T1	C1	*P. radiata*	Ok core
NZ-46S	T1	C2	*P. radiata*	Ok core
NZ-46S	T2	C1	*P. radiata*	SELECTED
NZ-46S	T2	C2	*P. radiata*	SELECTED
NZ-46S	T2	C3	*P. radiata*	Broken near bark end
New Zealand Sub-Antarctic Islands				
MBS	T1	C1	D. *cupressinum*	Species
MBS	T1	C2	D. *cupressinum*	Species
MBS	T2	C1	D. *cupressinum*	Species

Continued...

Site	Tree	Core	Species	Selection Details
MBS	T2	C2	D. *cupressinum*	Species
KLB	T1	C1	C. *macrocarpa*	Bark not present
KLB	T1	C2	C. *macrocarpa*	Bark not present
KLB	T2	C1	C. *macrocarpa*	Bark not present, broken
KLB	T2	C2	C. *macrocarpa*	Bark not present, broken
KLB	T3	C1	*P. radiata*	Ok core
KLB	T3	C2	*P. radiata*	Ok core
KLB	T3	C3	*P. radiata*	Ok core
NZ-47S	T1	C1	C. *macrocarpa*	SELECTED
NZ-47S	T1	C2	C. *macrocarpa*	Broken near bark end
NZ-47S	T2	C1	C. *macrocarpa*	Broken near bark end
END	T1	C1	M. *umbellata*	Narrow rings
END	T1	C2	M. *umbellata*	Narrow rings
END	T2	C1	M. *umbellata*	Narrow rings
END	T2	C2	M. *umbellata*	Narrow rings
END	T3	C1	M. *umbellata*	Narrow rings
END	T3	C2	M. *umbellata*	Narrow rings
END	T4	C1	M. *umbellata*	Narrow rings
END	T4	C2	M. *umbellata*	Narrow rings
END	T5	C1	M. *umbellata*	Narrow rings
END	T5	C2	M. *umbellata*	Narrow rings
END	T6	C2	M. *umbellata*	Narrow rings
HAR	T1	C1	M. *umbellata*	Narrow rings
HAR	T1	C2	M. *umbellata*	Narrow rings
HAR	T2	C1	M. *umbellata*	Narrow rings

Continued...

Site	Tree	Core	Species	Selection Details
HAR	T2	C2	M. *umbellata*	Narrow rings
NZ-53S	T1	C1	P. *sitchensis*	Bark not present
NZ-53S	T1	C2	P. *sitchensis*	Ok, no bomb pulse
NZ-53S	T1	C3	P. *sitchensis*	Ok, no bomb pulse
NZ-53S	T2	C1	P. *sitchensis*	Ok, no bomb pulse
NZ-53S	T2	C2	P. *sitchensis*	SELECTED
NZ-53S	T3	C1	P. *sitchensis*	Ok, no bomb pulse
NZ-53S	T3	C2	P. *sitchensis*	SELECTED
NZ-53S	T3	C3	P. *sitchensis*	SELECTED
BEE	T1	C1	D. *longifolium*	Narrow rings
BEE	T2	C1	D. *longifolium*	Narrow rings
BEE	T3	C1	D. *longifolium*	Narrow rings
BEE	T4	C1	D. *longifolium*	Narrow rings
Southern Chile				
ESQ	T1	C1	*P. radiata*	Not enough rings
ESQ	T1	C2	*P. radiata*	Not enough rings
ESQ	T1	C3	*P. radiata*	Not enough rings
ESQ	T2	C1	E. *coccineum*	Species
ESQ	T2	C1	E. *coccineum*	Species
ESQ	T3	C1	L. *apiculate*	Species
ESQ	T4	C1	D. *winteri*	Rotten
ESQ	T5	C1	D. *winteri*	Broken near bark end
ESQ	T6	C1	A. *punctatum*	Bark not present
ESQ	T6	C2	A. *punctatum*	No bark, unclear boundaries
ESQ	T6	C3	A. *punctatum*	Unclear ring boundaries
ESQ(b)	T1	C1	P. *nubigenus*	Broken near bark end
ESQ(b)	T1	C2	P. *nubigenus*	SELECTED

Continued...

Site	Tree	Core	Species	Selection Details
ESQ(b)	T2	C1	N. *betuloides*	SELECTED
ESQ(b)	T2	C2	N. *betuloides*	Ok, unclear ring boundaries
ESQ(b)	T3	C1	A. *punctatum*	Species
ESQ(b)	T4	C1	A. *punctatum*	Species
ESQ(b)	T5	C1	A. *punctatum*	Species
ESQ(b)	T5	C2	A. *punctatum*	Species
ESQ(b)	T6	C1	P. *nubigenus*	Broken near bark end
ESQ(b)	T6	C2	P. *nubigenus*	Broken near bark end
ESQ(b)	T6	C3	P. *nubigenus*	Broken near bark end
PHL	T1	C1	*P. radiata*	Not enough rings
PHL	T2	C1	*P. radiata*	Not enough rings
PHL	T3	C1	C. *macrocarpa*	Unclear ring boundaries
PHL	T3	C2	C. *macrocarpa*	Broken, unclear boundaries
PHL	T4	C1	P. *nubigenus*	Ok core
PHL	T4	C2	P. *nubigenus*	Unclear ring boundaries
PHL	T5	C1	N. *betuloides*	Bark separate, unclear boundaries
PHL	T6	C1	A. *punctatum*	Broken, twisted
PHL	T7	C1	A. *punctatum*	Bark not attached, broken
PHL	T8	C1	A. *punctatum*	Broken, unclear boundaries
CUC	T1	C1	A. *punctatum*	Unclear ring boundaries
CUC	T1	C2	A. *punctatum*	Unclear ring boundaries
CUC	T2	C1	N. *betuloides*	Twisted, bent, unclear boundaries
CUC	T3	C1	N. *betuloides*	Broken, unclear boundaries
CUC	T3	C2	N. *betuloides*	Broken, bent
CUC	T4	C1	N. *betuloides*	Broken, bent
CUC	T4	C2	N. *betuloides*	Broken, bent, unclear boundaries

Continued...

Site	Tree	Core	Species	Selection Details
CH-44S	T1	C1	C. *macrocarpa*	Broken near bark end
CH-44S	T2	C1	C. *macrocarpa*	Not enough rings (rotten)
CH-44S	T2	C2	C. *macrocarpa*	Ok core
CH-44S	T3	C1	*P. radiata*	Ok core
CH-44S	T3	C2	*P. radiata*	SELECTED
CH-44S	T3	C3	*P. radiata*	SELECTED
CH-44S	T4	C1	*P. radiata*	SELECTED
CH-44S	T4	C2	*P. radiata*	Ok core
CH-44S	T6	C1	P. *nubigenus*	Broken near bark end
CH-44S	T6	C2	P. *nubigenus*	Broken near bark end
CH-44S	T7	C1	P. *nubigenus*	SELECTED
CH-44S	T7	C2	P. *nubigenus*	Unclear ring boundaries
CH-44S	T9	C1	N. *betuloides*	Bark separate, twisted, bent
CH-44S	T9	C2	N. *betuloides*	Broken near bark end
PAG	T1	C1	N. *betuloides*	Twisted, bent, rotten
PAG	T1	C2	N. *betuloides*	Not enough rings (rotten)
PAG	T2	C1	D. *winteri*	Species
PAG	T3	C1	P. *nubigenus*	Ok, no bark present
PAG	T4	C1	P. *nubigenus*	Broken near bark end
PAG	T5	C1	P. *nubigenus*	Ok, narrow rings
PAG	T5	C2	P. *nubigenus*	Broken near bark end
PAG	T6	C1	P. *nubigenus*	Twisted, bent
PAG	T6	C2	P. *nubigenus*	Ok, unclear boundaries
PAG	T7	C1	N. *betuloides*	Broken
PAG	T7	C2	N. *betuloides*	Twisted, bent, rotten
LSR	T1	C1	P. *nubigenus*	Ok, no bomb pulse
LSR	T2	C1	N. *betuloides*	Bark separate, twisted, bent

Continued...

Site	Tree	Core	Species	Selection Details
LSR	T3	C1	N. *betuloides*	Not enough rings (rotten)
LSR	T3	C2	N. *betuloides*	Twisted, bent
LSR	T3	C3	N. *betuloides*	Twisted, bent
LSR	T4	C1	N. *betuloides*	Ok core, no bomb pulse
LSR	T4	C2	N. *betuloides*	Ok core, no bomb pulse
LSR	T5	C1	N. *betuloides*	Ok core, no bomb pulse
LSR	T5	C2	N. *betuloides*	Bark separate, no bomb pulse
CH-48S	T1	C1	N. *betuloides*	Not enough rings
CH-48S	T1	C2	N. *betuloides*	Twisted, bent
CH-48S	T2	C1	N. *betuloides*	Broken
CH-48S	T3	C1	P. *nubigenus*	Broken
CH-48S	T3	C2	P. *nubigenus*	Broken near bark end
CH-48S	T4	C1	N. *betuloides*	SELECTED
CH-48S	T5	C1	N. *betuloides*	No bark, broken, twisted, bent
CH-48S	T5	C2	N. *betuloides*	Broken
CH-48S	T6	C1	N. *betuloides*	SELECTED
CH-48S	T6	C2	N. *betuloides*	Not enough rings (rotten)
CH-48S	T7	C1	N. *betuloides*	Ok core, bark not present
CH-48S	T7	C2	N. *betuloides*	Broken
CH-48S	T7	C3	N. *betuloides*	Broken
CH-48S	T7	C4	N. *betuloides*	Broken
CH-53S	T1	C1	N. *betuloides*	Not enough rings (rotten)
CH-53S	T2	C1	N. *pumilio*	Not enough rings (rotten)
CH-53S	T2	C2	N. *pumilio*	Not enough rings (rotten)
CH-53S	T3	C1	N. *betuloides*	SELECTED
CH-53S	T3	C2	N. *betuloides*	Ok core, bark not present
CH-53S	T4	C1	N. *betuloides*	Ok core

Continued...

Site	Tree	Core	Species	Selection Details
CH-53S	T4	C2	N. *betuloides*	SELECTED
CH-54S	T1	C1	P. *wiferum*	Bark not present
CH-54S	T1	C2	P. *wiferum*	Broken near bark end
CH-54S	T2	C1	P. *wiferum*	Ok core, no bomb pulse
CH-54S	T2	C2	P. *wiferum*	Ok core, no bomb pulse
CH-54S	T3	C1	P. *wiferum*	SELECTED
CH-54S	T3	C2	P. *wiferum*	Ok core
CH-54S	T4	C1	P. *wiferum*	Ok core, no bomb pulse
CH-54S	T4	C2	P. *wiferum*	Ok core, no bomb pulse
CH-54S	T5	C1	N. *betuloides*	SELECTED
CH-54S	T5	C2	N. *betuloides*	Ok core
CH-54S	T6	C1	N. *betuloides*	Ok core, narrow rings
CH-54S	T6	C2	N. *betuloides*	SELECTED
CH-54S	T7	C1	N. *betuloides*	SELECTED
CH-54S	T7	C2	N. *betuloides*	Broken near bark end
CH-55S(w)	T1	C1	N. *betuloides*	SELECTED
CH-55S(w)	T2	C1	N. *betuloides*	Not enough rings (rotten)
CH-55S(w)	T3	C1	N. *betuloides*	Rotten
CH-55S(w)	T4	C1	N. *betuloides*	Not enough rings
CH-55S(w)	T5	C1	N. *betuloides*	Not enough rings
CH-55S(w)	T6	C1	N. *betuloides*	Not enough rings
CH-55S(w)	T7	C1	N. *betuloides*	Not enough rings
CH-55S(w)	T8	C1	N. *betuloides*	Broken near bark end, rotten
CH-55S(w)	T8	C2	N. *betuloides*	Rotten
CH-55S(w)b	T1	C1	N. *pumilio*	Rotten
CH-55S(w)b	T2	C1	N. *pumilio*	Broken
CH-55S(w)b	T3	C1	N. *pumilio*	Unclear rings (rotten)

Continued...

Site	Tree	Core	Species	Selection Details
CH-55S(w)b	T3	C2	N. *pumilio*	Narrow rings
CH-55S	T1	C1	N. *betuloides*	Not enough rings
CH-55S	T2	C1	N. *betuloides*	Ok, not enough rings
CH-55S	T3	C1	N. *betuloides*	Unclear rings (rotten)
CH-55S	T3	C2	N. *betuloides*	Ok, no bomb pulse
CH-55S	T4	C1	N. *betuloides*	Not enough rings (rotten)
CH-55Sb	T1	C1	N. *betuloides*	SELECTED
CH-55Sb	T1	C2	N. *betuloides*	Ok, unclear boundaries
CH-55Sb	T2	C1	N. *betuloides*	Ok, no bomb pulse
CH-55Sb	T2	C2	N. *betuloides*	Ok, no bomb pulse
CH-55Sb	T3	C1	N. *betuloides*	Ok, no bomb pulse
CH-55Sb	T4	C1	N. *betuloides*	SELECTED
CH-55Sb	T4	C2	N. *betuloides*	Broken
CH-55Sb	T4	C3	N. *betuloides*	Ok core
OMO	T1	C1	N. *pumilio*	Unclear rings (rotten)
OMO	T1	C2	N. *pumilio*	Unclear rings (rotten)
OMO	T2	C1	N. *pumilio*	Bark not attached
OMO	T3	C1	N. *pumilio*	Ok, narrow rings
OMO	T3	C2	N. *pumilio*	Ok, narrow rings

3.2.5 Tree Core Preparation

Before beginning to work with the tree core samples, photographs are taken to thoroughly record all sample details. This is particularly important, because cores are sliced and destroyed during ^{14}C sample processing, such that the photographic evidence is the only way to look back at the original sample form should it be necessary. Photographic evidence is used throughout processing to thoroughly record all aspects of the tree core samples and associated processing.

For tree core preparation, a large piece of flat foil-covered cardboard is secured to the work surface. Two gloves are placed on the left hand as protection (assuming right-handed for using the scalpel), and a clean scalpel blade is attached to a scalpel handle. In turn, selected cores are secured to the foil-covered cardboard surface for preparation. Elastic bands, used to secure the tree cores to their mount can be left on for security, or removed if they cause an uneven mount, and thus potentially contribute to breaks in tree cores.

The purpose of tree core preparation is to improve the visibility of the annual growth rings, thereby aiding ring counting. This is achieved by creating a flat surface perpendicular to the tracheids, increasing definition of annual growth ring boundaries.

To prepare a selected tree core, the tracheids must first be vertically aligned. This is achieved through looking down the end of the core, and ensuring that the visible cells (tracheids) are vertical. Vertical tracheid alignment is important for ring counting. Throughout sample preparation, the angle of the tracheids should be checked, because tree cores often rotate during preparation with the scalpel. A new scalpel blade should be used when it appears that the blade is becoming blunt. In the meantime, the blade can be wiped clean to remove sample shavings. Sample shavings should also be cleared from the work area to reduce contamination if a small piece of core breaks off the sample being prepared.

The left forearm is firmly placed on the bench behind the tree core, holding the sample securely behind the direction of cutting. Sitting down on a low chair also helps, as it aligns eye-level with the sample, thus allowing close examination of the tree core surface. To slice the surface off the tree core, the scalpel is applied using a diagonal movement from the 'bark end' simultaneously pushing down with the forefinger and away with the thumb. The aim is for long, smooth strokes of the scalpel along the length of the tree core, so that the surface is as smooth as possible.

Near the bark-end of the tree core, moving the scalpel across the core rather than along its length helps to reduce the possibility of the bark or end breaking off, which can happen very easily. Particular care should thus be taken whilst working with the ends of the tree cores. The bark is often already separate to the main core because it breaks off naturally when

removing the tree core from the tree. It is important to keep the bark because it provides validation that none of the outer rings have been lost in a section from the end of the core. It is also common that initial ring growth of the most recent year is broken off with the bark. This is verified under microscope.

Initially a large subset of tree cores is initially prepared, before proceeding to further prepare the surface of tree cores of a smaller selection to progress with.

A smooth surface is important because it allows annual ring boundaries to be easily identified, whilst reducing potential for scalpel cuts to appear similarly to boundaries. Having created a smooth surface perpendicular to the tracheids, the annual ring boundaries are much more defined than on initial inspection of the rough edge of the core, thus facilitating ring counting.

3.2.6 Tree Ring Counting

Throughout tree core preparation attempts to identify annual growth rings assesses the suitability of a tree core sample. Prepared tree core samples are assessed, typically first selecting cores that appear relatively easy to identify rings and that also extend back to the bomb period, subsequently working with other cores depending on the success of initial samples and with selection criteria in mind (Section 3.2.8).

To proceed with ring counting, a prepared tree core with relatively clear and defined annual ring boundaries to the naked eye is selected. An initial ring count is conducted to gain a rough gauge of the number of rings, such that if there is at least 30 rings the sample has sufficient rings for this study. A first ring count is conducted with the naked eye, which can help identify different colour gradients of earlywood and latewood boundaries that are sometimes overlooked when looking at a microscopic scale. The core is then examined under microscope for a different perspective, typically making ring boundaries clearer to the eye, as well as the cell structure density, i.e., cell-size variation along the core.

Once satisfied with a rough ring count for a core, the centre of each annual growth ring is marked using a pin. It is good practice to work along the core from the bark-end, although challenging areas can be returned to. For such challenging sections, it is often beneficial to clean up the sample surface further with a scalpel under the microscope. This helps to clarify whether a mark is a ring boundary or simply a surface defect. Discussion with another person whilst projecting the microscope visual onto a computer monitor can also be helpful.

With a confident ring count established, pins are placed every five years along the core, i.e., 2015, 2010... The ring count is then further validated, before photographing the sample in detail under the microscope in preparation for slicing the core, which will then be destroyed.

3.2.7 Tree Ring Slicing

Having conducted a confident ring count of a tree core, the sample is then assessed for its suitability for slicing. This is considered throughout preparation and selection, however a final decision must be made at this point.

The key factors concerning the slicing of tree cores are the width of annual growth rings and the line of the ring boundaries; rings must be of suitable width to confidently slice along the boundaries (providing sufficient material), whilst boundaries must be clear and straight such that a scalpel can be used to slice the annual rings with suitable accuracy.

Selecting a tree core to slice, individual tree ring samples' identities related to the tree core sample are created in the laboratory database. This allows vials to be labelled in preparation for slicing. Rings are labelled by their number within the core, starting with 'R1' at the (outer) bark-end. As a partial safety precaution, this allows the year tagged to a sample to be adjusted, if the initial ring count is later found to be inaccurate.

Detailed microscope photos are taken of sections along the tree core to ensure that the sample is fully documented and can be investigated once sliced into its annual growth rings.

The selected core is placed under the microscope ensuring a sharp scalpel blade is available for slicing.

As with the ring counting, typically slicing is started at the bark-end of the tree core. Having examined the bark (and the likely attached partial ring) under microscope, the bark is placed in a vial before proceeding to slice. Tree core slicing is conducted under microscope to allow for improved clarity in slicing with the scalpel.

In order to slice a ring from the tree core, an indent is made along the ring boundary with the scalpel. Pressure is then applied to the scalpel, moving it around; left and right, forwards and backwards, such that the ring naturally fractures off along the ring boundary. The sliced ring is placed in the corresponding vial, slicing subsequent rings similarly. Rings are sliced until reaching a suitable stopping point, which can be for a number of reasons.

For this project a 30-year record is desired from chosen cores: 1985 – 2015. Ideally the selected cores extend back to the bomb period, thus slicing to ~1960 is appropriate, such that the ring count can be validated through the bomb-pulse (Section 5.1). Some cores stretch beyond this, such that further rings are sliced where the core continues to be of good quality, but it is otherwise not essential. In some cases tree cores are selected that do not continue until the bomb spike, meaning that instead two cores are required to validate the ring count (Section 5.1.2). Therefore in these case slicing stops when the centre of the tree is reached or rings become hard to count/slice for other reasons, e.g., rotten or very narrow rings. Some sections within a tree core can contain very narrow rings or have boundaries that are not suitably straight to slice with a scalpel. Such sections of a core are therefore placed in a vial together, with detailed notes made should the sample be used in the future.

With a range of tree cores sliced, a selection of rings is chosen to prepare for ^{14}C analysis for this project.

3.2.8 Tree Ring Sample Selection

Having determined the best quality tree core samples and prepared the most suitable for this project, a range of tree ring samples is selected to proceed with ^{14}C preparation and analysis (Chapter 4).

Overall the selected samples must achieve good coverage across the latitudinal range sampled, thereby tree core samples are considered in regional groups to minimise latitudinal intervals of ^{14}C records. Tree core samples are then assessed, seeking samples that extend to the bomb-pulse where possible. In regions that lack samples spanning the bomb-pulse, multiple cores are selected for alternative ring count validation.

Samples are also considered in context of other suitable samples, such that the number of different species analysed is minimised where possible to avoid any natural associated differences (Section 2.3). Where this is not possible, different species with good ring counting characteristics should ideally be linked at a common site. Location and site details of tree core samples are also considered, whereby some sites and locations are well-situated, whilst others pose more potential of local terrestrial (or similar non-oceanic) signals.

The first tree ring samples analysed are tree rings corresponding with the bomb-pulse from selected tree core samples: typically 1963 – 1966 (Section 5.1.1).

Alternatively, corresponding subsets of tree rings from two cores are analysed and compared to establish ring count validation (Section 5.1.2).

Having confirmed the ring count through bomb-pulse validation or otherwise, selected tree rings from the core are prepared for ^{14}C analysis. In some cases errors in ring counts may be identifiable such that an accurate ring count is established, however in other cases a ring counting error may not be identifiable and thus tree core samples are not further analysed (Section 5.1).

In some cases, an individual tree ring is not analysed for a variety of reasons, commonly associated with tree ring slicing, including curvy ring boundaries and narrow rings within a small section of a core. If a boundary was not sliced satisfactorily or fractured badly, then a tree ring sample could contain growth material from an adjacent year or lack some of its own material, and would thus not give an accurate ^{14}C analysis.

3.2.9 Tree Ring ^{14}C Preparation and Analysis

Sample organisation of tree ring samples into AMS measurement wheels is considered throughout laboratory work (Section 4.1). Samples must be prioritised for processing and overall laboratory scheduling. As stated above, bomb-pulse and replicate core samples are prepared and analysed first to validate ring counts, before proceeding with analysis of other tree rings in the core. Different numbers of samples can be processed within a batch depending on personal work-style preferences.

As with all tree core sample laboratory preparation, the first suite of tree ring samples analysed is the New Zealand samples. Having completed these, an initial suite of Chile samples is analysed before a further final mixed suite of samples to address any additional areas.

Alongside ^{14}C analysis of tree ring samples, repeat measurements of a modern secondary standard and other replicate sample measurements are conducted for data quality analysis (Chapter 5).

3.3 Fieldwork Acknowledgements

Fieldwork was a large part of this project, and would not have been as successful without the range of people involved.

South Island New Zealand fieldwork was primarily conducted by Margaret Norris and Jocelyn Turnbull, with assistance from Cameron Johns, Bjorn Johns and Malcolm Turnbull.

Ian Turnbull and Jane Forsyth also provided invaluable advice on potential sampling locations.

Jocelyn Turnbull conducted fieldwork of the Sub-Antarctic Islands of New Zealand, in coordination with Dave Bowen and Alex Fergus of Heritage Expeditions, and Spencer Clubb of DOC. Also with help collecting tree cores from others on the cruise including Edin Whitehead, Paul Charman and Hamish.

%Tree Core collection was also assisted by others on the cruise
The fieldwork in Chile would not have been possible without Carolyn McCarthy and Vince Beasley, who both provided regional insight and knowledge that allowed us to find accessible sites for the project and outline fieldwork. Fieldwork was thus conducted by Jocelyn Turnbull and Rachel Corran alongside a range of others including Carolyn, Vince, Ricardo de Pol-Holz, Juan Carlos Aravena and Guillermo Duarte.

Existing tree core samples and tree ring ^{14}C records from near Wellington, New Zealand, were also used in this project. These were sampled and prepared by a number of people including Margaret Norris and India Ansell.

Chapter 4

Methodology for ^{14}C Measurement of Tree Rings

In this PhD project I use tree rings to reconstruct modern atmospheric $\Delta^{14}CO_2$ over the Southern Ocean. Having presented coastal fieldwork and tree ring sampling rationale (Chapter 3), in this chapter I detail subsequent ^{14}C sample preparation and measurement methodology.

The chapter is largely written in the form of a manuscript draft, which is to be submitted to the Radiocarbon journal following completion of this thesis.

I begin by outlining the established protocols for ^{14}C analysis of tree rings at RRL (Section 4.1). This provides background for the manuscript draft that details recent methodology development for organic samples, including tree rings, at RRL (Section 4.2).

The methodology development within this PhD project is the automation of the organic solvent wash process using an automated extraction system (ASE). On arrival at RRL, I took advantage of the availability of an ASE system that posed the potential to improve sample processing efficiency. This developed methodology was employed for the large number of samples analysed within this project. I have also instructed RRL Team members to operate the ASE system, such that this automated method is now employed for all organic samples subject to solvent washes at RRL. I created a Standard Operating Procedure (SOP) document, which details associated health and safety information (Appendix A).

This automation follows previous investigation into the organic solvent wash and cellulose extraction procedures (Norris, 2015). These developments are presented together in the publication.

During my PhD I supervised two Victoria University of Wellington (VUW) summer scholarship students, whom I trained to independently prepare tree ring samples for ^{14}C analysis, including physical preparation, organic solvent washes and cellulose extraction. I conducted sample preparation for this PhD project, with directed assistance from Nikita Turton. Having sufficiently developed my tree ring counting experience, I taught Taylor Ferrick to conduct ring counting and the process of selecting tree core samples to proceed with analysis (Section 3.2).

4.1 Tree Ring Preparation for ^{14}C Analysis

All of the tree ring samples for this project come from tree cores collected from field campaigns in New Zealand and Chile (Chapter 3). The tree ring samples undergo ring counting and slicing ready for ^{14}C preparation and analysis (Section 3.2).

Tree ring samples for this project are considered 'modern' wood, in that they are from the last century, i.e., influenced by the bomb period (Section 2.2.3). They are therefore subject to the standard modern wood procedure at RRL, detailed here.

Following preparation, samples for ^{14}C analysis are pressed into wheels of 40 targets for analysis in the AMS at RRL (Section 4.1.5). Each wheel of 40 targets comprises of a number of standards alongside samples. In a wheel of organic samples, i.e., tree ring samples, for high-precision ^{14}C measurement, targets typically comprise:

- 25 samples
- 8 primary standards (oxalic acid (OxI))
- 4 control materials
- 1 background material (^{14}C-free ('blank'), e.g., swamp kauri)
- 2 tuning targets (ANU sucrose and kapuni)

The range of standards and other materials are used for preparing the AMS system for measurement and for subsequent data analysis, including standardisation using NBS oxalic acid (OxI; Olsson, 1970) (Sections 2.2 & 4.1.5). The tuning targets, namely ANU sucrose

(modern ^{14}C content) and kapuni ^{14}C-free CO_2 from the Kapuni natural gas field), are used to tune the system for ^{14}C measurement. AMS calibration is important to prepare the system for measurement, such that parameters are optimised for efficient and accurate ^{14}C detection. ANU sucrose (IAEA-C6; Polach, 1979; Rozanski et al., 1992) is combusted alongside OxI and other samples (Section 4.1.3), whilst aliquots from a kapuni tank are directly transferred to graphitisation reactors (Section 4.1.4).

Control material samples are treated as 'unknown' samples; subject to the same pretreatment as corresponding samples, thus providing a check on result quality within each AMS wheel. A control material must have sufficient material for replicate measurements and be of the same type and similar ^{14}C content to samples. For this project a single annual growth tree ring (1981) from a kauri cross-section at RRL is used (Section 5.4.2). Blank material, i.e., ^{14}C-free, corresponding to the sample type is also subject to the same pretreatment as samples, so to assess contamination and use for blank correction after measurement (Section 4.1.5). Here swamp kauri wood greater than 140 000 years old is used (Hogg et al., 2006; Marra et al., 2006).

4.1.1 Physical Preparation

Although a summary of physical preparation is included in the draft publication (Section 4.2.5), I expand on the details here.

Before tree ring samples undergo chemical pretreatment they are examined under microscope to check for any visible contaminants. Foreign material or borer residue present is removed from the surface with a scalpel and the sample mass is recorded. The minimum wood mass required to provide sufficient material for analysis is ~6 mg, whilst an ideal mass is ~10 – 15 mg, allowing for additional material loss or multiple analyses. A sample above ~30 mg is thus subsampled along the direction of growth, such that a subsample incorporates material from the whole annual growth tree ring. The tree ring sample (or subsample) is subsequently finely sliced into small sticks with a scalpel to increase the surface area, thereby improving chemical processing efficiency. Tree ring samples are not shaved into a finer wood dust as this would increase contamination potential and make it

harder to visibly identify any foreign material present. The sliced sample is finally wrapped in glass-fibre filter paper (Whatman Glass Microfiber Filters (GF/C, 47 mm diameter), before placing in a labelled glass vial for storage until further preparation.

4.1.2 Chemical Preparation

All background and methodology of organic solvent washes and cellulose extraction is presented in the complementary draft publication (Section 4.2). Following findings detailed in the publication, RRL ASE solvent wash method and subsequent ANSTO cellulose extraction is employed for all other tree ring samples within this PhD project.

4.1.3 Elemental Analyser Combustion

Following cellulose extraction, 1.9 – 2.1 mg of extracted cellulose undergoes elemental analyser (EA) combustion to CO_2. Prior to combustion, each sample cellulose is cut into small pieces to increase uniformity within the cellulose sample, such that the subsample combusted, and subsequently analysed, is representative of the whole annual growth tree ring.

Each EA combustion run consists of 12 samples, including a minimum of two standards (OxI, ANU sucrose or control material), which provides a basis for data quality analysis of a particular EA combustion run if required.

Samples are weighed into tin boats and combusted with a Europa ANCA EA connected to a Europa 20-20 isotope ratio mass spectrometer (IRMS; Sercon Ltd., Cheshire, UK) (Basiden et al 2013). 1 % of the CO_2 produced flows onto the IRMS, allowing for determination of a $\delta^{13}C$ value.

EA combustion is the main part of sample preparation and analysis that I have not been trained to conduct. The EA and CO_2-collection system are a collaboration between co-located RRL and GNS Science's Stable Isotope Laboratory. During this PhD project, the EA

has typically been operated by two of our senior technicians (Cathy Ginnane and Helen Zhang), alongside the Stable Isotope Laboratory Team.

4.1.4 Graphitisation

CO_2 produced through EA combustion is graphitised using hydrogen and an iron catalyst (Fe_2O_3). The current Rafter Graphitisation 20 reactor system (RG20) at RRL was installed in 2012 to update the previous system in place since the 1980s (Turnbull et al., 2015).

In preparation for the graphitisation reaction, 1.6 – 2.0 mg of Fe_2O_3 (Sigma Aldrich, 99.999 % purity) is reduced to form the iron catalyst. The reaction takes approximately an hour with ~1300 mbar of hydrogen at 400 °C with a thermoelectric cooler freezing out water produced at -18 °C.

The CO_2 sample is manually transferred to the reactor along with sufficient hydrogen gas for the graphitisation reaction to proceed to completion. (At this point in processing, the kapuni gas standard (CO_2) can be introduced to a reactor to produce the kapuni AMS tuning target.) The graphitisation reaction takes approximately two hours at 550 °C again with a thermoelectric cooler freezing out any water produced at -18 °C. Both reactions are monitored through a pressure transducer in the reactor vessel, which automatically turns off the furnace upon completion. Completion requires passing a minimum threshold pressure, which is calculated from different parameters.

Graphite is stored in the reactor vials to reduce loss of product. The vials are covered with aluminium foil and a label identifier. Graphite can be stored in this way for a month, beyond which samples begin to absorb sufficient carbon from the atmosphere to affect results.

I have been trained to use vacuum lines, specifically RG20, and due to the nature of sample scheduling and measurement I have graphitised a mixture of samples for this PhD project and other samples, following established protocols.

4.1.5 Accelerator Mass Spectrometry

The graphite samples are pressed into aluminium targets (cathode holders) in aluminium wheels, in preparation for ^{14}C measurement through AMS.

The AMS system at RRL is a Compact ^{14}C AMS (CAMS) eXtended for ^{10}Be and ^{26}Al (XCAMS), designed by National Electrostatic Corporation (NEC, US) in 2010 (Zondervan et al., 2015). XCAMS consists of a range of components, including an ion source for caesium sputtering, electrostatic and magnetic steerers, bending magnets, a Pelletron 0.5 MV tandem accelerator and a particle detector.

A wheel, consisting of 40 targets including standards (Section 4.1), is mounted in the source before the system is pumped down to a sufficient vacuum. If the accelerator and magnets have been turned off since a previous measurement, these are started up and stabilised, otherwise they remain at previous settings. On reaching a sufficient vacuum, the ion source is turned on. The oven is subsequently turned on to release caesium to sputter the targets, and once a stable beam is established, XCAMS is tuned for ^{14}C, such that the system is optimised for the particle detector to count ^{14}C.

The measurement is then started and rotates through targets for 1200 cycles on each target within a rotation of the sample wheel. Measurement continues for the set number of rotations, or until stopped in the control room or remotely. Complete measurement is stopped after approximately two days, when sufficient ^{14}C counts have been recorded, which is ~650 000 ^{14}C counts on modern ^{14}C targets (i.e., not for ^{14}C-depleted targets) (Turnbull et al., 2015). The measured wheel is then removed from the source and the next wheel is mounted.

Following AMS measurement, the data is ready for export and subsequent analysis using CalAMS (in-house regression program; Zondervan et al., 2015). Blank corrections are then conducted within the laboratory sample processing database, considering results in context of processing blanks and applying suitable correction factors, following Donahue et al., (1990) (Turnbull et al., 2015).

I have been trained to operate XCAMS, including to assist with measurements and run/maintain the system whilst Albert Zondervan is on leave (with technical assistance from Chris Purcell, a co-located senior accelerator engineer who operates other accelerators). Whilst learning to operate XCAMS I found that the initial manual could be challenging to understand from a basic level. Therefore I produced my own manual to include more detail to form a comprehensive document that in part aided my learning of the operating procedures (Appendix B).

4.2 Organic Sample Pretreatment for ^{14}C Measurement at the Rafter Radiocarbon Laboratory

(Rachel Corran, Margaret Norris, Jocelyn Turnbull, Albert Zondervan and Andy Phillips)

4.2.1 Abstract

This publication details methodology for the pretreatment of modern wood samples for radiocarbon measurement at the Rafter Radiocarbon Laboratory (RRL). With the large variation in atmospheric radiocarbon throughout the past century, effective removal of organic material that is mobile within the tree system, and isolation of the cellulose fraction is paramount in determining the atmospheric radiocarbon content at the time an annual growth ring of a tree was laid down. Commonly, solvent extraction to remove lipids, waxes and resins followed by cellulose extraction is used. Yet most laboratories use their own variation on this general method, varying the solvents used and the details of the cellulose extraction method. Here we compare the method demonstrated by the Australian Nuclear Science and Technology Organisation (ANSTO) Laboratory to be effective for modern tree rings, and the methods long used at RRL for prehistoric wood materials. We show that the RRL solvent wash sequence is equally effective as the ANSTO solvent sequence, and also uses less toxic solvents and faster processing time. For prehistoric woods and post-bomb tree rings, there is no significant difference between the ANSTO and RRL cellulose extraction methods, but for tree rings grown during the bomb period (1950s – 1960s) when atmospheric radiocarbon content changed very rapidly, the ANSTO method appears to give radiocarbon content more consistent with atmospheric observations at the same time. We

also demonstrate that using an accelerated solvent extraction (ASE) system for the RRL solvent wash procedure delivers comparable result accuracy to the commonly employed Soxhlet extraction technique for modern woods, as well as a range of organic samples commonly pretreated for radiocarbon measurement, with substantially reduced processing time and operating costs.

4.2.2 Introduction

Tree ring radiocarbon (^{14}C) analyses are being increasingly used for a wide range of applications. Traditionally tree ring ^{14}C chronologies have been used to form the basis of atmospheric radiocarbon in carbon dioxide ($^{14}CO_2$) reconstructions used to calibrate ^{14}C measurements to calendar ages (e.g. Stuiver and Reimer, 1993; Ramsey, 1995; Hogg et al., 2013; Reimer et al., 2013). 'Modern' tree rings corresponding to years leading up to (1950s), during (1960s), and following the 'bomb period' (1970s – present) can be a useful tool to reconstruct atmospheric $^{14}CO_2$ (as $\Delta^{14}CO_2$) throughout this period and thus investigate exchange of ^{14}C within the carbon cycle (Suess, 1955; Tans 1981; Hua and Barbetti, 2004).

The atmospheric $\Delta^{14}CO_2$ bomb perturbation and subsequent exchange with the ocean and terrestrial biosphere provided an excellent opportunity to use ^{14}C as a tracer to investigate the carbon cycle, owing to its distinct signatures of sources and sinks (Nydal and Lovseth, 1970; Guilderson et al., 2000; Levin and Hesshaimer, 2000; Randerson et al., 2002; Naegler et al., 2006). Yet only a small number of sites with long-term atmospheric $\Delta^{14}CO_2$ measurements exist (Graven et al., 2012; Levin et al., 2010; Nydal and Lovseth, 1983; Turnbull et al., 2017; Meijer et al, 2006). Thus ^{14}C analyses of modern tree rings provide a mechanism through which additional spatial and temporal $\Delta^{14}CO_2$ data can be determined, allowing expansion of ^{14}C-based carbon cycle and climate model studies.

Further tree ring ^{14}C applications include ^{14}C bomb-pulse dating of tree rings, which provides independent validation of chronologies to compliment traditional dendrochronology (e.g., Andreu-Hayles et al., 2015; Pearson et al., 2011). Also, where traditional dendrochronology is unsuitable, including tropical tree species, ^{14}C analysis of tree rings is applied to confirm

the annual nature of growth rings (Biondi et al., 2007; Fichtler et al., 2003) and estimate the growth rate of non-annular trees (Bowman et al., 2011; Kurokawa et al., 2003).

Trees sequester atmospheric carbon through photosynthetic uptake of carbon dioxide (CO_2). Atmospheric carbon taken up during a growing season is deposited in annular growth rings, comprising of a cellulosic cell structure, hemicellulose, lignin and mobile extractives (Fritts, 1976; Park and Epstein, 1961; Pettersen 1984). Cellulose is commonly used as the target material for ^{14}C analysis in wood samples, because after formation no translocation, environmental or atmospheric exchange occurs (Fritts, 1976; Gaudinski et al., 2005; McCarroll and Loader, 2004; Southon and Magana, 2010). Although cellulose formation largely uses photosynthetic CO_2 uptake, there can be a contribution from stored carbohydrate of the previous year. Grootes et al., (1989a and b) estimated that a maximum of 15 % of cellulose carbon could be derived from stored carbohydrate. More recent stable isotope studies have shown that this effect is more likely less than 5 % and most significant in deciduous species. Incorporation of stored carbohydrate in cellulose is not apparent in studies of stable isotopes in evergreen species (Gessler 2014; Gessler et al., 2009; Helle and Schlesser, 2004).

Both the subsequent formation of hemicellulose and lignin, and radial translocation of mobile extractives formed in adjacent years, contribute to potential contamination. Prior to the atmospheric $\Delta^{14}CO_2$ bomb perturbation, gradual variation in natural atmospheric $\Delta^{14}CO_2$ content meant that the cellulosic cell structure of annual tree rings had similar ^{14}C content to hemicellulose and lignin formed subsequently. For the same reasons, there were only small differences to the ^{14}C content of mobile extractives used for growth and energy, including starches and resins (Pettersen, 1984), and in ancient wood these will likely have leached out. Contrastingly, rapid, large changes in atmospheric $\Delta^{14}CO_2$ content during the bomb period can lead to significant differences between the ^{14}C content of the cellulosic cell structure and hemicellulose, lignin and mobile extractives even if those mobile materials are only a year or two different in age. The removal of non-cellulosic material through effective pretreatment is thus paramount in determining an accurate ^{14}C analysis for wood samples.

For this reason modern wood sample pretreatment may need to be more rigourous than conventional wood sample pretreatment, i.e., incomplete removal of non-cellulosic material through conventional methods (Tans et al., 1978). In addition, sample processing needs to improve in line with increasing measurement precision (Baisden et al., 2013). Although the pretreatment of organic samples, including modern wood samples, is not standardised across ^{14}C laboratories, it is common that where preservatives or similar are present, organic samples are subject to organic solvent washes and acid-base-acid (ABA) treatment (e.g. Bruhn et al., 2001, Dee et al., 2011, Brock et al., 2018), whilst modern woods are subject to organic solvent washes and cellulose extraction (e.g., Hua et al., 2000; Staff et al., 2014). In this study we review the general principles and details of existing pretreatment methods for modern woods as well as considering the more general case of organic materials.

4.2.3 Review of Wood Sample Pretreatment Techniques

SOLVENT WASHES

In wood samples, particularly softwoods, organic solvent washes seek to remove mobile extractives such as starches and resins that are often genus or species specific. In early modern ^{14}C tree ring studies, the removal of resin extractives was found imperative to determining an accurate atmospheric $\Delta^{14}CO_2$ value (Baxter and Farmer, 1973; Jansen, 1970; Olsson, 1972). This was apparently due to the large difference in ^{14}C content of such mobile extractives subject to radial translocation across the annual growth rings. Solvent washes are thus less essential for older wood samples, where mobile extractives have similar ^{14}C content to the cellulosic cell structure due to only gradually varying atmospheric $\Delta^{14}CO_2$. Many other types of organic samples for ^{14}C analysis also undergo solvent washes prior to standard chemical pretreatment. This includes textiles, bone, and antiquities, for example where dye or preservatives may have been applied (e.g., Hajdas et al., 2004; Brock et al., 2010).

Solvent washes involve applying a sequence of solvents to a sample in order of increasing polarity, such that each removes remnants of the previous solvent in addition to solvent-

soluble material (Head, 1979). Having identified the necessity of solvent washes for modern wood samples, early researchers' extraction choices were acetone (Baxter and Farmer, 1973; Cain and Suess, 1976) or 2:1 benzene-ethanol extractions (Head, 1979; Olsson, 1980; Tans et al., 1978). Benzene has since been superseded by toluene or 2:1 toluene-ethanol mixtures (McCarroll and Loader, 2004; Rinne et al., 2005), owing to benzene's carcinogenic properties, although toluene also poses hazards. Alternative solvent sequences used include: acetone, methanol and chloroform (Staff et al., 2014), 2:1 chloroform-ethanol mixture (Hoper et al., 1998), 2:1 cyclohexane-ethanol, ethanol and deionised water (Hua et al., 2000), and n-hexane, 2-propanol and acetone (Rafter Radiocarbon Laboratory, RRL). Although such a range of solvent sequences are applied to samples for ^{14}C analysis, there is little published on the efficacy of the different choices.

SOLVENT WASH TECHNIQUES

Organic solvent washes are conventionally employed through Soxhlet extraction: applying the principal of bringing solvents to their corresponding boiling points and siphoning with the sample. Mobile extractives dissolve if they are soluble in the particular solvent. Soxhlet apparatus consists of an extraction chamber, which sits below a water condenser and above a round-bottom flask of boiling solvent on a hotplate. The sample is suspended in the extraction chamber in a glass thimble with porous filter. Typically multiple apparatus are used to process several samples simultaneously. Siphoning times for different solvents and methods vary (as detailed below). Soxhlet extractions are commonly conducted for a minimum of 6 hours per extraction (e.g., Head, 1979; Hoper et al., 1998; Olsson, 1980).

An alternative to Soxhlet is to use accelerated solvent extraction (ASE, Richter et al., 1996). ASE can potentially improve sample processing efficiency and consistency through automation of the conventional Soxhlet extraction solvent wash process. ASE systems use elevated temperature and pressure to achieve increased sample processing efficiency. The intended application of ASE is for collection of desired eluents produced from the organic solvent washes, e.g., the determination of different solvent-soluble materials. In contrast to this, we seek to remove organic extractives and retain the solid sample residue; thus eluent collection is unimportant for this application.

ASE has proven to be more favourable than Soxhlet for a range of applications. Such applications include isolation of micro-pollutants (Heemken et al., 1997), aromatic hydrocarbons to investigate diesel engine particulates (Oukebdane et al., 2010) and determination of polychlorinated biphenyls (PCBs) in environmental samples, which pose a health threat (e.g., Abrha and Raghavan, 2000; Wang et al., 2010). Previous comparisons have found that ASE provides effective extraction of organic soluble material and thus produces indistinguishable results from conventional Soxhlet extractions, in context of many other benefits. These benefits include: reduced processing time, reduced solvent consumption, greater batch processing and automation, in contrast to the large solvent volume and labour required for Soxhlet (Rajput et al., 2011). The main drawback of ASE concerns the significantly higher capital investment required (Abrha and Raghavan, 2000).

A previous ^{14}C focused study demonstrated that ASE is a suitable organic contaminant extraction technique for the pretreatment of foraminifera (Ohkouchi et al., 2005), with another reporting the use of ASE for small bone samples (Retheymer et al., 2013). To extract lipids from a range of sediment samples for ^{14}C analysis, ASE has also been employed for its intended purpose of solvent-soluble material collection (e.g., Bray et al., 2012; Rethemeyer et al., 2004; Uchida et al., 2000).

Hogg et al., (2013) conducted an inter-laboratory comparison of ^{14}C dating of New Zealand pre-Holocene Kauri samples, in which Oxford Radiocarbon Accelerator Unit (ORAU) used a specifically developed ASE solvent wash method. Inconsistent ORAU ^{14}C results compared to other laboratories were attributed to their ASE solvent wash method and 'old' (^{14}C-free) contamination from the solvents resulting in reduced ^{14}C, further confirmed by tests on modern kauri, although there was no systematic problem identified. Following this, they not only abandoned their ASE solvent wash method, but also deemed their Soxhlet solvent wash unnecessary, thus removing the solvent wash from standard procedures (Staff et al., 2014). This followed from consistent results between subsamples subject to Soxhlet solvent washes and those not subject to any solvent wash.

Contrasting this, Fines-Neuschild et al., (2015) demonstrated the use of ASE as an equivalent to Soxhlet for effective resin extraction from tree rings for dendrochronological applications,

with no damage to samples caused by the increased temperature and pressure conditions of ASE. Stable isotope ($\delta^{13}C$) results were comparable with no systematic bias observed, however ^{14}C analysis was not conducted.

CELLULOSE EXTRACTION

Early ^{14}C tree ring pretreatment was based on acid-base-acid (ABA) pretreatment (e.g., De Vries and Barendsen, 1954). Subsequent investigation into the performance of such treatment found ABA insufficient in determining an accurate ^{14}C analysis for modern tree rings (Tans et al., 1978). In addition to mobile extractives, wood comprises of cellulose, hemicellulose and lignin, the latter of which are removed during cellulose extraction (Goldstein, 2004).

Thus following organic solvent washes, most ^{14}C laboratories that process wood samples conduct cellulose extraction to remove remaining non-cellulosic material. This seeks to isolate the 'pure' alpha(α) cellulose, commonly used to broadly define the cellulosic material remaining after bleaching and alkali treatments. The α-cellulose forms the cellular structure of the wood prior to hemicellulose and lignin formation, and is thus considered most representative of atmospheric $^{14}CO_2$ at the time of formation (Head, 1979).

The Jayme-Wise method (Green, 1963) is most commonly used for cellulose extraction for ^{14}C analysis (e.g., Loader et al., 1997; Gaudinski et al., 2005). The method consists of acidified sodium chlorite ($NaClO_2$) oxidation, which breaks down the lignin to produce holocellulose. The hollocellulose is subsequently treated with sodium hydroxide (NaOH) under a nitrogen (N_2) atmosphere to remove the polysaccharide (starch and pectin) and hemicellulose components of the holocellulose, with the insoluble α-cellulose predominantly remaining. A final hydrochloric acid (HCl) treatment is applied to remove any CO_2 absorbed during the NaOH treatment, which conducting the NaOH treatment under a N_2 environment aims to reduce, but may not completely eliminate.

Although the Jayme-Wise method is commonly employed for the production of α-cellulose, it is recognised that the resultant cellulose has some non-cellulosic material present

including hemicellulose and lignin (Li and Liu, 2013). It is also a particularly destructive method, with significant loss of sample mass, and in our laboratory takes up to three working days to complete a batch of 14 samples.

The cellulose extraction method employed at RRL was developed in-house, based on pulp and paper treatment methods, and we are not aware of any other ^{14}C laboratories employing this method for cellulose extraction. The RRL method was developed with a view to using less toxic chemicals and shorter pretreatment time than the Jayme-Wise method. The RRL cellulose extraction method applies a sequence of treatments: acid, base and oxidation (ABOx). This method is similar to background ^{14}C-free ('blank') material pretreatment conducted in some other ^{14}C laboratories (e.g., Bird et al., 1999, Santos et al., 2001, Southon et al., 2010). Hot treatments of HCl and NaOH remove humic acids absorbed and some lignin, resulting in a pulp suitable for bleaching. Oxidation by hydrogen peroxide (H_2O_2) under alkaline conditions then seeks to remove lignin. Similar to the Jayme-Wise method, a final acid treatment (HCl) is conducted to remove any CO_2 absorbed during processing. The RRL cellulose extraction method uses less toxic chemicals, and takes up to two laboratory days, shorter than the Jayme-Wise method, but observing similar mass loss. This method has been used at RRL since the 1990s, but has not previously been directly evaluated against other methods, although it has been compared with other methods tangentially through RRL participation in inter-laboratory intercomparison activities (e.g., Scott, 2003; Scott et al., 2017).

4.2.4 Goals of this Study

First, we select two solvent sequences to compare: the existing solvents used at RRL (n-hexane, 2-propanol and acetone), and the solvents used at the Australian Nuclear Science and Technology Organisation (ANSTO) Laboratory (2:1 cyclohexane-ethanol, ethanol and deionised water), where a large number of modern wood samples have been processed (e.g., Hua et al., 2003; Hua et al., 2004). Second, we evaluate the performance of two different solvent wash techniques: conventional Soxhlet and ASE. Finally, we compare a variation of the widely-used Jayme-Wise cellulose extraction employed at the ANSTO

Laboratory (Hua et al., 2000), with the less-hazardous cellulose extraction method that has long been used at RRL, but has not previously been evaluated for its efficacy.

4.2.5 Methods

Table 4.1: Pretreatment of subsamples for the different method comparisons and corresponding codes.

Pretreatment applied to subsamples	Subsample code
Solvent sequence and cellulose extraction method variations	
Untreated whole wood (no pretreatment)	ww
ANSTO Soxhlet solvent wash only (no cellulose extraction)	A_s
RRL Soxhlet solvent wash only (no cellulose extraction)	R_s
ANSTO Soxhlet solvent wash – ANSTO cellulose extraction	A_s-A
ANSTO Soxhlet solvent wash – RRL cellulose extraction	A_s-R
RRL Soxhlet solvent wash – RRL cellulose extraction	R_s-R
RRL Soxhlet solvent wash – ANSTO cellulose extraction	R_s-A
Soxhlet and ASE solvent wash method variations	
RRL Soxhlet solvent wash – ANSTO cellulose extraction	R_s-A
RRL ASE solvent wash – ANSTO cellulose extraction	R_a-A

Table 4.2: Sample details and results, ($\delta^{13}C$ and $F^{14}C$), for different method comparisons. [1]Year of tree ring growth, [2]NZA is the RRL measurement identifying number, [3]NZA numbers removed for client confidentiality (All three measurements are from the same piece of material).

Sample Type	Year[1]	NZA[2]	Method	$\delta^{13}C$	$F^{14}C$	$F^{14}C$ error
Bomb period tree ring samples						
Bomb period oak tree ring	1950	56840	ww	-25.7	0.9905	0.0022
		56843	R_s	-25.8	0.9820	0.0021
		56179	A_s-A	-24.5	0.9704	0.0020
		56842		-24.7	0.9717	0.0023
		56181	A_s-R	-25.1	0.9815	0.0020
		56178	R_s-A	-24.9	0.9855	0.0021
		56841		-25.5	0.9796	0.0021
		56180	R_s-A	-25.0	0.9698	0.0020
Bomb period oak tree ring	1956	57793	ww	-25.0	1.0006	0.0022
		57795	A_s	-24.8	0.9976	0.0022
		57794	R_s	-24.9	0.9815	0.0022
		57792	A_s-A	-24.1	0.9879	0.0022
		57791	R_s-A	-24.3	0.9919	0.0022
Bomb period kauri tree ring	1957	62645	R_s-A	-18.6	1.0148	0.0025
		62647		-18.6	1.0165	0.0025
		62646	R_a-A	-18.7	1.0111	0.0025
		62648		-18.7	1.0174	0.0025
Bomb period oak tree ring	1958	57788	ww	-24.6	1.0597	0.0023
		57790	A_s	-24.3	1.0591	0.0023
		57789	R_s	-25.3	1.0500	0.0023

Continued...

Sample Type	Year[1]	NZA[2]	Method	$\delta^{13}C$	$F^{14}C$	$F^{14}C$ error
		57787	A_s-A	-24.3	1.0566	0.0023
		57786	R_s-A	-24.6	1.0663	0.0023
Bomb period kauri tree ring	1961	62643	R_s-A	-19.1	1.1832	0.0028
		62644	R_a-A	-18.8	1.1863	0.0028
Bomb period kauri tree ring	1966	62329	R_s-A	-19.0	1.5996	0.0037
		62330	R_a-A	-19.2	1.6012	0.0037
Bomb period kauri tree ring	1968	62327	R_s-A	-19.1	1.5582	0.0036
		62328	R_a-A	-19.3	1.5637	0.0037
Post-bomb period tree ring samples						
Post-bomb pine tree ring	1986	56187	A_s-A	-24.0	1.2002	0.0024
		56189	A_s-R	-25.6	1.1982	0.0024
		56186	R_s-R	-25.2	1.1957	0.0024
		56188	R_s-A	-24.5	1.2023	0.0024
Post-bomb pine tree ring	1988	62641	R_s-A	-24.5	1.1833	0.0028
		62642	R_a-A	-23.6	1.1769	0.0028
Post-bomb chestnut tree ring	1990	56191	A_s-A	-25.2	1.1597	0.0023
		56193	A_s-R	-25.5	1.1630	0.0024
		56190	R_s-R	-25.8	1.1623	0.0023
		56192	R_s-A	-25.1	1.1608	0.0024
Post-bomb chestnut tree ring	1991	62325	R_s-A	-23.8	1.1512	0.0029
		62326	R_a-A	-24.1	1.1515	0.0028

Continued...

Sample Type	Year[1]	NZA[2]	Method	$\delta^{13}C$	$F^{14}C$	$F^{14}C$ error
Post-bomb chestnut tree ring	1994	62323	R_s-A	-23.2	1.1296	0.0028
		62324	R_a-A	-24.1	1.1304	0.0028
Post-bomb chestnut tree ring	1995	62639	R_s-A	-23.9	1.1241	0.0027
		62640	R_a-A	-23.9	1.1235	0.0027
Post-bomb pine tree ring	1999	56183	A_s-A	-25.6	1.0929	0.0024
		56185	A_s-R	-26.1	1.0897	0.0022
		56182	R_s-R	-25.6	1.0932	0.0022
		56184	R_s-A	-24.8	1.0882	0.0022
Post-bomb pine tree ring	2000	62638	R_s-A	-23.8	1.0969	0.0026
		62637	R_a-A	-23.1	1.0975	0.0027
Ancient/blank wood samples						
Known-age wood (FIRI-D)		62313	R_s-A	-22.9	0.5656	0.0017
		62625		-23.2	0.5672	0.0017
		62311	R_a-A	-23.1	0.5670	0.0017
		62626		-23.3	0.5668	0.0017
Known-age wood (SIRI-F)		56174	A_s-A	-24.3	0.9548	0.0024
		56176	A_s-R	-24.3	0.9579	0.0024
		56173	R_s-R	-24.6	0.9529	0.0024
		56175	R_s-A	-24.2	0.9517	0.0024
'Blank' wood (Kauri)		56167	A_s-A	-21.7	0.0027	0.0001
		56169	A_s-R	-23.3	0.0017	0.0001
		56166	R_s-R	-23.4	0.0032	0.0001
		56168	R_s-A	-22.0	0.0028	0.0001

Continued...

Sample Type	Year[1]	NZA[2]	Method	$\delta^{13}C$	$F^{14}C$	$F^{14}C$ error
		62322	R_s-A	-22.3	0.0021	0.0001
		62635		-22.0	0.0036	0.0001
		62321	R_a-A	-22.3	0.0024	0.0001
		62636		-22.1	0.0026	0.0001
Other organic materials						
Modern bone		n/a[3]	R_s-A	-21.2	1.0832	0.0025
		n/a[3]	R_a-A	-21.2	1.0830	0.0026
		n/a[3]		-20.9	1.0851	0.0026
Known-age leather (FIRI-Q)		12357	R_s-A	-18.3	0.7372	0.0054
		12358		-18.5	0.7381	0.0053
		64289	R_a-A	-15.8	0.7368	0.0020
		64290		-15.7	0.7315	0.0020
Parchment (FIRI optional)		12340	R_s-A	-22.1	1.1183	0.0085
		12341		-22.2	1.1039	0.0082
		64291	R_a-A	-22.8	1.1161	0.0027
		64292		-22.9	1.1135	0.0027
Textile (FIRI optional)		12954	R_s-A	-19.3	0.7414	0.0043
		12955		-19.2	0.7539	0.0044
		12956		-20.9	0.7452	0.0043
		12957		-20.9	0.7383	0.0058
		64293	R_a-A	-21.1	0.7480	0.0020
		64294		-21.5	0.7456	0.0020

SAMPLE SELECTION AND PREPARATION

Samples for the comparison of different methods (Table 4.1) included a range of modern tree rings (Table 4.2). These were selected to cover the rapid atmospheric $\Delta^{14}CO_2$ increase observed in the 1950s – 1960s bomb period, in addition to steadily declining atmospheric $\Delta^{14}CO_2$ following the 1970s (post-bomb period). During the rapid atmospheric $\Delta^{14}CO_2$ increase of the bomb period we expect organic material formed after cellulose to be of higher ^{14}C content, hence these samples were chosen to highlight incomplete removal of non-cellulosic material. With steady decline of atmospheric $\Delta^{14}CO_2$ during the post-bomb period, non-cellulosic material is of more similar ^{14}C content to cellulose, making it harder to detect remaining contaminants.

All of the tree rings came from New Zealand tree cores that had previously been divided into annual rings, undergoing ring counting and slicing, ready for ^{14}C analysis (Norris, 2015; Ansell, 2016). Known-age wood samples and other materials already used in radiocarbon intercomparisons (FIRI: Boaretto et al., 2002; Scott, 2003; and SIRI: Scott et al., 2017) were analysed to demonstrate that the methods we compare are also suitable for a broader range of samples for ^{14}C analysis. The ^{14}C-free blank is sub-fossil New Zealand kauri wood (Hogg et al., 2006; Marra et al., 2006). The modern bone sample was submitted to RRL by a commercial client.

Samples were each divided into the appropriate number of equal aliquots, such that each subsample followed a pretreatment pathway that was a variation of ANSTO (A) Soxhlet solvent wash (A_s-) and ANSTO cellulose extraction (-A), and RRL (R) (Soxhlet (R_s-) or ASE (R_a-)) solvent wash and RRL cellulose extraction (-R) methods (Table 4.3.1). Untreated whole wood (ww) subsamples undergoing no pretreatment, were also tested as a control.

In the results section we justify using the RRL solvent sequence in preference to the ANSTO solvent sequence, so conduct the comparison of Soxhlet and ASE solvent wash methods with the RRL solvent sequence only (R_s- and R_a-). We also demonstrate in the results that the ANSTO cellulose extraction method (-A) is more effective than the RRL cellulose

extraction method (-R) so proceed the different solvent wash methods (R_s- and R_a-) with the ANSTO cellulose extraction method only.

Physical preparation for all the solvent wash methods followed the same procedure. We examined the selected samples under microscope and removed any visible contaminants with a scalpel. We took subsamples of a tree ring parallel to the direction of growth, such that each subsample contained an equivalent cross-section of the total year growth. Each subsample was then finely sliced into sticks, before enclosing in glass-fibre filter paper (Whatman Glass Microfiber Filters (GF/C), 47 mm diameter). The known-age wood and other materials were treated similarly, without the need to subsample across the year of growth.

ANSTO AND RRL SOXHLET SOLVENT WASH METHODS

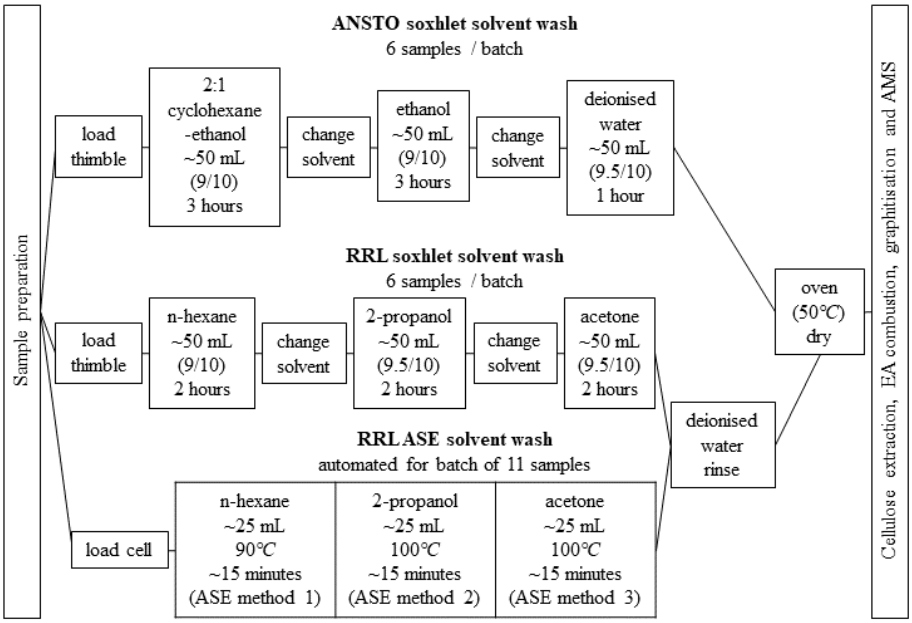

Figure 4.1: Schematic of the three solvent wash methods, ANSTO and RRL Soxhlet solvent washes and RRL ASE solvent wash, detailing the different solvents, timings and conditions.

The ANSTO Soxhlet solvent wash method applies 2:1 cyclohexane-ethanol, ethanol and deionised water, each for six hours, to the sample in turn (Hua et al., 2000, modified from

Head, 1979). The RRL Soxhlet solvent wash method applies three solvents (n-hexane, 2-propanol and acetone), each for two hours, to the sample in turn.

In this investigation, to increase efficiency, the solvents in our amended ANSTO Soxhlet solvent wash method were applied for reduced times: three hours each for the first two solvents and one hour for deionised water. These reduced times allowed either the ANSTO or RRL Soxhlet solvent wash methods to be conducted within a single working day (Figure 4.1).

Each solvent wash was conducted through the standard Soxhlet technique. A small spatula of anti-bumping granules was placed in a round-bottom flask, which was then filled with ~50 mL of solvent. The prepared sample was placed in a Soxhlet thimble above the round-bottom flask in the hotplate, which was adjusted such that the solvent boiled. For example the RRL Soxhlet method utilised approximately the maximum setting for 2-propanol and acetone, whereas for n-hexane a slightly lower setting was used due to its lower boiling point. The solvent then siphoned with the sample for the specified time, after which the round-bottom flask was removed from the hotplate. The solvent was then replaced with the subsequent solvent, ensuring that the anti-bumping granules still remained. The hotplate setting was adjusted accordingly such that the solvent reached its boiling point and siphoned with the sample. Having applied the sequence of solvents for the RRL Soxhlet method, a thorough rinse of the sample with deionised water was essential to remove any remaining solvent. Following Soxhlet extraction, samples were then left to dry in an oven at 50 °C.

RRL ASE SOLVENT WASH METHOD

Following no significant difference between the RRL and ANSTO solvent sequence results (see results section), the ANSTO solvent sequence was not tested on ASE.

The RRL ASE solvent wash method utilised a Dionex ASE 350 (Thermo Fisher Scientific, US). An ASE system has a few key elements: high pressure nitrogen gas (N_2) and air, a compression oven, pressurised solvent bottles, a carousel for sample cells and a carousel for

collection vials. On reaching the desired temperature, a cell (containing a sample) is loaded into the oven and pumped with the specified solvent, whilst heating and pressurising to reach equilibrium ('heating', Table 4.3), before a static extraction phase ('static', Table 4.3), during which fresh solvent is injected to help maintain optimum extraction equilibrium. Several static extraction phases are useful where samples are large and thus minimal solvent is present for extraction. At the end of a static phase, the cell is rinsed with fresh solvent ('flush volume', Table 4.3), before N_2 is purged through the cell to remove any remaining solvent, finally depressurising and returning the cell to the carousel.

Samples were packed in 10 mL ASE cells (Thermo Fischer Scientific, catalogue no. 068087), as they provided sufficient space for the sample and packing material. Although multiple samples can be loaded into a single cell to speed up processing, we chose to load only a single sample into each cell to avoid mislabelling.

Table 4.3: Details of the three RRL ASE solvent wash 'method' programs, as input into the ASE system to run the solvent washes.

ASE Method	Solvent	Temperature /°C	Heating /minutes	Flush volume /%	Static /minutes	N_2 Purge /seconds
1	n-hexane	90	5	50	5	40
2	2-propanol	100	5	50	5	40
3	acetone	100	5	50	5	40

The cells were fitted with polytetrafluoroethylene (PTFE) O-rings as Viton O-rings cannot be used with acetone. The cell (body with two end-caps) was cleaned with a lint-free tissue and briefly blown with an air gun. One end-cap was screwed onto the body, which was then packed ~2/3 with glass beads (Borosilicate, 3 mm diameter, Sigma-Aldrich). The glass beads played an important role in dispersing the solvent and creating sufficient pressure within the cell, whilst minimising contamination risk to the sample. The prepared sample enclosed in filter paper (as detailed above in sample preparation), was placed into the cell, with remaining space filled with glass beads to reduce solvent consumption. An ASE 27 mm diameter glass-fibre filter (Thermo Fischer Scientific, catalogue no. 068092) was placed in

the remaining cell end-cap, ensuring no overlap with the seal. This filter was downstream of the sample to ensure no problems with the instrument were caused by leaks or residue carried downstream in the system. Even though the sample was upstream of the filter, we used a glass-fibre filter, as the standard cellulose filters would pose a small contamination risk to the target material (cellulose) that we seek to isolate. The cell was closed (hand-tightened) and placed (sample towards the bottom of the cell) on the carousel.

Each sample was subject to the three solvents of the RRL Soxhlet solvent wash method: n-hexane, 2-propanol and acetone (Figure 4.1). All variables, i.e., solvent, volume, temperature and time, were programmed as an ASE 'method' into the system before commencing (Table 4.3). Similarly to the RRL Soxhlet solvent wash method, we found that a lower temperature was suitable for n-hexane (Table 4.3, ASE method 1). All other parameters were optimised to ensure both effective processing and time efficiency. Each sample took ~45 minutes in total (~15 minutes per solvent), using ~20 mL of solvent (Figure 4.1). Solvent-soluble material was collected into separate collection vials for each solvent for each sample, to allow us to observe colour.

We used a programmed ASE operating 'sequence' whereby each sample (cell) underwent total processing before progressing onto the next sample (Table 4.3). Processing the cells in our programmed order allowed for cells to be loaded onto the carousel after the first cell had started processing. Subsequently, processed cells could also be removed, allowing for efficiency through to the next step, e.g., cellulose extraction, where time was a particular constraint.

Cells were extremely hot immediately after processing, so they were left to cool sufficiently before removing from the carousel and unloading at any time. To unload the cell, an end-cap was removed and glass beads poured out, before removing the sample and conducting a thorough deionised water rinse to remove any remaining solvent (see results section for introduction of deionised water rinse). The samples were left to dry in an oven at 50 °C and used glass beads and glass-fibre cell filters were collected.

To minimise operating costs and environmental impact, the glass beads and glass-fibre cell filters were cleaned and reused, as they don't come into direct contact with the sample so don't pose a contamination risk after treatment. For the glass beads we conducted a 15-minute sonication with acetone, followed by thorough rinsing with deionised water and baking at 500 °C. The glass-fibre cell filters were baked with the glass beads, thereby removing any organic contaminants.

ANSTO CELLULOSE EXTRACTION METHOD (BASED ON THE JAYME-WISE METHOD)

Once the sample had dried from the solvent washes, we removed it from the filter paper and transferred to a 15 mL centrifuge tube in preparation for ANSTO cellulose extraction (Figure 4.2). The first treatment was $NaClO_2$ (15 g/L) oxidation under acidified conditions (~3 mL of 0.5 M HCl). A Pasteur pipette was used to add acid to the sample, before filling the tube with $NaClO_2$ solution and inverting. This treatment was at 90 °C for 60 – 90 minutes, or until the sample was sufficiently bleached. The sample was then centrifuged and rinsed with deionised water to achieve a neutral pH.

Two consecutive NaOH treatments were then applied (12 % w/v and 7 % w/v) under an N_2 atmosphere, each for an hour at 60 °C. Between the two treatments the sample was centrifuged and decanted, but if left overnight after the first NaOH treatment, the sample had to also be rinsed with deionised water until a neutral pH was reached. After the two NaOH treatments, the sample was centrifuged and rinsed to a neutral pH with deionised water.

Finally, the sample was acidified with 2 M HCl at room temperature for two hours, again centrifuging and rinsing with deionised water to achieve a neutral pH before leaving to dry in an oven at 50 °C.

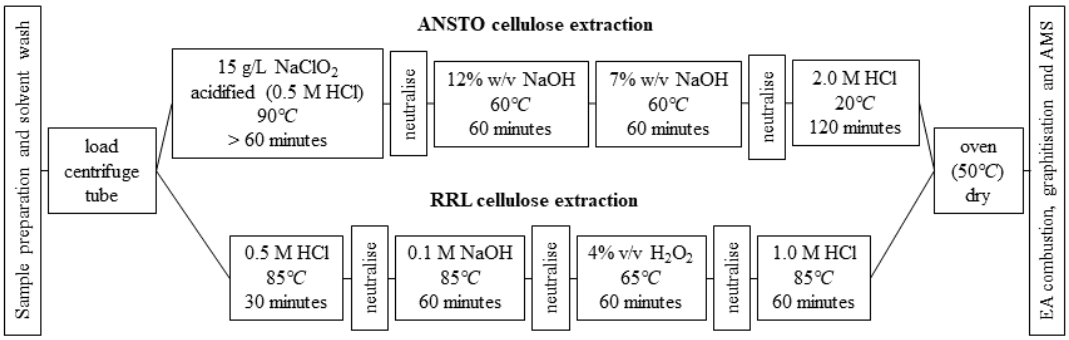

Figure 4.2: Summary diagram of the ANSTO and RRL cellulose extraction methods, detailing chemicals, timings and conditions.

RRL CELLULOSE EXTRACTION METHOD

Once the sample had dried from the solvent washes, we removed it from the filter paper and transferred to a 15 mL centrifuge tube in preparation for RRL cellulose extraction (Figure 4.2). The sample then underwent a sequence of treatments at 85 °C: an initial 30-minute acid treatment (0.5 M HCL) and subsequent 1-hour NaOH treatment. If the resulting NaOH solution was darker than amber then the NaOH treatment was repeated as required. Oxidation was then conducted (H_2O_2 4 % v/v) under alkaline conditions (1.5 g NaOH/ 100 mL H_2O_2 solution) at 60 °C. The oxidation treatment could also be repeated if required, although we found that one was largely sufficient. Between treatments the sample was centrifuged and rinsed with deionised water to achieve a neutral pH before proceeding to the next treatment. A final 30-minute acid treatment (1.0 M HCl) was conducted, before centrifuging and rinsing with deionised water to achieve a neutral pH and leaving to dry in an oven at 50 °C.

RRL BONE GELATINISATION

Having dried from solvent washes, bone samples at RRL undergo a sequence of treatments designed to isolate the gelatine of the bone. This involves: overnight demineralisation (0.5 M HCl), before rinsing to neutral and drying in the oven; gelatinisation at 100 °C in the oven

(0.01 M HCl, for ~8 hours); gross filtration at 0.45 micro/millimetres, before finally freezing/freeze drying for several days depending on the sample consistency.

RRL ACID-BASE-ACID (ABA) TREATMENT FOR OTHER ORGANIC SAMPLES

Having dried from solvent washes, a non-wood organic sample was removed from the filter paper and transferred to a 15 mL centrifuge tube in preparation for ABA treatment. The sample was then subject to a sequence of treatments, each carried out for 15 minutes, at temperatures dependent on the size and nature of the sample, as to ensure that the treatments are not too aggressive, and that sufficient sample remains after processing. The samples in this study were subject to: 0.1 M HCl at 55 °C, 0.1 M NaOH at 20 °C (textile) or 55 °C (leather and parchment) and 0.1 M HCl at 20 °C, between which the samples were centrifuged and rinsed with deionised water until a neutral pH was achieved. The samples were then left to dry in the oven at 50 °C.

COMBUSTION, GRAPHITISATION, AND AMS MEASUREMENT AND REPORTING OF RESULTS

Following cellulose extraction, samples subsequently underwent elemental analyser (EA) combustion, graphitisation and AMS analysis in the RRL (Baisden et al., 2013; Turnbull et al., 2015; Zondervan et al., 2015). All samples followed the same procedure, and roughly the same mass was combusted for each sample to minimise any possible bias due to sample size difference.

$\delta^{13}C$ MEASUREMENTS

$\delta^{13}C$ measurements were obtained during the EA combustion of all samples (Baisden et al., 2013). In this study we use $\delta^{13}C$ as a qualitative indicator of cellulose purity, and an additional measure of the success of different pretreatment methods of contaminant removal. Uncertainty in this $\delta^{13}C$ measurement is nominally 0.3 ‰.

Lignin and mobile organic material, e.g., resins, are depleted in $\delta^{13}C$ relative to cellulose, with lignin giving a $\delta^{13}C$ ~3 ‰ lower than cellulose (Tans et al., 1978; Wilson and Grinsted 1977). We therefore expect a less negative $\delta^{13}C$ value for cellulose of greater purity, associated with effective removal of contaminants of lower $\delta^{13}C$ content present in whole wood.

4.2.6 Results

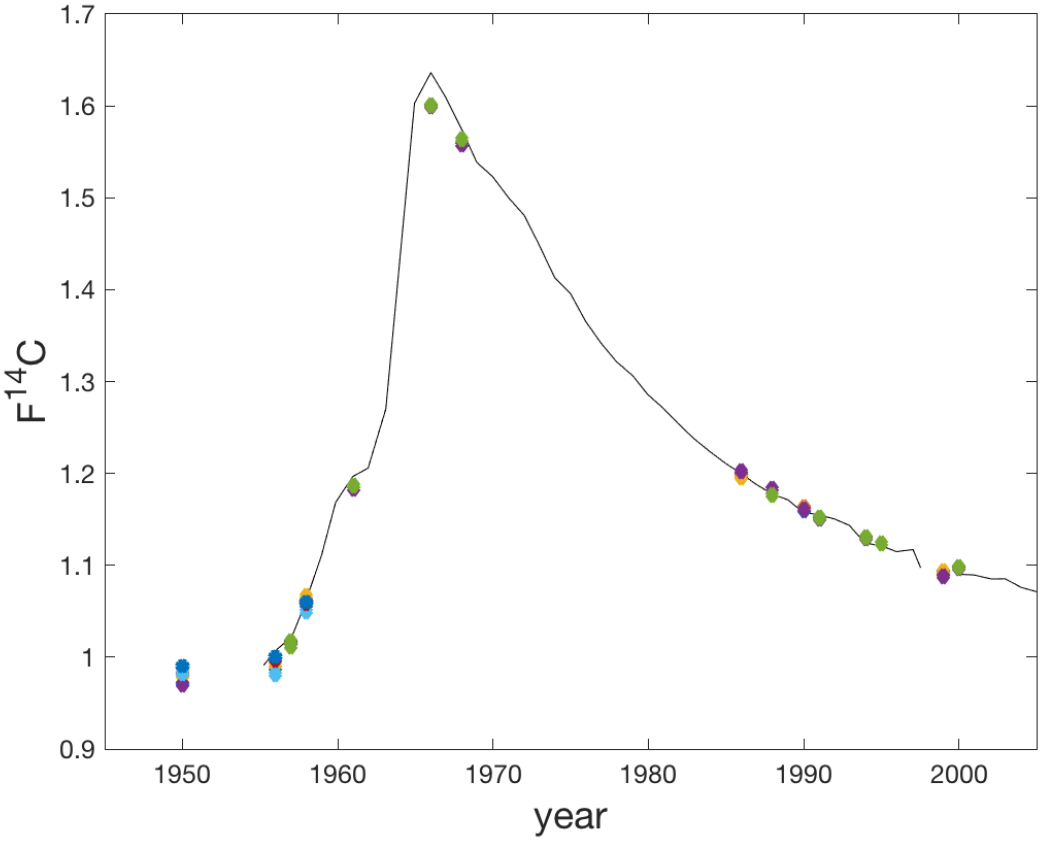

Figure 4.3: $F^{14}C$ of modern tree ring subsamples spanning 1950 – 2000 (Table 4.2) with annual mean $F^{14}C$ of the atmospheric record from Wellington, New Zealand for context (Turnbull et al., 2017), with different colours representing method variations. Note that error bars are too small to identify on this scale.

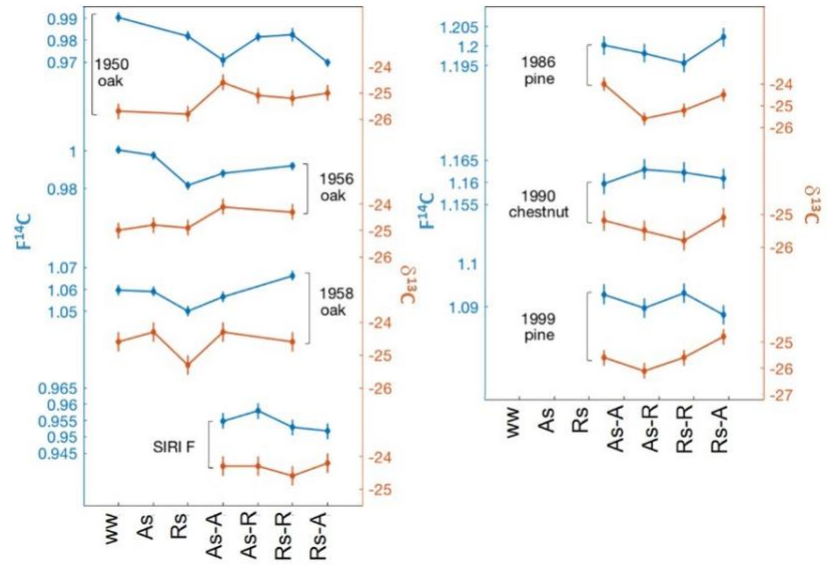

Figure 4.4: $F^{14}C$ and $\delta^{13}C$ of bomb period and post-bomb period tree ring subsamples (Tables 4.1 & 4.2) of the solvent wash and cellulose extraction method comparison, with lines to guide the eye. Note that where multiple measurements were made using the same sample and method, the mean and standard error is used.

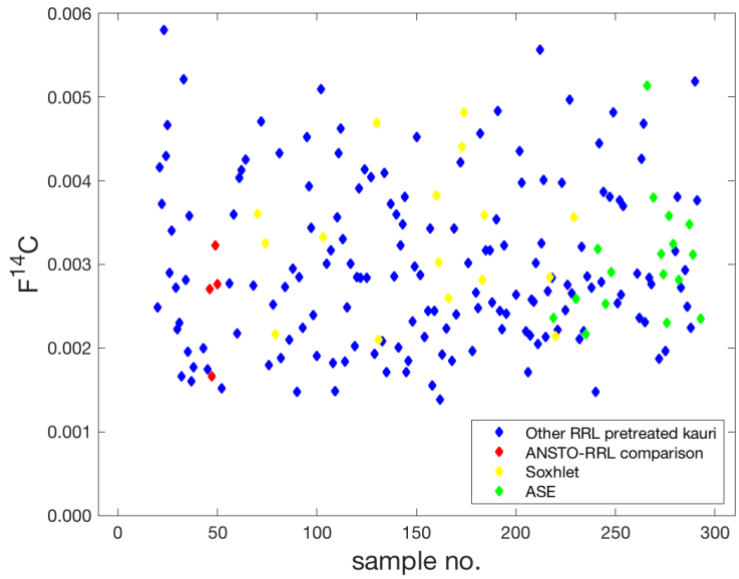

Figure 4.5: $F^{14}C$ of RRL cellulose-extracted sub-fossil kauri blank (blue), aligning with all solvent sequence and cellulose extraction method comparison results (red), and Soxhlet/ASE (yellow/green respectively) solvent wash method comparison results.

SOLVENT SEQUENCE

Comparing subsample pairs with the same subsequent cellulose extraction, i.e., A_s-A with R_s-A, and A_s-R with R_s-R, allowed us to directly compare the ANSTO and RRL solvent sequences, independent of the cellulose extraction applied.

With rapidly increasing atmospheric $\Delta^{14}CO_2$ in the early bomb period (Figure 4.3), organic material formed after cellulose and present in an annual growth ring, i.e., hemicellulose, lignin and some mobile extractives, will have a higher ^{14}C content relative to the cellulose. We would therefore expect the presence of non-cellulosic material with higher relative ^{14}C content to be most apparent in these samples. Our results of ANSTO and RRL solvent sequence pairs are in agreement within one standard deviation for the 1950 bomb period tree ring sample examined (Figure 4.4, Table 4.2), thus demonstrating that the different solvent sequences are comparable in their removal of mobile extractives (e.g., starches and resins). Samples from the post-bomb period further validate this, with all pairs agreeing within one standard deviation (Figure 4.4, Table 4.2). Although remaining non-cellulosic material, including mobile extractives, would be harder to detect during the slow steady decline of atmospheric $\Delta^{14}CO_2$ in this period. Similarly, the slightly pre-modern SIRI-F wood also shows no significant difference between the two solvent sequences, agreeing within 2 standard deviation, because it is from a time of gradual rate of change of atmospheric $\Delta^{14}CO_2$ (Figure 4.4, Table 4.2).

The sub-fossil kauri blank is used as a control for sample preparation within the RRL, because with no inherent ^{14}C due to old age and radioactive decay, any ^{14}C content is a result of incorporated modern carbon during processing. Although the scatter amongst measurements is much larger than the nominal AMS measurement uncertainty, we find no evidence of higher contamination resulting from the different methods, with results aligning with previous measurements in the RRL (Figure 4.5).

To further investigate the ANSTO and RRL solvent sequences, we subject subsamples to solvent washes without subsequent cellulose extraction (A_s- and R_s-). Seeking to greater understand the different solvent sequences and identify incomplete solvent removal, we

analysed bomb period samples to highlight greater differences in ^{14}C content. We find that the RRL solvent sequence (without cellulose extraction) commonly generates the lowest $F^{14}C$ of all subsamples including untreated whole wood (ww), by over 2 sigma in 2 out of 3 cases (Figure 4.4). We attribute these systematically low $F^{14}C$ values to ^{14}C-free solvent residue. This occurs because the RRL solvent sequence uses ^{14}C-free solvents, seeking to minimise modern contamination to older samples. The ANSTO solvent sequence avoids this effect through application of a final modern-^{14}C solvent (ethanol). This was specifically chosen, and validated through measurement at the ANSTO Laboratory, to reduce any such effects that solvent residue may have on the ^{14}C content of modern wood samples (Hua, pers comm). It is likely that incomplete solvent removal also occurs in the ANSTO solvent sequence, but it is less apparent in modern samples due to the ^{14}C content of the modern solvent. Nevertheless, as stated above, with subsequent cellulose extraction we find that the ANSTO and RRL solvent sequences produce comparable results, independent of the cellulose extraction method used (Figure 4.4). This demonstrates that the subsequent cellulose extraction removes any solvent residue present following solvent washes.

Corresponding $\delta^{13}C$ values support the above conclusions. Increases in $\delta^{13}C$ values of subsamples relative to untreated whole wood (ww) indicate removal of $\delta^{13}C$-depleted non-cellulosic material, including lignin and resins. Where samples are subject only to solvent washes (without cellulose extraction, A_s- and R_s-) we observe some increase in $\delta^{13}C$ relative to untreated whole wood (ww). However, with subsequent cellulose extraction we observe further increase in $\delta^{13}C$ and thus effective removal of non-cellulosic material that the solvents do not remove (Figure 4.4). The exception to this trend of increased $\delta^{13}C$ is the RRL solvent sequence 1958 subsample (without cellulose extraction, R_s-). In addition to uncharacteristically low $\delta^{13}C$, this subsample demonstrates much lower $F^{14}C$ than that of untreated whole wood (ww) and other subsamples. We attribute this to acetone residue, as acetone is also depleted in ^{13}C (~-28 ‰) relative to the sample. The addition of a final deionised water rinse to the RRL solvent sequence therefore seeks to remove solvent residue, as water is more polar than acetone.

Where untreated whole wood (ww) was analysed as a control for some of the early bomb period samples, our results of lower $F^{14}C$ of subsamples relative to whole wood demonstrate that all pretreatment methods must be removing at least some (younger) non-cellulosic material. The exception to this pattern is the 1958 R_s-R subsample. We hypothesize that this outlier results from effective removal of lower ^{14}C content mobile extractives, but incomplete removal of hemicellulose and/or lignin that form after the cellulose, thereby appearing to have a higher ^{14}C content than the untreated whole wood.

Overall, we demonstrate that the ANSTO and RRL solvent sequences are comparable, and therefore find no advantage in changing to use the ANSTO solvent sequence and find the RRL solvent sequence preferable as it utilises less toxic solvents.

SOLVENT WASH METHOD

Satisfied with the performance of the RRL solvent sequence, we investigated the automation of the RRL solvent wash method using a Dionex ASE 350 in context of the conventional Soxhlet method commonly employed.

We compare Soxhlet and ASE solvent wash methods, having established that the RRL solvent sequence is sufficient, and follow with ANSTO cellulose extraction (see following section for justification). Across blank, ancient, bomb and post-bomb period wood samples, we see good agreement between the methods (Figures 4.5 & 4.6), with an overall paired-t value of 0.63 for tree ring samples. We find that most pairs agree within 1 sigma and then have a few results 2 sigma apart (Figure 4.6). If we were to observe a bias due to incomplete organic contaminant removal by either of the methods we would expect opposite trends in the pre-bomb and post-bomb period samples due to the relative higher and lower ^{14}C mobile extractives, respectively. Across our organic sample range, we find no systematic bias towards either the Soxhlet or ASE solvent wash method within our uncertainties.

a b

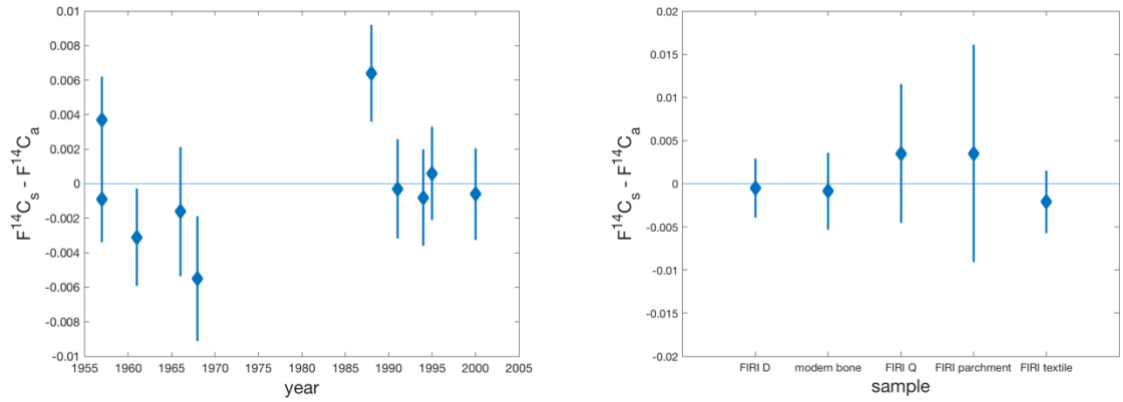

Figure 4.6: $F^{14}C$ of the RRL Soxhlet solvent wash method subsample minus $F^{14}C$ of the corresponding RRL ASE solvent wash method subsample for modern tree ring samples (left, a) and other samples (right, b), with error bars calculated from measurement uncertainty. The difference of $F^{14}C$ between methods demonstrates agreement of 6 pairs within 1 sigma, 3 pairs within 2 sigma, and 1 pair within 3 sigma. Other samples (b) include FIRI-D (non-modern wood), modern bone, FIRI-Q (leather), FIRI optional parchment and FIRI optional textile. Where multiple subsamples were analysed (Table 4.2), the mean and standard error were calculated and used for the comparison of methods. Error bars are larger in some cases due to lower ^{14}C counting statistics, but the differences of $F^{14}C$ for the comparisons of these different materials are all within 1 sigma.

Other organic materials that undergo solvent washes were also tested, and similarly showed good agreement and demonstrated no systematic bias (Figure 4.6b).

We therefore conclude that the RRL Soxhlet and ASE solvent wash methods give comparable results. Due to the nature of the more efficient and automated ASE method, we now conduct all our solvent washes using our newly developed ASE method.

CELLULOSE EXTRACTION METHOD

The $F^{14}C$ results of the ANSTO cellulose extraction subsamples are consistently a minimum of 1 standard deviation lower than corresponding RRL cellulose extraction subsample $F^{14}C$ results from the early bomb period (Figure 4.4, Table 4.2), independent of prior solvent

sequence applied (A_s-A and A_s-R, R_s-A and R_s-R). This indicates that the ANSTO cellulose extraction method is more effective at removing organic material, i.e., hemicellulose and lignin, formed after the cellulose was laid down and thus with higher ^{14}C content during this time period.

The $F^{14}C$ of post-bomb ANSTO and RRL cellulose extraction subsamples show some variability but there is no clear pattern. This is not unexpected, because with the slowing decrease of atmospheric $\Delta^{14}CO_2$ following the 1970s, non-cellulosic material likely forms at more similar atmospheric $\Delta^{14}CO_2$ levels to corresponding cellulose. However, the results do not contradict the results of the bomb period samples, but indicate that choice of RRL or ANSTO cellulose extraction method is not as important for periods such as the post-bomb period, where lesser atmospheric $\Delta^{14}CO_2$ change is observed, and thus non-cellulosic material remaining does not as strongly influence the $F^{14}C$ result (Figure 4.4). The $F^{14}C$ results of pre-modern SIRI F wood support this, with agreement between methods within 2 sigma. Therefore for older samples within the radiocarbon dating range, either of these cellulose extraction methods is also appropriate. The sub-fossil kauri blank results are comparable to previous results and raise no particular concern with any method variation.

Further evidence of the more effective nature of the ANSTO cellulose extraction method, compared to the RRL method, is small $\delta^{13}C$ increases in the ANSTO subsamples compared to the RRL subsamples of some of the bomb and post-bomb period tree ring samples. Again this supports more effective removal of non-cellulosic material through the ANSTO cellulose extraction method, with non-cellulosic material being depleted in $\delta^{13}C$ relative to cellulose. The 1999 tree ring does not show as much difference but does not contradict this trend.

We therefore conclude that the ANSTO cellulose extraction method is more effective at removing the non-cellulosic material formed after cellulose, highlighted clearly by the bomb period tree ring samples (Figure 4.3). However, for the ancient and post-bomb period samples either method is sufficient. For consistency, we therefore implement the ANSTO cellulose extraction method for modern samples spanning from the early bomb period to present, as samples spanning the bomb period demand this more effective cellulose

extraction. For pre-modern samples we continue to use the RRL cellulose extraction method as it is sufficient and results are statistically indistinguishable from subsamples undergoing the ANSTO cellulose extraction. We choose to avoid the ANSTO cellulose extraction method here because it uses more toxic solvents and requires longer processing time.

4.2.7 Conclusions

We present our previously unpublished RRL solvent wash and cellulose extraction pretreatment methods for wood, before conducting a comparison with equivalent ANSTO pretreatment methods to assess their efficacy. With a particular focus on modern tree ring samples, we demonstrate that the ANSTO and RRL solvent sequences generate $F^{14}C$ results that are in good agreement, and thus determine that the lower toxicity RRL solvent sequence (n-hexane, isopropanol, acetone and water) is sufficient for all organic samples. We then demonstrate that our automated ASE RRL solvent wash method is a comparable solvent wash technique to Soxhlet for both modern woods and a range of organic samples, but with improved efficiency, and hence now employ this method for all solvent washes. We find that both the ANSTO and RRL cellulose extraction methods are effective, with indication from $F^{14}C$ and $\delta^{13}C$ of tested samples that the ANSTO cellulose extraction method is more effective for tree ring samples during the bomb period, where a rapid change in atmospheric $\Delta^{14}CO_2$ is observed. We therefore implement the ANSTO cellulose extraction method for modern wood pretreatment at RRL, but continue to employ the faster RRL cellulose extraction method for non-modern wood samples.

Chapter 5

Data Quality

This PhD project seeks to reconstruct modern atmospheric $\Delta^{14}CO_2$ over the Southern Ocean through ^{14}C analysis of tree rings. Investigation of the subtle atmospheric $\Delta^{14}CO_2$ variability over the Southern Ocean requires highly accurate and precise data, such that small signals, similar to the ~2 ‰ measurement precision achieved, can be analysed with confidence.

I have previously presented the fieldwork and sampling rationale (Chapter 3), with the methodology employed for ^{14}C measurement of tree rings (Chapter 4). In this Chapter I investigate data quality: I first provide independent validation of tree ring counts (Section 5.1) and include a discussion of the exclusion of one site for which no ring count validation was possible. I include a specific analysis of two sites in southern Chile, to evaluate whether these two locations can be treated as consistent (Section 5.2). Finally, I evaluate measurement uncertainty of the new tree ring $\Delta^{14}CO_2$ records presented in this PhD project (Sections 5.3 & 5.4).

As a result of this analysis, I present my validated dataset (Section 5.5), which can be used in combination with the harmonised atmospheric $\Delta^{14}CO_2$ dataset for the Southern Hemisphere (Chapter 6) to inform accurate analysis of atmospheric $\Delta^{14}CO_2$ variability (Chapter 7).

NOTES ON NOMENCLATURE AND STATISTICS

Fraction modern, $F^{14}C$, is used for the majority of statistical analysis throughout this chapter, as defined by Reimer et al., (2004). Atmospheric $^{14}CO_2$ measurements are typically reported as $\Delta^{14}C$ (or $\Delta^{14}CO_2$), which is derived from $F^{14}C$ (Section 2.2). Whilst $F^{14}C$ incorporates a correction for mass-dependent fractionation, a further correction for decay is also incorporated in $\Delta^{14}C$. The use of $F^{14}C$ here avoids inaccuracies: an incorrect ring count, thus wrongly assigned year of collection, would lead to an inaccurate decay correction. Having

validated ring counts, $\Delta^{14}CO_2$ is used elsewhere in this thesis to conform with standard atmospheric $^{14}CO_2$ nomenclature.

The statistical analysis conducted includes the use of the t-test and chi-squared (χ^2) test, for which a brief introduction is provided here.

A t-test is typically used to determine whether there is significant difference between the mean value of two groups (Equation 5.1). It is assumed that the dependent variable fits a normal distribution. A t-test statistic of one indicates that the pair agrees within one sigma, likewise, values of two and three indicate agreement within two and three sigma respectively. Here t-tests are used to evaluate the difference between individual pairs of measurements, e.g., replicate tree core or tree ring samples (e.g., Section 5.1.2).

$$t = \frac{x_1 - x_2}{\sqrt{{\sigma_{x_1}}^2 + {\sigma_{x_2}}^2}} \quad (5.1)$$

A χ^2 test measures how well the observed distribution of data fits with the distribution expected if the variables are independent, with normally distributed data (Equation 5.2). A χ^2 value for the entire distribution is expected to be equivalent to the degrees of freedom, ν, i.e., $\chi^2 \approx \nu$.

$$\chi^2 = \frac{(F_i - \bar{F})^2}{{\sigma_{F_i}}^2} \quad (5.2)$$

A reduced chi-squared, χ^2_ν, test summarises the fit of observed and expected distributions for a group of n results, where ν = n - 1 (Equation 5.3).

$$\chi^2_\nu = \frac{1}{\nu}\sum[\frac{(F_i - \bar{F})^2}{{\sigma_{F_i}}^2}] \quad (5.3)$$

A χ_ν^2value of one indicates the observed data point lies within one sigma of the expected distribution, likewise, values of two and three indicate agreement within two and three sigma respectively.

Here a χ_ν^2 test is used as a statistical method to assess the distribution of replicate measurements in context of the measurement uncertainty (Section 5.3). The hypothesis is of replicate measurements being equal, with a corresponding χ_ν^2 value of 1 reflecting appropriately assigned uncertainties. A χ_ν^2 value smaller than 1 indicates that assigned uncertainties are too large, conversely a χ_ν^2 value greater than 1 indicates that assigned uncertainties are too small and should be increased to more accurately reflect the distribution of measurements. Therefore, to determine the appropriate measurement uncertainty to assign, the uncertainty is amended to produce a χ_ν^2 value of 1.

5.1 Ring Count Validation

Ring count validation helps to identify missing or false rings in tree cores. This is particularly important in this project because full chronologies (through cross-dating) are not established for samples (Section 2.3).

Having conducted initial tree ring counting (Section 3.2.6), independent validation of ring counts is conducted through ^{14}C analysis of (annual growth) tree rings spanning the bomb period with rapidly changing atmospheric $F^{14}C$ (Section 5.1.1). Where tree core samples do not extend to the bomb period, ^{14}C analysis of tree rings from replicate tree core samples is used to demonstrate independent ring count validation (Section 5.1.2).

5.1.1 Bomb-Pulse Validation

The bomb-pulse complicated traditional ^{14}C dating by its significant perturbation of the ^{14}C cycle (Section 2.2.3). However, tree rings from the bomb period have a recognisable isotopic signature that is very distinct due to the large rapid changes in atmospheric $F^{14}C$ (and $\Delta^{14}CO_2$): increasing from pre-bomb period levels of ~1.0 in $F^{14}C$ (~100 ‰ in $\Delta^{14}CO_2$) to a high of ~1.7 in $F^{14}C$ (~600 ‰ in $\Delta^{14}CO_2$) over the short bomb period from 1950s to 1960s (Figure

5.1) (Section 2.2.3). The bomb-pulse can thus be characterised within the tree ring records, such that the shape of the records corresponds with that of atmospheric measurements/calibration curve. A ring counting error of one year is immediately apparent due to the rapid changes of ~0.1 in $F^{14}C$ each year from around 1955 to 1965 (~100 ‰ in $\Delta^{14}CO_2$), relative to ^{14}C measurement precision of around 2 ‰ (quantified later in this chapter in section 5.2). Dating tree rings using the bomb-pulse is a technique that can thus be used alongside traditional dendrochronology and is used here to provide an independent validation of the ring count (Section 2.3).

The atmospheric $\Delta^{14}CO_2$ record from Wellington, New Zealand (referred to as Baring Head, BHD; Turnbull et al., 2017; described in more detail in Sections 6.2.1 & 6.4.5) is used for bomb-pulse validation here, because it is representative of mid-latitude Southern Hemisphere background air and also measured at the same laboratory (RRL). For the purposes of this comparison, I determine the November to February (spring – summer, inclusive) average from the BHD record for each year, such that the resultant record is suitably comparable to the tree ring ^{14}C measurements (Section 2.3 & Figure 5.1).

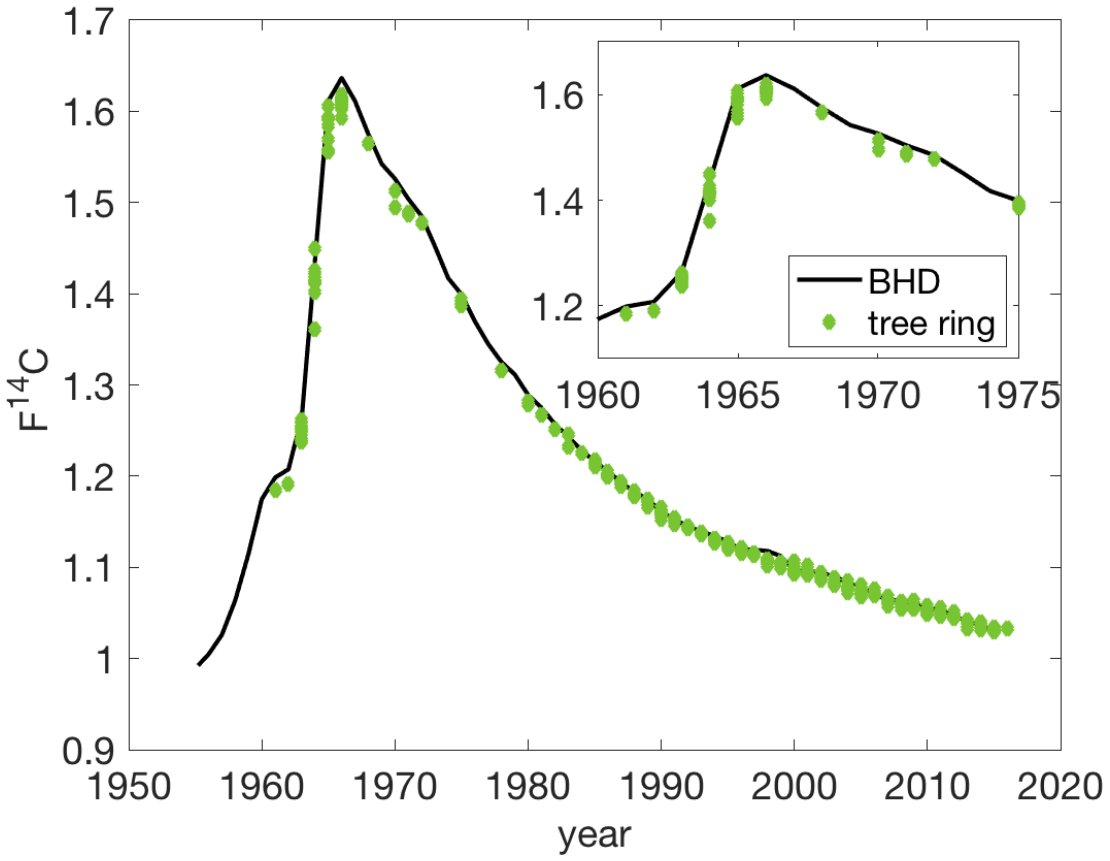

Figure 5.1: BHD atmospheric $\Delta^{14}CO_2$ record (black) (smoothed timeseries subsampled for tree growth months November – February, data from Turnbull et al., 2017), with tree ring measurements from this thesis (green). Inset shows the bomb period and following years in more detail.

Atmospheric $\Delta^{14}CO_2$ at BHD rapidly increased from ~1.25 ($F^{14}C$) in 1963 to ~1.6 in 1965, before slowly decreasing towards ~1.5 around 1970 (Figure 5.1 & Section 2.2.3). Where initial ring counts of tree core samples are correct, ^{14}C analysis of tree rings captures the steep atmospheric $\Delta^{14}CO_2$ increase observed in the early 1960s, thereby validating the ring count. Ring counts for most cores are successful: NZ-53S(I), CH-44S(I)/(II), CH-48S(I)/(II), CH-54S(I)/(II) and CH-55S(I)/(II) (Figure 5.2 & Table 5.1). The CH-54S(II) tree ring corresponding to 1965 was too small to measure, however the remaining measurements sufficiently capture the bomb-pulse, thereby validating the ring count (Figure 5.2).

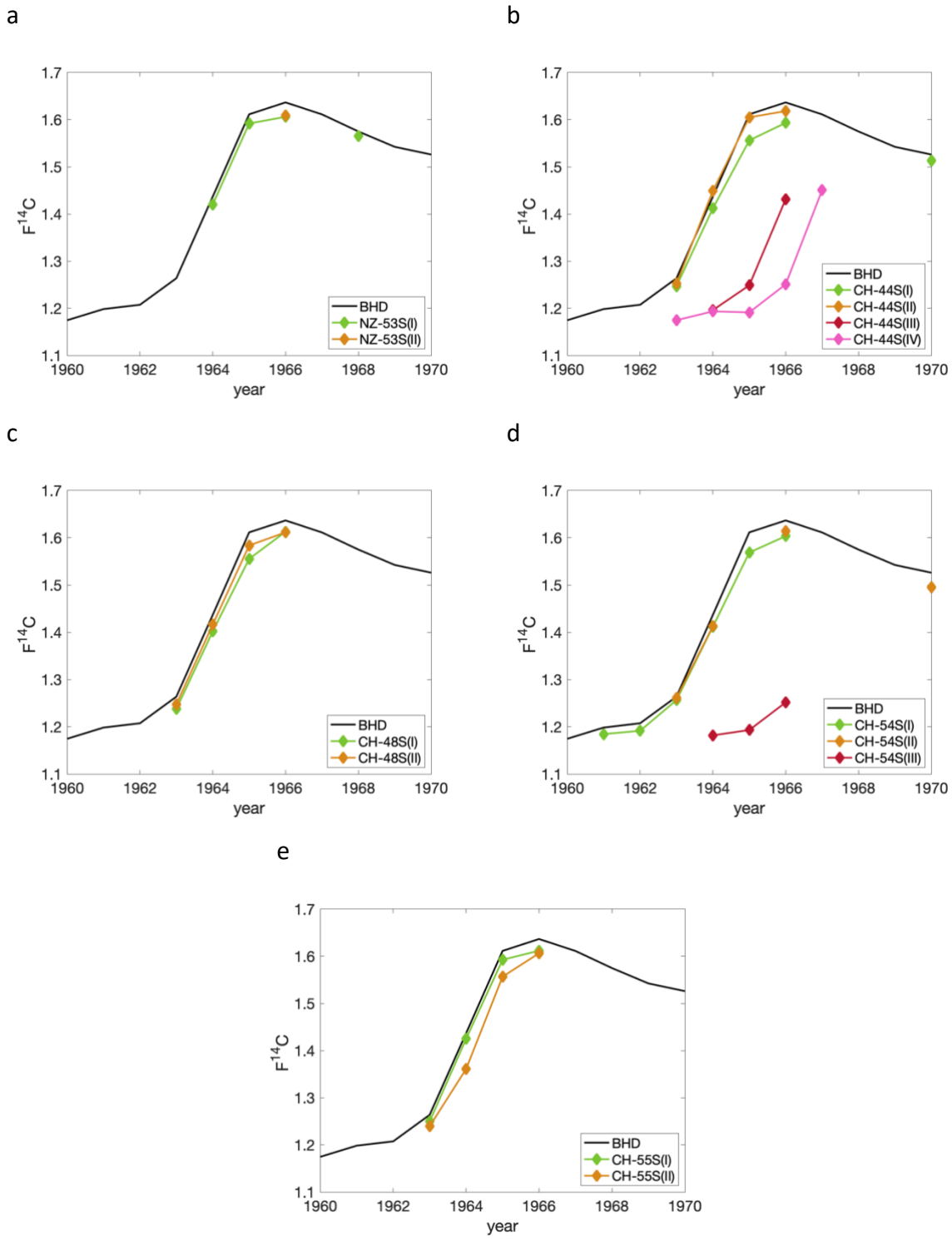

Figure 5.2: Results from bomb-pulse validation of tree core samples compared to the BHD atmospheric $\Delta^{14}CO_2$ record (smoothed timeseries subsampled for growth months November – February, data from Turnbull et al., 2017), grouped by sampling site: (top left, a) NZ-53S; (top right, b) CH-44S; (mid left, c) CH-48S; (mid right, d) CH-54S; (bottom centre, e) CH-55S.

In other cases, it is very apparent that tree ring ^{14}C measurements do not accurately reflect the bomb-pulse, indicative of an error in the initial ring count of at least one year. Detailed microscopic photos were taken of sections of the tree core samples when slicing into rings to ensure that the samples were fully documented and to allow investigation into ring counting errors such as this. However, despite labelling photographs, attempting to piece them together in order to ascertain which photograph corresponds to which tree core section was more challenging than anticipated. Based on this analysis, tree core samples CH-44S(III), CH-44S(IV) and CH-54S(III) that do not match the bomb-pulse are not pursued further.

Table 5.1: $F^{14}C$ values for each assigned year for successfully bomb-pulse validated tree cores, as shown in Figure 5.2.

Core / Year	1963	1964	1965	1966
NZ-53S(I)	-	1.4202	1.5920	1.6060
CH-44S(I)	1.2468	1.4120	1.5562	1.5933
CH-44S(II)	1.2527	1.4490	1.6050	1.6182
CH-48S(I)	1.2377	1.4021	1.5554	1.6128
CH-48S(II)	1.2474	1.4165	1.5838	1.6114
CH-54S(I)	1.2564	1.4119	1.5687	1.6035
CH-54S(I)	1.2613	1.4129	-	1.6139
CH-55S(I)	1.2499	1.4251	1.5926	1.6119
CH-55S(II)	1.2395	1.3611	1.5568	1.6064

5.1.2 Replicate Tree Core Validation

Some regions lack suitable tree core samples that date back to the bomb-period (Section 3.2.4), and thus bomb-pulse validation of ring counts cannot be conducted for selected cores. This is a result of a number of factors (discussed in further detail in Chapter 3): some trees are not suitable (e.g., do not extend to the bomb-pulse, rotten, insufficient rings or too narrow rings), and some tree core samples are not good quality (e.g., bark was lost after sampling or cores were broken during inspection and initial processing). This highlights the

importance of collecting many different tree core samples from each tree and sampling many different trees at a particular site.

In regions that lack suitable tree core samples with sufficient annual growth tree rings to reach the bomb period, replicate measurements of two co-located tree core samples are conducted to independently validate ring counts. A primary core (I) and a secondary core (II) are selected, such that the entire time series of (I) is subsequently analysed, with a subset of tree rings from (II). Replicate tree ring measurements are typically conducted at five-year intervals throughout the period of interest, i.e., 1985, 1990, ..., 2010, 2015. Note that the CH-53S replicate tree ring measurement years are offset from the other replicate pairs, i.e., 1989, 1999, 2004 and 2009.

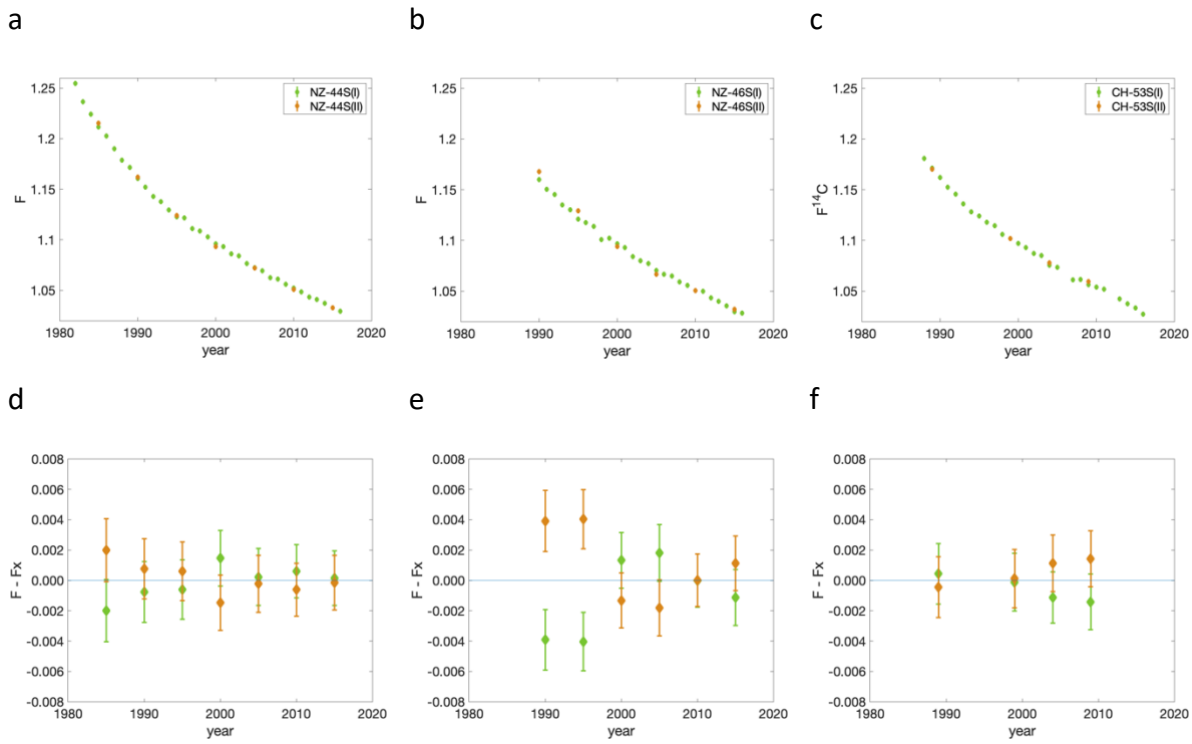

Figure 5.3: Ring count validation for sites without bomb-pulse validation, where measured $F^{14}C$ of replicate tree cores are compared for Core 1 ((I) green) and Core 2 ((II) orange), with the timeseries (top row; a, b, c) and offset of each from the pair mean (bottom row; d, e, f): NZ-44S (a, d); NZ-46S (b, e); CH-53S (c, f).

In most cases the pairs of tree core samples are from different trees at a site, with the exceptions of NZ-44S and NZ-46S. The motivation for using two different trees at a site is to identify any false or missing rings that may be present throughout a single tree or site that would otherwise be overlooked (Section 2.3). Despite NZ-44S and NZ-46S replicate tree core samples being from the same trees, the replicate measurements allow false or missing rings to be captured except for those consistent throughout a tree trunk. Therefore, although not as rigorous as replicate cores from different trees, the samples are from good sites, good trees and good tree core samples, and therefore appear to be suitable for conducting ring count validation.

Replicate tree core measurements of NZ-44S, CH-53S and CH-55S/CH-55S(w) typically agree within approximately one sigma (Table 5.2 & Figure 5.3). The results visually and statistically demonstrate agreement, and thus provide validation of the ring counts for NZ-44S, CH-53S and CH-55S/CH-55S(w).

However, the NZ-46S replicate tree core samples show deviation from one another. The four pair results from 2000 to 2015 inclusive, are comparable (Figure 5.3 & Table 5.2). Pair results initially assigned years 1990 and 1995, demonstrate more deviation, with differences of ~0.008 in $F^{14}C$, similar to observed annual differences in the BHD record during this period. The results of NZ-46S(I) fall consistently below the pair average in both 1990 and 1995, which is also reflected in the similar t-values of the two pairs (Figure 5.3 & Table 5.2). This is indicative of either a missing ring present in NZ-46S(II), or a false ring identified as an annual growth ring in NZ-46S(I). Considering the first hypothesis of a missing ring between 1995 and 2005 in NZ-46S(II), means that the rings assigned 1990 and 1995 are identifying as older years, i.e., higher $F^{14}C$ than corresponding NZ-46S(I) rings, with decreasing atmospheric $\Delta^{14}CO_2$. Conversely, the second hypothesis is of a false ring identified as an annual growth ring in NZ-46S(I), in which a potential ring boundary is observed within an annual growth ring, but incorrectly counted as an annual growth ring, thereby dividing an annual growth ring. This is indicative of a more modern year in NZ-46S(I) rings assigned 1990 and 1995 than corresponding NZ-46S(II) rings, i.e., lower $F^{14}C$.

The initial approach is to investigate such ring counting errors through microscopic photos, but this is particularly challenging (Chapter 3). Instead, the NZ-46S(I) and (II) data is first plotted in comparison to the ring-count validated tree ring data from NZ-44S and NZ-53S. The year-to-year changes in NZ-46S(I) are consistent with the bomb-pulse validated records, whereas the ring assigned '1995' in NZ-46S(II) looks more comparable to the 1994 ring of the bomb-pulse validated records suggesting that NZ-46S(II) most likely has a missing (or at least misidentified) ring between 1995 and 2000. Therefore, here the NZ-46S(I) data is considered valid (whilst NZ-46S(II) is not), but caution is taken with further analysis as this sample is not successful in ring count validation in the same way as other samples.

Only a single tree core from NZ-47S was of sufficient quality and time span for analysis (Section 3.2.4). However, without a replicate tree core sample, the ring count cannot be validated. Initial visualisation of the New Zealand ^{14}C tree ring records together highlights that NZ-47S is offset from the others (data not shown). NZ-47S has a clear offset from the other sites, appearing to observe the lowest ^{14}C of all, despite falling within the latitudinal distribution. Therefore, without a method for ring count validation for this core, it is unclear whether these results represent a real signal that differs from the other sites, or whether they represent a ring counting error and are consistent with the other sites. The NZ-47S data is thus discounted from further analysis. This highlights the importance of ring count validation to enable accurate interpretation of results.

Table 5.2: $F^{14}C$ values for measured years of replicate tree cores (Core 1 & 2, C1 & C2), as shown in Figure 5.3, with corresponding t values and p values (at 0.05 significance, 2-tailed and 1 degree of freedom). CH-48S is also included as replicate tree core measurements were also conducted for these bomb-pulse validated cores.

Site	**Year**	**C1 $F^{14}C$**	**C1 $F^{14}C$ error**	**C2 $F^{14}C$**	**C2 $F^{14}C$ error**	**t value**	**p value**
NZ-44S	1985	1.2115	0.0021	1.2155	0.0021	-1.3642	0.403
	1990	1.1605	0.0020	1.1621	0.0020	-0.5376	0.686
	1995	1.1229	0.0020	1.1241	0.0019	-0.4379	0.737
	2000	1.0961	0.0018	1.0932	0.0018	1.1332	0.460
	2005	1.0725	0.0019	1.0721	0.0019	0.1684	0.894
	2010	1.0521	0.0018	1.0509	0.0018	0.4950	0.707
	2015	1.0330	0.0018	1.0327	0.0018	0.1139	0.928
NZ-46S	1990	1.1600	0.0020	1.1678	0.0020	-2.7648	0.221
	1995	1.1210	0.0019	1.1291	0.0019	-2.9518	0.208
	2000	1.0967	0.0018	1.0941	0.0018	1.0263	0.492
	2005	1.0703	0.0019	1.0667	0.0018	1.3828	0.399
	2010	1.0507	0.0017	1.0507	0.0017	-0.0084	0.995
	2015	1.0298	0.0018	1.0321	0.0018	-0.8810	0.540
CH-53S	1989	1.1712	0.0020	1.1703	0.0020	0.3124	0.807
	1999	1.1017	0.0019	1.1020	0.0019	-0.0884	0.944
	2004	1.0757	0.0017	1.0779	0.0019	-0.8939	0.536
	2009	1.0565	0.0018	1.0594	0.0018	-1.0890	0.473
CH-48S	1990	1.1610	0.0019	1.1597	0.0019	0.4771	0.717
	1995	1.1250	0.0019	1.1220	0.0019	1.1344	0.460
	2000	1.0973	0.0019	1.0942	0.0019	1.1632	0.452
	2005	1.0735	0.0019	1.0733	0.0019	0.0504	0.968
	2010	1.0527	0.0019	1.0524	0.0018	0.1227	0.922
	2015	1.0321	0.0019	1.0324	0.0016	-0.1293	0.918

5.2 Isla Navarino (CH-55S) Site Comparison

Isla Navarino is a particularly important site because it is the southernmost site within this project at 55 °S (Chapter 3). West coast accessibility is very limited, but the Beagle Channel (north of Isla Navarino) funnels westerly winds, such that sites along the Beagle Channel should observe a strong westerly signal and are thus suitable for this project. Although there are some good quality cores from the northwest of Isla Navarino (CH-55S(w)), they do not extend to the bomb period (Section 3.2.4). The best quality cores from Isla Navarino are from the northeast of Isla Navarino (CH-55S): good width annual growth rings divided by straight, well-defined ring boundaries (Section 3.2.4). However, the sampling site of CH-55S is located east of the city of Ushuaia (~50 000 people), Argentina, which lies to the north of the Beagle Channel (Section 3.1.4).

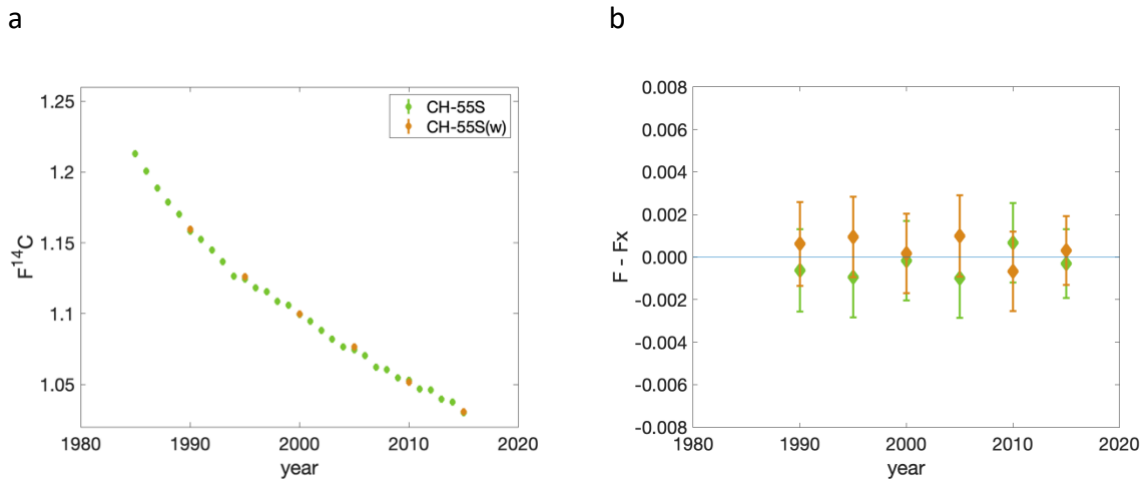

Figure 5.4: $F^{14}C$ for measured years of CH-55S and CH-55S(w), with measured values for assigned years (left, a), and deviations from the pair mean (right, b).

Therefore, here CH-55S tree core samples are compared to CH-55S(w) samples to determine if the same signal is observed, or if any bias is observed between the two sites. Having used bomb-pulse validation to confirm the ring counts for CH-55S(I) and (II) (Section 5.1.2), the ring count of the tree core from CH-55S(w) is validated through replicate tree core measurement, whereby CH-55S(w) is used as the secondary core to the primary CH-55S(I) core (see above). CH-55S(w) and CH-55S(I) demonstrate good agreement within one sigma, with corresponding t-values less than 0.8 (Figure 5.3 & Table 5.3). Therefore, having

demonstrated that CH-55S(w) and CH-55S(I) are equivalent, CH-55S is thus determined as a suitable sampling site for this project, appropriate for use in further analysis.

Table 5.3: $F^{14}C$ values for measured years of CH-55S (Core 1, C1) and CH-55S(w) (Core 2, C2) sites, as shown in Figure 5.4, with corresponding t values.

Site	Year	C1 $F^{14}C$	C1 $F^{14}C$ error	C2 $F^{14}C$	C2 $F^{14}C$ error	t value	p value
CH-55S/(w)	1990	1.1583	0.0019	1.1595	0.0020	-0.4523	0.723
	1995	1.1243	0.0019	1.1262	0.0019	-0.7094	0.607
	2000	1.0996	0.0019	1.1000	0.0019	-0.1336	0.915
	2005	1.0747	0.0019	1.0766	0.0019	-0.7369	0.596
	2010	1.0531	0.0019	1.0518	0.0019	0.5046	0.702
	2015	1.0302	0.0016	1.0308	0.0016	-0.2691	0.833

5.3 Determination of Measurement Uncertainty

The investigation of subtle atmospheric $\Delta^{14}CO_2$ variability within this PhD project requires the best possible measurement precision with well characterised uncertainties.

High-precision ^{14}C measurements are achieved through efficient measurement that yields high counts from reasonable exposure time. In the past, ^{14}C measurement statistical uncertainty, associated with counting, dominated the overall measurement uncertainty, such that its reduction through increased counting leads to improved result precision (e.g., Zondervan et al., 2015). However, high-precision ^{14}C measurements are now such that the statistical uncertainty no longer remains the only limiting factor of overall uncertainty, with other factors now also playing a relatively more important role (e.g., Meijer et al., 2006).

For ^{14}C measurement, in addition to primary standard and processing blank sample preparation, further quality control material is routinely prepared and analysed alongside samples, such that long-term repeatability can be assessed (Section 4.1), thus providing a good constraint on overall measurement uncertainty. Here a range of additional replicate measurements is used to determine measurement uncertainty associated with tree ring

$\Delta^{14}CO_2$ records presented in this PhD project. The uncertainty analysis conducted here is comparable to that conducted by Graven (2008).

5.3.1 Measurement Uncertainty Methods

Following tree core collection and preparation into tree rings (Chapter 3), tree ring samples undergo preparation for ^{14}C analysis, including physical and chemical pretreatment, combustion, graphitisation and AMS measurement (Section 4.1). Thus, the overall measurement uncertainty associated with tree ring samples can be defined as:

$$\sigma_{x_i} = \sqrt{\sigma_{tree}{}^2 + \sigma_{prep}{}^2 + \sigma_{EAG}{}^2 + \sigma_{AMS}{}^2 + \sigma_{btwn}{}^2} \quad (5.4)$$

with the different contributing uncertainties combined in quadrature (Ellison et al., 2000): natural variability and sampling of tree (tree), tree ring slicing and chemical pretreatment (prep), EA combustion and graphitisation (EAG), AMS measurement wheel (AMS) and long-term between-wheel variability (btwn). Each uncertainty component can be determined as follows.

AMS statistical uncertainty, σ_{AMS}, is derived from ^{14}C counting statistics. At RRL, AMS data is visualised and analysed through an in-house program (CalAMS), in which samples are analysed with respect to oxalic acid (I) standard (OxI) as is convention (Stuiver and Polach, 1977; Section 2.2). Further analysis details can be found in Appendix (A.9). The CalAMS output is ratio-to-standard (rts), which places the ^{14}C /^{12}C ratio of the sample, 'i', in terms of OxI standard prior to any further corrections applied:

$$rts = \frac{\left[\frac{(^{14}C\ countrate)(^{12}C\ current)}{(^{13}C\ current)^2}\right]_i}{\left[\frac{(^{14}C\ countrate)(^{12}C\ current)}{(^{13}C\ current)^2}\right]_{OxI}} \quad (5.5)$$

The uncertainty associated with rts stems mostly from the poisson error of the ^{14}C count rate of a sample, because ^{12}C and ^{13}C current measurements are not limited in the same

way that the ^{14}C count statistic is. There is also a small contribution from the poisson error of the ^{14}C count rate of OxI targets within the AMS measurement wheel used to determine rts, however this is much smaller than that of a sample. This is a reflection of the greater total count rate resulting from eight OxI targets relative to each individual sample. AMS uncertainty for the dataset reported here ranges from 0.0012 to 0.0020 in $F^{14}C$, depending on the number of counts obtained for a particular sample. We strive for 0.0012 (~650,000 ^{14}C counts), but this was not achieved in every case.

Having established the AMS uncertainty (σ_{AMS}), the uncertainty associated with EA combustion and graphitization, $\sigma_{EAG,}$ can then be determined from replicate analyses of material from the same tree ring, which has been physically and chemically pretreated as one, and then divided into multiple aliquots prior to combustion and all aliquots measured within, 'w', the same AMS measurement wheel. This replication is named "ring(w)". The overall uncertainty for ring(w) is determined from the scatter of measurements of these replicates. σ_{EAG} is then determined from:

$$\sigma_{ring_{(w)}} = \sqrt{{\sigma_{EAG}}^2 + {\sigma_{AMS}}^2} \quad (5.6)$$

Similarly, by measuring another set of ring replicates with common pretreatment, and division prior to combustion, but this time measured in separate AMS measurement wheels "ring(b)", the "between wheel" variability, σ_{btwn}, can be determined:

$$\sigma_{ring_{(b)}} = \sqrt{+{\sigma_{EAG}}^2 + {\sigma_{AMS}}^2 + {\sigma_{btwn}}^2} \quad (5.7)$$

Next, now that σ_{EAG} has been assessed, in principle, the contribution of physical and chemical pretreatment can be determined from a control material, 'cm', whereby each replicate is subsampled from a large tree ring and treated as independent right through the process from physical pretreatment to measurement. These can be measured in the same wheel (within, 'w') and in different wheels (between, 'b') to evaluate both the preparation (σ_{prep}) and between wheel (σ_{btwn}) uncertainty contributions.

$$\sigma_{cm_{(w)}} = \sqrt{{\sigma_{prep}}^2 + {\sigma_{EAG}}^2 + {\sigma_{AMS}}^2} \quad (5.8)$$

$$\sigma_{cm_{(b)}} = \sqrt{{\sigma_{prep}}^2 + {\sigma_{EAG}}^2 + {\sigma_{AMS}}^2 + {\sigma_{btwn}}^2} \quad (5.9)$$

Finally, by measuring samples from the same annual growth year in different trees from the same site, the uncertainty due to the 'tree', or all factors prior to pretreatment, can be assessed (σ_{tree}). However as shown later, I was unable to determine σ_{prep}, thus I instead combine σ_{prep} and σ_{tree}.

$$\sigma_{core_{(w)}} = \sqrt{{\sigma_{tree}}^2 + {\sigma_{prep}}^2 + {\sigma_{EAG}}^2 + {\sigma_{AMS}}^2} \quad (5.10)$$

σ_{AMS} is defined by initial assigned uncertainty from the AMS measurement output (Equation 5.5). The different contributing uncertainties specified in Equation 5.4 are thus evaluated through rearranging and combining Equations 5.6 – 5.10. This is achieved through use of reduced χ^2, χ_ν^2 statistics. For each replicate measurement group, as identified by the different equations 5.6 – 5.10, the appropriate measurement uncertainty is determined through use of χ_ν^2 statistics. A χ_ν^2 value of 1 is sought for a group. If χ_ν^2 is larger than 1, then σ_{group} is increased until χ_ν^2 of 1 is obtained for that group. σ_x (where σ_x is the σ for that component, x) is determined by rearranging the appropriate equation 5.6 – 5.10.

Table 5.4: Determined $F^{14}C$ uncertainty components associated with the tree ring ^{14}C measurements in this project, based on χ^2_ν of different groups of replicate analyses.

Uncertainty component	1 σ uncertainty in $F^{14}C$	Determination
σ_{AMS}	0.0014 – 0.0020	Counting statistics
σ_{EAG}	0.0003	Equation 5.6 (within-wheel ring replicates)
σ_{btwn}	0.0000	Equation 5.7 (between-wheel ring replicates)
$\sigma_{prep+tree}$	0.0006	Equation 5.10 (within-wheel core replicates)
Overall Uncertainty	**0.0016 – 0.0021**	

5.4 Measurement Uncertainty Results

5.4.1 Replicate Tree Ring Measurements

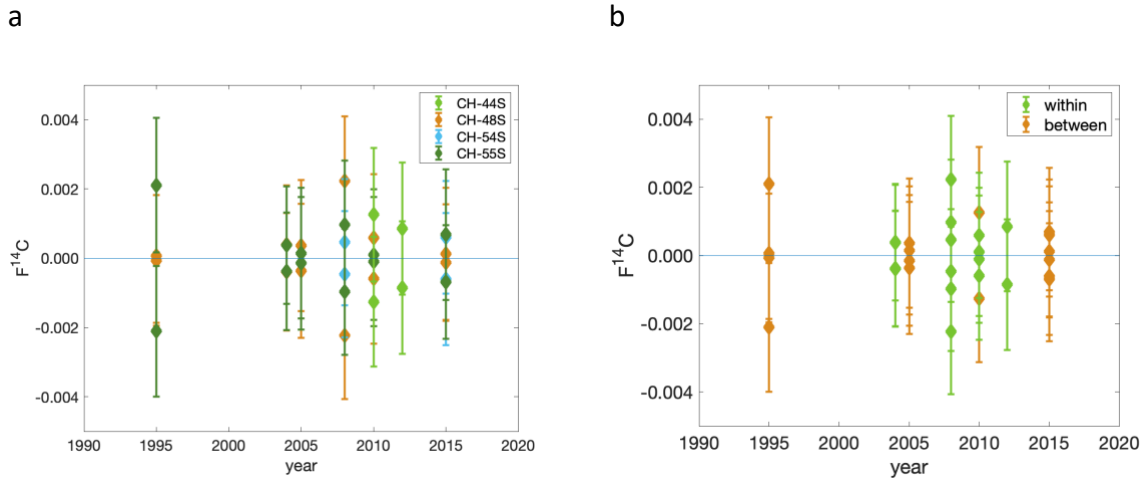

Figure 5.5: $F^{14}C$ deviation for measured replicate tree rings from pair means, where tree rings are treated as a single sample for preparation and divided prior to EA combustion, with pairs grouped by tree core (left, a) and within/between AMS wheel (right, b).

Tree ring replicate measurements are conducted to enable investigation into measurement uncertainty.

Tree ring replicates here are replicate measurements of the isolated cellulose of a tree ring sample from chemical preparation, after which replicates are treated as individual samples for combustion, graphitisation and AMS measurement. Variability of replicate tree ring measurements thus incorporates uncertainty from combustion, graphitisation and AMS measurement.

σ_{EAG} is determined as 0.0003 (Table 5.4). σ_{btwn} is determined as 0.0000, i.e., in this dataset there is no additional variability due to difference between AMS wheels.

5.4.2 Replicate Measurements of Control Material Kauri Sample

Within RRL there exists a previously-dated kauri tree biscuit (full cross section of the trunk) from the Wellington Region (tree felled in 2012; Ansell 2016). A subsection of the cross section was previously divided into annual growth tree rings for ^{14}C analysis, of which a selection was used for methodology development within this PhD project (Section 4.2). Whereas tree cores yield sufficient material for only one to three subsamples of an individual ring, this large biscuit affords the opportunity to make many replicate measurements of the same ring as a control material. Unfortunately, the subsampling technique was insufficient to make this a reliable control material, but the results and explanations are laid out here to facilitate understanding of potential problems in data quality analysis for tree rings.

The 1981 wide, clear ring was chosen as the control material. Typically, two subsamples are analysed within each AMS measurement wheel (Section 4.1), thereby allowing assessment of both within-wheel and long-term between-wheel repeatability.

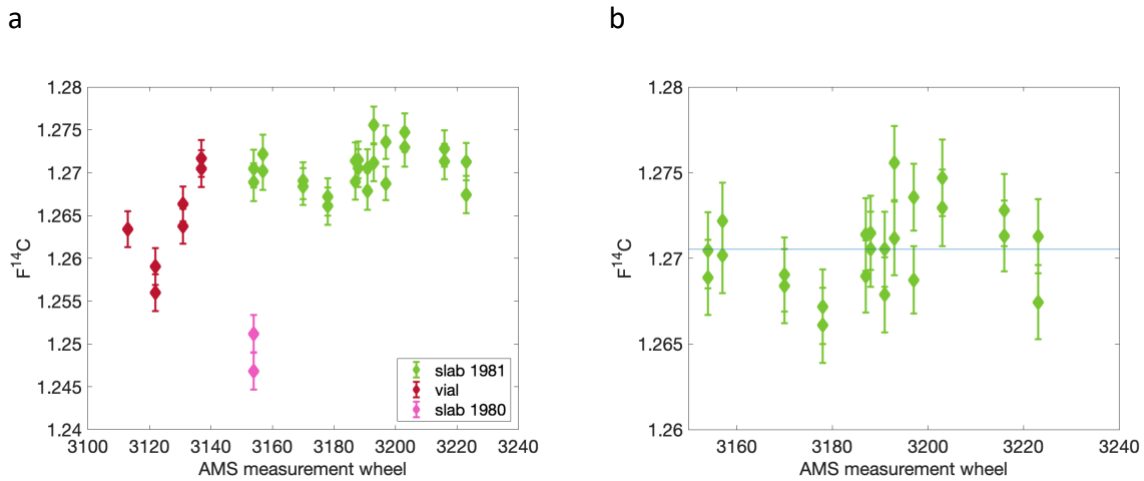

Figure 5.6: $F^{14}C$ values of Kauri control replicates, separated by different sampling (left, a) and valid measurements shown relative to the control mean (right, b).

The control material subsamples in the first four AMS measurement wheels of this project are from the subsection previously divided into annual growth tree rings (Ansell, 2016). More variability of control material results is observed than expected with a range of 0.015 in $F^{14}C$ (Figure 5.6). The difference is smaller than the interannual trend during this time period, as measured samples from the previous ring (1980) are lower again by 0.01. Thus the difference cannot be due to a labelling error.

Evaluation of the 1981 control ring results together instead suggests an issue with the subsampling technique (Figure 5.6). Ideally each subsample should include equal weighting of material from across the full growth ring, therefore representing the full growth season in every subsample. However, it appears that instead different periods of growth are subsampled in this case, likely because sampling from the cross-section was conducted along the surface, concentrated in the centre of the growth ring. Fortunately this is not a challenge with tree core samples as the direction of growth is clear in divided annual growth tree rings due to the cylindrical nature of a tree core.

Thus the variability in this control material likely reflects a subsampling problem rather than identifying uncertainties that we might expect in authentic tree core samples. Therefore this control material is not used in assessing variability further.

5.4.3 Replicate Tree Core Measurements

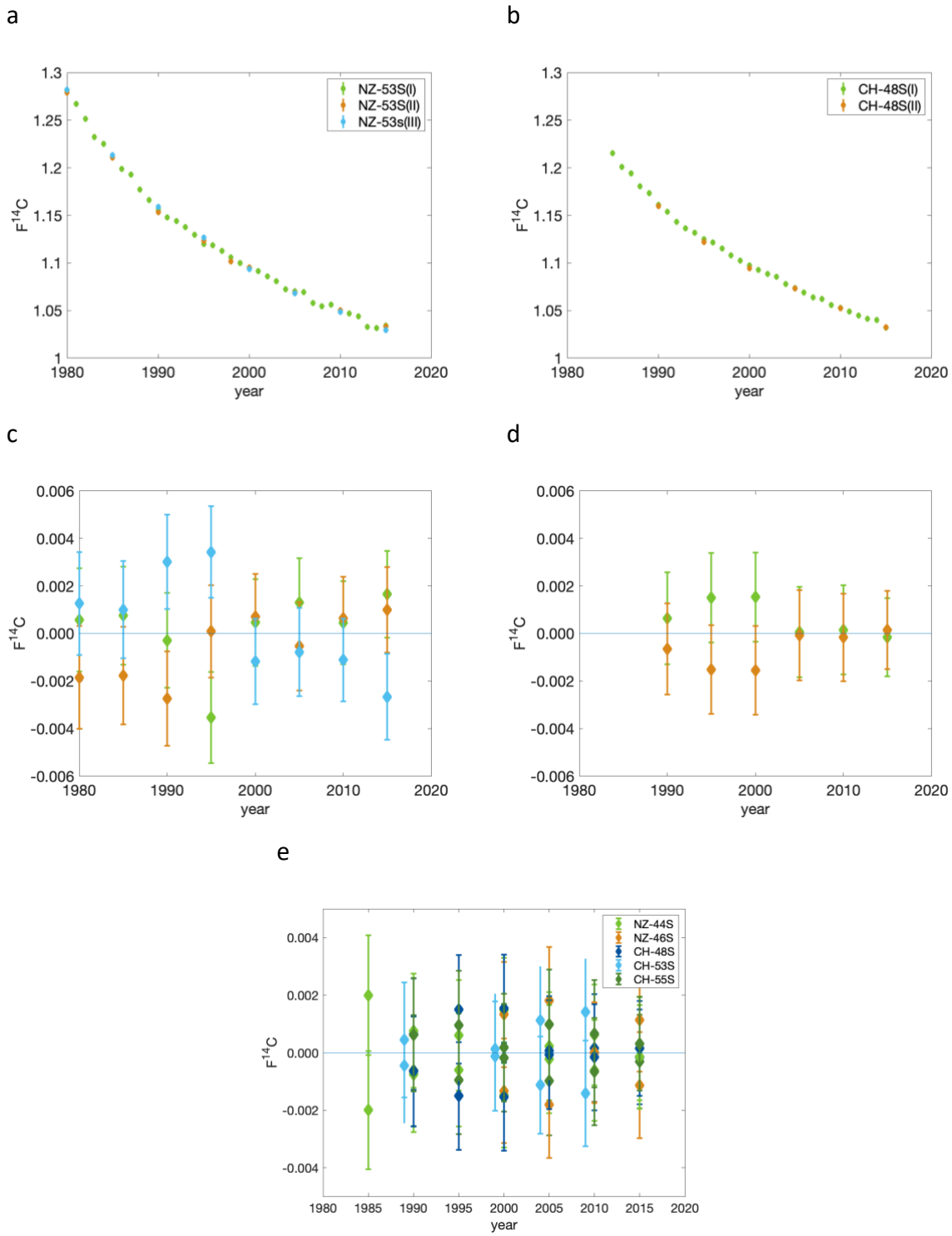

Figure 5.7: $F^{14}C$ of replicate tree cores, including timeseries and deviation from mean for cores with bomb-pulse validated ring counts, NZ-53S (a, c) and CH-48S (b, d), and a summary of all replicate tree cores (including those used successfully for ring count validation (bottom, e).

a b

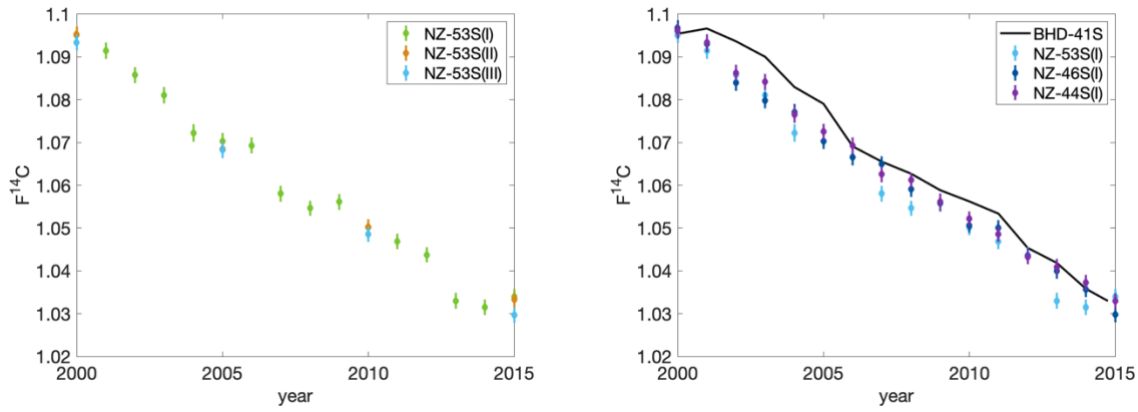

Figure 5.8: $F^{14}C$ of NZ-53S(I) with core repeats (left, a), and other NZ cores (right, b) for 2000 – 2015.

In addition to replicate tree core measurements used for ring count validation (Section 5.1.2), replicate measurements are conducted of bomb-pulse validated tree cores (Figure 5.7). This enables investigation into measurement uncertainty beyond the sample preparation and measurement variability captured by the control material.

Between 2005 and 2015, NZ-53S(I) also observes a variable downwards trend that is not smooth. It is possible that although bomb-pulse validated, that this core has false/missing rings that balance one another. Through the analysis of replicate bomb-pulse validated cores of NZ-53S, this trend is demonstrated to be consistent across the multiple cores, across each 5-year gap (Figures 5.7 & 5.8). This would appear to suggest that if false/missing rings are present, they are equally present across the multiple cores. Given that these cores are from different branches of a tree, this could be a large-scale climate-induced phenomenon causing false/missing rings, however the identification of false rings as annual rings is unlikely given that this problem has not been observed elsewhere in this project as care was taken in observing clear early/latewood structure when conducting ring counting (Section 3.2.6). Therefore, the more likely explanation for this is that it is an accurate representation of the atmospheric $\Delta^{14}CO_2$ observed, given that it also aligns approximately with nearby MCQ and the other New Zealand tree ring $\Delta^{14}CO_2$ records (Figures 5.7 & 7.5).

Replicate tree cores are tree cores from different trees at a sampling site, or two cores from the same tree, thus observed variability incorporates natural variability of trees and sampling variability, in addition to sample preparation and measurement variability observed by the control material (and replicate tree ring samples). All of the validated replicate tree cores demonstrate good agreement, hence validating the ring counts (Section 5.1.2, Figure 5.3 & Table 5.2). Similarly good agreement is observed by CH-48S replicate trees cores that already have bomb-pulse ring count validation (Figure 5.7; Section 5.1.2). Replicate tree core samples of NZ-44S, NZ-46S and NZ-53S are predominantly spread across the first four AMS measurement wheels. Where valid control material is lacking, these replicate measurements can thus be considered to assess data quality. The data of these NZ replicate cores is inline with variability observed in Chile replicate cores of other AMS measurement wheels (data not shown).

The replicate core measurements show $\sigma_{prep+tree}$ of 0.0006 in $F^{14}C$, somewhat larger than σ_{EAG}, but still smaller than σ_{AMS}.

Overall measurement uncertainty is therefore 0.0016 to 0.0021 in $F^{14}C$, which is comparable to that achieved for direct atmospheric ^{14}C measurements.

5.5 Atmospheric $\Delta^{14}CO_2$ Tree Ring Dataset from this Project

Having evaluated data quality, here I present my validated dataset of atmospheric $\Delta^{14}CO_2$ tree ring records for recent decades. This dataset excludes data that has been discarded as a result of data quality evaluation within this chapter, thus is the key outcome of preceding chapters.

Table 5.5: NZ tree ring records: NZ-44S, NZ-46S and NZ-53S: $\Delta^{14}C$ and $F^{14}C$ (and errors).

Year	NZ-44S		NZ-46S		NZ-53S	
	$\Delta^{14}C$	$F^{14}C$	$\Delta^{14}C$	$F^{14}C$	$\Delta^{14}C$	$F^{14}C$
1980	-	-	-	-	276.81(2.2)	1.2815(0.0022)
1981	-	-	-	-	262.32(2.1)	1.2671(0.0021)
1982	249.91(2.2)	1.2548(0.0022)	-	-	246.38(2.1)	1.2512(0.0021)
1983	231.49(2.2)	1.2364(0.0022)	-	-	227.57(2.1)	1.2325(0.0021)
1984	219.28(2.1)	1.2243(0.0021)	-	-	220.14(2.2)	1.2252(0.0022)
1985	206.42(2.1)	1.2115(0.0021)	-	-	207.91(2.1)	1.2130(0.0021)
1986	197.58(2.1)	1.2028(0.0021)	-	-	193.61(2.1)	1.1988(0.0021)
1987	184.61(2.0)	1.1899(0.0020)	-	-	187.55(2.0)	1.1929(0.0020)
1988	173.50(2.0)	1.1789(0.0020)	-	-	171.84(2.0)	1.1772(0.0020)
1989	166.08(2.1)	1.1716(0.0021)	-	-	160.48(2.0)	1.1660(0.0020)
1990	154.94(2.0)	1.1605(0.0020)	-	-	150.23(2.0)	1.1558(0.0020)
1991	146.40(2.0)	1.1521(0.0020)	-	-	142.09(2.0)	1.1478(0.0020)
1992	137.11(2.0)	1.1429(0.0020)	-	-	138.12(2.0)	1.1439(0.0020)
1993	131.85(2.0)	1.1378(0.0020)	-	-	131.91(2.0)	1.1378(0.0020)
1994	123.72(2.0)	1.1297(0.0020)	-	-	123.46(2.0)	1.1295(0.0020)
1995	116.77(2.0)	1.1229(0.0020)	-	-	113.75(1.9)	1.1198(0.0019)
1996	115.53(2.0)	1.1218(0.0020)	-	-	112.26(1.9)	1.1185(0.0019)
1997	104.74(1.9)	1.1110(0.0019)	-	-	106.45(1.9)	1.1128(0.0019)
1998	102.24(1.9)	1.1087(0.0019)	-	-	99.61(1.9)	1.1060(0.0019)
1999	96.32(2.0)	1.1028(0.0020)	-	-	93.55(1.9)	1.1001(0.0019)
2000	89.51(1.8)	1.0961(0.0018)	90.11(1.8)	1.0967(0.0018)	88.44(1.8)	1.0950(0.0018)
2001	86.61(1.9)	1.0933(0.0019)	86.30(1.9)	1.0930(0.0019)	84.72(1.9)	1.0914(0.0019)
2002	79.43(1.9)	1.0862(0.0019)	77.17(1.9)	1.0840(0.0019)	78.95(1.9)	1.0858(0.0019)
2003	77.23(1.9)	1.0842(0.0019)	72.96(1.9)	1.0799(0.0019)	74.12(1.9)	1.0810(0.0019)
2004	69.48(1.9)	1.0765(0.0019)	70.09(1.9)	1.0771(0.0019)	65.24(2.1)	1.0722(0.0021)
2005	65.39(1.9)	1.0725(0.0019)	63.25(1.9)	1.0703(0.0019)	63.23(1.9)	1.0703(0.0019)
2006	62.11(1.9)	1.0693(0.0019)	59.32(1.9)	1.0665(0.0019)	62.10(1.9)	1.0693(0.0019)
2007	55.28(1.9)	1.0626(0.0019)	57.61(1.9)	1.0649(0.0019)	50.76(1.9)	1.0580(0.0019)
2008	53.77(1.8)	1.0612(0.0018)	51.64(1.8)	1.0590(0.0018)	47.26(1.8)	1.0546(0.0018)
2009	48.65(1.9)	1.0562(0.0019)	48.27(1.8)	1.0558(0.0018)	48.26(1.8)	1.0561(0.0018)
2010	44.54(1.8)	1.0521(0.0018)	43.05(1.7)	1.0507(0.0017)	42.50(1.7)	1.0501(0.0017)
2011	40.84(1.8)	1.0485(0.0018)	42.28(1.8)	1.0500(0.0018)	39.16(1.8)	1.0469(0.0018)
2012	35.49(1.7)	1.0433(0.0017)	35.69(1.8)	1.0435(0.0018)	35.92(1.8)	1.0437(0.0018)
2013	33.03(1.8)	1.0409(0.0018)	32.08(1.8)	1.0400(0.0018)	25.16(1.8)	1.0330(0.0018)
2014	29.27(1.8)	1.0373(0.0018)	27.73(1.8)	1.0357(0.0018)	23.51(1.8)	1.0315(0.0018)
2015	24.88(1.8)	1.0330(0.0018)	21.78(1.8)	1.0298(0.0018)	25.86(1.8)	1.0340(0.0018)
2016	21.29(1.7)	1.0295(0.0017)	20.28(1.8)	1.0285(0.0018)	-	-

Table 5.6: : Chile tree ring records: CH-48S, CH-53S and CH-55S: $\Delta^{14}C$ and $F^{14}C$ (and associated errors).

Year	CH-48S		CH-53S		CH-55S	
	$\Delta^{14}C$	$F^{14}C$	$\Delta^{14}C$	$F^{14}C$	$\Delta^{14}C$	$F^{14}C$
1985	210.06(2.0)	1.2152(0.0020)	-	-	207.88(2.1)	1.2130(0.0021)
1986	195.81(1.9)	1.2010(0.0019)	-	-	195.43(1.9)	1.2007(0.0019)
1987	188.81(1.9)	1.1941(0.0019)	-	-	183.56(1.9)	1.1889(0.0019)
1988	175.05(2.1)	1.1805(0.0021)	175.49(2.1)	1.1809(0.0021)	173.32(2.1)	1.1787(0.0021)
1989	167.98(2.0)	1.1735(0.0020)	165.64(2.0)	1.1712(0.0020)	164.73(2.0)	1.1702(0.0020)
1990	155.36(1.9)	1.1610(0.0019)	156.43(1.9)	1.1620(0.0019)	152.71(1.9)	1.1583(0.0019)
1991	148.29(2.0)	1.1540(0.0020)	146.62(2.0)	1.1523(0.0020)	146.92(2.0)	1.1526(0.0020)
1992	137.23(2.0)	1.1430(0.0020)	139.75(2.0)	1.1456(0.0020)	138.99(2.0)	1.1448(0.0020)
1993	130.42(2.0)	1.1363(0.0020)	130.13(1.9)	1.1360(0.0019)	130.92(2.0)	1.1368(0.0020)
1994	125.78(1.8)	1.1318(0.0018)	122.30(1.8)	1.1283(0.0018)	120.36(1.8)	1.1263(0.0018)
1995	118.86(1.9)	1.1250(0.0019)	117.90(1.9)	1.1240(0.0019)	118.24(1.9)	1.1243(0.0019)
1996	115.34(1.9)	1.1216(0.0019)	111.63(1.9)	1.1178(0.0019)	112.00(1.9)	1.1182(0.0019)
1997	108.94(2.0)	1.1153(0.0020)	108.30(2.0)	1.1146(0.0020)	109.23(2.0)	1.1156(0.0020)
1998	101.71(1.9)	1.1081(0.0019)	99.54(1.9)	1.1059(0.0019)	102.34(1.9)	1.2088(0.0019)
1999	96.07(1.9)	1.1026(0.0019)	95.22(1.9)	1.1017(0.0019)	99.31(1.9)	1.1058(0.0019)
2000	90.70(1.9)	1.0973(0.0019)	90.63(1.9)	1.0972(0.0019)	93.00(1.9)	1.0996(0.0019)
2001	86.19(2.0)	1.0929(0.0020)	86.28(1.9)	1.0930(0.0019)	88.01(2.0)	1.0947(0.0020)
2002	81.45(1.9)	1.0883(0.0019)	80.38(1.8)	1.0872(0.0018)	81.26(1.9)	1.0881(0.0019)
2003	78.50(2.2)	1.0854(0.0022)	78.10(1.9)	1.0850(0.0019)	75.20(2.0)	1.0821(0.0020)
2004	70.72(1.7)	1.0777(0.0017)	68.66(1.7)	1.0757(0.0017)	69.53(1.7)	1.0765(0.0017)
2005	66.37(1.9)	1.0735(0.0019)	66.34(1.9)	1.0735(0.0019)	67.54(1.9)	1.0747(0.0019)
2006	61.67(1.9)	1.0689(0.0019)	-	-	63.20(1.9)	1.0704(0.0019)
2007	56.56(1.9)	1.0639(0.0019)	53.80(1.9)	1.0611(0.0019)	54.77(1.9)	1.0621(0.0019)
2008	54.71(1.8)	1.0621(0.0018)	54.23(1.8)	1.0617(0.0018)	53.26(1.8)	1.0607(0.0018)
2009	48.13(1.8)	1.0556(0.0018)	49.03(1.8)	1.0565(0.0018)	47.10(1.8)	1.0546(0.0018)
2010	45.06(1.9)	1.0527(0.0019)	46.42(1.8)	1.0540(0.0018)	45.50(1.9)	1.0531(0.0019)
2011	41.16(1.9)	1.0489(0.0019)	44.09(1.9)	1.0518(0.0019)	39.21(1.9)	1.0469(0.0019)
2012	37.10(1.9)	1.0449(0.0019)	-	-	38.32(2.2)	1.0461(0.0022)
2013	33.67(1.9)	1.0416(0.0019)	34.32(1.8)	1.0422(0.0018)	31.79(1.9)	1.0397(0.0019)
2014	32.26(1.9)	1.0403(0.0019)	29.60(1.9)	1.0376(0.0019)	29.44(1.9)	1.0374(0.0019)
2015	24.06(1.6)	1.0321(0.0016)	25.39(1.6)	1.0335(0.0016)	22.13(1.6)	1.0302(0.0016)
2016	-	-	19.26(1.9)	1.0274(0.0019)	-	-

Chapter 6

Integrating Results from this Project with Other Atmospheric $\Delta^{14}CO_2$ Records

In Chapter 5 I presented a new 30-year annual-resolution atmospheric $\Delta^{14}CO_2$ dataset from tree rings across a latitudinal range of the Southern Ocean Region (44 – 55 °S). This doubles the number of sites with recent atmospheric $\Delta^{14}CO_2$ records from mid-high latitudes of the Southern Hemisphere. These new results will be much more powerful if they can be used alongside the sparse existing atmospheric $\Delta^{14}CO_2$ records.

I therefore explore the comparability of the tree ring $\Delta^{14}CO_2$ records from this project with existing atmospheric $\Delta^{14}CO_2$ measurements in the Southern Hemisphere, made by several different research groups with differing methodologies. Similar to the tree sampling sites, here I am only interested in atmospheric sampling sites that observe atmospheric $\Delta^{14}CO_2$ of clean air and minimal local influence, i.e., background sites.

In Chapter 5, I assessed the data quality of the tree ring $\Delta^{14}CO_2$ records from this project and demonstrated that they are comparable to atmospheric $\Delta^{14}CO_2$ measurements. I now investigate atmospheric $\Delta^{14}CO_2$ measurement comparability of different groups, through analysing results of atmospheric $\Delta^{14}CO_2$ intercomparison activities in context of different laboratory sampling and measurement procedures. A number of intercomparison activities have been conducted but not all laboratories have participated in all intercomparison activities. As yet, there has been no effort to combine individual intercomparison activities together and evaluate offsets between laboratories. I report on new intercomparisons performed as part of this thesis, and compile these alongside all existing atmospheric $\Delta^{14}CO_2$ intercomparison activities, to evaluate interlaboratory offsets. I also use these existing intercomparisons as well as within laboratory studies to present some possible explanations for the observed offsets and possible ways to reduce these offsets in the future.

Having quantified interlaboratory offsets, I present a harmonised atmospheric $\Delta^{14}CO_2$ dataset for the Southern Hemisphere, combining data from different groups and accounting for identified offsets. This allows me to investigate atmospheric $\Delta^{14}CO_2$ over the Southern Ocean using the new tree ring $\Delta^{14}CO_2$ records from this project alongside the harmonised atmospheric $\Delta^{14}CO_2$ dataset (Chapter 7).

6.1 Introduction

Combining modern atmospheric $\Delta^{14}CO_2$ measurements from different groups into a harmonised $\Delta^{14}CO_2$ dataset is useful for a wide range of applications, including age calibration, atmospheric and ocean circulation/exchange, and investigating the carbon cycle and associated model forcing (e.g., Wanninkhof et al., 2009; Hua et al., 2013; Graven et al., 2017; Section 2.2). We strive to investigate small signals and differences, including precise fossil fuel CO_2 detection (better than 1 ppm CO_2), subtle $\Delta^{14}CO_2$ annual and seasonal cycles and background spatial gradients of ~5 ‰, particularly in the Southern Hemisphere (e.g., Turnbull et al., 2006; Turnbull et al., 2007; Levin et al., 2010; Graven et al., 2012b). Atmospheric $\Delta^{14}CO_2$ in the Southern Hemisphere is sensitive to the upwelling of 'old' ^{14}C-depleted water at high southern latitudes, such that atmospheric $\Delta^{14}CO_2$ could help understand variability of the Southern Ocean carbon sink in recent decades (Graven et al., 2012a; Section 2.2.6). The Southern Hemisphere has limited atmospheric $\Delta^{14}CO_2$ in measurements both in space and time, thus a harmonised dataset could play an important role in helping to accurately analyse the small signals of interest.

Identification of these offsets is becoming increasingly important, with high-precision atmospheric $\Delta^{14}CO_2$ measurement uncertainties now below 2 ‰, whilst small $\Delta^{14}CO_2$ gradients are observed with atmospheric $\Delta^{14}CO_2$ slowly decreasing (e.g., Graven et al., 2007; Turnbull et al., 2007; Levin et al., 2010; Graven et al., 2012b; Turnbull et al., 2015). Such $\Delta^{14}CO_2$ signals are similar to the uncertainty achieved with high-precision measurements, highlighting both the importance of laboratories working towards high-precision measurement alongside quantifying interlaboratory offsets, ultimately seeking to reduce

these offsets to enable accurate identification of atmospheric $\Delta^{14}CO_2$ variability (e.g., Turnbull et al., 2007; Turnbull et al., 2013; Turnbull et al., 2015).

The most recent World Meteorological Organisation – Global Atmospheric Watch (WMO-GAW) Greenhouse Gas Measurement Techniques (GGMT) guidelines set an interlaboratory compatibility goal for $\Delta^{14}CO_2$ of 0.5 ‰ (WMO, 2020). Note that this value is a measure of the averaged deviation between laboratories, i.e., systematic bias across comparable measurements, and not individual sample uncertainties, which can, and typically will be, larger than this value. Interlaboratory offsets are the systematic bias observed between laboratories. This WMO-GAW goal reflects the precision and accuracy of atmospheric $\Delta^{14}CO_2$ measurements required to investigate subtle $\Delta^{14}CO_2$ gradients, and further highlights the importance of ongoing efforts to achieve high-precision measurement and activities to determine interlaboratory comparability (e.g., Turnbull et al., 2007; Miller et al., 2013; Turnbull et al., 2015). We therefore want to determine offsets at the sub-permil level to account for systematic bias and ensure that observed atmospheric $\Delta^{14}CO_2$ variability is not an artefact of interlaboratory offsets. The WMO-GAW $\Delta^{14}CO_2$ compatibility goal is ambitious, but it has been demonstrated that this is achievable in isolated cases (Turnbull et al., 2007; Graven et al., 2013; Hammer et al., 2016). However, larger scale $\Delta^{14}CO_2$ intercomparison activities are merely approaching this goal within a few permil range (Miller et al., 2013; Hammer et al., 2016). This demonstrates that further work to quantify, understand and minimise interlaboratory offsets is crucial for ongoing atmospheric $\Delta^{14}CO_2$ investigations.

A number of intercomparison activities have been conducted within the atmospheric $\Delta^{14}CO_2$ community (e.g., Graven et al 2013; Miller et al 2013; Turnbull et al 2015; Hammer et al 2016). A number of broader international ^{14}C intercomparison exercises have also been regularly conducted, however no air samples have been included in these and much higher interlaboratory offsets are observed than is useful for high-precision atmospheric $\Delta^{14}CO_2$ measurements, therefore they are not included in this analysis.

Compilations of direct atmospheric and tree ring derived background $\Delta^{14}CO_2$ measurements from selected groups have been made available for use as age calibration and model boundary conditions (e.g., Hua et al., 2013; Graven et al., 2017). The compilation of Hua et al. (2013) provides data for 1950 – 2010 regional ^{14}C calibration curves and models, including the use of tree ring $\Delta^{14}CO_2$ records to supplement the lack of atmospheric $\Delta^{14}CO_2$ records in the Southern Hemisphere. Atmospheric $\Delta^{14}CO_2$ records used included data from the Heidelberg Network, Manning et al., 1990, and Graven et al., 2012(b), alongside tree ring data (Hua et al., 2000; 2003; 2012). Interlaboratory offsets were not considered in this study that was primarily interested in radiocarbon age calibration, for which slightly lower precision is sufficient. Graven et al., (2017) produced a complication of $\Delta^{14}CO_2$ (and $\delta^{13}C$) for 1850 – 2015, seeking to promote the use of carbon isotopes in modelling, specifically CMIP6, which contributes to the work of the International Panel on Climate Change (IPCC). Direct atmospheric $\Delta^{14}CO_2$ measurements included are primarily from the Heidelberg Network (Section 6.2.3), thereby offering good global coverage whilst not requiring identification of interlaboratory offsets. A correction of -4 is applied to $\Delta^{14}CO_2$ data from the Rafter Radiocarbon Laboratory (Section 6.2.1), following results of Manning and Melhuish (1994).

Therefore, this study provides the first quantification of interlaboratory offsets by assessing results of published atmospheric $\Delta^{14}CO_2$ intercomparison activities and new intercomparison measurements, before considering these in context of different laboratory sampling and measurement procedures. As a result of this investigation a modern harmonised atmospheric $\Delta^{14}CO_2$ dataset is developed for the Southern Hemisphere, combining background $\Delta^{14}CO_2$ data from different groups and accounting for offsets accordingly.

6.2 Measurement Details of Groups with Existing Atmospheric $\Delta^{14}CO_2$ Records in the Southern Hemisphere

Table 6.1: Details, including latitude (Lat, °N), longitude (Lon, °E) and altitude (Alt, masl), of atmospheric $\Delta^{14}CO_2$ records for the Southern Hemisphere for 1985 – 2015: Heidelberg (Levin et al., 2010); INSTAAR/UCI (Lindsay, 2016); RRL (Turnbull et al., 2017); SIO/LLNL (Graven et al., 2012b); SIO/CIO (Meijer et al., 2006); further references in text. All measurements were made by AMS except for early RRL measurements and Heidelberg. DRP data is not publicly available. Two records from the Northern Hemisphere are included (VER/JFJ and NWR (Lehman et al., 2013)) as these are also used in this analysis.

Group	Site	Code	Lat	Lon	Alt	Year
Heidelberg	Vermunt, Austria	VER	47	10	1800	1959 – 1986
	Jungfraujoch, Germany	JFJ	47	8	3450	1986 – 2008
	Cape Grim, Tasmania	CGO	-41	145	104	1987 – 2006
	Macquarie Island	MCQ	-55	159	20	1999 – 2004
	Neumayer	GVN	-71	8	30	1938 – 2008
INSTAAR/	Niwot Ridge, USA	NWR	40	-106	3475	2003 – present
UCI	Drake Passage	DRP	-59	-174	10	2006 – 2012
RRL	Baring Head, NZ	BHD	-41	174	80	1954 – present
SIO/LLNL	Cape Matatula, Samoa	SAM	-14	-171	30	2001 – 2007
	Palmer Station, Antarctica	PSA	-65	-64	10	2005 – 2007
	South Pole, Antarctica	SPO	-90	n/a	2810	1999 – 2007
SIO/CIO	South Pole, Antarctica	SPO	‘’	‘’	‘’	1985 – 1991
RRL tree	Haast Beach, NZ	NZ-44S	-44	169		1982 – 2015
rings	Oreti Beach, NZ	NZ-46S	-46	168		1990 – 2015
	Campbell Island, NZ	NZ-53S	-53	169		1980 – 2015
	Tortel, Chile	CH-48S	-48	-74		1985 – 2015
	Seno Skyrig, Chile	CH-53S	-53	-72		1988 – 2015
	Isla Navarino, Chile	CH-55S	-55	-67		1985 – 2015

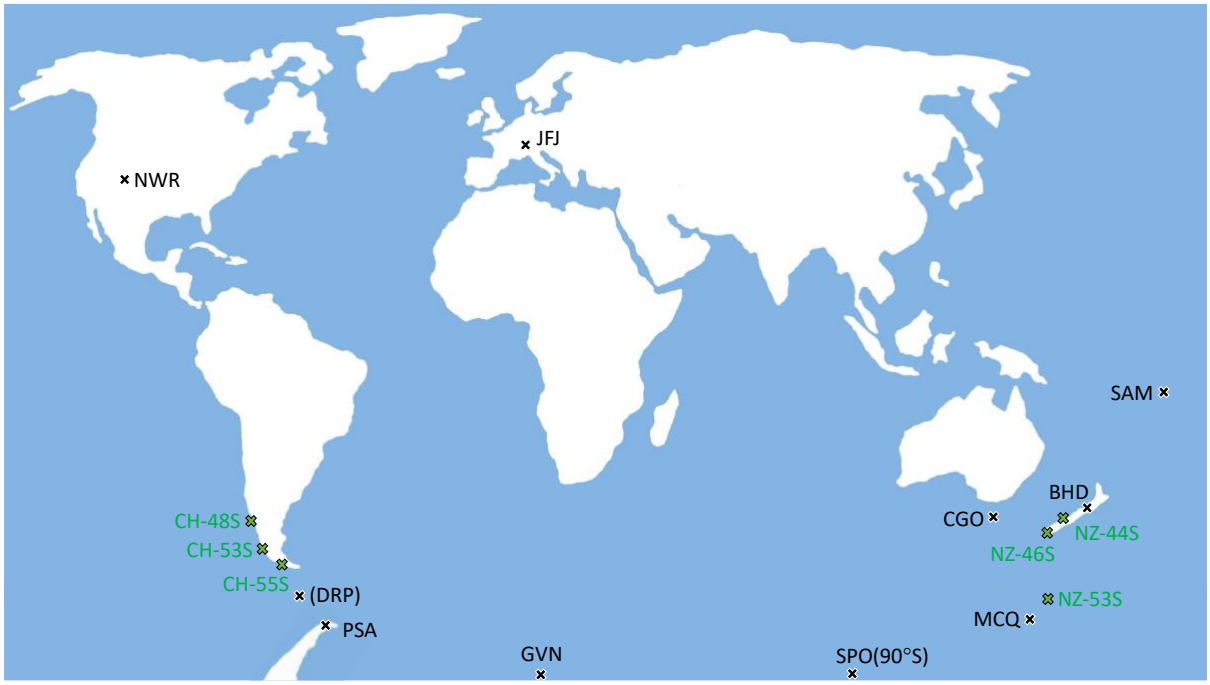

Figure 6.1: Map of sampling sites with atmospheric $\Delta^{14}CO_2$ records (black) and tree ring records (green) included in this study: (VER/)JFJ, CGO, MCQ, GVN (Levin et al., 2010); NWR (Lehman et al., 2013); DRP (Lindsay, 2016); SAM, PSA, SPO (Graven et al., 2012(b)); SPO (Meijer et al., 2006); BHD (Turnbull et al., 2017); and tree ring records from this project. Further details in Table 6.1 and in text.

In this section we provide a summary of atmospheric $\Delta^{14}CO_2$ measurements in the Southern Hemisphere from different groups. A number of $\Delta^{14}CO_2$ records from the Northern Hemisphere that are used in analysis are also included (Table 6.1). We include details of sampling, preparation and measurement procedures to provide context for the analysis of interlaboratory offsets in this study.

Atmospheric CO_2 is collected through in situ absorption of atmospheric CO_2 into sodium hydroxide (NaOH) solution (e.g., Levin et al., 1980; Currie et al., 2011), or collection of flasks of whole air (e.g., Graven et al., 2007; Turnbull et al., 2007), although methodology varies between groups. Collection into NaOH provides integrated CO_2 samples for the duration of the solution exposure, typically ~biweekly (Rafter, 1955), thereby capturing atmospheric CO_2 from all wind directions, or restricted by conditions e.g., wind direction/speed or aerosols (e.g., Levin et al., 2010; Currie et al., 2011). Flask samples are collected by opening

evacuated flasks to the atmosphere, or filling using a pump. This is ideally conducted at a given time/day under clean air conditions (e.g., Turnbull et al., 2007; Graven et al., 2012c; Stephens et al., 2013; Turnbull et al., 2017). This is not always possible, thus where non-clean air samples are collected, they can be flagged and removed from the clean air background record (e.g., Turnbull et al., 2007).

Following sample collection using NaOH or flasks, CO_2 is subsequently evolved or extracted, respectively, before graphitisation and ^{14}C measurement through accelerator mass spectrometry (AMS), or gas counting of CO (e.g., Kromer and Munnich, 1992; Levin et al., 1980; Meijer et al., 2006; Graven et al., 2007; Turnbull et al., 2007; Turnbull et al., 2015). (Graphitisation and AMS measurement are detailed in Chapter 4.)

Atmospheric ^{14}C results are typically reported as $\Delta^{14}CO_2$ (i.e., $\Delta^{14}C$, since ^{14}C rapidly oxidizes to ^{14}CO and $^{14}CO_2$), which places the $^{14}C/^{12}C$ ratio of the sample in context of NBS oxalic acid (OxI) primary standard material (NIST standard reference material SRM4990B), with corrections for mass-dependent fractionation and decay included (Olsson, 1970; Stuiver and Polach, 1977; Section 2.2). Although OxI defines the relative ^{14}C scale, some laboratories use oxalic acid II (OxII) or other material, such as control tanks, instead of OxI as their primary (working) standard (e.g., Section 6.2.4). In that case, the working standard must be characterised against OxI (e.g., Stuiver, 1983; Graven, 2008). The primary standard material, whether OxI or otherwise, is subject to combustion (except if an air standard), gas counting, or graphitisation and AMS measurement alongside samples (e.g., Graven et al., 2007; Graven, 2008; Turnbull et al., 2007; Baisden et al., 2013; Turnbull et al., 2015). Measurement of $\delta^{13}C$ for the fractionation correction is either done by applying the $\delta^{13}C$ determined from isotope-ratio mass-spectrometry (IRMS) measurement on CO_2 gas to the ^{14}C results, or from an online ^{13}C measurement within the AMS system which thereby also accounts for fractionation during graphitisation or measurement (e.g., Levin et al., 1985; Meijer et al., 2006; Graven et al., 2007; Turnbull et al., 2007; Graven, 2008; Turnbull et al., 2017). Processing blank material, i.e., ^{14}C-free air, is prepared alongside samples to assess contamination introduced through sample preparation (e.g. Meijer et al., 2006; Turnbull et al., 2015). A blank correction is thus applied, but with insignificant effects on modern $\Delta^{14}CO_2$

results (e.g., Donahue et al., 1990; Turnbull et al., 2007). However, blank material provides useful validation of minimal preparation and measurement contamination.

AMS ^{14}C measurement is typically conducted with the primary standard measured alongside samples in a measurement wheel, used to standardise results. Gas counting requires regular careful calibration with periodic primary standard measurement and interpolation. Precision of 1.2 ‰ has long been achievable with gas counting although time consuming and using ~15 m^3 air (e.g., Tans et al., 1979), but typical precisions reported are 2 – 4 ‰ (e.g. Levin et al., 2010). However, AMS developments now allow ^{14}C measurement of 2 – 5 L whole air flask samples, with up to 1.6 ‰ precision but often 2 – 5 ‰ (e.g., Graven et al., 2007; Turnbull et al., 2007; Turnbull et al., 2017; pers. Comm. J Turnbull). This can be applied to existing air sampling networks, thereby also allowing comparison of $\Delta^{14}CO_2$ with other atmospheric species measured in the same flasks.

In addition to primary standard and processing blank preparation, further quality control material is routinely prepared and analysed alongside samples, i.e., control tanks, derived from whole air, or repeat air samples, such that long-term within-laboratory repeatability can be assessed (e.g., Graven et al., 2007; Turnbull et al., 2007; Turnbull et al., 2015). Control tanks (elsewhere referred to as reference cylinders, secondary standards and target tanks) or alternatives, comprise an important part of quality control checks typically conducted within laboratories to assess variability introduced through sample preparation and measurement. Therefore the long-term repeatability of control tanks also provides a good constraint on measurement precision rather than individual sample measurement precision derived from counting statistics (Graven et al., 2007; Turnbull et al., 2007; Lehman et al., 2013). Two control tanks are often used: one ambient $\Delta^{14}CO_2$ control tank, and a further ambient control tank spiked with ^{14}C-free-CO_2; thereby spanning a modern atmospheric $\Delta^{14}CO_2$ range (e.g., Graven, 2008; Lehman et al., 2013; Turnbull et al., 2017).

6.2.1 RRL

Since 1954, background atmospheric $\Delta^{14}CO_2$ measurements have been made of clean air near Wellington, New Zealand, with ongoing integrated ~biweekly NaOH samples (Table 6.1) (Rafter, 1955; Manning et al., 1990; Currie et al., 2011; Turnbull et al., 2017). Prior to 1988 samples were collected at Makara, on the west coast from Wellington (MAK, 41.25 °S, 174.69 °E, 300 masl (metres above mean sea level); Rafter, 1955; Manning et al., 1990; Currie et al., 2011), after which samples are from Baring Head, east of Wellington (BHD, 41.07 °S, 174.15 °E, 80 masl). Both sites predominantly observe clean air, with minimal influence from Wellington, thereby considering all these samples together as the BHD atmospheric $\Delta^{14}CO_2$ record. Since 2012, NaOH samples are also supplemented by whole air flask collection, as well as tree ring samples (Turnbull et al., 2017) (differences in sampling methods are discussed in Section 6.7.1).

Sampling, preparation and ^{14}C measurement is conducted as a collaboration between the National Institute of Water and Atmospheric Research (NIWA) and the Rafter Radiocarbon Laboratory (RRL) of GNS Science, and their predecessor the Department of Scientific and Industrial Research (DSIR, NZ) with a range of methodologies used through the sampling history of the BHD atmospheric $\Delta^{14}CO_2$ record. The current graphitisation system at RRL was installed in 2012, which replaced an older system employed since the 1980s (Lowe and Judd, 1997; Turnbull et al., 2015). ^{14}C measurement was through gas counting (also known as low-level counting) until 1995 (Manning et al., 1990; Currie et al., 2011), after which measurement has been using AMS (Currie et al., 2011; Turnbull et al., 2017). The large sample size necessary for gas counting required trays of NaOH for atmospheric sampling prior to 1995 (~5 L), after which smaller bottles of NaOH (~250 mL) have been used for AMS. It has been demonstrated that these sampling methods are equivalent (Currie et al., 2011). Although pumping air through NaOH solution can reduce fractionation and more tightly constrain the sampling period, RRL continue to use static NaOH for consistency.

OxI is used as the primary standard, prepared through multiple different procedures: sealed tube combustion, elemental analyser combustion and flasks of OxI prepared from a single

large combustion (Turnbull et al., 2015; pers. Comm. J Turnbull). From 1995 to 2005, $\delta^{13}C$ was determined through IRMS, after which online $\delta^{13}C$ measurement was introduced, with better long-term repeatability observed (Zondervan et al., 2015; Turnbull et al., 2017; Section 6.4.5).

A range of blank and control tank aliquots are routinely prepared and measured alongside samples (Turnbull et al., 2015). Two ^{14}C-free CO_2 tanks (one each housed at RRL and INSTAAR (see Section 6.2.6)), are employed to assess the overall processing blank, whilst a further blank (kapuni CO_2) isolates effects of graphitisation and AMS measurement. In addition to RRL ambient and ^{14}C-free spiked control tank measurements, aliquots of INSTAAR control tanks are regularly analysed at RRL (Lehman et al., 2013; Turnbull et al., 2015; Section 6.4.4). RRL report measurement precision as a combination of AMS measurement uncertainty and long-term repeatability, including sample preparation and AMS between-wheel variability (Turnbull et al., 2015). High-precision of 1.8 ‰ was previously demonstrated at RRL (Turnbull et al., 2015). Recently, two flasks of CO_2 derived from large combustions of OxI (sufficient for several hundred aliquots each) were introduced, replacing much smaller/individual combustions, and yielding higher precision of 1.6 ‰ (pers. Comm. J Turnbull). (These different primary standard preparation procedures are discussed in more detail in Section 6.7.3.)

6.2.2 RRL Tree Rings

Tree ring records were developed for this thesis and are described in detail in the preceding chapters. In addition, tree ring samples from Baring Head and Eastbourne, 15 km from Baring Head were previously measured as additional validation of the BHD atmospheric record (Turnbull et al., 2017; Section 6.2.1). These measurements followed the same methodology as described for the tree rings in this thesis.

6.2.3 Heidelberg

In 1955 the Heidelberg Radiocarbon Laboratory (Heidelberg) began atmospheric ^{14}C measurements using NaOH absorption from a number of sites across Europe, starting with Vermunt, Austria (VER, 47.07 °N, 9.57 °E, 1800 masl, 1959 – 1986) established in 1959 (Table 6.1) (Levin et al., 1985). Measurements continued there until 1986, when the site was moved to Jungfraujoch, Germany (JFJ, 46.73 °N, 7.98 °E, 3450 masl, 1986 – 2008) and is ongoing (Levin et al., 2010). These sites are at similar latitudes and both observe clean background air of continental Europe with minimal local influence so are combined into a single VER/JFJ record (Levin et al., 1985; Levin and Kromer, 2004). The VER/JFJ atmospheric $\Delta^{14}CO_2$ record is one of a number of records from the Northern Hemisphere included in this study, to allow comparison with atmospheric $\Delta^{14}CO_2$ in the Southern Hemisphere. Specifically, VER/JFJ is selected because of its length and its compatibility with other sites of the Heidelberg Network in the Southern Hemisphere.

The Heidelberg $\Delta^{14}CO_2$ Sampling Network has varied over time, with good global coverage in recent decades, including the Southern Hemisphere: Cape Grim, Australia (CGO, 40.68 °S, 144.68 °E, 104 masl, 1987 – 2006), Macquarie Island, Subantarctic Island of Australia (MCQ, 54.50 °S, 158.93 °E, 20 masl, 1999 – 2004) and Neumayer Station, Antarctica (GVN, 70.65 °S, 8.25 °E, 30 masl, 1983 – 2008) (Table 6.1) (Levin et al., 2010). Although measurement continues at some of these Heidelberg sites, the data has yet to be published, with some additional data incorporated into the CMIP ^{14}C forcing dataset (Graven et al., 2017). CGO is at a similar latitude to BHD (of RRL, see above), and has been treated as similar to BHD by several authors (Currie et al., 2011; Turnbull et al., 2017) although no explicit intercomparison has yet been performed.

Although the Heidelberg Network has varied, sampling and measurement procedures have remained largely consistent over the years, including integrated weekly/biweekly pumped NaOH samples and measurement through gas counting (e.g., Kromer and Munnich, 1992; Levin et al., 1980; Levin et al., 1985; Levin and Hesshaimer, 2000; Levin et al., 2008; Levin et al., 2010; Hammer et al., 2016). Pumping air through a sampling system of NaOH allows use

of a smaller volume of NaOH than would otherwise be required for static absorption (e.g., Levin et al., 1980). Pumped NaOH also allows selective sampling under specified conditions, e.g., wind direction/speed at MCQ, and aerosol monitoring at GVN (Levin et al., 2010).

Mass spectrometry is used for $\delta^{13}C$, with $\Delta^{14}CO_2$ results reported relative to OxI (Levin et al., 1985; Levin and Kromer, 2004; Levin et al., 2010). Increasing sample size and extending counting time has led to increased precision of ~2 ‰ or better since 2000, before which precision was ~2 – 4 ‰ (Levin et al., 2010).

6.2.4 SIO/LLNL

Flask samples are collected at ~monthly intervals as part of the Scripps Institution of Oceanography (SIO) CO_2 Program, which are measured for CO_2 mole fraction, before cryogenic extraction of CO_2 and storage into glass breakseals (e.g., Graven et al., 2007; Graven, 2008; Keeling at al., 2012). A subset of these samples have been analysed for $\Delta^{14}CO_2$, including a number of sites in the Southern Hemisphere: Cape Matatula, Samoa (SAM, 14.25 °S, 170.57 °W, 30 masl, 2001 – 2007), Palmer Station, Antarctica (PSA, 64.92 °S, 64.00 °W, 10 masl, 2005 – 2007) and South Pole, Antarctica (SPO, 89.98 °S, 24.80 °W, 2810 masl, 1999 – 2007) (Table 6.1) (Graven, 2008; Graven et al., 2012b,c). PSA is part of the SIO Oxygen (O_2) Program that uses different flasks and sampling procedures to the CO_2 Program, but it is believed to be comparable (Graven, 2008; Graven et al., 2012b). A Northern Hemisphere site, namely Mauna Loa, Hawaii, (MLO, 19.53 °N, 155.58 °W, 3397 masl, 2001 – 2007) is also included in this study for analysis purposes (Graven et al., 2012b).

Flask samples from all sites were extracted at SIO shortly after collection, but with subsequent graphitisation and AMS measurement at Laurence Livermore National Laboratory (LLNL) between 2003 and 2009 for all samples, with random batch processing (Graven et al., 2007; Graven, 2008; Graven et al., 2012c). OxI primary standard ^{14}C measurements were found to have larger associated uncertainties than corresponding routine control tank ^{14}C measurements (Graven et al., 2007; Graven, 2008). Therefore, seeking the highest feasible precision, one of their two control tanks derived from whole air,

with similar $\delta^{13}C$ and $\Delta^{14}CO_2$ to samples, was largely used in measurement standardisation (Graven, 2008). The second control tank, whole air spiked with ^{14}C-free CO_2, thereby remaining as a routine quality control tank. In some early measurements prior to the introduction of control tanks, a more complex alternative standardisation was applied, derived through grouping OxI measurements (Graven, 2008). Blank correction is also determined for modern CO_2 measured at LLNL (Brown and Southon, 1997; Graven, 2008).

At the time of these measurements ^{12}C was not measured online at LLNL, instead $\delta^{13}C$ was obtained by IRMS on an aliquot of the same CO_2 (Graven et al., 2012c). Therefore fractionation during graphitisation or AMS measurement is not accounted for, including standardisation using OxI, which is of characteristically different $\delta^{13}C$ content to atmospheric CO_2 samples. Reported measurement uncertainties are determined from the long-term repeatability of control tanks (Graven et al., 2007; Graven, 2008).

6.2.5 SIO/CIO

SIO-extracted samples from SPO (as above) for 1985 – 1991, were together graphitised and measured for ^{14}C with AMS at the University of Groningen Centre for Isotope Research (CIO) (Aerts-Bijma et al., 1997; Van der Plicht et al., 2000; Meijer et al., 2006). Alongside samples, each AMS measurement wheel contained OxI primary standard, IAEA-C6 (ANU sucrose) control material and background Rommenholler CO_2 gas (Meijer et al., 2006). These were together used, with $\delta^{13}C$ IRMS measurement, to determine $\Delta^{14}CO_2$ (Roeloffzen et al., 1991; Meijer et al., 2006). Reported measurement uncertainty (~±3 ‰) is determined from a combination of statistical/counting uncertainty and variability of corresponding background and OxI measurements, also including $\delta^{13}C$ (Meijer et al., 2006).

6.2.6 INSTAAR/UCI

Collection of flask samples from Niwot Ridge, USA (NWR, 40.05 °N, 105.58 °W, 3475 masl, 2003 – present) has long been conducted by the National Oceanic and Atmospheric Administration Earth System Research Laboratory (NOAA/ESRL; Schnell et al., 2004). The

capability for atmospheric $\Delta^{14}CO_2$ measurement of these flask samples was established in 2003 (Turnbull et al., 2007). This was started in 2003 as a North American long-term atmospheric $\Delta^{14}CO_2$ observation (background) site, seeking to provide increased long-term global coverage. The NWR atmospheric $\Delta^{14}CO_2$ record is an additional Northern Hemisphere site included in this study, because the University of Colorado Institute for Arctic and Alpine Research (INSTAAR) has participated in many atmospheric $\Delta^{14}CO_2$ intercomparison activities.

More importantly for this study, flask samples have been collected ~biweekly in the Drake Passage since 2006 (DRP, 59 °S, 64.69 °W, 10 masl, 2006 – 2012), but data has been published only in a PhD thesis and is not publicly available (Lindsay, 2016). The DRP atmospheric $\Delta^{14}CO_2$ record will contribute additional invaluable measurements to the sparse $\Delta^{14}CO_2$ data of the Southern Hemisphere.

Sample preparation, including CO_2 extraction and graphitisation is at INSTAAR, with subsequent AMS measurement at the University of California, Irvine (UCI) (Turnbull et al., 2007). Early AMS measurement prior to June 2004 was at RRL, however we do not include those measurements in this study, because the measurements are not exactly comparable with the UCI measurements and are not directly relevant to this study. For INSTAAR/UCI, OxI is used as the primary standard, either prepared through a single flask or combustions divided into multiple aliquots, with a tank of ^{14}C-free air as the blank material, and OxII and control tank aliquots prepared for quality control, all of which are prepared and measured alongside samples. Following AMS measurement, corrections for blank measurement and isotopic fractionation are conducted, using AMS online $\delta^{13}C$. Assigned sample precision is determined as the larger of either AMS reported uncertainty or long-term repeatability, typically ~1.8 ‰ (Turnbull 2007). AMS reported uncertainty incorporates the statistical/counting uncertainty of the sample and the variability of primary standard (OxI) targets within the measurement, whilst the long-term repeatability is determined from routine control tank measurements.

6.2.7 Other Atmospheric $\Delta^{14}CO_2$ Measurements in the Southern Hemisphere

In this study we investigate modern atmospheric $\Delta^{14}CO_2$ measurements of groups with high-precision and ongoing measurements: seeking to develop a harmonised $\Delta^{14}CO_2$ dataset for the Southern Hemisphere and understand interlaboratory offsets, ultimately working towards the WMO-GAW compatibility goal of 0.5 ‰. We therefore do not consider atmospheric $\Delta^{14}CO_2$ records that span the bomb period and have since ceased, e.g., Manning et al., 1990; Nydal and Lovseth, 1983. Similarly, we do not consider other tree ring records from this period (e.g., Hua et al., 2000; Hua et al., 2013; Turney et al., 2018). However high-precision ^{14}C measurement and participation in intercomparison activities is encouraged, such that such additional data could be included in future iterations of a harmonised atmospheric $\Delta^{14}CO_2$ dataset.

Automatic flask sampling has been conducted by the National Institute for Environmental Studies (NIES, Japan) on a container ship with a Japan – Australia transect since 1992 (Kitagawa et al., 2004). A subset of samples spanning 10 – 15 °N and 23 – 28 °S during 1994 – 2002 was analysed for $\Delta^{14}CO_2$ using the NIES-TERRA AMS (Nakamura et al., 2004; Kobayashi et al., 2007). In this study we do not include NIES due to no recent published data and limited intercomparison data available (Miller et al., 2013).

6.3 Methodology

A range of recent Southern Hemisphere background atmospheric $\Delta^{14}CO_2$ records exist from a number of different groups and associated laboratories, as detailed above (Table 6.1) (e.g., Meijer et al., 2006; Levin et al., 2010; Graven et al., 2012; Turnbull et al., 2017). In this study $\Delta^{14}CO_2$ measurement comparability is investigated for these groups through analysing results from atmospheric $\Delta^{14}CO_2$ intercomparison activities. There is naturally a focus on Heidelberg, RRL and SIO/LLNL, as groups with multiple/long relevant atmospheric $\Delta^{14}CO_2$ records and good participation in intercomparison activities. Whilst INSTAAR/UCI is also included in this study for a number of reasons, this indirectly allows the incorporation of the DRP $\Delta^{14}CO_2$ record into the harmonised $\Delta^{14}CO_2$ C dataset once available.

Two background Northern Hemisphere $\Delta^{14}CO_2$ records are also included in this study, namely VER/JFJ and NWR (Section 6.2). Their inclusion is for a number of reasons, including allowing comparison of the Southern Hemisphere with the Northern Hemisphere. These sites also enable intercomparison of different groups, because they are mid-latitude Northern Hemisphere sites that we expect to be of similar atmospheric $\Delta^{14}CO_2$ (Section 6.4.6).

In this study we develop a first iteration of a harmonised atmospheric $\Delta^{14}CO_2$ dataset for the Southern Hemisphere and associated interlaboratory offsets. The scope of this is limited by the atmospheric $\Delta^{14}CO_2$ intercomparison results available, and thus only a single offset for each laboratory is determined, i.e., no time-dependency of interlaboratory offsets is investigated. Further intercomparison activities, e.g., ongoing rounds of whole air intercomparison (Miller et al., 2013; Section 6.4.1) will enable investigation of temporal variability, and thereby refinement of interlaboratory offsets.

Although interlaboratory offsets may vary through time with methodology developments, such details are not necessarily published. In such instances, laboratories will typically conduct testing to ensure that any changes do not affect results, and thus combine atmospheric $\Delta^{14}CO_2$ measurements (e.g., Turnbull et al., 2010; Turnbull et al., 2015). Quality control checks within laboratories assess ongoing measurements, therefore where changes in results are observed, suitable adjustments can be made (e.g., Turnbull et al., 2015; Turnbull et al., 2017). Elsewhere the possibility of such variability is avoided through largely consistent methodology (e.g., Levin et al 1980; Levin et al 2010). In this study we therefore seek to identify systematic bias between laboratories and assume within-laboratory consistency. A limitations of this study is that no time-dependent changes in interlaboratory offsets are considered due to insufficient data.

Each intercomparison activity involves a different subset of participating laboratories. Therefore assessing results relative to the mean of a given study is dependent on participating laboratories in that study. Thus we examine results relative to a reference

laboratory, choosing RRL as that reference laboratory against which other laboratories are compared. This is not to say that RRL results are 'correct' or 'absolute', but rather provides a consistent reference point for the intercomparison of laboratories.

RRL is selected as the reference laboratory for a number of reasons. We (RRL) participate in a range of atmospheric $\Delta^{14}CO_2$ intercomparison activities (e.g., Miller et al., 2013; Turnbull et al., 2015; Hammer et al., 2016). Further to this, it has been demonstrated that RRL now achieves high-precision (better than 2 ‰) ^{14}C measurement (Turnbull et al., 2015, similarly to e.g., Graven et al., 2007; Lehman et al., 2013). Our BHD atmospheric $\Delta^{14}CO_2$ record is not only the longest such record but is also representative of mid-latitude clean background air in the Southern Hemisphere, and thus particularly relevant to this study.

In this study we therefore quantify laboratory offsets from RRL, as the reference laboratory, before adjusting data as necessary to combine with RRL. As a result of this investigation a modern atmospheric $\Delta^{14}CO_2$ dataset is developed for the Southern Hemisphere, combining data from different groups and accounting for offsets accordingly. The same groups have atmospheric $\Delta^{14}CO_2$ records for the Northern Hemisphere that could be harmonised using the same laboratory offset adjustments.

6.4 Atmospheric $\Delta^{14}CO_2$ Measurement Intercomparison Activities

Here we consider atmospheric $\Delta^{14}CO_2$ intercomparison activities, seeking to quantify and understand interlaboratory offsets.

6.4.1 Whole Air $\Delta^{14}CO_2$ Intercomparison

A long-term intercomparison of $\Delta^{14}CO_2$ AMS measurement of whole air samples is ongoing, with results of the first three rounds published (Miller et al., 2013). This intercomparison assesses interlaboratory differences alongside within-laboratory longer term repeatability. All AMS laboratories with background atmospheric $\Delta^{14}CO_2$ measurements in the Southern Hemisphere participate in this intercomparison activity, although RRL only participate in

later rounds that have yet to be published (Tables 6.1 & 6.2) (Miller et al., 2013; Turnbull et al., 2015). The Heidelberg Laboratory is unable to participate, as a non-AMS laboratory, thereby unable to measure the $\Delta^{14}CO_2$ content of small whole air flasks (Miller et al., 2013; Hammer et al., 2016).

The samples used for ongoing intercomparison are FARI-A and FARI-B; whole air tanks with ambient $\Delta^{14}CO_2$ air collected at Niwot Ridge, Colorado, USA in 2005/2006 (FARI-A), and ambient air spiked with ^{14}C-free fossil-fuel-derived CO_2 (FARI-B) (Miller et al., 2013). In such intercomparison activities it is typical to use ambient and spiked $\Delta^{14}CO_2$ samples such that results span a range of atmospheric $\Delta^{14}CO_2$ observed currently at background sites, with globally decreasing atmospheric $\Delta^{14}CO_2$ and polluted sites. Flasks from participating groups are filled from the master tank (i.e., FARI-A or FARI-B), alongside a NOAA/ESRL flask of which the $\delta^{13}C$ is measured to check for fractionation with the master tanks (Miller et al., 2013). No significant fractionation effects, assumed to be mass-dependent fractionation, are observed during flask filling: measurements by NOAA/ESRL and other laboratories demonstrate effects of less than 0.1 on average, which should theoretically be corrected by $\delta^{13}C$ normalisation following measurement.

Of the first three rounds presented by Miller et al., (2013), three groups were com- parable within 1 ‰ for ambient $\Delta^{14}CO_2$ air (FARI-A), whilst four groups were comparable within 2 ‰ for the span of ambient/depleted $\Delta^{14}CO_2$ air (i.e., FARI-A – FARI-B). For FARI-A and FARI-B the mean (with associated uncertainty) of all groups overlaps with the overall mean, which suggests that all results are relatively consistent on a large scale.

6.4.2 Pure CO_2 $\Delta^{14}CO_2$ Intercomparison

The Heidelberg Laboratory has a large atmospheric $\Delta^{14}CO_2$ sampling network, but as a non-AMS laboratory is thus not included in the ongoing intercomparison of $\Delta^{14}CO_2$ in whole air, because much larger samples would be required for gas counting. A separate pure CO_2 intercomparison was conducted to assess the Heidelberg Laboratory in context of AMS

laboratories, thereby also isolating variability associated with graphitisation and AMS analysis, from extraction (Hammer et al., 2016).

Five pure CO_2 samples were measured through gas counting at the Heidelberg Laboratory and then split volumetrically into 1 mgC aliquots in breakseals (Hammer et al., 2016). One of these five samples was in fact OxI primary standard material, but was treated as an unknown. 20 aliquots of each sample were distributed to the 12 participating AMS laboratories, with results remaining anonymous. The five samples selected for this intercomparison spanned a $\delta^{13}C$ range (-22.25 - -8.38 ‰) in addition to a modern $\Delta^{14}CO_2$ range (9.6 – 40.4 ‰).

The Heidelberg Laboratory was found to have an average offset of -0.3 ±0.5 ‰ from the AMS ^{14}C mean (Hammer et al., 2016). This demonstrates that the gas counting of Heidelberg Laboratory is of comparable precision and accuracy to AMS measurement techniques and is broadly consistent with the WMO-GAW compatibility goal of 0.5 ‰.

However, variability amongst participating AMS laboratories is largely within ±3 ‰ of consensus, much larger than the WMO-GAW compatibility goal. Despite the small number of measurements generating large associated uncertainties, it is clear that the interlaboratory offsets observed here are significant and remain some way off from achieving the WMO-GAW compatibility goal. For OxI (as unknown), the measurement uncertainties of most AMS laboratories overlap with the AMS mean, although in some cases this appears to be a result of the relatively large uncertainties (Hammer et al., 2016). Somewhat more variability is observed across all samples.

Further samples would be required to assess the compatibility of each participating AMS laboratory. In this pure CO_2 $\Delta^{14}CO_2$ intercomparison INSTAAR/UCI and RRL are AMS laboratories five and four respectively.

6.4.3 SIO/LLNL - UCI Co-located $\Delta^{14}CO_2$ Intercomparison

Co-located flask sampling was employed by SIO/LLNL and UCI at Point Barrow, Alaska (PTB, 71.38 °N,156.47 °W, 10 masl), including 22 sampling days over five years (Graven et al., 2013). UCI has a much longer, but unpublished atmospheric $\Delta^{14}CO_2$ record from Point Barrow. These two independent measurement programs use different flask sampling and processing techniques, such that any variability introduced was incorporated in results (Graven et al., 2007; Graven, 2008; Xu et al., 2007). Methodology associated with the SIO/LLNL PTB measurements is consistent with the other SIO/LLNL $\Delta^{14}CO_2$ records considered in this study. No significant offset was observed between programs, with an average residual of 0.2 ±0.7 ‰ of UCI compared to SIO/LLNL. Following the small offset observed, it was suggested that SIO/LLNL and UCI $\Delta^{14}CO_2$ measurements can be combined without adjustment (Graven et al., 2013). Such intercomparison activities cannot be widely conducted due to limited resources, but compliment activities such as presented by Miller et al., (2013) (Section 6.4.1).

6.4.4 INSTAAR/UCI - RRL - SIO/LLNL $\Delta^{14}CO_2$ Intercomparison

Further to the larger atmospheric $\Delta^{14}CO_2$ intercomparisons detailed above (Sections 6.4.1 & 6.4.2), LLNL and RRL have graphitised and measured large numbers of pure CO_2 aliquots of control tanks from INSTAAR/UCI (NWTstd, NWT3, NWT4; Table 6.2) (Turnbull et al., 2015). The INSTAAR-extracted aliquots are analysed at RRL, alongside a suite of urban flask samples also extracted at INSTAAR.

The control tanks have similar $\Delta^{14}CO_2$ content to atmospheric samples and are measured repeatedly within INSTAAR/UCI laboratory to monitor long-term repeatability. Here extraction is considered an unlikely source of variability (Section 6.7; Turnbull et al., 2007). It is therefore assumed that extracted samples from INSTAAR with graphitisation and measurement at LLNL and RRL are equivalent to SIO/LLNL and RRL respectively, thereby observing the same measurement offset. The comparison of INSTAAR/UCI and RRL is also

ongoing, thereby this intercomparison has much larger laboratory datasets than wider community intercomparison activities (e.g., Sections 6.4.1 & 6.4.2).

6.4.5 BHD - CGO Southern Hemisphere Mid-latitude Intercomparison

BHD and CGO are mid-latitude sites in the Southern Hemisphere where NaOH sampling for atmospheric $\Delta^{14}CO_2$ measurement is conducted by RRL and Heidelberg respectively. At similar latitudes (~41 °S), they have largely consistent $\Delta^{14}CO_2$ records that demonstrate no obvious longitudinal offset, with similar long-term trends and features (e.g., Currie et al., 2011; Turnbull et al., 2017).

In 2017 – 2018, RRL and NIWA collected a set of NaOH absorption samples at CGO, for a total of 20 samples over the two years. This data has not previously been reported. The aim was to match the sampling dates at both sites, although ultimately some sampling periods differed by a day or two. Good agreement was observed between resulting atmospheric $\Delta^{14}CO_2$ measurements of BHD and CGO over 2017 – 2018, with a mean offset of 0.0 ±0.3 ‰. This observed agreement is somewhat expected, because BHD and CGO are at similar latitudes, largely observing dynamic air masses from over the Southern Ocean. Although CGO is in close proximity to the large land mass of Australia, strong westerly winds appear to generate no clear longitudinal offset. Since no offset is observed during this time period, we therefore assume no long-term difference (on average) between atmospheric $\Delta^{14}CO_2$ at BHD and CGO.

The atmospheric $\Delta^{14}CO_2$ data for CGO from the Heidelberg Network has not yet been reported for the period of overlapping RRL BHD and CGO records in 2017 – 2018. Therefore we look to compare a common measurement period of BHD (RRL) and CGO (Heidelberg) atmospheric $\Delta^{14}CO_2$ records. We select a period when both records exist as NaOH samples, with no known problems in either record: this period is 2005 – 2008. For this period, NaOH at BHD (RRL) and CGO (Heidelberg) are in agreement with an average offset of 0.08 ±0.45‰ determined from 31 sample pairs. A previous period (1990 – 1995) when both records exist, but much of the BHD record has been substituted with flask measurements is not

considered here, as there is potential for differences due to sample method, discussed later in Section 6.7.1.

6.4.6 Northern Hemisphere Mid-latitude Intercomparison

As an alternative approach to other intercomparison activities or co-located sampling, we compare mid-latitude Northern Hemisphere sites JFJ, Switzerland (Heidelberg; VER/JFJ see Section 6.2.3) and NWR, USA (INSTAAR/UCI see Section 6.2.6) that we expect to observe similar atmospheric $\Delta^{14}CO_2$ (Turnbull et al., 2009). Both are mid-latitude Northern Hemisphere background sites (47 °N and 40 °N respectively) that observe tropospheric air, i.e., at altitude (Levin et al., 2010; Turnbull et al., 2007). We also considered two other Northern Hemisphere sites, Mt Waliguan (WLG; Turnbull et al., 2011) and Mauna Loa (MLO; Graven et al., 2012b), but WLG is a short record so the comparison is less meaningful. MLO is at 20 °N lat and may be influenced by different sources. NWR observes a mean offset of -1.24 ±0.17 ‰ from JFJ between 2003 and 2008.

6.4.7 BHD atmospheric - Tree Ring Intercomparison

Atmospheric $\Delta^{14}CO_2$ from the long-term BHD record was compared with tree rings collected from a pine tree located 10 m from the NaOH sampler at Baring Head. The comparison was made by comparing the annual tree ring result with the atmospheric record subsampled for November – February (inclusive) for the same year. Similarly, two NZ kauri trees located in Eastbourne, 15 km from Baring Head, were sampled; these trees are ~100 years old and gave longer records than the pine. No offset was observed (Turnbull et al., 2017).

6.5 Determined Laboratory Offsets from RRL

Table 6.2: Determined $\Delta^{14}CO_2$ offsets (and associated one sigma error) from RRL for each group (see text Section 6.2), determined from each intercomparison (see text Section 6.4), with the overall offset determined. See text for further details.

Intercomparison	RRLtree	Heidelberg	SIO/LLNL	SIO/CIO	INSTAAR/UCI	UCI
FARI-A			-2.8(1.8)	-0.1(1.4)	-2.2(1.6)	-3.1(1.4)
FARI-B			-0.6(2.3)	0.2(1.7)	-2.1(1.9)	-1.5(1.3)
Pure CO_2		-1.4(0.7)			-2.5(1.2)	
NWT3			-3.0(1.2)		-1.33(0.3)	
NWT4			-2.6(0.8)		-1.12(0.3)	
BHD-CGO						
JFJ-NWR					-1.2(0.2)	
BHD atmos-tree	0.0					
Overall	**0.0**	**0.0**	**-2.6(1.4)**	**0.0(1.1)**	**-1.3(0.2)**	**-2.3(1.0)**

Having assessed atmospheric $\Delta^{14}CO_2$ intercomparison activities as a whole, here we analyse the results for each laboratory separately and quantify offsets relative to RRL, the reference laboratory used in this study (Section 6.3). For each laboratory, judgement is then made on whether to adjust data by the overall offset determined, in preparation for combining with RRL data to develop the harmonised atmospheric $\Delta^{14}CO_2$ dataset for the Southern Hemisphere.

6.5.1 RRL Tree Rings

No offset from RRL is observed, so these are not adjusted.

6.5.2 Heidelberg

Recent atmospheric $\Delta^{14}CO_2$ measurements from BHD and CGO, of RRL and Heidelberg respectively, demonstrate good agreement, with an average offset of 0.08 ±0.45 ‰ across 31 samples (Section 6.4.5). Whilst the comparison of sites is more complex over time, in this study we do not explore time dependency of offsets with limited data available (Section 5.3).

The participation of RRL in the pure CO_2 $\Delta^{14}CO_2$ intercomparison activity of Heidelberg, leads to an offset of -1.4 ±0.7 ‰ of Heidelberg relative to RRL, but this is only based on a few samples (Section 6.4.2 & Table 6.2). Although there is limited RRL and Heidelberg $\Delta^{14}CO_2$ intercomparison data, INSTAAR/UCI can be considered to indirectly compare these laboratories, through the intercomparison of JFJ (Heidelberg) and NWR (INSTAAR/UCI) in the Northern Hemisphere (Section 6.4.6). INSTAAR/UCI observes comparable offsets to RRL and Heidelberg (Table 6.2; see below), thus indicative of agreement between RRL and Heidelberg. Therefore overall, we consider that RRL and Heidelberg atmospheric $\Delta^{14}CO_2$ measurements are consistent, thereby making no adjustment to Heidelberg data before combining with RRL data for the harmonised $\Delta^{14}CO_2$ dataset.

6.5.3 SIO/LLNL

During the period of flask sample $\Delta^{14}CO_2$ measurement at SIO/LLNL (2003 – 2009), the large AMS at LLNL did not have the capability for ^{12}C measurement, thereby not accounting for fractionation within the system (Graven et al., 2007). There were also complexities in the standardisation of the measurements, such that the control materials were used instead of the primary standard (OxI) (Graven, 2008). ^{12}C measurement has since been introduced at the low energy side of the AMS system. The intercomparison activities investigated in this

study have largely been conducted after the $\Delta^{14}CO_2$ flask measurements at SIO/LLNL, with OxI used for standardisation.

Although UCI don't have any background $\Delta^{14}CO_2$ records in the Southern Hemisphere, i.e., relevant to this study, UCI is used here as a further comparison for SIO/LLNL, with their co-located intercomparison (Graven et al., 2013; Section 6.4.3) and both groups also participating in the whole air $\Delta^{14}CO_2$ intercomparison (Miller et al., 2013; Section 6.4.1). The co-located intercomparison also uses $\Delta^{14}CO_2$ measurements from flask samples analysed 2003 – 2009, thereby providing a point of comparison between the SIO/LLNL flask measurements and other more recent SIO/LLNL $\Delta^{14}CO_2$ intercomparison results.

The results for SIO/LLNL and UCI in the whole air $\Delta^{14}CO_2$ intercomparison, appear to be consistent with the comparability of 0.2 ±0.7 ‰ in the co-located $\Delta^{14}CO_2$ intercomparison (FARI-A and FARI-B in Table 6.2) (Graven et al., 2013; Miller et al., 2013). Somewhat similar offsets are also determined overall for SIO/LLNL and UCI from RRL of -2.6 ±1.4 ‰ and -2.3 ±1.04 ‰ respectively (Table 6.2). In this study we thus make the assumption that these $\Delta^{14}CO_2$ flask measurements at SIO/LLNL are inline with their intercomparison $\Delta^{14}CO_2$ measurements. However, further investigation would be required to confirm this, so we therefore advise exercising caution when considering SIO/LLNL results in the harmonised dataset.

Further to the $\Delta^{14}CO_2$ intercomparisons detailed above, SIO/LLNL have graphitised and measured pure CO_2 aliquots of secondary standard material from INSTAAR/UCI (NWT3 and NWT4 in Table 6.2, Section 6.4.4; Turnbull et al., 2015). The offsets of SIO/LLNL from RRL are fairly consistent for the control material and the whole air $\Delta^{14}CO_2$ intercomparison, despite a relatively small number of measurements (Table 6.2).

The results of SIO/LLNL in these different $\Delta^{14}CO_2$ interlaboratory intercomparisons were considered together, with the overall offset quantified as -2.6 ±1.4 ‰ from RRL. Therefore in this study SIO/LLNL $\Delta^{14}CO_2$ data is increased by 2.6 (±1.4 ‰) to account for this offset, before combining with RRL $\Delta^{14}CO_2$ data as part of the harmonised Southern Hemisphere

dataset. However, with method variability between atmospheric $\Delta^{14}CO_2$ measurements and intercomparison measurements, caution should be taken with this data.

6.5.4 SIO/CIO

For FARI-A and FARI-B, SIO/CIO demonstrates offsets of -0.1 ±1.4 ‰ and 0.2 ±2.1 ‰ respectively from RRL (Table 6.2) (Miller et al., 2013). Although these are the only published atmospheric $\Delta^{14}CO_2$ intercomparison data for SIO/CIO, these results indicate agreement/consistency with RRL, with an overall quantified offset of 0.0±1.1‰ (Table 6.2). In this study we therefore apply no adjustment to SIO/CIO $\Delta^{14}CO_2$ data to combine it with RRL $\Delta^{14}CO_2$ data as part of the harmonised atmospheric $\Delta^{14}CO_2$ dataset for the Southern Hemisphere. Although SIO/CIO also only have a short $\Delta^{14}CO_2$ record in the Southern Hemisphere, the data is consistent with that of other laboratories, thus no adjustment appears appropriate given the limited data available (Tables 6.1 & 6.2).

These SIO/CIO results include a correction applied after initial reporting, bringing results more inline with the mean, but meaning that results are not fully blind. This highlights the importance of data analysis in addition to measurement methodology, for relatively small, high-precision atmospheric $\Delta^{14}CO_2$ samples.

6.5.5 INSTAAR/UCI

INSTAAR/UCI participates in a number of $\Delta^{14}CO_2$ intercomparison activities (e.g., Sections 6.4.1, 6.4.2 & 6.4.4; Miller et al., 2013; Turnbull et al., 2015; Hammer et al., 2016). Offsets of INSTAAR/UCI against RRL are consistent across these intercomparison activities, with an average offset of -1.2±0.2 ‰ determined (Table 6.2). This result partly comprises ^{14}C measurement of control tanks from INSTAAR/UCI (Section 6.4.4) and is thus derived from a large number of measurements.

In the Northern Hemisphere mid-latitude intercomparison, NWR (INSTAAR/UCI) is offset by -1.2 ±0.2 ‰ from JFJ, a site of the Heidelberg Network (Section 6.4.6). Measurements from

the Heidelberg Network are combined with RRL without adjustment (see above, Section 6.5.1), thereby this observed offset is consistent with the overall determined laboratory offset. This offset is also consistent with the offset of -1.1 ±1.2 ‰ of INSTAAR/UCI from Heidelberg in the pure CO_2 intercomparison, although only based on a small number of measurements (Section 6.4.2). In this study INSTAAR/UCI $\Delta^{14}CO_2$ data is therefore increased by 1.2 (±0.2 ‰), subsequently combining with RRL $\Delta^{14}CO_2$ data for intrahemisphere analysis, i.e., with NWR. Although there is currently no Southern Hemisphere published $\Delta^{14}CO_2$ data yet, when the DRP atmospheric $\Delta^{14}CO_2$ record becomes available this further valuable record can be combined with the harmonised dataset. Also, not applicable for this study but this determined offset could be used for further studies including a range of Northern Hemisphere records (e.g., Miller et al., 2012).

6.6. Harmonised Atmospheric $\Delta^{14}CO_2$ Dataset for the Southern Hemisphere

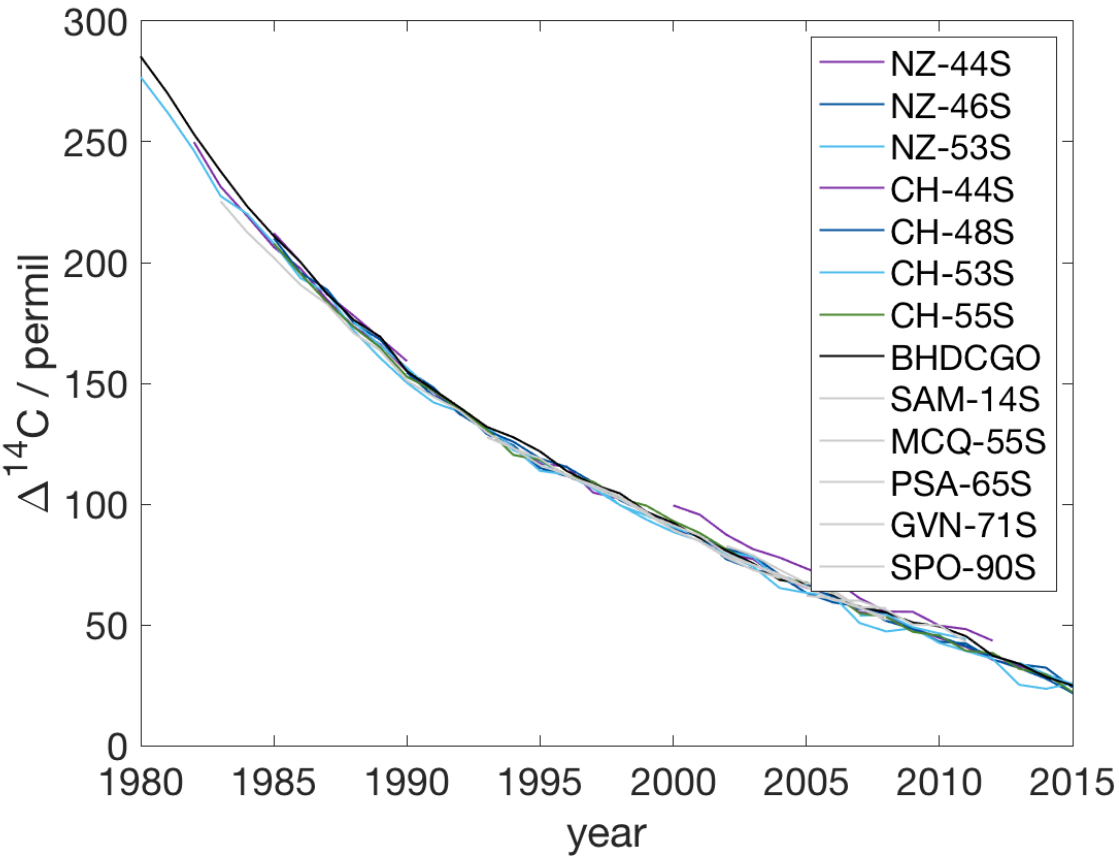

Figure 6.2: All tree ring and atmospheric $\Delta^{14}CO_2$ records of the harmonized dataset.

Through assessment of atmospheric $\Delta^{14}CO_2$ intercomparison activities, laboratory offsets from a reference laboratory, RRL, have been established. Here we apply the determined adjustments to each laboratory $\Delta^{14}CO_2$ dataset, before combining with RRL $\Delta^{14}CO_2$ data to develop the harmonised atmospheric $\Delta^{14}CO_2$ dataset for the Southern Hemisphere. Developing this dataset enables investigation of subtle atmospheric $\Delta^{14}CO_2$ variability using more measurements than has previously been possible through any individual laboratory $\Delta^{14}CO_2$ dataset. Interpretation of spatial and temporal gradients in this harmonized dataset is presented in Chapter 6.

6.7 Discussion: Potential Sources of Interlaboratory Variability

6.7.1 Sampling Methods

Atmospheric $\Delta^{14}CO_2$ measurements have been conducted through NaOH or flask sampling of atmospheric CO2 (Section 6.2). These two techniques are fundamentally different, with NaOH traditionally used and more recently developed capabilities for measurement of flask samples (including archives), collected for a range of atmospheric analyses (Section 6.2; e.g., Levin et al., 1980; Meijer et al., 2006; Graven et al., 2007; Turnbull et al., 2007; Turnbull et al., 2017). It therefore seems plausible that interlaboratory offsets, at least in part, could be a result of sampling differences. Although Turnbull et al., (2017) found no significant differences between corresponding NaOH and flask sample measurements from BHD, here we reassess this, now with further measurements.

Atmospheric $\Delta^{14}CO_2$ measurements at BHD have typically been through NaOH sampling, which is now complimented with flask sampling (Turnbull et al., 2017; Section 6.2.1). Although archived flask samples from BHD (1984 – 1992) were analysed for $\Delta^{14}CO_2$, these measurements largely replace anomalous NaOH data so cannot be used for NaOH – flask sampling comparison.

Flask sampling for $\Delta^{14}CO_2$ analysis restarted at BHD in 2012, with 12 early $\Delta^{14}CO_2$ flask sample measurements showing good agreement with NaOH data (Turnbull et al., 2017).

Flask sampling has continued alongside regular NaOH sampling, such that we now have 37 $\Delta^{14}CO_2$ flask sample measurements with corresponding NaOH $\Delta^{14}CO_2$ measurements (2012 – 2017). A mean offset of 1.0 ±0.2 ‰ is observed of flask $\Delta^{14}CO_2$ measurements relative to corresponding NaOH $\Delta^{14}CO_2$ measurements, with no sampling period bias. Valid flask background samples are typically collected during southerly, clean air conditions (Stephens et al., 2013). NaOH integrated samples include all wind conditions, thereby potentially incorporating some polluted air. The positive offset observed of flask $\Delta^{14}CO_2$ measurements from NaOH could be as a result of this. In Section 5.5.2 I concluded that that RRL and Heidelberg observe no interlaboratory offset based on recent NaOH $\Delta^{14}CO_2$ data from the BHD and CGO intercomparison (Section 6.4.5). However, prior to 1995, an offset of 1.7 is observed of CGO from BHD, including flask samples that replace anomalous NaOH samples 1990 – 1993. With the exclusion of BHD flask $\Delta^{14}CO_2$ measurements, this observed offset is instead 0.8. We therefore observe ~1 difference in this calculated offset depending on the inclusion of flask samples. This is consistent with the more recent NaOH – flask intercomparison at BHD, indicating that flasks may have a positive bias here.

Although there appears to be an offset between RRL NaOH and flask $\Delta^{14}CO_2$ measurements, in this study we do not progress this analysis any further, primarily because with limited data available it is challenging to discern further details of such variability. Since each lab (with the exception of RRL) uses only flask or only NaOH in their records, any inter lab offsets due to the sampling method are implicitly included in the offsets determined in Section 6.5.

6.7.2 CO_2 Extraction

Different atmospheric $\Delta^{14}CO_2$ intercomparison activities are not only useful to identify interlaboratory offsets, but also to diagnose/disentangle sources of variability leading to observed interlaboratory offsets.

In the ongoing larger scale flask $\Delta^{14}CO_2$ intercomparison activity, interlaboratory offsets of ±3 ‰ are observed, which encompass variability from extraction, graphitisation, and AMS

measurement and associated analysis including primary standard preparation and $\delta^{13}C$ measurement (Section 6.4.1; Miller et al., 2013). $\delta^{13}C$ measurement was used to determine the absence of mass-dependent fractionation, e.g., Miller et al., (2013) demonstrate no significant fractionation occurs during flask filling and that it is an unlikely source of variability (Section 6.4.1). Results therefore indicate the presence of a significant source of interlaboratory variability from sample preparation and measurement, i.e. independent of sampling rationale.

The large scale pure CO_2 $\Delta^{14}CO_2$ intercomparison activity observes similar interlaboratory offsets of ~3 ‰, although using pure CO_2 aliquots removes any effects of flask storage and CO_2extraction, thus only encompassing variability associated with graphitisation, ^{14}C measurement and associated analysis (Hammer et al., 2016).

These two intercomparison studies support the argument that extraction of CO_2 is unlikely to produce a significant offset (Miller et al., 2013; Hammer et al., 2016). It therefore follows that interlaboratory variability observed is most likely a result of steps after extraction: graphitisation, measurement and/or analysis, including contamination from graphitisation reagents, OxI prep for standardisation, $\delta^{13}C$ measurement for normalisation, and blank correction.

6.7.3 Fractionation Correction

The measurement of $\delta^{13}C$ for fractionation correction is can be conducted through IRMS, thereby not accounting for any fractionation during graphitisation/measurement. Alternatively, the $\delta^{13}C$ correction is done using online measurements within the AMS system and therefore accounting for fractionation during graphitisation and measurement (Section 6.2). There is indication of fractionation effects from graphitisation and AMS measurement that are not captured by $\delta^{13}C$ IRMS measurement, including the use of OxI as the primary standard, with characteristically different $\delta^{13}C$ content to atmospheric CO_2 samples (Graven et al., 2007; Turnbull et al., 2017).

6.7.4 Primary Standard Preparation and Standardisation

Elsewhere, it has also been proposed that primary standard preparation potentially limits atmospheric $\Delta^{14}CO_2$ measurement precision (Graven et al., 2007; Graven, 2008; Turnbull et al., 2013). High-precision atmospheric $\Delta^{14}CO_2$ measurements are achievable, in part, due to the minimal CO_2 sample preparation relative to typical solid samples for ^{14}C analysis. As a solid standard material, OxI must be combusted to CO_2 gas, requiring reagents that could introduce contamination. Air control tank measurements have better repeatability than OxI measurements (Graven et al., 2007), potentially because of the CO_2 samples have relatively less preparation. This indicates that the use of OxI as the primary standard could be a large source of uncertainty for high-precision atmospheric $\Delta^{14}CO_2$ measurements.

This is not totally unexpected, given that prior investigation at RRL found that OxI combusted through different procedures introduced an offset (Turnbull et al., 2015). It has also been demonstrated that use of a flask of Ox for standardisation produces better repeatability than smaller batch combustions/preparation (Meijer et al., 2006; Turnbull et al., 2007; J. Turnbull pers. Comm.).

In addition to the ongoing comparison of INSTAAR/UCI and RRL through control tank measurements (Section 6.4.4; Turnbull et al., 2015), I report for the first time the results from five pure CO_2 aliquots of OxI extracted at INSTAAR and treated as unknowns at RRL. Since OxI is used as the primary standard, these results are reported ratio to standard (rts) instead of $\Delta^{14}CO_2$, thereby directly comparing the the measured isotopic ratio of the sample to the RRL OxI used as primary standard in the same measurement wheel without further corrections.

This comparison of INSTAAR-extracted OxI and RRL-extracted OxI, both graphitisation, $\delta^{13}C$ and AMS measurement in the same way (at RRL) thereby isolates variability introduced through OxI preparation. Although more scatter of 'unknown' OxI results (rts) is observed than would be expected from a small sample group, there is a bias towards lower ^{14}C

content, i.e., smaller $^{14}C/^{12}C$ ratio than corresponding OxI primary standards prepared and measured at RRL.

This difference in OxI is consistent with the control tank intercomparison which showed an offset of -1.2 ±0.2 ‰ between INSTAAR/UCI from RRL (NWT3 NWT4; Table 6.2). Similar to the OxI test, the control tank samples are extracted at INSTAAR, with graphitisation and AMS measurement at RRL. This therefore suggests that these results are indicative of OxI preparation as a source of interlaboratory variability. In fact, the previous work and these new results suggest that OxI preparation and measurement may be the most significant source of interlaboratory variability.

6.8 Conclusions

Through evaluation of atmospheric $\Delta^{14}CO_2$ intercomparison results we have developed a harmonised atmospheric $\Delta^{14}CO_2$ dataset for the Southern Hemisphere with adjustments made for determined offsets. This new harmonised dataset is now available for use in a variety of applications. In Chapter 7, I use it to investigate Southern Ocean upwelling. It can also be used in regional calibration, including the upcoming update of the "Calibomb" calibration dataset (Hua et al., 2013), and global modelling studies (e.g. Randerson et al., 2002).

Generally, the small number of samples in intercomparison activities remains an obstacle to improving characterisation of interlaboratory offsets and associated precision. This can be further improved with more measurements; thus we encourage a range of intercomparison activities to characterise interlaboratory offsets. Furthermore, more regular intercomparisons will help to investigate temporal variability in interlaboratory offsets, which could not be addressed here with the existing intercomparison datasets.

It is worth noting that the currently employed cylinders for the whole air $^{14}CO_2$ intercomparison activity (Miller et al., 2013) will soon be empty (FARI-A and FARI-B), such that new cylinders will shortly need producing, and ideally with measurements crossing over between old and new cylinders. Pure CO_2 intercomparisons (e.g. Hammer et al., 2016) could

be more widely used, as it has been demonstrated that flask filling and extraction have minimal influence on measurement variability (Turnbull et al., 2007; Miller et al., 2013).

Pure CO_2 aliquots would appear to be logistically easier, negating the need to send flasks between laboratories, although CO_2 sample size should be suited to each laboratory (Hammer et al., 2016). An ongoing pure CO_2 intercomparison would require large combustions of a given material, but this material does not necessarily need to be air derived; this technique is similar/somewhat comparable to use of a flask of OxI for standardisation, which has demonstrated good repeatability (Meijer et al., 2006; J. Turnbull pers. Comm.). Atmospheric $\Delta^{14}CO_2$ measurements are at the forefront of ^{14}C measurement precision, such that we are effectively reaching the limits/edge of the relative 14C scale and standardisation (Turnbull et al., 2013). Conventionally we report relative to OxI but now find/it appears that Ox, the very definition of the scale, is a source of variability, which brings into question the use of conventional OxI as a primary standard for atmospheric $\Delta^{14}CO_2$ measurements.

It is the additional preparation of OxI relative to gas samples, i.e., combustion, that appears to introduce variability, which is likely a result of small batch combustion. Therefore a potential solution could be to prepare a large volume of CO_2 derived from OxI, thus effectively using this as a working standard, (Turnbull et al., 2013). An alternative is to use control tanks as a working standard, i.e., gas standards derived of natural whole air, which have already previously demonstrated less variability than individually prepared aliquots of OxI (Graven et al., 2007; Graven 2008). There are challenges associated with using an OxI or alternative large-batch working gas standard, in that a working standard should be routinely characterised against OxI, and a gas standard may drift and logistically has a finite lifetime (Turnbull et al., 2013).

Although using an OxI working gas standard (or otherwise) provides a resolution for improving within-laboratory repeatability thus improving measurement precision, it does not as such address interlaboratory variability, the primary purpose of this study. This is because with different combustion methodology introducing systematic bias,

interlaboratory offsets could still be observed between the large combustions of OxI at different laboratories.

To overcome this, these offsets could be constrained, similarly to in this study, through intercomparison activities. Alternatively, there has been suggestions of development of a new gas standard, whether whole air or CO_2, such that all laboratories making atmospheric $\Delta^{14}CO_2$ measurements use the same gas standard (Turnbull et al., 2013). A third possibility is that a single lab could produce large batches of CO_2 from OxI and distribute it to many labs. This concept also has many underlying challenges and would similarly require routine characterisation against OxI to remain tied to the relative ^{14}C scale used conventionally for all other ^{14}C measurements.

These possibilities for intercomparison activities and standardization must be carefully considered by the atmospheric $\Delta^{14}CO_2$ community together. The existing Greenhouse Gas Measurement Techniques (GGMT) conference and guidelines provide an excellent venue for these discussions and decisions.

Chapter 7

Atmospheric $\Delta^{14}CO_2$ over the Southern Ocean in Recent Decades

This PhD project investigates modern atmospheric $\Delta^{14}CO_2$ variability over the Southern Ocean through tree ring reconstruction. In this chapter I conduct this analysis using the new tree ring $\Delta^{14}CO_2$ records from this PhD project, alongside the harmonised atmospheric $\Delta^{14}CO_2$ dataset for the Southern Hemisphere (Chapter 6). The application of this large dataset enables investigation into regional variability where data is sparse, thereby previously limiting such investigation.

I first present details of analysis techniques used (Section 7.1), before assessing trends and variability of atmospheric $\Delta^{14}CO_2$ over the Southern Ocean (Sections 7.2 & 7.3). This includes determining differences from a reference record to help examine subtle spatial and temporal variability.

7.1 Methodology: Data Analysis and Modelling Techniques

A number of techniques are used in the interpretation of the tree ring $\Delta^{14}CO_2$ records from this PhD project, which are detailed here.

7.1.1 Measurements Included in this Analysis

The measurements used here are the full harmonized dataset described in Chapter 6, including the new tree ring $\Delta^{14}CO_2$ measurements and the sites listed in Table 6.1.

7.1.2 Using BHDCGO as a Southern Hemisphere Reference Record

The global atmospheric $\Delta^{14}CO_2$ downward trend observed in recent decades is prominent in all atmospheric $\Delta^{14}CO_2$ records (Section 2.2.4). This strong downward trend makes it challenging to identify any spatial or temporal variability that may be present, yet subtle relative to the overall trend. This is not unexpected, given that global atmospheric $\Delta^{14}CO_2$ is decreasing by ~5‰ each year, but contributes to the challenge of investigating the relatively weak latitudinal variability of the Southern Hemisphere which is of comparable magnitude to ~2‰ measurement precision commonly achieved (e.g., Graven et al., 2007; Turnbull et al., 2015). Through the use of a reference record, the long-term trend component can be removed, allowing subtle spatial variability to become apparent. For example, Levin et al., (2010) used the Neumayer Station record as their reference record; Graven et al., (2012b) used the difference from a mean of all sites as their reference.

A range of long-term background atmospheric $\Delta^{14}CO_2$ measurement sites are considered as reference records here (e.g., see Section 6.2). Of these, the composite of Baring Head, New Zealand (BHD) and Cape Grim, Australia (CGO) developed by Turnbull et al., (2017), also using data from Levin et al. (2010), is selected as the reference record for this study (BHDCGO, Section 6.4.5). This is for a number of reasons, detailed below.

The BHD record is the longest atmospheric $\Delta^{14}CO_2$ record available, spanning the period of interest in this study and extending further back in time (Section 6.2), i.e., also useful for its application in bomb-pulse dating (Section 5.1). Although methodology has varied over time, the record is maintained by RRL; a well-established laboratory with a long history of making atmospheric $\Delta^{14}CO_2$ measurements (e.g., Manning et al., 1990; Currie et al., 2011; Turnbull et al., 2017). As a background site in the Southern Hemisphere mid-latitudes, BHD is typically subject to well-mixed air masses with minimal local ^{14}C influences, i.e., fossil fuel emissions, terrestrial biosphere and nuclear power (e.g., Stephens et al., 2013). The BHD atmospheric $\Delta^{14}CO_2$ record can be directly compared to the tree ring $\Delta^{14}CO_2$ records presented in this thesis as it has previously been demonstrated that tree ring $\Delta^{14}CO_2$ records

from BHD are comparable to the BHD atmospheric $\Delta^{14}CO_2$ record (Turnbull et al., 2017; Section 2.3.2 & 6.4.7).

However, for the period 1995 – 2005, the BHD atmospheric $\Delta^{14}CO_2$ record shows an increase in noise as well as an apparent high bias (Turnbull et al., 2017; Section 6.4.5). The bias and increased noise are attributed to measurement uncertainty, corresponding with the introduction of accelerator mass spectrometry (AMS) ^{14}C measurement at RRL in 1995, yet without online ^{12}C measurement for accurate fractionation correction prior to 2005. BHD data from 1995 – 2005 is therefore removed and substituted with CGO data for this period, forming a composite, BHDCGO record (Turnbull et al., 2017).

BHD and CGO are at similar latitudes and observe comparable long-term atmospheric $\Delta^{14}CO_2$ (Section 6.4.5). Although the atmospheric $\Delta^{14}CO_2$ record at CGO is maintained by the Heidelberg Laboratory (Levin et al., 2010; Section 6.2), I have demonstrated that atmospheric $\Delta^{14}CO_2$ data of Heidelberg and RRL is comparable, such that it can be combined without adjustment (Section 6.5.2). CGO is a background atmospheric $\Delta^{14}CO_2$ site of a well-established laboratory, however measurement at CGO only began in 1987 so it is not a long enough record to be used alone.

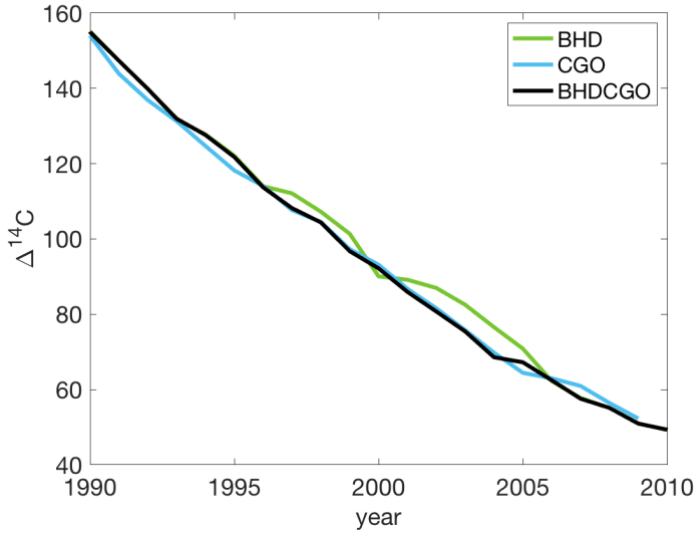

Figure 7.1: Smoothed BHDCGO record (and BHD and CGO separately) from Turnbull et al., 2017 (CGO data from Levin et al., 2010).

A smooth-curve trend of BHDCGO is used to remove noise from the raw BHDCGO data (Turnbull et al., 2017), and it is subsampled for summer tree growth months in the Southern Hemisphere of November – February (Figure 7.1) (Section 2.3), then applied as a reference record. This is used to effectively detrend the remaining $\Delta^{14}CO_2$ records and allows any variability present to be more easily identified. In related analyses any short-term bias effects of using this particular BHDCGO reference record are considered (Section 7.2.3).

7.1.3 HYSPLIT: Atmospheric Transport Model Backward Trajectories

Variability of atmospheric $\Delta^{14}CO_2$ in the Southern Hemisphere is sensitive to the upwelling of (carbon-rich/^{14}C-depleted) deep water (Section 2.2.5). It is therefore the combination of atmospheric $\Delta^{14}CO_2$ measurements with an understanding of air mass transport that enables interpretation of atmospheric $\Delta^{14}CO_2$ spatial variability and associated upwelling. Here an atmospheric transport model, namely HYSPLIT (see below), is used to gain insight into the air masses observed in the different atmospheric $\Delta^{14}CO_2$ records presented in this project.

The Hybrid Single Particle Lagrangian Integrated Trajectory (HYSPLIT) model computes air parcel trajectories and dispersion/deposition of atmospheric pollutants (Stein et al., 2015). HYSPLIT was developed by NOAA and has a limited online version as well as an executable for download. Here the focus is on the relevant trajectory model features for this study.

From a given starting location, trajectories can be forwards or backwards using different meteorological data, whether forecast or archive. For this study NCEP/NCAR reanalysis data is used, with a 2.5 ° resolution, as it has regional coverage and spans the period of interest with sufficient resolution to identify large scale atmospheric circulation (Kalney et al., 1996). Multiple time/space simultaneous trajectories can be performed, alongside further options including a trajectory ensemble that utilises meteorological variations.

Sampling locations are very important for this study, such that tree ring $\Delta^{14}CO_2$ records represent atmospheric $\Delta^{14}CO_2$ observed in oceanic air masses transported by westerly

winds (Section 3.1). Therefore similarly the position of these sampling sites within the model seeks to accurately observe air masses observed by the sampled trees; representing the carbon uptake of trees, and thus deposited in annual growth tree rings analysed (Section 2.3).

Mean backward trajectories are shown in Figures 7.2 and 7.3. In many cases the site has been moved slightly offshore to avoid model misrepresentation errors.

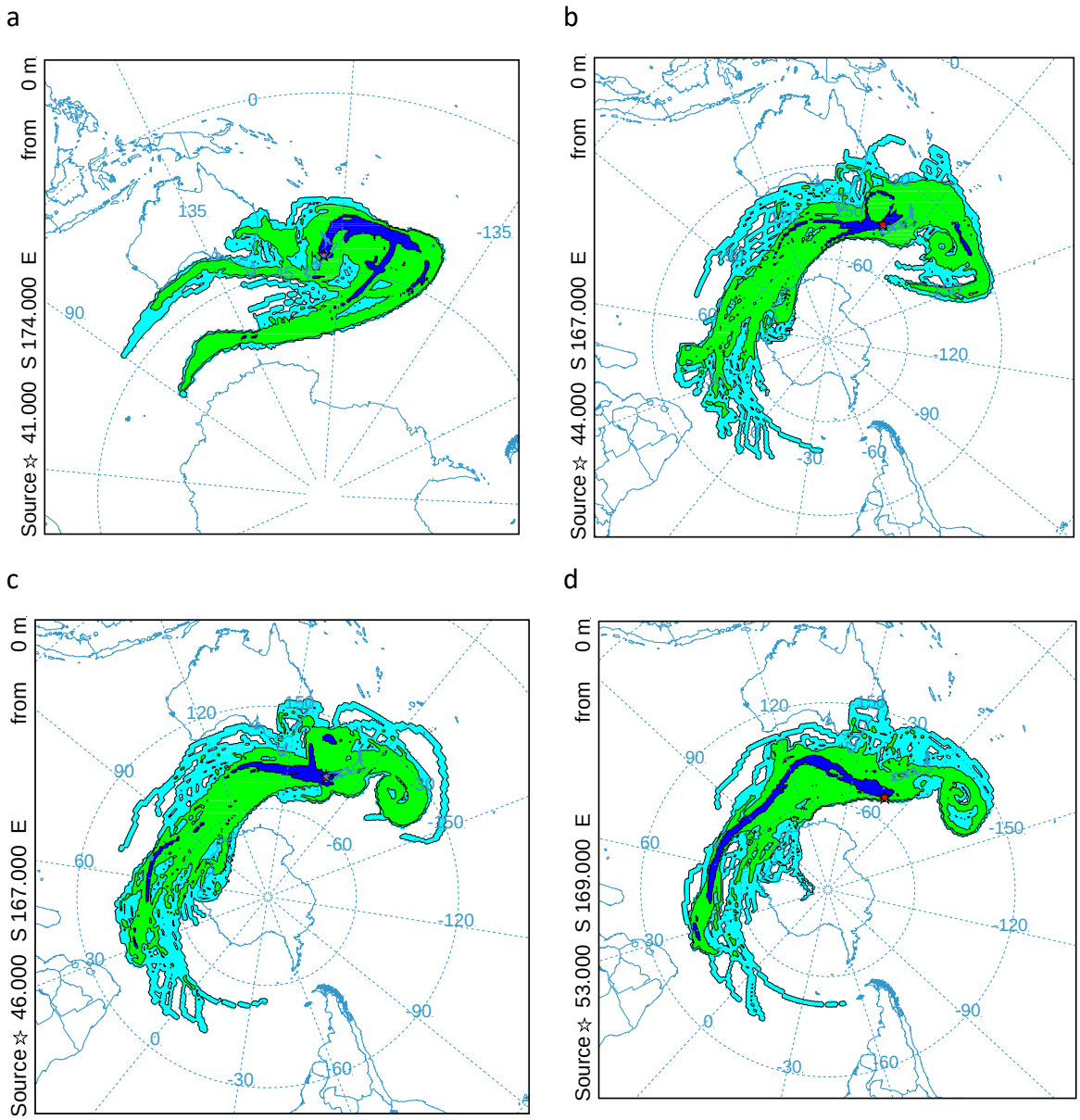

Figure 7.2: HYSPLIT backward trajectory distribution for New Zealand measurement sites for November - February growth months, 1985 – 2015: BHD-41S (top left), NZ-44S (top right), NZ-46S (bottom left) and NZ-53S (bottom right).

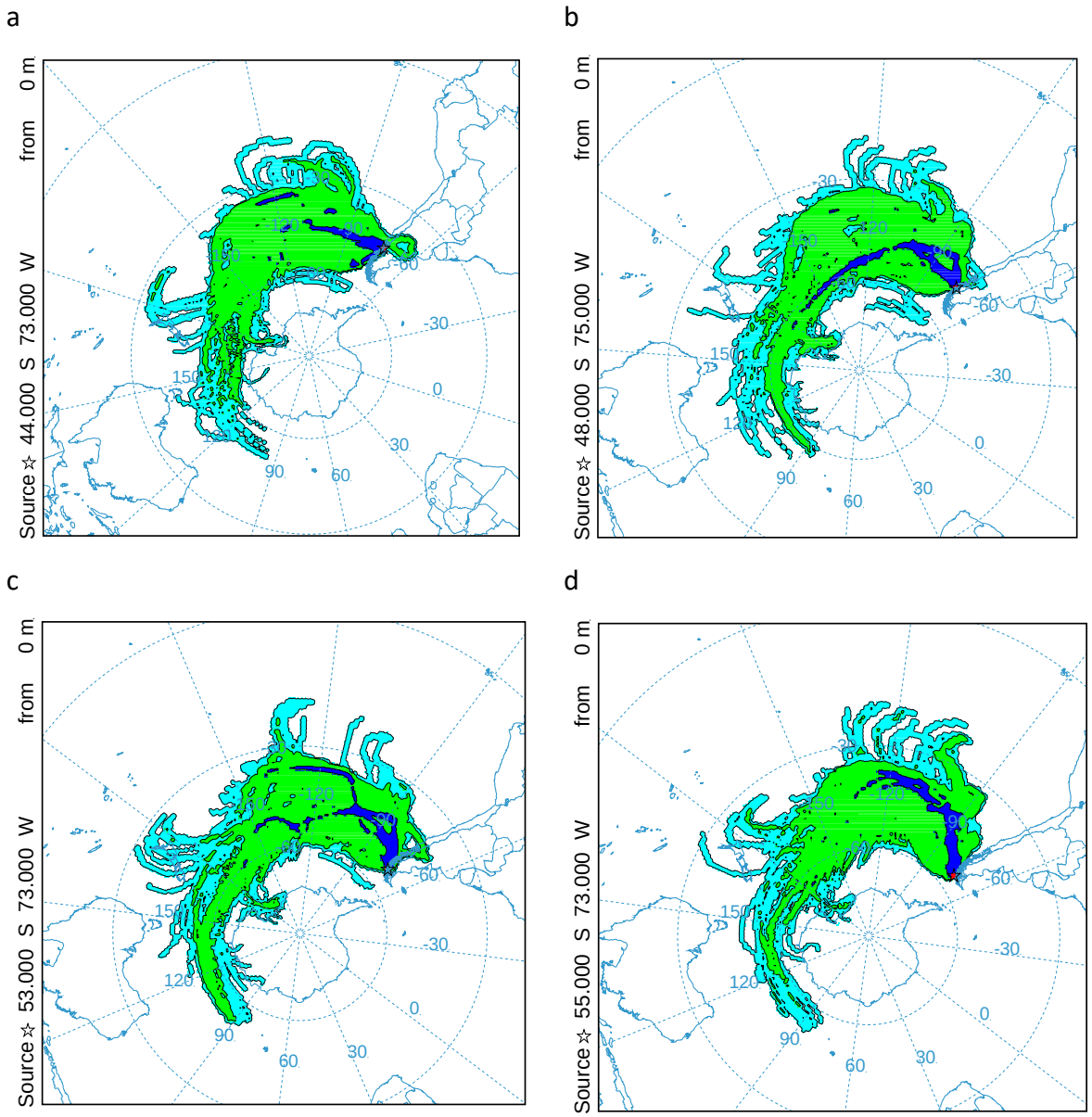

Figure 7.3: HYSPLIT backward trajectory distribution for Chile tree ring sites for November - February growth months, 1985 – 2015: CH-44S (top left, a), CH-48S (top right, b), CH-53S (bottom left, c) and CH-55S (bottom right, d).

7.2 Results

7.2.1 Atmospheric $\Delta^{14}CO_2$ Results from this Project

The atmospheric $\Delta^{14}CO_2$ tree ring records from New Zealand and Chile all demonstrate a prominent downward trend throughout recent decades (Figure 7.4). This is consistent with

the global atmospheric $\Delta^{14}CO_2$ downward trend observed in all the records of the harmonized dataset (Chapter 6).

The exception to this is the CH-44S tree ring $\Delta^{14}CO_2$ record, which despite ring count validation appears anomalously high relative to all the other records (Figure 7.4). Whilst we expect higher $\Delta^{14}CO_2$ towards the lower latitudes of the Southern Hemisphere, the CH-44S record sits higher than other global atmospheric $\Delta^{14}CO_2$ records, including Samoa (SAM-14S; Graven et al., 2012b). The CH-44S record is also incomplete, making it hard to interpret, and is thus excluded from further analysis. A plausible explanation for this result could be that although the record is accurately bomb-pulse validated, annual growth tree rings somewhere within the record are incorrectly assigned such that false and missing rings balance out (Section 2.3). An alternative explanation could be that high atmospheric $\Delta^{14}CO_2$ is observed locally as a result of overturning bomb ^{14}C exchanging with the atmosphere from the surface ocean or terrestrial biosphere (Section 2.2.4). Further investigation would be required to confirm the reason for the high atmospheric $\Delta^{14}CO_2$ observed in the CH-44S record.

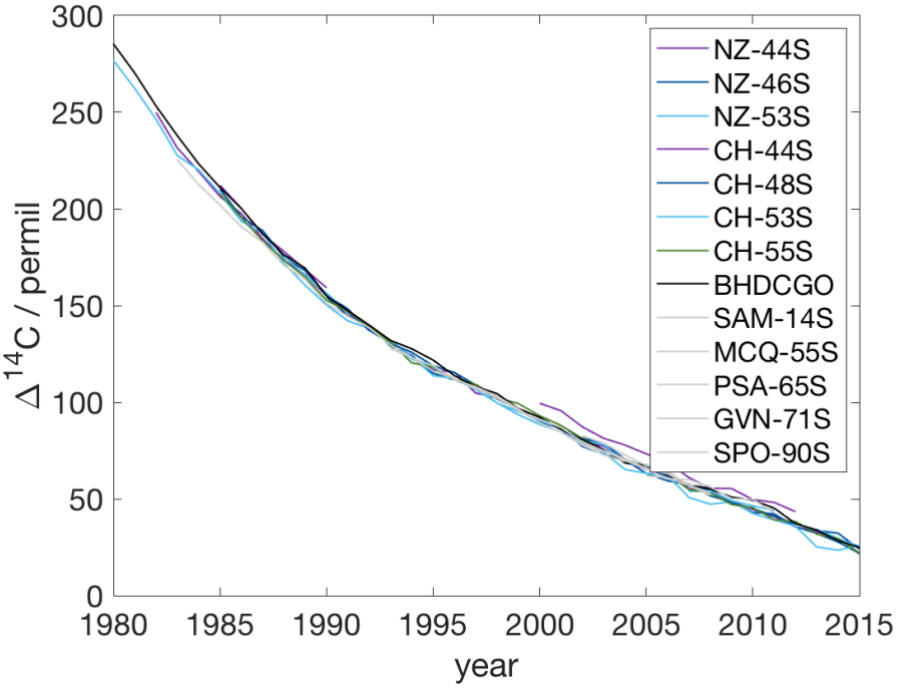

Figure 7.4: All tree ring and atmospheric $\Delta^{14}CO_2$ records used in this study (see Chapter 6 for more details; Meijer et al., 2006; Levin et al., 2010; Graven et al 2012(b), Turnbull et al., 2017) alongside the BHDCGO reference record.

7.2.2 Spatial Variability of Atmospheric $\Delta^{14}CO_2$ over the Southern Ocean

The differences of the new tree ring $\Delta^{14}CO_2$ records relative to the BHDCGO reference record are presented in Figure 7.5 and summarized as the average offset over the period 1985 – 2015 in Figure 7.6. For the most part, the atmospheric $\Delta^{14}CO_2$ tree ring records from New Zealand are lower than BHDCGO (Figure 7.5a) and a latitudinal gradient of 3.7 ‰ is apparent between 41 °S and 53 °S. This decreased atmospheric $\Delta^{14}CO_2$ over the Southern Ocean is consistent with other observations and studies, attributed to air-sea ^{14}C disequilibrium from deep water upwelling in the Southern Ocean, discussed further in Section 7.3 (e.g., Levin and Hesshaimer, 2000; Randerson et al., 2002; Levin et al., 2010; Graven et al., 2012b; Section 2.2.5).

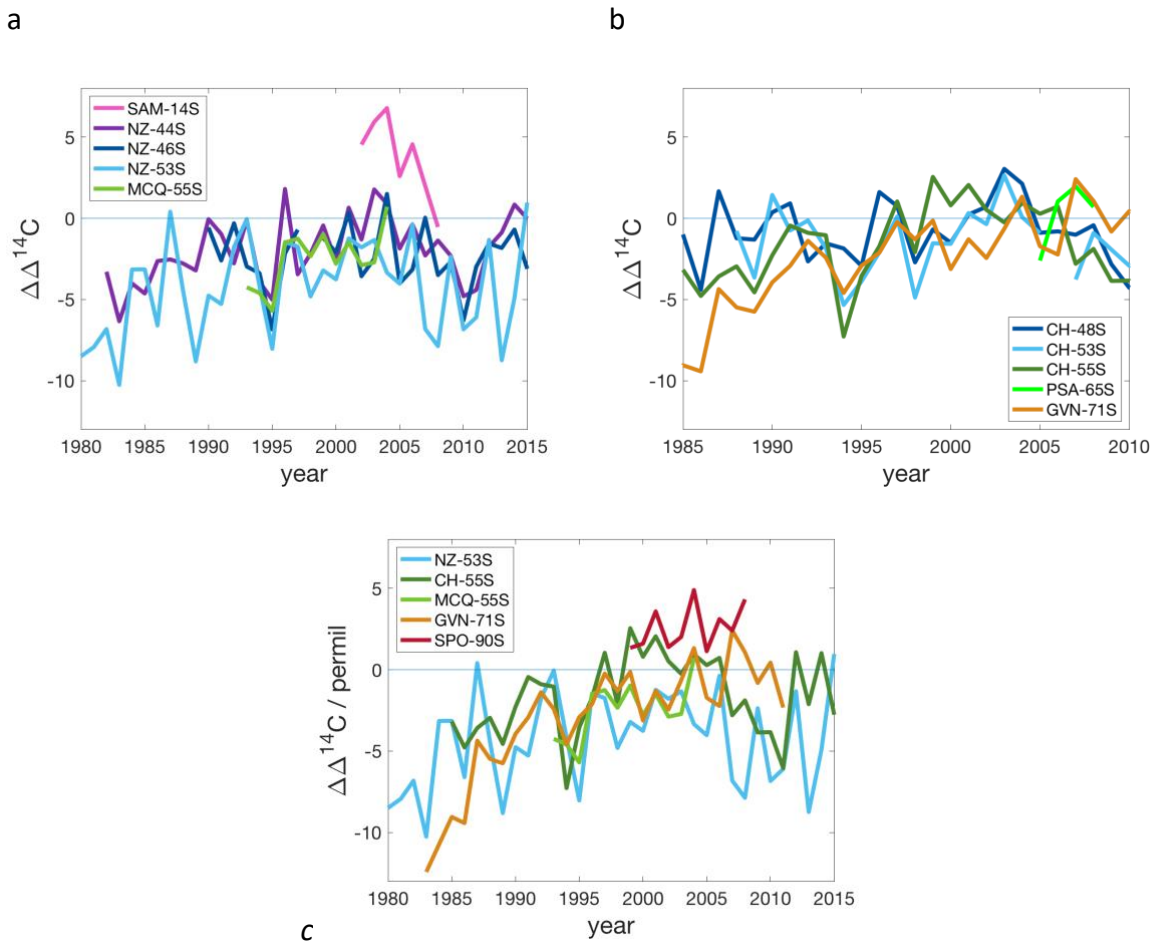

Figure 7.5: Difference of atmospheric and tree ring $\Delta^{14}CO_2$ records from BHDCGO for growth months, i.e., Nov – Feb (Turnbull et al., 2017): in the Indian Sector (top left, a), Pacific Sector and GVN (top right, b), and high latitudes above 53 °S, excluding the short record of PSA (bottom, c).

This latitudinal gradient is less clearly identifiable in the tree ring $\Delta^{14}CO_2$ records from Chile, with a gradient of only 0.6 ‰ between 48 °S and 55 °S, despite the wider latitudinal range (Figure 7.5b). The 55 °S site is only 1.2 ‰ lower than BHDCGO at 41 °S.

Whilst other atmospheric $\Delta^{14}CO_2$ records from the harmonised dataset vary in length, they demonstrate similar spatial variability to the new tree ring $\Delta^{14}CO_2$ records (Figures 7.5 & 7.7). A relative $\Delta^{14}CO_2$ maximum is observed at SAM (14 °S), and similarly SPO (90 °S) observes relatively high $\Delta^{14}CO_2$ compared to mid-high latitude sites, with lowest values at MCQ and NZ-53S. While MCQ (55 °S) is a much shorter record (1999 – 2004), it shows a similar gradient to NZ-53S for the period of overlap.

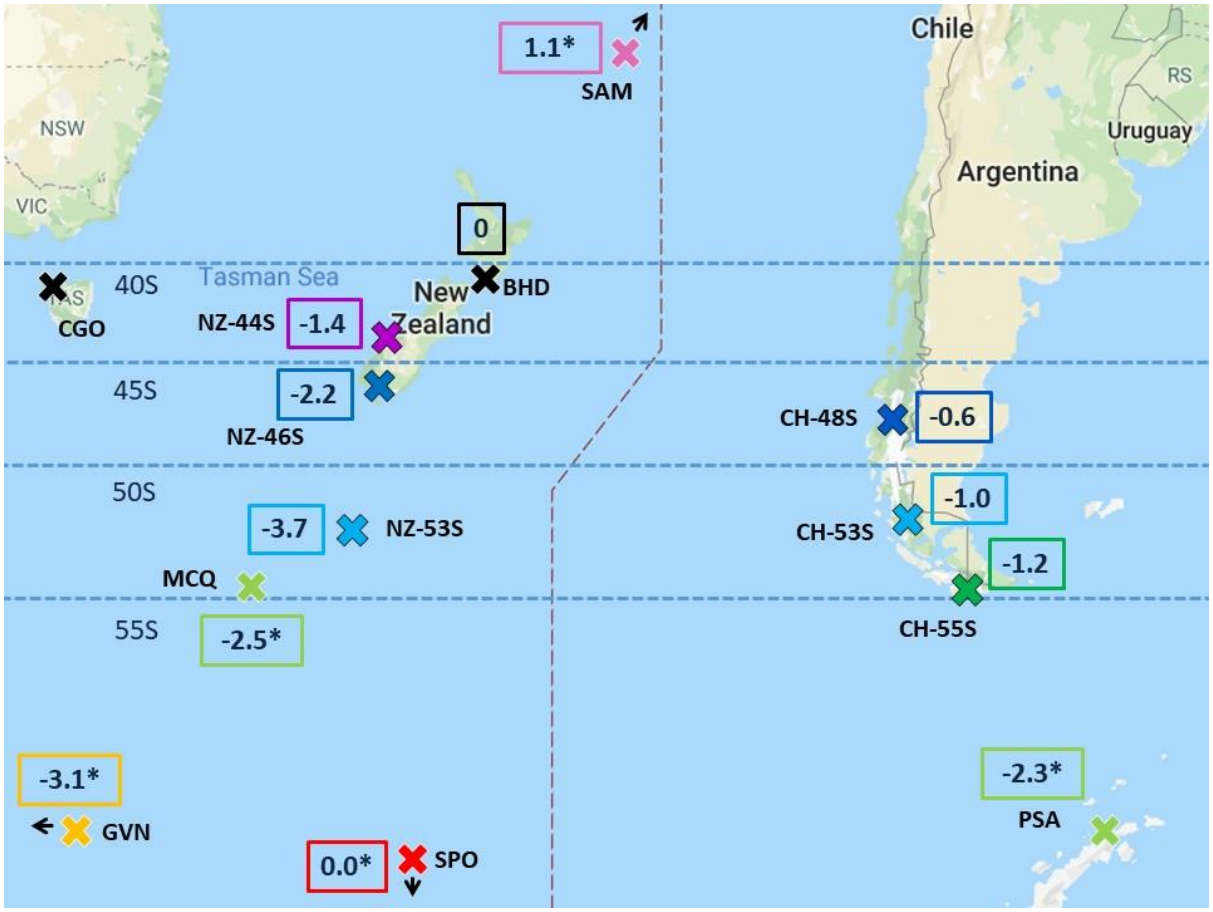

Figure 7.6: Average deviation $\Delta\Delta^{14}CO_2$ (‰) of each site from BHDCGO $\Delta^{14}CO_2$ record. Tree ring records are the average deviation 1985 – 2015, other records are the average deviation for the available years of each record (*).

The data in this study can only diagnose variability in the summer growth months, thus any spatial/temporal trends observed are consistent over the summer, but results here may not reflect the entire year.

The spatial variability of atmospheric $\Delta^{14}CO_2$ observed between New Zealand and Chile highlights the presence of longitudinal (or zonal) variability in addition to the large-scale latitudinal gradient observed in the Southern Hemisphere. Results are therefore considered in terms of atmospheric transport model output (Section 7.1.3) to help interpret the spatial variability. The sampling sites/west coast of New Zealand typically observe strong westerly winds that bring oceanic air masses from 50 – 60 °S latitudes of the Indian Ocean Sector of the Southern Ocean (Figure 7.2).

Whilst the sampling sites/west coast of Chile observe some influence of westerly winds, these do not appear to be as zonally consistent as those observed in New Zealand (Figures 7.2 & 7.3). Some air masses observed along the coast of Chile originate from high southern latitudes (i.e., ~60 °S), whereas much of the time the air masses come from as far North as 30 °S, often following the Chilean coast. So while the Chilean sampling sites extend further south than the New Zealand sites, they typically sample air from more northerly latitudes, and the coastal tracking of incoming air masses may explain why differences between the Chilean sites are less apparent.

7.2.3 Temporal Variability of Atmospheric $\Delta^{14}CO_2$ over the Southern Ocean

Although it is challenging to assess interannual variability observed in the atmospheric $\Delta^{14}CO_2$ and tree ring records, some broad temporal patterns are apparent in the annual $\Delta\Delta^{14}CO_2$ (Figure 7.5). To further elucidate the temporal variability Figure 7.7 shows the decadal average $\Delta\Delta^{14}CO_2$ for each site, for 1986 – 1995, 1996 – 2005 and 2006 – 2015. Stronger latitudinal gradients of atmospheric $\Delta^{14}CO_2$ are observed in 1986 – 1995 relative to 1996 – 2005 and the gradients increase again in 2006 – 2015. This pattern is apparent in every tree ring record reported here. $\Delta\Delta^{14}CO_2$ at NZ-53S changes from -4.3 ‰ to -2.7 ‰ to -4.4‰ across the three decades. Although $\Delta\Delta^{14}CO_2$ is of smaller magnitude at the other tree

ring sites, the decadal changes in magnitude of $\Delta\Delta^{14}CO_2$ are even greater at some sites (Figure 7.7). Although the MCQ record is short, it supports the same trend. PSA could not be included in this analysis as it includes only two years of data (2005 – 2007). GVN is the clear exception to this trend, showing a decreasing $\Delta\Delta^{14}CO_2$ through time (Figure 7.7).

The prominent feature of reduced $\Delta^{14}CO_2$ in all the $\Delta^{14}CO_2$ records in 1994/1995 appears to be a bias (Figure 7.5): all records observe a similar feature, that disappears with the use of an alternative reference record (not shown) and is also not identified in other previous studies (Levin et al., 2010; Graven et al., 2012b).

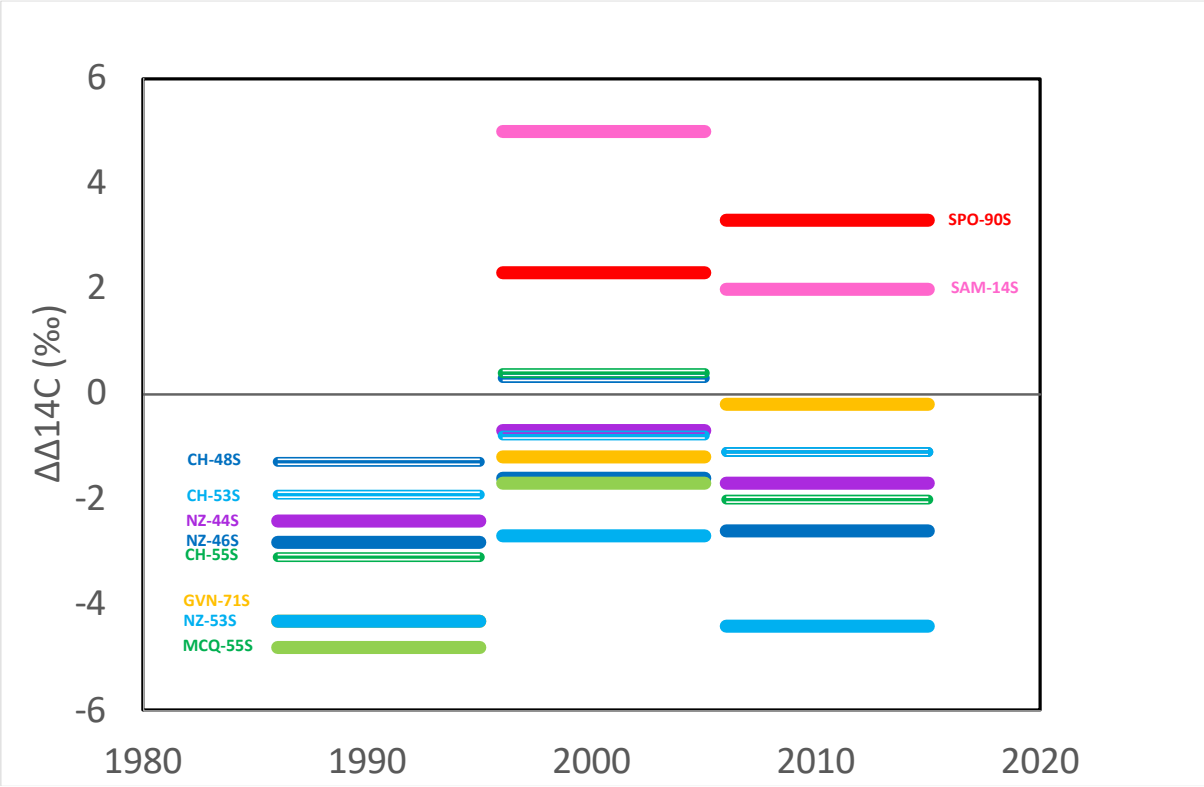

Figure 7.7: Average deviation $\Delta\Delta^{14}CO_2$ (‰) of each site from BHDCGO $\Delta^{14}CO_2$ record for (growth months Nov – Feb) of the years 1986 – 1995, 1996 – 2005, 2006 – 2015. Tree ring records are the average deviation over the entire decade, other records are the average deviation for the available years of each record.

Other than the 1994/1995 feature, there is no indication that the choice of BHDCGO reference record largely influences observed atmospheric $\Delta^{14}CO_2$ variability, although it is considered in further analysis.

7.3 Discussion

7.3.1 Drivers of the Latitudinal $\Delta^{14}CO_2$ Gradient

The overall downward $\Delta^{14}CO_2$ trend (Figure 7.4) is a result of different processes within the radiocarbon cycle: immediately following the bomb period the distribution of bomb ^{14}C through the carbon cycle dominated, with other factors now playing an increasingly important role (Sections 2.2.4). Previous research has shown that in recent years this downward trend has been dominated by increasing fossil fuel ^{14}C-free CO_2 emissions, with smaller contributions from other factors. The upwelling of ^{14}C-depleted deep water at high latitudes of the Southern Hemisphere also contributes to the downward trend (Section 2.2.5), whilst the terrestrial biosphere (predominantly in the tropics and Northern Hemisphere) and low-latitude surface ocean with fast turnover rates have started releasing bomb ^{14}C back into the atmosphere.

This is supported by the relative $\Delta^{14}CO_2$ maximum observed at SAM (14° S), between ^{14}C-depleted fossil fuel CO_2 emissions predominantly in the Northern Hemisphere mid-latitudes, and outgassing from ^{14}C-depleted deep water upwelling at high southern latitudes (Graven et al., 2012a; Turnbull et al., 2009; Levin et al., 2010; Randerson et al., 2002). Similarly, SPO (90 °S) observes relatively high $\Delta^{14}CO_2$ compared to mid-high latitude sites, which has been argued is due to its high altitude, observing higher $\Delta^{14}CO_2$ stratospheric air inputs, and at a distance from the Southern Ocean (Graven et al., 2012b).

Lower atmospheric $\Delta^{14}CO_2$ is observed over the Southern Ocean between ~50 and 70 °S (Figure 7.6). Previous research has argued that this $\Delta^{14}CO_2$ spatial gradient is associated with deep water upwelling which brings carbon rich, ^{14}C-depleted water to the surface ocean (e.g., Levin et al., 2010; Graven et al., 2012b; Turnbull et al., 2009; Section 2.2.5). The resulting air-sea carbon disequilibrium drives CO_2 outgassing, with a strong ^{14}C disequilibrium flux thereby reducing atmospheric $\Delta^{14}CO_2$ in the overlying air. In this study, the lowest values are observed in samples from MCQ (55°S) and NZ-53S (53°S), and

importantly at these sites, the incoming air comes from latitudes of 50 – 60 °S (Figure 7.2). This is the latitudinal band where previous observational and modelling studies indicate that most upwelling of deep water occurs (e.g., Caldeira and Duffy, 2000; Sabine et al., 2004; Ito et al., 2010; Section 2.1.3).

Previous atmospheric $\Delta^{14}CO_2$ studies primarily observed Northern to Southern Hemisphere $\Delta^{14}CO_2$ differences. Northern Hemisphere ^{14}C-free fossil fuel emissions are known to contribute to the atmospheric $\Delta^{14}CO_2$ latitudinal gradient with lower $\Delta^{14}CO_2$ at mid-latitudes of the Northern Hemisphere (Levin et al., 2010; Graven et al., 2012b). Here, through increased spatial resolution of atmospheric $\Delta^{14}CO_2$ measurements across the mid to high Southern latitudes, we observe a latitudinal gradient in the Southern Hemisphere that cannot be driven by fossil fuel emissions in the Northern Hemisphere, which would produce an opposite gradient to that observed here. Therefore our results demonstrate influence of upwelling on atmospheric $\Delta^{14}CO_2$ in the Southern Hemisphere. These results do not rule out the possibility of re-release of bomb ^{14}C from low latitude surface oceans and low-latitude terrestrial biosphere contributing to the Southern hemisphere latitudinal gradient. Further investigation would be needed to evaluate this.

7.3.2 Drivers of the Temporal Trend in $\Delta\Delta^{14}CO_2$

In the previous section, I argued that the Southern Hemisphere latitudinal gradient in $\Delta^{14}CO_2$ is driven by Southern Ocean upwelling. Here I consider how the temporal changes in this latitudinal gradient can be interpreted.

Existing atmospheric CO_2 literature argues that the decadal changes in the Southern Ocean carbon sink anomaly are, in part, driven by decadal changes in the strength of deep-water upwelling (Section 2.1.5). In particular, DeVries et al., (2017) argues that stronger upwelling of carbon-rich (^{14}C-depleted) deep water in the 1980s/1990s led to increased CO_2 outgassing, thus to a negative Southern Ocean carbon sink anomaly (i.e., less net carbon uptake than otherwise expected). Then around 2000 this upwelling reduced, leading to

reduced CO_2 outgassing and a positive Southern Ocean sink anomaly (Section 2.1.5; e.g., Mikaloff-Fletcher et al., 2015; Landschutzer et al., 2016; Gruber et al., 2019).

In Section 2.2.5, I discussed the expected response of atmospheric $\Delta^{14}CO_2$ to changes in upwelling. Increased upwelling of carbon-rich deep waters, which leads to more CO_2 outgassing and therefore reduced net CO_2 uptake, will bring lower $\Delta^{14}CO_2$ waters to the surface, and thus we expect to observe lower atmospheric $\Delta^{14}CO_2$ driven by the stronger disequilibrium flux. This is associated with a stronger atmospheric $\Delta^{14}CO_2$ latitudinal gradient ($\Delta\Delta^{14}CO_2$), with reduced $\Delta^{14}CO_2$ at higher Southern latitudes. The atmospheric $\Delta^{14}CO_2$ observations reported here are consistent with previous research (Section 2.2.6), observing stronger $\Delta\Delta^{14}CO_2$ in 1986 – 1995, indicative of stronger upwelling and associated carbon-rich, ^{14}C-depleted CO_2 outgassing. This subsequently weakens in 1996 – 2005 (Figures 7.5 & 7.7), suggesting reduced upwelling and associated outgassing of relatively ^{14}C-depleted CO_2. The results reported here appear to suggest a return to stronger deep water upwelling over the most recent decade.

These observations therefore indicate a period of stronger upwelling ~1990, followed by reduced upwelling ~2000. These results approximately match with the timing in changes in Southern Ocean carbon sink anomaly, and are thus consistent with study results, i.e., Devries et al., (2017), of a reduced carbon sink anomaly ~1990s driven by increased upwelling, with subsequently reduced upwelling and the Southern Ocean carbon sink regaining its strength ~2000.

Although changes in deep water upwelling appear the most likely, other possible explanations for the decadal changes in $\Delta\Delta^{14}CO_2$ could be changes in $\Delta^{14}CO_2$ of upwelled water masses; changes in atmospheric circulation patterns; or changes in non-ocean contributors to atmospheric $\Delta^{14}CO_2$ (terrestrial biosphere, stratosphere).

7.4 Conclusions

The results of the new tree ring measurements and harmonized Southern Hemisphere dataset are consistent with one another, and show a latitudinal gradient in $\Delta^{14}CO_2$ that is consistent with Southern Ocean upwelling of deep water. Zonal variability is also observed, with a stronger atmospheric $\Delta^{14}CO_2$ gradient in New Zealand than Chile, which appears to be associated with differences in atmospheric circulation.

The temporal trends observed here are consistent with decadal changes in the strength of deep-water upwelling produced by models, and align with observations of recent variability in the Southern Ocean carbon sink anomaly. Thus, these results provide the first observational evidence indicating that decadal changes in deep water upwelling indeed drive changes in the Southern Ocean carbon sink.

Chapter 8

Conclusions

Within this PhD project I reconstruct modern atmospheric $\Delta^{14}CO_2$ over the Southern Ocean through annual-resolution $\Delta^{14}CO_2$ tree ring records spanning 44 – 55 °S for 1985 – 2015. With limited previous regional atmospheric $\Delta^{14}CO_2$ measurements, this contributes valuable new data that enables investigation of atmospheric $\Delta^{14}CO_2$ variability over the Southern Ocean in recent decades.

Whilst largely existing protocols are followed for the preparation of annual growth tree rings for ^{14}C measurement, the automation of the organic solvent wash process developed in this thesis improves sample processing efficiency.

Through data quality analysis I determine that the uncertainties associated with the $\Delta^{14}CO_2$ tree ring measurements approach the high-precision that atmospheric $\Delta^{14}CO_2$ measurements achieve, i.e., ~1.9 ‰. With tree ring samples subject to additional preparation for ^{14}C measurement relative to atmospheric samples, careful and consistent sampling and preparation is particularly important, such that natural and introduced variability is minimised, thereby accurately reflecting atmospheric $\Delta^{14}CO_2$.

The biggest limitation of the application of tree rings in this project is determining an accurate ring count free of false or missing rings, and having a way to evaluate this is critically important, given the size of the atmospheric $\Delta^{14}CO_2$ signal of interest is comparable to the annual difference. In the exposed coastal locations at high latitudes required for this study, traditional chronologies requiring multiple cores from multiple trees were not possible. The results from this study demonstrate that ^{14}C bomb-pulse validation, and where this is not possible, ^{14}C measurements from replicate cores, address this well for the

purpose of reconstructing ^{14}C in the atmosphere. The sampling of whole annual growth rings is also a technical limitation, whereby with increased capability it could be possible to gain further insight from these samples by sampling very narrow tree rings accurately or subsampling annual growth rings into early and late growth seasons.

Where atmospheric $\Delta^{14}CO_2$ measurements are lacking, tree rings prove to be a useful tool to investigate recent atmospheric $\Delta^{14}CO_2$. These new tree ring records, alongside existing atmospheric $\Delta^{14}CO_2$ records, therefore enable more detailed investigation into recent atmospheric $\Delta^{14}CO_2$ in the Southern Ocean Region than was previously possible. Whilst tree rings provide retrospective atmospheric $\Delta^{14}CO_2$ measurements, I recommend that where possible, ongoing flask measurements are preferable as they don't have the extra preparation or risks of false and missing rings associated with tree rings.

Development of a harmonised atmospheric $\Delta^{14}CO_2$ dataset for the Southern Hemisphere further enables investigation of subtle atmospheric $\Delta^{14}CO_2$ variability. This dataset is the outcome of evaluating results of $\Delta^{14}CO_2$ intercomparison activities such that adjustments are made for systematic offsets observed between laboratories. The investigation is currently limited by data available, such that further refinement can be achieved through a range of ongoing intercomparison activities. This initial iteration of the dataset can therefore be developed; better constraining interlaboratory offsets (including temporal variability), whilst striving for ever-higher precision and minimising sources of interlaboratory variability.

Finally, I conducted an initial analysis of recent atmospheric $\Delta^{14}CO_2$ variability over the Southern Ocean through the atmospheric $\Delta^{14}CO_2$ tree ring records presented in this PhD project, in context of the harmonised dataset for the Southern Hemisphere. The tree ring records observe a latitudinal gradient, with reduced atmospheric $\Delta^{14}CO_2$ at higher southern latitudes associated with ^{14}C-depleted deep-water upwelling. This is consistent with other atmospheric $\Delta^{14}CO_2$ records of the harmonised dataset. Regional atmospheric $\Delta^{14}CO_2$ variability is also observed, with a stronger latitudinal gradient in New Zealand than Chile, with more zonally consistent air masses also observed in New Zealand.

Further examination of the patterns and variability can be conducted through the use of a curve fitting procedure, e.g., ccgcrv, to help identify the long-term trends and variability. This will help to overcome the challenge of assessing the long-term trend aside from the significant interannual variability present, particularly given the annual resolution of tree ring records. Ongoing atmospheric $\Delta^{14}CO_2$ measurements within the scope of the harmonised dataset will also help to investigate long term variability, because despite limited coverage, the interannual/decadal variability present will be easier to identify from the long-term trend.

Here I used an atmospheric transport model (HYSPLIT) to assess air mass origin to help interpret the observed atmospheric $\Delta^{14}CO_2$ variability. This could be further developed through more extensive or sophisticated modelling, including different process model simulations to explore how well results correlate with upwelling. The new tree ring records and harmonised dataset could also be used within an atmospheric transport model coupled with an ocean carbon cycle model to investigate upwelling variability. Additionally, results may be considered in context of other regional data, e.g., WOCE and GEOSECS.

Whilst the results of this PhD project go some way in contributing to the efforts of investigation into mechanistic understanding of recent Southern Ocean carbon sink variability, many questions remain, and observations of this vast region are still sparse. If we are to understand the underlying mechanisms and variability of the Southern Ocean carbon sink, further investigations will be needed. Observations of tracers such as ^{14}C can continue to play an important role in isolating different processes, such as upwelling, which are otherwise hard to disentangle with carbon/pCO_2 measurements alone.

Moving forward, expanding background atmospheric $\Delta^{14}CO_2$ flask observations throughout the Southern Hemisphere will provide further insight into spatial and temporal variability of atmospheric $\Delta^{14}CO_2$, in particular the latitudinal $\Delta^{14}CO_2$ gradient, and associated upwelling variability. These observations can be utilised within atmospheric transport models to understand the origins of observed air masses and thus further investigate upwelling and

air-sea carbon exchange. The seasonal variability of upwelling trends can be explored, to assess whether trends observed here in summer are representative of annual trends. Comparisons can also be made with ocean carbon cycle models to assess if the output is consistent with atmospheric $\Delta^{14}CO_2$ observations.

Nonetheless, with the results of this study, I find that atmospheric $\Delta^{14}CO_2$ variability observed over the Southern Ocean in recent decades is consistent with model-suggested upwelling trends. These results are also consistent with studies that suggest variability in upwelling is the underlying mechanism responsible for Southern Ocean carbon sink variability in recent decades. Therefore this observational evidence, including the new tree ring $\Delta^{14}CO_2$ records and harmonised atmospheric $\Delta^{14}CO_2$ dataset, demonstrates that recent decadal variability in upwelling can explain decadal variability of the Southern Ocean carbon sink.

Appendix A

Standard Operating Procedure:

Organic Solvent Washes using an Accelerated Solvent Extraction (ASE) System

Created: Wednesday 11th October 2017

Site:	Gracefield (National Isotope Centre)		
Laboratory:	Radiocarbon Laboratory		
Department:	Environment and Materials		
Last Updated:	20/04/18	**By**:	Rachel Corran

Scope

This procedure describes the organic solvent wash method conducted using an accelerated solvent extraction (ASE) system. This method was initially performed as part of the pretreatment process for modern tree ring samples, with subsequent cellulose extraction. All organic samples that undergo solvent washes, including bones and textiles, are now subject to this ASE solvent wash method, seeking to remove different organic contaminants.

Health & Safety

Hazards

- High pressure gas (~1000 kPa nitrogen and air).
- Organic solvents with potential solvent vapour release.
- ASE system (ASE Dionex 350) gives safety warnings when any minor problem occurs. The user is therefore always aware of problems, even if they do not pose hazards.

Controls

- Use of eye protection and lab coat, (and ear protection when using the air gun).

Environment

- Evaporation of waste solvents in the evaporating dish in the fumehood.
- Reuse of filters and glass beads through baking (at 500℃, and the beads are first sonicated with acetone and rinsed with deionised water).

Sample Collection, Preservation and Storage

Current samples processed with ASE include bones, textiles and tree rings. Samples undergo physical pretreatment of inspection and sometimes fine slicing, before wrapping in glass-fibre filter paper and placing in a labelled glass vial ready for the ASE solvent wash method. Samples are collected ready for processing, then loaded into the ASE cells. Following processing, the samples remain in the filter paper, and are rinsed with deionised water before returning to the glass vial and drying in the 50℃ oven.

Form 618 – ASE SOP

Equipment & Apparatus

- ASE Dionex 350
- ASE 10 mL cells
- 27 mm ASE glass fibre filters for the cell end caps
- Solid glass beads, 3mm (borosilicate)
- Measuring cylinder
- Funnel
- ASE cell funnel

Reagents & Standards

- N-hexane
- Isopropanol
- Acetone
- Food grade nitrogen
- High pressure air
- Deionised water

Technical Notes

Any problems that occur in the procedure are identified by the ASE system, resulting in an error message. Details of the error messages and how to understand and resolve these problems are found in the ASE manual in the draw beneath the system.

Quality Control

A notepad is used to record the errors and operation of samples on ASE, with regular cycling of the cells to ensure even and regular use. The solvents collected in the vials are also recorded if unusual, so that the discharge from the sample can be further assessed if required. A thorough deionised water rinse is conducted to remove any remaining acetone.

Procedure

Daily Operation

Initial checks and start-up

- Check that solvent bottle attachments are tight as they may gradually loosen over time.
- Open the nitrogen tank before turning on the ASE instrument. Note that the regulator on the nitrogen tank should remain unchanged at ~1000 kPa, but if this has significantly dropped or increased then adjust accordingly.
- Press rinse for the system to perform an initial rinse.
- Check that the instrument is set-up to perform sequence 10 (starting at row 1): pressing (1) should bring up the programmed sequence.
- Ensure that vials and rinse bottles are empty, with septa (top filter disc) of suitable condition.

Packing and loading cells

- Each cell (and two corresponding end caps) is labelled with a letter so ensure that these match.
- Use a kimwipe to clean the end caps and inside of the cell column.
- Use the air gun to briefly blow off any dirt or remaining residue.
- Attach a cell end cap to the cell end without a logo.
- Pour clean glass beads into the measuring cylinder (using the funnel) and pour into the cell (using the cell funnel), leaving about 1 cm free inside the top of the cell, or sufficient space to fit the sample.
- Use tweezers to remove the sample in filter paper from the glass vial and hold in place in the top of the cell, whilst pouring glass beads carefully from the measuring cylinder to fill the remaining space in the cell. Packing more beads into the cell reduces the solvent volumes used during processing.
- Fit a clean cell filter into the remaining cell end cap, ensuring no filter overlap with the seal, else the cell will not be able to maintain pressure for processing.
- Screw the end cap onto the cell, tightening sufficiently hand-tight.
- Note the sample and cell details in the logbook and record the cell on the sample bag.
- If the system is ready to load the cell, then place it on the carousel, with the logo (and sample) towards the bottom of the cell to ensure that the beads allow dispersion of the solvent before reaching the sample.
- Record the position of the sample/cell in the logbook.

Running the instrument

- Press start (and the instrument is in sequence 10).
- If the instrument hasn't been run for a while, then the cell pressure should be checked for the first run. Having started the run, press 6 (diagnostics) and then 3 (pressure) to display the cell pressure. Once the oven has reached temperature, the cell will be loaded into the oven, and the compression should read ~135 psi (ideally between 130-140 psi).
- Sequence 10: runs through method 11(n-hexane), method 12 (isopropanol), and method 13 (acetone) for cells in turn, which should be loaded according to the labels by the loading wheel (1,21,17,13,9,5…), so that the cells can be removed easily after processing, and only 2 cells need to be loaded to start the sequence.
- Once started, to monitor the run, press (2) to give the system status.

Unloading and unpacking cells

- After the cell has been processed it will be hot (having been in the oven at 100 degrees), so should be left on the loading wheel until it has cooled sufficiently.
- Place the cell with the sample end at the top, unscrew the top end cap and place the used cell filter into the 'used-filter' beaker.
- Use tweezers to hold the sample, pouring the used beads into the beaker of 'used beads'.
  - Holding the sample with the tweezers, hold it over the 'rinse beaker', and rinse well with

deionised water, before putting back into its glass vial and in the beaker of processed samples ready for the 50℃ oven to dry.
- Place the empty cell at the back of the others so that they are all used in turn, ensuring equal use.
- Once all samples for the day or sequence have been unloaded, place the beaker of samples in the 50℃ oven.
- Record all processing details in the laboratory database.

Other Routine Tasks:

Changing the nitrogen tank

This needs to be done when the tank becomes almost empty, i.e., at a pressure ~1000 kPa, and thus cannot supply the pressure required for ASE to work (~1000 kPa).

- First ensure that ASE has been turned off and the 'empty' nitrogen tank has been closed off.
- Use a large spanner to loosen the regulator on the tank, before loosening by hand and removing.
- Go to the tank store shed and find a ^{14}C labelled food grade nitrogen tank (If it is the last then email Jeremy to notify him and request an order).
- Load the new tank onto a trolley and take it to the lab - ask for assistance if required.
- Unchain the old empty tank and replace with the new tank, returning the empty tank to the chained area outside the tank store.
- Reattach the regulator to the new tank using the spanner.
- Open the tank and turn ASE on, before performing a rinse to start up.

Topping up solvent bottles

This should be done when solvent bottles become low, so that no air is taken up into the system instead of solvent, thereby causing problems. This can be done for one or multiple solvents at a time and should be recorded in the log book.

- Unclick the 'click' attachment BEFORE unscrewing the second screw attachment.
- Proceed to top up the solvents from the solvent cupboard and ensure that the lid is screwed on tightly.
- If a new solvent bottle is needed from the solvent stor:, use the chemical carrier, take the key from the office, and find the required solvents in the store. Leave the used empty solvent bottle in the fumehood to evaporate any residue and notify Jeremy of the solvent transfer from the store to the laboratory (and if using the last bottle of that solvent from the store notify Jeremy and request an order).
- Attach the screw attachment BEFORE clicking the 'click' attachment into place.

Preparing the cell filters and glass beads for reuse

This should be done when the supply of clean beads and filters is becoming low, but not too often as this reduces efficiency.

- Used cell filters should be placed in a small beaker and lightly covered with foil, then placed in the 500℃ oven.
- Used beads should be placed in a beaker with acetone and sonicated for 15-20 minutes, before rinsing with deionised water into the solvent evaporating dish, and then thoroughly rinsing into the sink with deionised water.
- The beads should be placed into the 500℃ oven with a light foil covering, as with the filters.
- Turn the 500℃ oven on at the end of the day to run overnight.

Related Guidelines/Information

Relevant MSDS can be found in the HazChem database on GNS online, and instrument details are in the ASE manual next to the instrument and can also be found online.

Appendix B

XCAMS Procedures

B.1 General Notes

- XCAMS: eXtended Compact ^{14}C Accelerator Mass Spectrometer
- All actions of XCAMS should be recorded in the logbook, giving the time/date and sufficient details to allow others to follow and understand.
- Unless stated, computer-based instructions refer to the control room computer (unless the network pc, using windows, is specified).
- 'K snapshots' can be taken of any control computer window to record a particular observation or setting. This is particularly important when observing something unusual, and notes should also be made in the logbook.
- The 'pen recorder' on the right computer monitor displays selected parameters, which can be selected or rescaled using the parameter list on the right.
- AccelNET on the left computer monitor is predominantly used for remote system control, usually displaying the system diagram (page 51), unless otherwise stated. To change parameters in AccelNET, select and right click to change setting, e.g., on/off or press F9 to enter a new value for the selected parameter.
- Select the CPO from the oscilloscope menu on the left monitor when not using beam profile monitors (BPMs). This ensures that no BPMs are left in-line. The Pelletron provides the voltage (CPO): up to 10 V oscillations. The CPO should show a small but steady oscillation, but nothing too drastic. The adjacent menu on the left monitor selects the group to appear on the control panel display (with control/read-back shown on bottom/top of panel respectively). The control panel should be cleared ('blank') when not using to avoid catching control dials by accident.

B.2 Mounting a Wheel

When the wheel is prepared, a 'runlist' is produced from the laboratory database and saved (on the shared drive) in a folder for the new wheel. The wheel, with pressed samples, is wrapped in foil and placed with the 'wheel layout' list, which details the samples in the wheel. The pressed wheel is then ready to mount in the system, alongside removing a previously measured wheel if one remains in the system.

From the control room computer:

- Turn the isolation transformer off (ITX). This ensures that the ion source (ION), bias (BIA) and oven (OVN) are turned off, although these will already be off unless a wheel measurement has just finished.
- Ensure that the first faraday cup (FC01) is in place and the valve in beam-line 1 (BLV01) is then closed. This is a precaution, so that in the case of a leak there is no loss of vacuum throughout the system.

Setting up and entering the cage:

- Grab disposable gloves and the new wheel, placing carefully on the side outside the cage.
- Open the cage door carefully (the key may be on top of the control box in the control room). Attach the manual grounding stick as a further precaution to the automatic grounding that occurs on opening the door.
- Turn on the scroll pump (just outside the cage), to evacuate up to the horizontal plastic dial (that should be turned horizontal, i.e., closed). By the scroll pump, turn the power control to manual (from remote), to allow manual control from within the cage.
- Remove the acrylic controller rods by undoing them from within the cage, then removing them from outside the cage and hanging on the wall.
- Connect the power cord to the rack. This gives the rack power, to then allow manual control from within the cage.

- Flick the manual switch (on the rack control console) to retract the wheel. This removes the wheel out of the gate position, and then displays a red light on the control console.
- Flick the manual switch (on the rack control console) to close the gate. This changes the light from green (open) to red (closed). The chamber containing the wheel is now isolated from the rest of the system to maintain vacuum.
- Evenly loosen and remove the 4 screws by the gate valve (with the spanner and then by hand), to prepare for opening the system to mount the wheel.
- Turn the green handle to add argon into the first chamber (containing the wheel), such that the vacuum is overcome, and the system can be opened. The ball can be heard clicking into place and the argon tank can be heard within the room once the argon flushes in.
- Manually ease the wheel mount backwards, being careful to pull evenly so that it remains straight. The argon has now served its purpose, so the green handle can be turned off.
- To prepare the in-flow line for evacuating the system once the new wheel has been mounted, turn the small black dial to vertical (i.e., 'off') to isolate the argon. Then open the plastic vacuum dial (to vertical), aiming for a 5e-2 vacuum through the in-flow line.

Removing the measured wheel (if remaining in the system):

- Put on the disposable gloves and use a blue lint cloth to wipe around the front of the remaining wheel, paying particular attention to the lock-knut front. This removes any significant caesium residue from the sputtering.
- Undo the lock-knut screws evenly, loosening a little on opposite screws in the circle, ensuring that the long end of the allen key points across the centre of the lock-knut. Once all screws are loosened sufficiently, use the long end of the allen key to loosen each screw a little, so that they aren't in contact with the wheel.
- The lock-knut should now easily loosen with your hand. Entirely remove it, but be aware that the wheel now has nothing securing it, so theoretically could come off at any moment.

- Ease the wheel off the mount evenly and straight. Be particularly careful with this step as to not damage the wheel or mount, because these contact areas are particularly important. Place the old wheel on the side by the new wheel. If there is any confusion, the old wheel has obvious sputtering residue patterns on the surface, whereas the new wheel is clean and ready to mount.
- Wipe the wheel mount with the blue lint cloth after removing the wheel to remove any remaining caesium residue.

Mounting the new wheel:

- Unwrap the new wheel from the foil, transfer the molybdenum strip carefully from the old wheel, leaving a gap evenly where the indexer key for position 0 is.
- Move the new wheel into the cage, steer it gradually onto the indexer key, and carefully adjust the wheel so that it sits in place.
- Loosely twist the lock-knut into place. Then turn the wheel as far clockwise as possible before tightening the lock-knut firmly by hand.
- If one of the lock-knut screws lies directly over position 0, remove that screw, otherwise gradually tighten opposite lock-knut screws little-by-little. The wheel is now firmly in place.
- Manually slide the wheel mount straight towards the ion gate. Open the chamber up to the scroll pump by turning the green handle, and leave to reach a vacuum of 5e-2.
- Meanwhile add the four screws back in and gradually evenly tighten.

Whilst waiting for a suitable vacuum, the old (measured) wheel can be unloaded and cleaned:

- Place the wheel face-down on the unloading mount and screw the mount top into place.
- Unscrew the back parts of the wheel, removing the screws and parts, and placing aside.
- Open a plastic microcentrifuge tray and label with corresponding TW.
- Starting with cathode 0, push targets up from underneath with a finger and use tweezers to remove them from the wheel and place into the tray in order.
- Close the lid on the microcentrifuge tray and set aside with the others.

- Remove the wheel from the unloading mount. Use water and ethanol with a scouring pad to remove as much caesium residue as possible.
- Place the wheel in a pot of ethanol in the sonicater bath for about 20 minutes. Use ear protection during this.
- Roughly dry the wheel with the air gun and then place into the oven, ready to be baked with other parts.

Having reached a sufficient vacuum (5e-2):

- Close the green handle to isolate the first chamber of the system from the scroll pump, then turn the plastic dial to horizontal and turn the scroll pump off.
- Flick the manual switch (on the rack control console) to open the ion gate (the light will turn from green to red), before flicking the manual switch to move the wheel forward into place (the red light will disappear).
- Turn the small black plastic dial to 'open' (horizontal) to flood the in-flow line with argon. This step is important, as a weak vacuum in the line acts to somewhat ground the system.
- Unplug the power cable to the rack and flick the switch to remote operating, as no more manual control is required from within the cage.
- Place the acrylic rods into the cage, and clip into place from within the cage.
- Return the manual grounding hooks to the cage, and close the cage door, ensuring that the door clicks into place so that the sensor recognises it. Lock and return the key to the top of the control box in the control room.
- Returning to the control room computer, leave ion gate pressure (IGC01) on the pen recorder so that you can monitor the vacuum, until it reaches a sufficient vacuum of 5e-7.

B.3 Starting the Ion Source (SNICS)

Whilst preparing SNICS for measurement, we want to work with a vacuum at/better than 5e-7. Note that the beam created has the extraction (EXT) potential and that most acceleration comes from the BIA.

From the control room computer (in AccelNET):

- Turn the ITX transformer on to give power to the rack, meanwhile ensure that the ion source and oven settings are down, so that that they do not shoot up to previous working values. The settings will depend on how the previous measurement was stopped, i.e., if 'park' mode was used or not. Also note that although the ITX transformer turns the BIA off, the BIA needs to be turned on separately.
- Open BLV01 so that the whole system is now opened up, and ensure that beam-line 1 is turned on (green circle on the far left of the system diagram).
- Place FC06 in interlock (nlk), using the square by the cup in the system diagram. This acts as a safety mechanism such that it cannot be removed from the beam-line by accident, thereby subjecting the detector to high beam current.
- Go to page 10 in AccelNET to get MCSNICS to 'home' position at 0, which then allows cathode voltage to be produced. Then return to the system diagram (page 51).
- Set the position to cathode 38, which is always the kapuni for tuning.
- Gradually increase the ioniser (ION), being careful not to increase such that the vacuum worsens too much or you go above 200W, as this will ruin the filament eventually. (Note that 130 W is a good value for the ioniser.) Depending on how the last measurement was stopped there may also be significant caesium present in the system. Steps of 10, 15, 18, 21 A can be used, progressing depending on system response. Return the ioniser to the previous measurement setting.
- Once the vacuum has stabilised with the ioniser setting, turn on the oven (OVN) to the previous measurement voltage (~20 – 26 V). Depending on outgassing, apply 'boosts' of additional voltage (using AccelNET page 10), being careful not to overshoot. (Note that once a boost has been applied it cannot be nulled, except to null the voltage applied, whilst the timer will continue.) FC01 should be placed on pen recorder and monitored until sufficient stable current of >50 mA is obtained in FC01. ION and OVN settings should be adjusted accordingly to achieve this.

B.4 Tuning XCAMS for ^{14}C measurement

- If the measurement from the previous wheel is good, then after mounting a wheel, only a slight adjustment of the acrylic rods to optimise current in FC01 may be required.
- The instrument should return to a state of good measurement, assuming that nothing major has changed and it has been less than a week since the previous tune. The time since the last tune should be taken into consideration, as over time the system can drift.
- Note that BPMs display the y-peak and x-peak on the left and right of the oscilloscope display, respectively. Centre bars appear by turning the green dial. The square button can be used to move down the oscilloscope menu, so that the scaling can then be changed using the dial.
- Note that magnets must be removed from feedback loops when adjusting their field, else the adjustment will not be applied to the field. This is achieved through selecting the adjacent square to the magnet on the system diagram, which will turn from green (enable SC) to grey.

Adjustment of the Controller Adjuster Rods (CARs, for all wheels):

- Ensure that FC01 remains in place (else insert it) to optimise the current detected by FC01.
- Select FC01 on the system diagram and bring it up on the top-right read-back panel of the control panel, thereby relaying the value to the voltmeter on the cage.
- Go to the cage and turn the CARs until the maximum current is reached. First roughly adjust them in turn, and then conduct a finer check.
- Briefly check that the beam-line 1 profile (in BPM01) looks ok: check the general shape and overall peak characteristics.
- Remove BPM01 by selecting CPO on the oscilloscope so that there is no beam interference.

If not conducting a full system tune then proceed to starting measurement (B.5).
Otherwise proceed on the control room computer:

- Keeping FC01 in place, scale from ^{14}C to ^{13}C (a message will appear to confirm that you are wanting to do this). This is because for a first tune through the system we use a ^{13}C beam as if it is ^{14}C, because it gives a greater beam current to work with.
- Remove FC01 and ensure that FC04 is in place, so that we can roughly tune the bending magnet in beam-line 3 (BM03). BM03 distinguishes the different mass ions, i.e., ^{12}C, ^{13}C and ^{14}C.
- Insert BPM04 so that it appears on the oscilloscope, seeking to get the x-peak well aligned and central, as BM03 affects the horizontal component of the beam. The y-peak alignment isn't as important, so long as the baseline doesn't move, which can be a sign of secondary electron beams.
- Having removed BM03 from its feedback loop, bring BM03 up on the control and readback of the control panel, and adjust the field by turning the corresponding dial on the control panel. Note down the points where the peak is maximum shifted to either side and before the baseline moves. The optimum magnet setting should be halfway between these two points, but confirm this after setting the magnet, else recalculate and adjust. Press set magnet field control = magnet field readback on the little AccelNET menu at the bottom of the screen to set the magnet at the new setting.
- Return BM03 to its feedback loop. When a magnet is changing its field it appears yellow, before returning to green once stable at its assigned value. Remove BPM04 by selecting CPO on the oscilloscope so that there is no beam interference, as the following parameters will be tuned on FC04.
- Look at the beam in FC04 to check that the beam (having optimised BM03) is sitting around the maximum. This means that for finer tuning of the earlier part of the system that the beam is in the centre of the cup.

Tuning BM01 and horizontal and vertical electrostatic steerers (ES-X and ES-Y):

- Take the bending magnet in beam-line 1 (BM01) out of its feedback loop, and change all three of these parameters from jumping mode to DC (setup), sitting on registry 2 (reg2). Reg2 usually refers to ^{14}C, with reg1 being ^{13}C and reg0 being ^{12}C, however here we have scaled down, so reg2 is in fact ^{13}C.
- Select 'group 12' on the control panel (for tuning reg2 here).

- Looking at FC04, ensure that no BPM or otherwise remain in the beam-line causing interference. First save the values, before roughly tuning BM01, ES-X and ES-Y by turning the control panel dials and seeking the maximum FC04 current. Check that the sensitivity of the dials is reasonable (tfs = turn full scale).
- To more precisely tune the three parameters: find a point just below either side of the parameter value (the 'drop-off') that achieves maximum current in FC04. Calculate the average of each side of the drop-off points, and set the parameter values to the average (mid-point). Confirm the settings using a quick drop-off check by turning the control panel dials in either direction from the maximum. For BM01 use the field value to achieve this, and note that although BM03 appears on the panel, it was tuned using BPM04, but you can check its value.

Moving on to tune the next part of the system beyond FC04 for ^{13}C as ^{14}C:

- Place FC05 and BPM05 in line, ensuring that no earlier FCs or BPMs remain in line.
- With BPM05 on the oscilloscope, bring group 8 up onto the control panel. Using the baseline shift of the x-axis peak on the LHS and RHS, determine the optimum value for the ESA.
- Ensure that FC06 are BPM06 are in place, removing FC05 and BPM05. Bring group 9 up on the control panel.
- The magnetic steerer (MS05) is the only parameter tuned at this point with ^{13}C. Change the MS05 value, then change the EQ strength at a particular MS05 value. Changing the EQ strength should not have a large impact on the position of the y-peak on the oscilloscope. Try out different MS05 settings whilst adjusting the EQ strength, before determining the most suitable value.
- Print the ^{13}C tuning parameters ('print S1 to post' on the control room computer).

Input values to spreadsheet (found in 'TW data analysis' - 'tuning/performance') to check on values in terms of long-term variation and how they align with previous values

We are now ready to tune the system for 14C:

- Putting FC01 in place, and ensuring that all BMs are returned to close-loop feedback, scale back up from ^{13}C to 14C.

- Remove FC01 such that the beam reaches FC04 unobstructed (e.g., by BPMs), as FCs in beam-line 4 will again be used for tuning the first part of the system.
- Change BM01, ES-X and ES-Y to jumping mode from DC (setup). Having tuned BM01 with ^{13}C, the electrostatic chamber within the magnet that switches between the isotopes must be tuned, but the magnet stays in its feedback loop for this.
- Sufficient cathode current should remain on cat38, but otherwise transfer to cat39, which is ANU sucrose, also a tuning target.
- Start continuous collection by adjusting the collect ('coll') parameters. Although the beam will not reach the detector due to FCs, it will cycle through reg0, reg1 and reg2, which are now ^{12}C, ^{13}C and ^{14}C respectively. Having previously tuned reg2 (using ^{13}C as ^{14}C), we now tune reg1, then reg0 similarly.
- Select group 11 to appear on the control panel (relates to reg1), then as before, roughly tune BM01, ES-X and ES-Y, before finer tuning using the corresponding FC in beam-line 4 and calculating the mid-point of the maximum drop-off points.
- Similarly, select group 10 (for reg0) on the control panel and tune exactly as with reg1, but optimising current into the corresponding FC in beam-line 4.

Moving to finely tune the next part of the system beyond FC04 for ^{14}C:

- Note that the ESA doesn't need to be retuned with ^{14}C because it has the same energy as ^{13}C.
- If we are not sitting on cat39 already, then transfer to cat39 at this point, because sucrose (cat39) gives a higher ^{14}C count to tune the system with.
- Moving across to the network pc, find the tuning spreadsheet in a previous wheel folder and copy it to the folder of the current wheel that we are tuning on. This folder will have been created with the runlist and other documents. Change the name of the spreadsheet before opening it up.
- Bring up group 9 on the control panel and follow through the spreadsheet, first tuning BM05, then EQ strength and balance.

B.5 Starting Measurement

- Whether a full tune has been conducted or not, a 1200 cycle should be run on cat39 and key parameters recorded in the logbook. FC values should then be saved, through inserting them one by one and clicking on the square. Print the system parameters ('print S1 to post' on the control room computer).
- The system should now be ready for measurement, having run the 1200 cycle and got results consistent with expected/previous - check in log book a bit if unsure to remind of suitable values. Also ensure that the CPO is shown on the oscilloscope (so no BPMS remain in line) and that the control panel is cleared.
- The second display layout on the control room computer should then be selected, to view folders and open the command window.
- On the network pc open the runlist for the current wheel in notepad. Check it over and make any adjustment necessary, e.g., change the run number to 35 or 50 (using alt and selecting the column you can change the run numbers all at once). Save any changes.
- Copy the runlist for the current wheel onto the share drive, which is then visible on the control room computer (on selecting the folder, pressing F5 will refresh the contents of that specific folder).
- Moving to the control computer, before proceeding, check that the final output file from the previous measurement has been saved.
- Using the command window, use the following code to create a new wheel folder and load the runlist. Using the up arrow the code can easily be found from previous commands rather than retyping the full commands. Using the tab having started a command also automatically completes the rest of the command, e.g., if there is only one file name that could be used.
    - pwd: present working directory.
    - ls: show local files.
    - cd .. (or cd/datasets/C-14): change directory to. Note that navigating to the select the desired folder on the folder view layout and pressing F4 also moves to that folder.
    - mkdir TWXXXX_1: make directory.

    - mv TWXXXX_1.runlist runlist: move wheel runlist to runlist.
    - set_runlist: set the runlist.
- Returning to the original display layout on the control room computer, the blue DMAN window should now appear populated with details of the new wheel ready to start measurements.
- Double check that everything looks correct and that the system is ready, then press 'coll' in the DMAN window to start collecting data and thus start the measurement.
- Ensure that the 'park on' button is displayed in the DMAN window, so that measurement can be stopped using the park protocol, which can be activated by inserting FC01 from the control room or remotely from home.

B.6 Keeping Track of Measurement

Once measurement has started, keeping track of the progress of the measurement is key. There is potential that the measurement will need to be stopped and the system retuned if particularly bad results. Otherwise, it is just important to check the state of measurement in AccelNET and results in the blue DMAN window. The system can also be monitored remotely, using the vpn, putty and the NEC webpage, and filezilla can be used to transfer an output file created.

- In AccelNET the pen recorder of key parameters should be monitored alongside values displayed on the system diagram, e.g.,
    - $^{12}C^-$ (FC04-1) should be around 50-60
    - Cathode current (CAT CR) should be around 100
- In DMAN results, key standard values should be checked, including:
    - Transmission of all samples should be pretty consistent (around 43%)
    - Oxalic acid values should be consistent with expected
    - The chi-squared value of the oxalic acid cathodes should not be much above 10 ideally, and should be monitored.
    - Sucrose, kapuni and other standard values can also be checked.

B.7 Pausing Measurement

A measurement is sometimes temporarily stopped (paused), e.g., if wanting to retune the system before continuing with measurement. We therefore don't want to instigate the 'park' protocol as we want the oven to remain on.

- On the control room computer press 'stop' in the blue DMAN window on the left. This pauses the measurement, and is usually conducted at the end of a cycle on a cathode.
- Press 'endrun' in the same window. This finishes the measurement and closes the data file produced from that run.
- The system is then ready for retuning or otherwise. Remember to save the measurement data file using the command line (detailed below in finishing measurement).

B.8 Finishing Wheel Measurement

A wheel measurement is finished when sufficient counts have been collected on the oxalic I standards. This is usually ~350 000, or ~650 000 for high precision wheels.

- The measurement can be stopped in the same way as for pausing measurement, i.e., using 'stop' and 'endrun'. Alternatively, 'park' mode should have been left on, such that inserting FC01 triggers the park sequence, thereby stopping measurement, putting FCs in and turning the oven off. Stop measurement at the end of a run or ideally at the end of a rotation.
- The data file created on stopping the measurement must now be exported. In the command window of the second display layout, use the up arrow to scroll through previous commands to find the 'DMANprint v2' command. Edit the command with the current wheel name before executing. The full command is:

DMANprint-v2 - -template print - -report results | awk -f /datasets/C-14\/AWKscript/Dman2Xcalams_14C > /datasets/share/TWXXXX_1.out

- Pressing F5 whilst in the share drive should refresh the file and display the exported data file. Moving across to the network pc, this data file should be moved into the corresponding wheel file, using Filezilla.
- If measurement was stopped by inserting FC01 (and 'park' mode), then the final row of the exported data file must be deleted by opening the file in excel. This row will be incomplete as it is of the run that had started but was not populated with measurements.
- Otherwise if measurement was paused, and thus the wheel measurement is in two parts, then the tow data files must be combined in excel because CalAMS uses one input file only. A unique identifier code must be ensured throughout the datasets, for which alt+e+i+a produces a series.

B.9 CalAMS analysis

CalAMS is an in-house program created to visualise and analyse the data from XCAMS. Samples are considered in context of the standards (oxI) and adjusted accordingly. Note that HE and LE mean high and low energy, respectively. Remember to work in 'mode 5' and use this for export: $(^{14}C \times ^{12}C) / (^{13}C)^2$

- Open CalAMS on the network pc and go to file- load C-14 AMS data, and select the data file for the current wheel. Check that it is in mode 5 on the RHS panel.
- Holding down ctrl whilst scanning over the data with the mouse highlights the different cathodes and their trends over the measurement.
- Different y-axis options can be used to view different measurement parameters and get a feeling for the overall measurement. The parameters include:
    - ^{12}C HE (or similar to ^{12}C LE): check the ^{12}C current has not maxed out and gone beyond the detection limit, else calculations cannot be performed suitably. Check that cathodes are relatively stable and haven't burnt out, at which point the current will drop off quite fast.
    - transmission (^{12}C HE / ^{12}C LE): this should remain fairly constant, but will vary
    - ^{13}C: looks similar to ^{12}C currents
    - $^{13}C/^{12}C$ HE: this should be approximately horizontal

- At this point data points can be rejected. To reject a point, select it and then right click, and the point will fill in as a solid point. Data points in the middle of a run can be rejected if data corresponding to that run is anomalous in a number of parameters, suggesting a problem with that run. If points have anomalous values in multiple parameters then this could be reason for rejection, but in some cases if correct in $^{13}C/^{12}C$ HE then this correction has taken account for the observed variation.
- Some periods of the overall measurement may need to be discarded. For example, the first few runs on the 'blank' cathodes will likely have surface contamination and may need to be discarded. If all data for the start or a period during measurement need to be discarded, this can be done by creating multiple 'regions' in the RHS panel, to disregard periods of measurement.
- A regression using the oxI standards should then be conducted, by selecting the positions of the standards on the RHS panel and then ctrl+r to conduct a regression. ctrl+s will display the results, whilst ctrl+x will display a histogram of result distribution. Having conducted a regression, compare standard values with expected/consensus values, and look at different values shown on the results page:
    - separate probability (P) values for all individual cathodes: reflects the repeatability of each cathode throughout the measurement.
    - regression P: takes into account the repeatability of all cathodes.
    - calibration P: reflects the repeatability of all the oxI standard cathodes.
- Different parameters of the run should then be looked at again in context of the regression performed, including the reduced and residuals parameters. These parameters help to highlight any further points for rejection and far outliers.
- An error adjustment can be conducted if the statistics do not look good, but first try to optimise them without applying an error adjustment. The error adjustment is applied using ctrl+e. The error adjustment parameters in the bottom right can then be adjusted as desired. For example, the 'blank' cathode results can be clumped (and increased from 25), where there isn't enough data points to produce meaningful statistics. Having applied an error adjustment to the data, a new regression must be conducted (ctrl+r) and results (ctrl+s) may show additional parameters to account for this adjustment:

- global run-to-run var adjustment factor: adjustment factor applied to all cathodes as a result of the regression P.
- individ run-to-run var adjustment factors: these are adjustments applied to individual cathodes (e.g., 1.2(cat14) that have low P values. Calib pos-to-pos var system error: adjustment factor relating to the variability of the oxI standard cathodes (i.e., calibration P), that should have comparable values to one another.

B.10 Blank Corrections

- Once the blank correction is complete then email The Radiocarbon Laboratory, Margaret, Jen and Jocelyn (if it is her research samples). Put TW XXXX ready for signoff as the subject.

References

Abrha, Y. and Raghavan, D., 2000. Polychlorinated biphenyl (PCB) recovery from spiked organic matrix using accelerated solvent extraction (ASE) and Soxhlet extraction. Journal of hazardous materials, 80(1-3), pp.147-157.

Aerts-Bijma, A.T., Meijer, H.A.J. and Van Der Plicht, J., 1997. AMS sample handling in Groningen. Nuclear Instruments and Methods in Physics Research Section B: Beam Interactions with Materials and Atoms, 123(1-4), pp.221-225.

Andres, R.J., Boden, T.A., Bréon, F.M., Ciais, P., Davis, S., Erickson, D., Gregg, J.S., Jacobson, A., Marland, G., Miller, J. and Oda, T., 2012. A synthesis of carbon dioxide emissions from fossil-fuel combustion.

Andreu-Hayles, L., Santos, G.M., Herrera-Ramírez, D.A., Martin-Fernández, J., Ruiz-Carrascal, D., Boza-Espinoza, T.E., Fuentes, A.F. and MJ, P., 2015. Matching dendrochronological dates with the Southern Hemisphere 14 C bomb curve to confirm annual tree rings in Pseudolmedia rigida from Bolivia. Radiocarbon, 57(1), pp.1-13.

Ansell, I.A., 2016. RECONSTRUCTING URBAN CO2 EMISSIONS UTILISING THE RADIOCARBON COMPOSITION OF TREE RINGS FROM THE WELLINGTON REGION, NEW ZEALAND (Doctoral dissertation, Victoria University of Wellington).

Arrigo, K.R., van Dijken, G. and Pabi, S., 2008. Impact of a shrinking Arctic ice cover on marine primary production. Geophysical Research Letters, 35(19).

Baisden, W.T., Prior, C.A., Chambers, D., Canessa, S., Phillips, A., Bertrand, C., Zondervan, A., Turnbull, J.C., Kaiser, J. and Bruhn, F., 2013. Rafter radiocarbon sample preparation and data flow: Accommodating enhanced throughput and precision. Nuclear Instruments and Methods in Physics Research Section B: Beam Interactions with Materials and Atoms, 294, pp.194-198.

Bakker, D.C.E., De Baar, H.J.W. and Bathmann, U.V., 1997. Changes of carbon dioxide in surface waters during spring in the Southern Ocean. Deep Sea Research Part II: Topical Studies in Oceanography, 44(1-2), pp.91-127.

Ballantyne, A.P., Alden, C.B., Miller, J.B., Tans, P.P. and White, J.W.C., 2012. Increase in observed net carbon dioxide uptake by land and oceans during the past 50 years. Nature, 488(7409), pp.70-72.

Battle, M., Bender, M.L., Tans, P.P., White, J.W.C., Ellis, J.T., Conway, T. and Francey, R.J., 2000. Global carbon sinks and their variability inferred from atmospheric O2 and δ13C. Science, 287(5462), pp.2467-2470.

Baxter, M.S. and Farmer, J.G., 1973. Radiocarbon: short-term variations. E&PSL, 20(3), pp.295-299.

Biondi, F., Strachan, S.D., Mensing, S. and Piovesan, G., 2007. Radiocarbon analysis confirms the annual nature of sagebrush growth rings. Radiocarbon, 49(3), pp.1231-1240.

Bird, M.I., Ayliffe, L.K., Fifield, L.K., Turney, C.S., Cresswell, R.G., Barrows, T.T. and David, B., 1999. Radiocarbon dating of “old” charcoal using a wet oxidation, stepped-combustion procedure. Radiocarbon, 41(2), pp.127-140.

Boaretto, E., Bryant, C., Carmi, I., Cook, G., Gulliksen, S., Harkness, D., Heinemeier, J., McClure, J., McGee, E., Naysmith, P. and Possnert, G., 2002. Summary findings of the fourth international radiocarbon intercomparison (FIRI)(1998–2001). Journal of Quaternary Science: Published for the Quaternary Research Association, 17(7), pp.633-637.

Boyd, P.W., Watson, A.J., Law, C.S., Abraham, E.R., Trull, T., Murdoch, R., Bakker, D.C., Bowie, A.R., Buesseler, K.O., Chang, H. and Charette, M., 2000. A mesoscale phytoplankton bloom in the polar Southern Ocean stimulated by iron fertilization. Nature, 407(6805), pp.695-702.

Bousquet, P., Peylin, P., Ciais, P., Le Quéré, C., Friedlingstein, P. and Tans, P.P., 2000. Regional changes in carbon dioxide fluxes of land and oceans since 1980. Science, 290(5495), pp.1342-1346.

Brock, F., Higham, T., Ditchfield, P. and Ramsey, C.B., 2010. Current pretreatment methods for AMS radiocarbon dating at the Oxford Radiocarbon Accelerator Unit (ORAU). Radiocarbon, 52(1), pp.103-112.

Brock, F., Dee, M., Hughes, A., Snoeck, C., Staff, R. and Ramsey, C.B., 2018. Testing the effectiveness of protocols for removal of common conservation treatments for radiocarbon dating. Radiocarbon, 60(1), pp.35-50.

Broecker, W.S. and Peng, T.H., 1974. Gas exchange rates between air and sea. Tellus, 26(1-2), pp.21-35.

Broecker, W.S. and Peng, T.H., 1982. Tracers in the Sea.

Broecker, W.S., Peng, T.H., Ostlund, G. and Stuiver, M., 1985. The distribution of bomb radiocarbon in the ocean. Journal of Geophysical Research: Oceans, 90(C4), pp.6953-6970.

Brown, T.A. and Southon, J.R., 1997. Corrections for contamination background in AMS 14C measurements. Nuclear Instruments and Methods in Physics Research Section B: Beam Interactions with Materials and Atoms, 123(1-4), pp.208-213.

Bruhn, F., Duhr, A., Grootes, P.M., Mintrop, A. and Nadeau, M.J., 2001. Chemical Removal of Conservation Substances by “Soxhlet “-Type Extraction. Radiocarbon, 43(2A), pp.229-237.

Buesseler, K.O., Andrews, J.E., Pike, S.M. and Charette, M.A., 2004. The effects of iron fertilization on carbon sequestration in the Southern Ocean. Science, 304(5669), pp.414-417.

Cain, W.F. and Suess, H.E., 1976. Carbon 14 in tree rings. Journal of Geophysical Research, 81(21), pp.3688-3694.

Caldeira, K., Rau, G.H. and Duffy, P.B., 1998. Predicted net efflux of radiocarbon from the ocean and increase in atmospheric radiocarbon content. Geophysical Research Letters, 25(20), pp.3811-3814.

Caldeira, K. and Duffy, P.B., 2000. The role of the Southern Ocean in uptake and storage of anthropogenic carbon dioxide. Science, 287(5453), pp.620-622.

Canadell, J.G., Le Quéré, C., Raupach, M.R., Field, C.B., Buitenhuis, E.T., Ciais, P., Conway, T.J., Gillett, N.P., Houghton, R.A. and Marland, G., 2007. Contributions to accelerating atmospheric CO2 growth from economic activity, carbon intensity, and efficiency of natural sinks. Proceedings of the national academy of sciences, 104(47), pp.18866-18870.

Ciais, P., C. Sabine, G. Bala, L. Bopp, V. Brovkin, J. Canadell, A. Chhabra, R. DeFries, J. Galloway, M. Heimann, C. Jones, C. Le Quéré, R.B. Myneni, S. Piao and P. Thornton, 2013: Carbon and Other Biogeochemical Cycles. In: Cli- mate Change 2013: The Physical Science Basis. Contribution of Working Group I to the Fifth Assessment Report of the Intergovernmental Panel on Climate Change [Stocker, T.F., D. Qin, G.-K. Plattner, M. Tignor, S.K. Allen, J. Boschung, A. Nauels, Y. Xia, V. Bex and P.M. Midgley (eds.)]. Cambridge University Press, Cambridge, United Kingdom and New York, NY, USA.

Coale, K.H., Johnson, K.S., Chavez, F.P., Buesseler, K.O., Barber, R.T., Brzezinski, M.A., Cochlan, W.P., Millero, F.J., Falkowski, P.G., Bauer, J.E. and Wanninkhof, R.H., 2004. Southern Ocean iron enrichment experiment: carbon cycling in high-and low-Si waters. science, 304(5669), pp.408-414.

Cox, P.M., Betts, R.A., Jones, C.D., Spall, S.A. and Totterdell, I.J., 2000. Acceleration of global warming due to carbon-cycle feedbacks in a coupled climate model. Nature, 408(6809), pp.184-187.

Currie, K.I., Brailsford, G., Nichol, S., Gomez, A., Sparks, R., Lassey, K.R. and Riedel, K., 2011. Tropospheric 14 CO 2 at Wellington, New Zealand: the world's longest record. Biogeochemistry, 104(1-3), pp.5-22.

De Vries, H.L. and Barendsen, G.W., 1954. Measurements of age by the carbon-14 technique. Nature, 174(4442), pp.1138-1141.

DeVries, T., Holzer, M. and Primeau, F., 2017. Recent increase in oceanic carbon uptake driven by weaker upper-ocean overturning. Nature, 542(7640), pp.215-218.

Dlugokencky, E.J., Lang, P.M., Masarie, K.A., Crotwell, A.M. and Crotwell, M.J., 2015. Atmospheric carbon dioxide dry air mole fractions from the NOAA ESRL Carbon Cycle Cooperative Global Air Sampling Network, 1968–2014. NOAA ESRL Global Monitoring Division, Boulder, CO, USA.

Donahue, D.J., Linick, T.W. and Jull, A.T., 1990. Isotope-ratio and background corrections for accelerator mass spectrometry radiocarbon measurements. Radiocarbon, 32(2), pp.135-142.

Fichtler, E., Clark, D.A. and Worbes, M., 2003. Age and long-term growth of trees in an old-growth tropical rain forest, based on analyses of tree rings and 14C1. Biotropica, 35(3), pp.306-317.

Fines-Neuschild, S., Boucher, É., de Vernal, A., Gélinas, Y. and Leclerc, P., 2015. Accelerated solvent extraction—An efficient tool to remove extractives from tree-rings. Dendrochronologia, 36, pp.45-48.

Friedlingstein, P., Bopp, L., Ciais, P., Dufresne, J.L., Fairhead, L., LeTreut, H., Monfray, P. and Orr, J., 2001. Positive feedback between future climate change and the carbon cycle. Geophysical Research Letters, 28(8), pp.1543-1546.

Friedlingstein, P., Cox, P., Betts, R., Bopp, L., von Bloh, W., Brovkin, V., Cadule, P., Doney, S., Eby, M., Fung, I. and Bala, G., 2006. Climate–carbon cycle feedback analysis: results from the C4MIP model intercomparison. Journal of climate, 19(14), pp.3337-3353.

Fritts, H.C., 1976. 1976: Tree rings and climate. London: Academic Press.

Gaudinski, J.B., Dawson, T.E., Quideau, S., Schuur, E.A., Roden, J.S., Trumbore, S.E., Sandquist, D.R., Oh, S.W. and Wasylishen, R.E., 2005. Comparative analysis of cellulose preparation techniques for use with 13C, 14C, and 18O isotopic measurements. Analytical Chemistry, 77(22), pp.7212-7224.

Gloor, M., Sarmiento, J.L. and Gruber, N., 2010. What can be learned about carbon cycle climate feedbacks from the CO2 airborne fraction?. Atmospheric Chemistry and Physics, 10(16), pp.7739-7751.

Godwin, H., 1962. Half-life of radiocarbon. Nature, 195(4845), pp.984-984.

Goldstein, I.S., 2004. Chemical Properties of Wood. Chap. Wood Formation and Properties In Encyclopedia of Forest Sciences, edited by J. Burley: Elsevier Ltd.

Graven, H.D., Guilderson, T.P. and Keeling, R.F., 2007. Methods for high-precision 14 C AMS measurement of atmospheric CO 2 at LLNL. Radiocarbon, 49(2), pp.349-356.

Graven, H.D., 2008. Advancing the use of radiocarbon in studies of global and regional carbon cycling with high precision measurements of ^{14}C in CO_2 from the Scripps CO_2 Program (Doctoral dissertation, UC San Diego).

Graven, H.D., Guilderson, T.P. and Keeling, R.F., 2012(a). Observations of radiocarbon in CO2at La Jolla, California, USA 1992–2007: Analysis of the long-term trend. *Journal of Geophysical Research: Atmospheres*, *117*(D2).

Graven, H.D., Guilderson, T.P. and Keeling, R.F., 2012(b). Observations of radiocarbon in CO2 at seven global sampling sites in the Scripps flask network: Analysis of spatial gradients and seasonal cycles. *Journal of Geophysical Research: Atmospheres*, *117*(D2).

Graven, H.D., Gruber, N., Key, R., Khatiwala, S. and Giraud, X., 2012(c). Changing controls on oceanic radiocarbon: New insights on shallow-to-deep ocean exchange and anthropogenic CO2 uptake. *Journal of Geophysical Research: Oceans*, *117*(C10).

Graven, H.D., Xu, X., Guilderson, T.P., Keeling, R.F., Trumbore, S.E. and Tyler, S., 2013. Comparison of independent Δ14CO2 records at Point Barrow, Alaska. Radiocarbon, 55(2–3), pp.1541-1545.

Graven, H., Allison, C.E., Etheridge, D.M., Hammer, S., Keeling, R.F., Levin, I., Meijer, H.A., Rubino, M., Tans, P.P., Trudinger, C.M. and Vaughn, B.H., 2017. Compiled records of carbon isotopes in atmospheric CO2 for historical simulations in CMIP6. Geoscientific Model Development (Online), 10(12).

Green, J.W., 1963. Wood cellulose. Methods in carbohydrate chemistry, pp.9-12.

Grootes, P.M., Farwell, G.W., Schmidt, F.H., Leach, D.D. and Stuiver, M., 1989(a). Importance of biospheric CO2 in a subcanopy atmosphere deduced from 14C AMS measurements. *Radiocarbon*, *31*(3), pp.475-480.

Grootes, P.M., Farwell, G.W., Schmidt, F.H., Leach, D.D. and Stuiver, M., 1989(b). Rapid response of tree cellulose radiocarbon content to changes in atmospheric 14; CO2 concentration. *Tellus B: Chemical and Physical Meteorology*, *41*(2), pp.134-148.

Gruber, N., Landschützer, P. and Lovenduski, N.S., 2019. The variable Southern Ocean carbon sink. *Annual review of marine science*, *11*, pp.159-186.

Guilderson, T.P., Caldeira, K. and Duffy, P.B., 2000. Radiocarbon as a diagnostic tracer in ocean and carbon cycle modeling. Global Biogeochemical Cycles, 14(3), pp.887-902.

Gurney, K.R., Law, R.M., Denning, A.S., Rayner, P.J., Baker, D., Bousquet, P., Bruhwiler, L., Chen, Y.H., Ciais, P., Fan, S. and Fung, I.Y., 2002. Towards robust regional estimates of CO 2 sources and sinks using atmospheric transport models. Nature, 415(6872), pp.626-630.

Hall, A. and Visbeck, M., 2002. Synchronous variability in the Southern Hemisphere atmosphere, sea ice, and ocean resulting from the annular mode. Journal of Climate, 15(21), pp.3043-3057.

Hammer, S., Friedrich, R., Kromer, B., Cherkinsky, A., Lehman, S.J., Meijer, H.A., Nakamura, T., Palonen, V., Reimer, R.W., Smith, A.M. and Southon, J.R., 2017. Compatibility of atmospheric 14 CO 2 measurements: Comparing the Heidelberg low-level counting facility to international accelerator mass spectrometry (AMS) laboratories. Radiocarbon, 59(3), pp.875-883.

Hansell, D.A., Carlson, C.A., Repeta, D.J. and Schlitzer, R., 2009. Dissolved organic matter in the ocean: A controversy stimulates new insights. Oceanography, 22(4), pp.202-211.

Hansen, J., Johnson, D., Lacis, A., Lebedeff, S., Lee, P., Rind, D. and Russell, G., 1981. Climate impact of increasing atmospheric carbon dioxide. Science, 213(4511), pp.957-966.

Hansen, J., Sato, M., Kharecha, P., Russell, G., Lea, D.W. and Siddall, M., 2007. Climate change and trace gases. Philosophical Transactions of the Royal Society A: Mathematical, Physical and Engineering Sciences, 365(1856), pp.1925-1954.

Hauck, J., Völker, C., Wolf-Gladrow, D.A., Laufkötter, C., Vogt, M., Aumont, O., Bopp, L., Buitenhuis, E.T., Doney, S.C., Dunne, J. and Gruber, N., 2015. On the Southern Ocean CO2 uptake and the role of the biological carbon pump in the 21st century. Global Biogeochemical Cycles, 29(9), pp.1451-1470.

Heemken, O.P., Theobald, N. and Wenclawiak, B.W., 1997. Comparison of ASE and SFE with soxhlet, sonication, and methanolic saponification extractions for the determination of

organic micropollutants in marine particulate matter. Analytical chemistry, 69(11), pp.2171-2180.

Hesshaimer, V. and Levin, I., 2000. Revision of the stratospheric bomb 14CO2 inventory. Journal of Geophysical Research: Atmospheres, 105(D9), pp.11641-11658.

Hofmann, D.J., Butler, J.H. and Tans, P.P., 2009. A new look at atmospheric carbon dioxide. Atmospheric Environment, 43(12), pp.2084-2086.

Hogg, A.G., Fifield, L.K., Turney, C.S., Palmer, J.G., Galbraith, R. and Baillie, M.G., 2006. Dating ancient wood by high-sensitivity liquid scintillation counting and accelerator mass spectrometry—pushing the boundaries. Quaternary Geochronology, 1(4), pp.241-248.

Hogg, A.G., Hua, Q., Blackwell, P.G., Niu, M., Buck, C.E., Guilderson, T.P., Heaton, T.J., Palmer, J.G., Reimer, P.J., Reimer, R.W. and Turney, C.S., 2013. SHCal13 Southern Hemisphere calibration, 0–50,000 years cal BP. Radiocarbon, 55(4), pp.1889-1903.

Houghton, R.A., 1995. Changes in the storage of terrestrial carbon since 1850. Soils and global change, pp.45-65.

Houghton, R.A., 2003. Revised estimates of the annual net flux of carbon to the atmosphere from changes in land use and land management 1850–2000. Tellus B: Chemical and Physical Meteorology, 55(2), pp.378-390.

Houghton, R.A., 2007. Balancing the global carbon budget. Annu. Rev. Earth Planet. Sci., 35, pp.313-347.

Hua, Q., Barbetti, M., Worbes, M., Head, J. and Levchenko, V.A., 1999. Review of radiocarbon data from atmospheric and tree ring samples for the period 1945-1997 AD. *IAWA journal*, *20*(3), pp.261-283.

Hua, Q., Barbetti, M., Jacobsen, G.E., Zoppi, U. and Lawson, E.M., 2000. Bomb radiocarbon in annual tree rings from Thailand and Australia. Nuclear Instruments and Methods in Physics Research Section B: Beam Interactions with Materials and Atoms, 172(1-4), pp.359-365.

Hua, Q., Barbetti, M., Zoppi, U., Chapman, D.M. and Thomson, B., 2003. Bomb radiocarbon in tree rings from northern New South Wales, Australia: implications for dendrochronology, atmospheric transport, and air-sea exchange of CO 2. Radiocarbon, 45(3), pp.431-447.

Hua, Q. and Barbetti, M., 2004. Review of tropospheric bomb 14 C data for carbon cycle modeling and age calibration purposes. Radiocarbon, 46(3), pp.1273-1298.

Hua, Q., Barbetti, M. and Rakowski, A.Z., 2013. Atmospheric radiocarbon for the period 1950–2010. Radiocarbon, 55(4), pp.2059-2072.

Ito, T., Woloszyn, M. and Mazloff, M., 2010. Anthropogenic carbon dioxide transport in the Southern Ocean driven by Ekman flow. Nature, 463(7277), pp.80-83.

Jansen, H.S., 1970. Secular variation of radiocarbon in New Zealand and Australian trees.—Radiocarbon Variations and Absolute Chronology. In Proceedings of the Twelfth Nobel Symposium held at the Institute of Physics at Uppsala University. Stockholm.

Kagawa, A., Sugimoto, A. and Maximov, T.C., 2006. 13CO2 pulse-labelling of photoassimilates reveals carbon allocation within and between tree rings. *Plant, Cell & Environment*, *29*(8), pp.1571-1584.

Kalnay, E., Kanamitsu, M., Kistler, R., Collins, W., Deaven, D., Gandin, L., Iredell, M., Saha, S., White, G., Woollen, J. and Zhu, Y., 1996. The NCEP/NCAR 40-year reanalysis project. Bulletin of the American meteorological Society, 77(3), pp.437-472.

Keeling, C.D., 1960. The concentration and isotopic abundances of carbon dioxide in the atmosphere. Tellus, 12(2), pp.200-203.

Khatiwala, S.P., Tanhua, T., Mikaloff Fletcher, S.E., Gerber, M., Doney, S.C., Graven, H.D., Gruber, N., McKinley, G.A., Murata, A., Ríos, A.F. and Sabine, C.L., 2013. Global ocean storage of anthropogenic carbon. Biogeosciences, 10(4), pp.2169-2191.

Kromer, B. and Münnich, K.O., 1992. CO 2 gas proportional counting in radiocarbon dating—review and perspective. In Radiocarbon after four decades (pp. 184-197). Springer, New York, NY.

Kurokawa, H., Yoshida, T., Nakamura, T., Lai, J. and Nakashizuka, T., 2003. The age of tropical rain-forest canopy species, Borneo ironwood(Eusideroxylon zwageri), determined by super (14) C dating. Journal of Tropical Ecology, 19(1), pp.1-7.

Lal, D. and Peters, B., 1962. Cosmic ray produced isotopes and their application to problems in geophysics. Progr. Elem. Particle Cosmic Ray Phys., 6.

Landschützer, P., Gruber, N., Bakker, D.C. and Schuster, U., 2014. Recent variability of the global ocean carbon sink. Global Biogeochemical Cycles, 28(9), pp.927-949.

Landschützer, P., Gruber, N., Haumann, F.A., Rödenbeck, C., Bakker, D.C., Van Heuven, S., Hoppema, M., Metzl, N., Sweeney, C., Takahashi, T. and Tilbrook, B., 2015. The reinvigoration of the Southern Ocean carbon sink. Science, 349(6253), pp.1221-1224.

Landschuetzer, P., Gruber, N. and Bakker, D.C., 2016. Decadal variations and trends of the global ocean carbon sink. *Global Biogeochemical Cycles*, *30*(10), pp.1396-1417.

Lashof, D.A., 1989. The dynamic greenhouse: feedback processes that may influence future concentrations of atmospheric trace gases and climatic change. Climatic change, 14(3), pp.213-242.

Law, R.M., Matear, R.J. and Francey, R.J., 2008. Comment on" Saturation of the Southern Ocean CO2 Sink Due to Recent Climate Change". science, 319(5863), pp.570-570.

Lehman, S.J., Miller, J.B., Wolak, C., Southon, J., Tans, P.P., Montzka, S.A., Sweeney, C., Andrews, A., LaFranchi, B., Guilderson, T.P. and Turnbull, J.C., 2013. Allocation of terrestrial carbon sources using 14CO2: Methods, measurement, and modeling. Radiocarbon, 55(2–3), pp.1484-1495.

Lenton, T.M., 2000. Land and ocean carbon cycle feedback effects on global warming in a simple Earth system model. Tellus B: Chemical and Physical Meteorology, 52(5), pp.1159-1188.

Lenton, A., Codron, F., Bopp, L., Metzl, N., Cadule, P., Tagliabue, A. and Le Sommer, J., 2009. Stratospheric ozone depletion reduces ocean carbon uptake and enhances ocean acidification. Geophysical Research Letters, 36(12).

Le Quéré, C., Andrew, R., Canadell, J.G., Sitch, S., Korsbakken, J.I., Peters, G.P., Manning, A.C., Boden, T.A., Tans, P.P., Houghton, R.A. and Keeling, R.F., 2016. Global carbon budget 2016.

Levin, I., Münnich, K.O. and Weiss, W., 1980. The effect of anthropogenic CO 2 and 14 C sources on the distribution of 14 C in the atmosphere. Radiocarbon, 22(2), pp.379-391.

Levin, I., Kromer, B., Schoch-Fischer, H., Bruns, M., Münnich, M., Berdau, D., Vogel, J.C. and Münnich, K.O., 1985. 25 years of tropospheric 14 C observations in central Europe. Radiocarbon, 27(1), pp.1-19.

Levin, I. and Kromer, B., 1997. Twenty years of atmospheric 14 CO 2 observations at Schauinsland station, Germany. Radiocarbon, 39(2), pp.205-218.

Levin, I. and Hesshaimer, V., 2000. Radiocarbon–a unique tracer of global carbon cycle dynamics. Radiocarbon, 42(1), pp.69-80.

Levin, I. and Kromer, B., 2004. The tropospheric 14 CO 2 level in mid-latitudes of the Northern Hemisphere (1959–2003). Radiocarbon, 46(3), pp.1261-1272.

Levin, I., Naegler, T., Kromer, B., Diehl, M., Francey, R., Gomez-Pelaez, A., Steele, P., Wagenbach, D., Weller, R. and Worthy, D., 2010. Observations and modelling of the global distribution and long-term trend of atmospheric 14CO2. Tellus B: Chemical and Physical Meteorology, 62(1), pp.26-46.

Li, Y., Liu, Y., Chen, W., Wang, Q., Liu, Y., Li, J. and Yu, H., 2016. Facile extraction of cellulose nanocrystals from wood using ethanol and peroxide solvothermal pretreatment followed by ultrasonic nanofibrillation. Green Chemistry, 18(4), pp.1010-1018.

Loader, N.J., Robertson, I., Barker, A.C., Switsur, V.R. and Waterhouse, J.S., 1997. An improved technique for the batch processing of small wholewood samples to α-cellulose. Chemical Geology, 136(3-4), pp.313-317.

Lovenduski, N.S., Gruber, N. and Doney, S.C., 2008. Toward a mechanistic understanding of the decadal trends in the Southern Ocean carbon sink. Global Biogeochemical Cycles, 22(3).

Lowe, D.C. and Judd, W.J., 1987. Graphite target preparation for radiocarbon dating by accelerator mass spectrometry. Nuclear Instruments and Methods in Physics Research Section B: Beam Interactions with Materials and Atoms, 28(1), pp.113-116.

Lumpkin, R. and Speer, K., 2007. Global ocean meridional overturning. Journal of Physical Oceanography, 37(10), pp.2550-2562.

Lüthi, D., Le Floch, M., Bereiter, B., Blunier, T., Barnola, J.M., Siegenthaler, U., Raynaud, D., Jouzel, J., Fischer, H., Kawamura, K. and Stocker, T.F., 2008. High-resolution carbon dioxide concentration record 650,000–800,000 years before present. Nature, 453(7193), pp.379-382.

MacKay, C., Pandow, M. and Wolfgang, R., 1963. On the chemistry of natural radiocarbon. Journal of Geophysical Research, 68(13), pp.3929-3931.

Manning, M.R., Lowe, D.C., Melhuish, W.H., Sparks, R.J., Wallace, G., Brenninkmeijer, C.A.M. and McGill, R.C., 1990. The Use of Radiocarbon Measurements in Atmospheric Studies 1. Radiocarbon, 32(1), pp.37-58.

Manning, M.R. and Melhuish, W.H., 1994. Atmospheric Δ 14 C record from Wellington. Methods, 1954, p.93.

Marra, M.J., Alloway, B.V. and Newnham, R.M., 2006. Paleoenvironmental reconstruction of a well-preserved Stage 7 forest sequence catastrophically buried by basaltic eruptive deposits, northern New Zealand. Quaternary Science Reviews, 25(17-18), pp.2143-2161.

Marshall, J. and Speer, K., 2012. Closure of the meridional overturning circulation through Southern Ocean upwelling. Nature Geoscience, 5(3), pp.171-180.

McCarroll, D. and Loader, N.J., 2004. Stable isotopes in tree rings. Quaternary Science Reviews, 23(7-8), pp.771-801.

McKinley, G.A., Fay, A.R., Lovenduski, N.S. and Pilcher, D.J., 2017. Natural variability and anthropogenic trends in the ocean carbon sink. *Annual review of marine science*, *9*, pp.125-150.

Meijer, H.A.J., Smid, H.M., Perez, E. and Keizer, M.G., 1996. Isotopic characterisation of anthropogenic CO2 emissions using isotopic and radiocarbon analysis. Physics and Chemistry of the Earth, 21(5-6), pp.483-487.

Meijer, H.A.J., Pertuisot, M.H. and van der Plicht, J., 2006. High-accuracy 14 C measurements for atmospheric CO 2 samples by AMS. Radiocarbon, 48(3), pp.355-372.

Mikaloff Fletcher, S.E., Gruber, N., Jacobson, A.R., Doney, S.C., Dutkiewicz, S., Gerber, M., Follows, M., Joos, F., Lindsay, K., Menemenlis, D. and Mouchet, A., 2006. Inverse estimates of anthropogenic CO2 uptake, transport, and storage by the ocean. Global biogeochemical cycles, 20(2).

Mikaloff-Fletcher, S.E., 2015. An increasing carbon sink?. Science, 349(6253), pp.1165-1165.

Miller, J.B., Lehman, S.J., Montzka, S.A., Sweeney, C., Miller, B.R., Karion, A., Wolak, C., Dlugokencky, E.J., Southon, J., Turnbull, J.C. and Tans, P.P., 2012. Linking emissions of fossil fuel CO2 and other anthropogenic trace gases using atmospheric 14CO2. Journal of Geophysical Research: Atmospheres, 117(D8).

Miller, J.B., Lehman, S., Wolak, C., Turnbull, J., Dunn, G., Graven, H., Keeling, R., Meijer, H.A., Aerts-Bijma, A.T., Palstra, S.W. and Smith, A.M., 2013. Initial results of an intercomparison of AMS-based atmospheric 14CO2 measurements. Radiocarbon, 55(2–3), pp.1475-1483.

Munro, D.R., Lovenduski, N.S., Takahashi, T., Stephens, B.B., Newberger, T. and Sweeney, C., 2015. Recent evidence for a strengthening CO2 sink in the Southern Ocean from carbonate system measurements in the Drake Passage (2002–2015). Geophysical Research Letters, 42(18), pp.7623-7630.

Naegler, T. and Levin, I., 2006. Closing the global radiocarbon budget 1945–2005. Journal of Geophysical Research: Atmospheres, 111(D12).

Naegler, T., Ciais, P., Rodgers, K. and Levin, I., 2006(b). Excess radiocarbon constraints on air-sea gas exchange and the uptake of CO2 by the oceans. Geophysical Research Letters, 33(11).

Naegler, T. and Levin, I., 2009. Biosphere-atmosphere gross carbon exchange flux and the δ13CO2 and Δ14CO2 disequilibria constrained by the biospheric excess radiocarbon inventory. Journal of Geophysical Research: Atmospheres, 114(D17).

Naegler, T. and Levin, I., 2009(b). Observation-based global biospheric excess radiocarbon inventory 1963–2005. Journal of Geophysical Research: Atmospheres, 114(D17).

Norris, M., 2015. Reconstruction of historic fossil CO_2 emissions using radiocarbon measurements from tree rings.

Nydal, R. and Lövseth, K., 1965. Distribution of radiocarbon from nuclear tests. Nature, 206(4988), pp.1029-1031.

Nydal, R., 1968. Further investigation on the transfer of radiocarbon in nature. Journal of Geophysical Research, 73(12), pp.3617-3635.

Nydal, R. and Lövseth, K., 1970. Prospective decrease in atmospheric radiocarbon. Journal of Geophysical Research, 75(12), pp.2271-2278.

Nydal, R. and Lövseth, K., 1983. Tracing bomb 14C in the atmosphere 1962–1980. Journal of Geophysical Research: Oceans, 88(C6), pp.3621-3642.

Ohkouchi, N., Eglinton, T.I., Hughen, K.A., Roosen, E. and Keigwin, L.D., 2005. Radiocarbon dating of Alkenones from marine sediments: III. Influence of solvent extraction procedures on 14 C measurements of foraminifera. Radiocarbon, 47(3), pp.425-432.

Olbers, D. and Visbeck, M., 2005. A model of the zonally averaged stratification and overturning in the Southern Ocean. Journal of physical oceanography, 35(7), pp.1190-1205.

Olsson, I.U., 1970. The use of oxalic acid as a standard. Radiocarbon variations and absolute chronology, p.17.

Olsson, I.U., Klasson, M. and Abd-El-Mageed, A., 1972. Uppsala natural radiocarbon measurements XI. Radiocarbon, 14(1), pp.247-271.

Oukebdane, K., Portet-Koltalo, F., Machour, N., Dionnet, F. and Desbène, P.L., 2010. Comparison of hot Soxhlet and accelerated solvent extractions with microwave and supercritical fluid extractions for the determination of polycyclic aromatic hydrocarbons and nitrated derivatives strongly adsorbed on soot collected inside a diesel particulate filter. Talanta, 82(1), pp.227-236.

Park, R. and Epstein, S., 1961. Metabolic fractionation of C13 & C12 in plants. Plant Physiology, 36(2), p.133.

Pearson, S., Hua, Q., Allen, K. and Bowman, D.M., 2011. Validating putatively cross-dated Callitris tree-ring chronologies using bomb-pulse radiocarbon analysis. Australian Journal of Botany, 59(1), pp.7-17.

Petit, J.R., Jouzel, J., Raynaud, D., Barkov, N.I., Barnola, J.M., Basile, I., Bender, M., Chappellaz, J., Davis, M., Delaygue, G. and Delmotte, M., 1999. Climate and atmospheric history of the past 420,000 years from the Vostok ice core, Antarctica. Nature, 399(6735), p.429.

Pettersen, R.C., 1984. The chemical composition of wood.

Polach, H.A., Berger, R. and Suess, H.E., 1979. Correlation of 14C activity of NBS oxalic acid with Arizona 1850 wood and ANU sucrose standards. In Radiocarbon Dating. Proceedings of the 9th International 14C Conference. Berkeley: University of California Press. p (pp. 115-24).

Prentice, K.C. and Fung, I.Y., 1990. The sensitivity of terrestrial carbon storage to climate change. Nature, 346(6279), pp.48-51.

Rafter, T.A., 1955. 14C variations in nature and the effect on radiocarbon dating. NZJ Dairy. Sci. Tech, 37, pp.26-38.

Rafter, T.A. and Fergusson, G.J., 1957. The Atom Bomb Effect•[Recent Increase in the Carbon-14 Content of the Atmosphere and Biosphere, Science 126: 557. Broecker, WS, Tucek, CS and EA Olson.(1959) Radiocarbon Analysis of Oceanic CO2 Intern. J. Appl. Radiation and Isotopes, 7, pp.1-18.

Rahmstorf, S., 2002. Ocean circulation and climate during the past 120,000 years. Nature, 419(6903), pp.207-214.

Rajput, P., Sarin, M. and Rengarajan, R., 2011. High-precision GC-MS analysis of atmospheric polycyclic aromatic hydrocarbons (PAHs) and isomer ratios from biomass burning emissions. Journal of Environmental Protection, 2(04), p.445.

Ramsey, C.B., 1995. Radiocarbon calibration and analysis of stratigraphy: the OxCal program. Radiocarbon, 37(2), pp.425-430.

Randerson, J.T., Thompson, M.V., Conway, T.J., Fung, I.Y. and Field, C.B., 1997. The contribution of terrestrial sources and sinks to trends in the seasonal cycle of atmospheric carbon dioxide. Global Biogeochemical Cycles, 11(4), pp.535-560.

Randerson, J.T., Enting, I.G., Schuur, E.A.G., Caldeira, K. and Fung, I.Y., 2002. Seasonal and latitudinal variability of troposphere Δ14CO2: Post bomb contributions from fossil fuels, oceans, the stratosphere, and the terrestrial biosphere. Global Biogeochemical Cycles, 16(4), pp.59-1.

Raupach, M.R., Marland, G., Ciais, P., Le Quéré, C., Canadell, J.G., Klepper, G. and Field, C.B., 2007. Global and regional drivers of accelerating CO2 emissions. Proceedings of the National Academy of Sciences, 104(24), pp.10288-10293.

Raupach, M.R., Canadell, J.G. and Le Quéré, C., 2008. Anthropogenic and biophysical contributions to increasing atmospheric CO 2 growth rate and airborne fraction. Biogeosciences, 5(6).

Reimer, P.J., Brown, T.A. and Reimer, R.W., 2004. Discussion: reporting and calibration of post-bomb 14C data. Radiocarbon, 46(3), pp.1299-1304.

Reimer, P.J., Bard, E., Bayliss, A., Beck, J.W., Blackwell, P.G., Ramsey, C.B., Buck, C.E., Cheng, H., Edwards, R.L., Friedrich, M. and Grootes, P.M., 2013. IntCal13 and Marine13 radiocarbon age calibration curves 0–50,000 years cal BP. Radiocarbon, 55(4), pp.1869-1887.

Richter, B.E., Jones, B.A., Ezzell, J.L., Porter, N.L., Avdalovic, N. and Pohl, C., 1996. Accelerated solvent extraction: a technique for sample preparation. Analytical chemistry, 68(6), pp.1033-1039.

Rinne, K.T., Boettger, T., Loader, N.J., Robertson, I., Switsur, V.R. and Waterhouse, J.S., 2005. On the purification of α-cellulose from resinous wood for stable isotope (H, C and O) analysis. Chemical Geology, 222(1-2), pp.75-82.

Ritter, R., Landschützer, P., Gruber, N., Fay, A.R., Iida, Y., Jones, S., Nakaoka, S., Park, G.H., Peylin, P., Rödenbeck, C. and Rodgers, K.B., 2017. Observation-based trends of the Southern Ocean carbon sink. *Geophysical Research Letters*, *44*(24), pp.12-339.

Rodgers, K.B., Mikaloff-Fletcher, S.E., Bianchi, D., Beaulieu, C., Galbraith, E.D., Gnanadesikan, A., Hogg, A.G., Iudicone, D., Lintner, B.R., Naegler, T. and Reimer, P.J., 2011. Interhemispheric gradient of atmospheric radiocarbon reveals natural variability of Southern Ocean winds. Climate of the Past, (7), pp.1123-1138.

Roeloffzen, J.C., Mook, W.G. and Keeling, C.D., 1991. Trends and variations in stable carbon isotopes of atmospheric carbon dioxide. In Stable isotopes in plant nutrition, soil fertility and environmental studies.

Rozanski, K., Stichler, W., Gonfiantini, R., Scott, E.M., Beukens, R.P., Kromer, B. and Van Der Plicht, J., 1992. The IAEA 14 C intercomparison exercise 1990. Radiocarbon, 34(3), pp.506-519.

Sabine, C.L., Feely, R.A., Gruber, N., Key, R.M., Lee, K., Bullister, J.L., Wanninkhof, R., Wong, C.S.L., Wallace, D.W., Tilbrook, B. and Millero, F.J., 2004. The oceanic sink for anthropogenic CO2. science, 305(5682), pp.367-371.

Santos, G.M., Bird, M.I., Pillans, B., Fifield, L.K., Alloway, B.V., Chappell, J., Hausladen, P.A. and Arneth, A., 2001. Radiocarbon dating of wood using different pretreatment procedures: application to the chronology of Rotoehu Ash, New Zealand. Radiocarbon, 43(2A), pp.239-248.

Sarmiento, J.L., Gloor, M., Gruber, N., Beaulieu, C., Jacobson, A.R., Mikaloff Fletcher, S.E., Pacala, S.W. and Rodgers, K.B., 2010. Trends and regional distributions of land and ocean carbon sinks. Biogeosciences, 7(8), pp.2351-2367.

Schimel, D.S., House, J.I., Hibbard, K.A., Bousquet, P., Ciais, P., Peylin, P., Braswell, B.H., Apps, M.J., Baker, D., Bondeau, A. and Canadell, J., 2001. Recent patterns and mechanisms of carbon exchange by terrestrial ecosystems. Nature, 414(6860), pp.169-172.

Schimel, D., Stephens, B.B. and Fisher, J.B., 2015. Effect of increasing CO2 on the terrestrial carbon cycle. Proceedings of the National Academy of Sciences, 112(2), pp.436-441.

Schmitz Jr, W.J., 1995. On the interbasin-scale thermohaline circulation. Reviews of Geophysics, 33(2), pp.151-173.

Schulze, E.D., 2006. Biological control of the terrestrial carbon sink.

Schuur, E.A., Druffel, E.R. and Trumbore, S.E., 2016. Radiocarbon and climate change. Switzerland: Springer International Publishing Switzerland.

Scott, E.M., 2003. Section 1: the fourth international radiocarbon intercomparison (FIRI). Radiocarbon, 45(2), pp.135-150.

Scott, E.M., Naysmith, P. and Cook, G.T., 2017. Should archaeologists care about 14C inter-comparisons? Why? A summary report on SIRI. Radiocarbon, 59(5), pp.1589-1596.

Siegenthaler, U. and Oeschger, H., 1987. Biospheric CO2 emissions during the past 200 years reconstructed by deconvolution of ice core data. Tellus B: Chemical and Physical Meteorology, 39(1-2), pp.140-154.

Siegenthaler, U. and Sarmiento, J.L., 1993. Atmospheric carbon dioxide and the ocean. Nature, 365(6442), pp.119-125.

Siegenthaler, U., Stocker, T.F., Monnin, E., Lüthi, D., Schwander, J., Stauffer, B., Raynaud, D., Barnola, J.M., Fischer, H., Masson-Delmotte, V. and Jouzel, J., 2005. Stable carbon cycle–climate relationship during the late Pleistocene. Science, 310(5752), pp.1313-1317.

Sitch, S., Friedlingstein, P., Gruber, N., Jones, S.D., Murray-Tortarolo, G., Ahlström, A., Doney, S.C., Graven, H., Heinze, C., Huntingford, C. and Levis, S., 2015. Recent trends and drivers of regional sources and sinks of carbon dioxide. Biogeosciences, 12(3), pp.653-679.

Solomon, S., Plattner, G.K., Knutti, R. and Friedlingstein, P., 2009. Irreversible climate change due to carbon dioxide emissions. Proceedings of the national academy of sciences, 106(6), pp.1704-1709.

Southon, J.R. and Magana, A.L., 2010. A comparison of cellulose extraction and ABA pretreatment methods for AMS 14 C dating of ancient wood. Radiocarbon, 52(3), pp.1371-1379.

Speer, K., Guilyardi, É. and Madec, G., 2000. Southern Ocean transformation in a coupled model with and without eddy mass fluxes. Tellus A, 52(5), pp.554-565.

Staff, R.A., Reynard, L., Brock, F. and Ramsey, C.B., 2014. Wood pretreatment protocols and measurement of tree-ring standards at the Oxford Radiocarbon Accelerator Unit (ORAU). Radiocarbon, 56(2), pp.709-715.

Stein, A.F., Draxler, R.R., Rolph, G.D., Stunder, B.J., Cohen, M.D. and Ngan, F., 2015. NOAA's HYSPLIT atmospheric transport and dispersion modeling system. Bulletin of the American Meteorological Society, 96(12), pp.2059-2077.

Stephens, B.B., Brailsford, G.W., Gomez, A.J., Riedel, K., Fletcher, S.M., Nichol, S. and Manning, M., 2013. Analysis of a 39-year continuous atmospheric CO2 record from Baring Head, New Zealand. Biogeosciences, 10(4), p.2683.

Stuiver, M. and Polach, H.A., 1977. Discussion reporting of 14 C data. Radiocarbon, 19(3), pp.355-363.

Stuiver, M. and Quay, P.D., 1980. Changes in atmospheric carbon-14 attributed to a variable sun. Science, 207(4426), pp.11-19.

Stuiver, M. and Quay, P.D., 1981. Atmospheric14C changes resulting from fossil fuel CO2 release and cosmic ray flux variability. Earth and Planetary Science Letters, 53(3), pp.349-362.

Stuiver, M., 1983. International agreements and the use of the new oxalic acid standard. Radiocarbon, 25(2), pp.793-795.

Stuiver, M. and Braziunas, T.F., 1989. Atmospheric 14 C and century-scale solar oscillations. Nature, 338(6214), pp.405-408.

Stuiver, M. and Braziunas, T.F., 1993. Sun, ocean, climate and atmospheric 14CO2: an evaluation of causal and spectral relationships. the holocene, 3(4), pp.289-305.

Stuiver, M. and Reimer, P.J., 1993. Extended 14 C data base and revised CALIB 3.0 14 C age calibration program. Radiocarbon, 35(1), pp.215-230.

Suess, H.E., 1955. Radiocarbon concentration in modern wood. Science, 122(3166), pp.415-417.

Suess, H.E., 1965. Secular variations of the cosmic-ray-produced carbon 14 in the atmosphere and their interpretations. Journal of Geophysical Research, 70(23), pp.5937-5952.

Sweeney, C., Gloor, E., Jacobson, A.R., Key, R.M., McKinley, G., Sarmiento, J.L. and Wanninkhof, R., 2007. Constraining global air-sea gas exchange for CO2 with recent bomb 14C measurements. Global Biogeochemical Cycles, 21(2).

Takahashi, T., Sutherland, S.C., Wanninkhof, R., Sweeney, C., Feely, R.A., Chipman, D.W., Hales, B., Friederich, G., Chavez, F., Sabine, C. and Watson, A., 2009. Climatological mean and decadal change in surface ocean pCO2, and net sea–air CO2 flux over the global oceans. Deep Sea Research Part II: Topical Studies in Oceanography, 56(8-10), pp.554-577.

Talley, L.D., 2011. Descriptive physical oceanography: an introduction. Academic press.

Talley, L.D., 2013. Closure of the global overturning circulation through the Indian, Pacific, and Southern Oceans: Schematics and transports. Oceanography, 26(1), pp.80-97.

Tamsitt, V., Drake, H.F., Morrison, A.K., Talley, L.D., Dufour, C.O., Gray, A.R., Griffies, S.M., Mazloff, M.R., Sarmiento, J.L., Wang, J. and Weijer, W., 2017. Spiraling pathways of global deep waters to the surface of the Southern Ocean. Nature communications, 8(1), pp.1-10.

Tans, P.P., De Jong, A.F.M. and Mook, W.G., 1978. Chemical pretreatment and radial flow of 14 C in tree rings. Nature, 271(5642), pp.234-235.

Tans, P.P., De Jong, A.F.M. and Mook, W.G., 1979. Natural atmospheric 14 C variation and the Suess effect. Nature, 280(5725), pp.826-828.

Tans, P.J.E.T.E.R., 1981. A compilation of bomb 14C data for use in global carbon model calculations. Carbon Cycle Modeling, pp.131-157.

Tans, P.P., Conway, T.J. and Nakazawa, T., 1989. Latitudinal distribution of the sources and sinks of atmospheric carbon dioxide derived from surface observations and an atmospheric transport model. Journal of Geophysical Research: Atmospheres, 94(D4), pp.5151-5172.

Telegadas, K., 1971. The seasonal atmospheric distribution and inventories of excess carbon-14 from March 1955 to July 1969. Report HASL, 243, pp.12-187.

Trumbore, S., 2000. Age of soil organic matter and soil respiration: radiocarbon constraints on belowground C dynamics. Ecological Applications, 10(2), pp.399-411.

Turnbull, J.C., Miller, J.B., Lehman, S.J., Tans, P.P., Sparks, R.J. and Southon, J., 2006. Comparison of 14CO2, CO, and SF6 as tracers for recently added fossil fuel CO2 in the atmosphere and implications for biological CO2 exchange. Geophysical research letters, 33(1).

Turnbull, J.C., Lehman, S.J., Miller, J.B., Sparks, R.J., Southon, J.R. and Tans, P.P., 2007. A new high precision 14CO2 time series for North American continental air. Journal of Geophysical Research: Atmospheres, 112(D11).

Turnbull, J.C., Graven, H., Miller, J. and Lehman, S., 2013. Atmospheric radiocarbon workshop report. Radiocarbon, 55(2–3), pp.1470-1474.

Turnbull, J.C., Zondervan, A., Kaiser, J., Norris, M., Dahl, J., Baisden, T. and Lehman, S., 2015. High-precision atmospheric 14CO2 measurement at the Rafter Radiocarbon Laboratory. Radiocarbon, 57(3), pp.377-388.

Turnbull, J.C., Fletcher, S.E.M., Brailsford, G.W., Moss, R.C., Norris, M.W. and Steinkamp, K., 2017. Sixty years of radiocarbon dioxide measurements at Wellington, New Zealand: 1954–2014. Atmospheric Chemistry and Physics, 17(23), p.14771.

Laan, V.D., Karstens, U., Neubert, R.E.M., Laan-Luijkx, V.D. and Meijer, H.A.J., 2010. Observation-based estimates of fossil fuel-derived CO2 emissions in the Netherlands using Δ14C, CO and 222Radon. Tellus B: Chemical and Physical Meteorology, 62(5), pp.389-402.

Van der Plicht, J., Wijma, S., Aerts, A.T., Pertuisot, M.H. and Meijer, H.A.J., 2000. Status report: the Groningen AMS facility. Nuclear Instruments and Methods in Physics Research Section B: Beam Interactions with Materials and Atoms, 172(1-4), pp.58-65.

Wang, P., Zhang, Q., Wang, Y., Wang, T., Li, X., Ding, L. and Jiang, G., 2010. Evaluation of Soxhlet extraction, accelerated solvent extraction and microwave-assisted extraction for the determination of polychlorinated biphenyls and polybrominated diphenyl ethers in soil and fish samples. Analytica Chimica Acta, 663(1), pp.43-48.

Wanninkhof, R., 1992. Relationship between wind speed and gas exchange over the ocean. Journal of Geophysical Research: Oceans, 97(C5), pp.7373-7382.

Wanninkhof, R., Asher, W.E., Ho, D.T., Sweeney, C. and McGillis, W.R., 2009. Advances in quantifying air-sea gas exchange and environmental forcing.

Wilson, A.T. and Grinsted, M.J., 1977. 12 C/13 C in cellulose and lignin as palaeothermometers. Nature, 265(5590), pp.133-135.

WMO, 20th WMO/IAEA Meeting on Carbon Dioxide, Other Greenhouse Gases and Related Measurement Techniques, 2020.

Zondervan, A., Hauser, T.M., Kaiser, J., Kitchen, R.L., Turnbull, J.C. and West, J.G., 2015. XCAMS: The compact 14C accelerator mass spectrometer extended for 10Be and 26Al at GNS Science, New Zealand. Nuclear Instruments and Methods in Physics Research Section B: Beam Interactions with Materials and Atoms, 361, pp.25-33.